Development of Advanced Adsorbent Beds for Storing Thermal Energy Derived from Solar and Waste Heat

Kapil Narwal

A DISSERTATION SUBMITTED TO
THE FACULTY OF GRADUATE STUDIES
IN PARTIAL FULFILLMENT OF THE REQUIREMENTS
FOR THE DEGREE OF
DOCTOR OF PHILOSOPHY

GRADUATE PROGRAM IN MECHANICAL ENGINEERING
YORK UNIVERSITY
TORONTO, ONTARIO

October 2023

Abstract

Climate change is an undeniable reality. A pivotal focus in the battle against climate change is sustainability. One way to achieve this is through safeguarding the environment, optimizing natural resource usage, and minimizing waste. Solar energy has played a vital role in advancing sustainability efforts. This energy can be harnessed as electricity or heat. Emerging technologies, including flat plate collectors and evacuated tube collectors, provide promising pathways for harvesting solar thermal energy.

Thermal energy storage for short-distance mobile applications is an attractive research domain. The first objective of this research work evaluate the zeolite 13X for short-distance mobile thermal energy storage applications. The study investigates the feasibility of storing thermal energy in zeolite 13X charged externally to dedicated heat recovery units. Impressively, the research demonstrates that zeolite 13X charged at 200°C and stored external to the discharging unit can achieve remarkable energy storage densities (ESD) exceeding 110 kWh/m3 under specific conditions. This achievement aligns with previously reported ESD values in the literature.

A particularly crucial aspect addressed in the research is the integration of adsorbents with solar thermal energy storage systems, a relatively underexplored avenue. The study explores diverse configurations, analyzing their impact on enhancing thermal energy storage performance. Through meticulous experimental analysis utilizing Zeolite 13X and water as the adsorbent-adsorbate pair, the research compares direct irradiation with a solar thermal collector.

Moreover, the research dives into a critical aspect of adsorbent-based thermal energy storage (ATES) systems. While these systems boast high energy storage densities over long durations, these often face limitations in terms of the heat provided by prevalent sources such as industrial waste heat and solar energy. To bridge this gap, the study explores experiments that leverage both simulated solar radiation and waste heat concurrently to charge Zeolite 13X for ATES applications.

Acknowledgements

I am deeply humbled and filled with gratitude as I stand at the culmination of my monumental journey in pursuing my PhD. This achievement would not have been possible without the unwavering support, guidance, and encouragement from numerous individuals and institutions, to whom I owe a debt of gratitude.

First and foremost, I express my sincere appreciation to my supervisors, Paul O'Brien (Dr), P.Eng., and Roger Kempers (Dr), P.Eng., Associate Professors in Mechanical Engineering at Lassonde School of Engineering, York University, Toronto, Canada. Their kind guidance, unending support, valuable comments, and unwavering belief in me have been the pillars of strength that have shaped this thesis.

I extend my heartfelt thanks to my thesis committee members, Thomas Cooper (Dr), P.Eng., and Sadek Hossam (Dr), P.Eng., Associate Professors in Mechanical Engineering at Lassonde School of Engineering, York University, Toronto, Canada. Their valuable time, constructive critique, and invaluable suggestions have significantly enriched the quality of this thesis.

Gratitude is also due to all the esteemed course directors and faculty members at Lassonde School of Engineering, York University, whose kind support, and insightful discussions during this research journey have been immensely valuable.

To my fellow research scholars, teammates, research assistants, visiting students, and colleagues, thank you for your love, camaraderie, and unwavering support. Our collaborations and shared ideas have created an inspiring environment for research.

A special mention goes to my dedicated lab mates, Ahmed Moustafa Sayed Elkholy, Nima Talebzadeh Gargari, and Behdad Rezanejad Zanjani. Your technical assistance, camaraderie, and willingness to share ideas have significantly influenced the course of this research.

I express my sincere appreciation to the technical support staff and administrative team at Lassonde School of Engineering, York University, for their seamless assistance, which has been essential in ensuring the smooth functioning of experiments and logistics.

To my friends and family, your unending love, encouragement, and patience throughout this arduous journey have been my greatest source of strength. I am forever grateful for your unwavering belief in me.

I wish to express my profound gratitude to Dr Sujata Nayak for her contributions that have played a vital role in shaping my academic and personal growth. I also extend my thanks to all the unknown individuals who have left lasting impacts on my journey through brief encounters, insightful discussions, and acts of kindness.

My heartfelt appreciation goes to the Canadian Government, York University, and its Lassonde School of Engineering for their support through scholarships, funding, and grants. This research work would not have been possible without their instrumental contributions.

In conclusion, this thesis is a culmination of the collective efforts and unwavering support from these incredible people and institutions. Your belief in me and this research has been the driving force behind its successful completion.

With profound gratitude,

Kapil Narwal

October 2023

Table of Contents

List of Figures

List of Tables

List of Symbols

AH_i	Inlet absolute humidity (g/m^3)
AH_o	Outlet absolute humidity (g/m^3)
$C_{p_{air}}$	Heat capacity of the air exiting the adsorption bed (kJ/kg·K)
$C_{p_{wv}}$	Heat capacity of the water vapour exiting the adsorption bed (kJ/kg·K)
$C_{p_{ma}}$	Heat capacity of the moist air exiting the adsorption bed (kJ/kg·K)
$\dot{m}$	Mass flow rate of the air through the adsorption bed (kg/s)
P_{std}	Standard air pressure (kPa)
$(P_{wv})_{sat}$	Partial water vapour pressure (kPa)
RH_i	Inlet relative humidity (%)
RH_o	Outlet relative humidity (%)
t	Time period (s)
ΔT	Difference between the air temperatures at the outlet and inlet of the adsorption bed (°C)
T_i	Inlet air temperature (°C)
T_1	Temperature in the adsorption bed 27 mm from the inlet (°C)
T_2	Temperature in the adsorption bed 53 mm from the inlet (°C)
T_3	Temperature in the adsorption bed 80 mm from the inlet (°C)
T_4	Temperature in the adsorption bed 107 mm from the inlet (°C)
T_5	Temperature in the adsorption bed 133 mm from the inlet (°C)
T_{C1}	Temperature in the adsorption bed 5 mm from the top of aluminum adsorption bed (°C)

T_{C2}	Temperature in the adsorption bed 15 mm from the top of aluminum adsorption bed (°C)
T_{C3}	Temperature in the adsorption bed 25 mm from the top of aluminum adsorption bed (°C)
T_{C4}	Temperature in the adsorption bed 35 mm from the top of aluminum adsorption bed (°C)
T_o	Outlet air temperature (°C)
V_1	Air control valve at the inlet manifold
V_2	Inlet valve
V_3	Outlet valve
V_4	Air control valve at the outlet manifold
x	Humidity ratio
ρ_{air}	Air density (kg/m^3)
η	Energy storage efficiency (%)

Glossary

Abbreviations

ADC	**A**dsorption **D**esalination-**C**ooling system
AP	**A**cidification **P**otential
ATES	**A**bsorbent-based **T**hermal **E**nergy **S**torage
CAGR	**C**ompound **A**nnual Growth **R**ate
CCS	**C**arbon **C**apture and **S**torage
CFC	**C**hloro**f**luoro**c**arbones
CECA	Communauté européenne du charbon et de l'acier
CFD	**C**omputational **F**luid **D**ynamics
COP	**C**oefficient of **P**erformance
CO_2	Carbon dioxide
CPC	**C**ompound **P**arabolic **C**oncentrator
CPVT	**C**oncentrating **P**hoto**v**oltaic/**T**hermal
EA	**E**conomic **A**ssessment
EBD	**E**nvironmental **B**urden of **D**isease
EHIA	**E**nvironmental **H**ealth **A**ssessment
EIA	**E**nvironmental **I**mpact **A**ssessment
EP	**E**utrophication **P**otential
ESD	**E**nergy **S**torage **D**ensity
EU	**E**uropean **U**nion
EU ETS	**E**uropean **U**nion **E**missions **T**rading **S**ystem
EV	**E**lectric **V**ehicle
FAU	**Fau**jasite, a mineral group in zeolite family of silicate minerals

GDP	**G**ross **D**omestic **P**roduct
GHG	**G**reen**h**ouse **G**as
GLAP	**G**ravimetric **L**arge **P**ressure **J**ump
GSM	**G**ross **S**quare **M**eters
GW	**G**iga**w**att, a unit of power
GWP	**G**lobal **W**arming **P**otential
HCFC	**H**ydro**c**hloro**f**luoro**c**arbons
IAM`	**I**ntegrated Assessment **M**odeling
IEA	**I**nternational **E**nergy **A**gency
IRENA	**I**nternational **R**enewable **En**ergy **A**gency
ISHPC	**I**nternational **S**orption **H**eat **P**ump **C**onference
ISO	**I**nternational **S**tandard **O**rganization
IWH	**I**ndustrial **W**aste **H**eat
IWHR	**I**ndustrial **W**aste **H**eat **R**ecovery
kWh	**K**ilo**w**att-**h**our, a unit of energy
LCA	**L**ife **C**ycle **A**ssessment
LCC	**L**ifecycle **C**osting
LED	**L**ight **E**mitting **D**iode
LEED	**L**eadership in **E**nergy and **E**nvironmental **D**esign
MOF	**M**etal **O**rganic **F**ramework
m-TES	**M**obile **T**hermal **E**nergy **S**torage
MW	**M**ega**w**att, a unit of power
PLA	**P**oly**l**actic **A**cid
POCP	**P**hotochemical **O**zone **C**reation **P**otential

PV	**P**hoto**v**oltaic
PVT	**P**hoto**v**oltaic **T**hermal collector
PW	**P**etawatt, a unit of power
RH	**R**elative **H**umidity
SEA	**S**trategic **E**nvironmental **A**ssessment
SACE	**S**olar **A**ir **C**onditioning in **E**urope
SBT	**S**cience-**B**ased **T**argets
SBTi	**S**cience-**B**ased **T**argets **I**nitiative
TCS	**T**hermo**c**hemical Heat **S**torage
TES	**T**hermal **E**nergy **S**torage
THS	**T**hermochemical **H**eat **S**torage
TPS	**T**ransient **P**lane **S**ource
TRNSYS	**T**ransient **S**ystem **S**imulation **T**ool
US	**U**nited **S**tates
UV-Vis	**U**ltraviolet-**v**isible
ZASC	**Z**eolite **A**ssociation **S**tructure **C**ommission

Definitions

Adsorption	It is the process by which adsorbate molecules or particles adhere to the surface of a solid or liquid adsorbent.
Adsorbate	It refers to a substance or molecule that gets adsorbed on the surface of a solid or liquid adsorbent.
Adsorbent	It refers to a solid or liquid medium on the surface of which adsorbate molecules gets adsorbed. Adsorbents are characterized by their high porosity and large specific surface areas, enabling the selective adsorption of adsorbate molecules on their surfaces.
Desorption	It is the opposite process of adsorption. It refers to the release or removal of adsorbate molecules or particles from the surface of solid or liquid adsorbent often through an external factor e.g., heat or pressure.
Charging of adsorbent	It refers to the process of desorbing adsorbate molecules from the surface of a solid or liquid adsorbent to prepare it for the adsorption process.
Discharging of adsorbent	It refers to the process of adsorbing adsorbate molecules on the surface of a solid or liquid adsorbent.
Adsorption bed	It refers to a structured arrangement of adsorbents to facilitate the adsorption or desorption of adsorbate molecules or particles on or from the surface of adsorbents.

1 Introduction

1.1 Importance of Reducing Emissions

Global greenhouse gas (GHG) emissions from fossil fuels and land use have steadily increased since the 19th century, reaching record levels in 2022. GHG emissions, primarily from burning fossil fuels, have led to a temperature increase of approximately 1.4 °C since pre-industrial times [1], [2]. This rise has resulted in a staggering 6.7 million premature deaths annually due to air pollution [3], [4]. Fossil fuels are responsible for nearly 90% of sulfur dioxide emissions [5]. Moreover, fossil fuels still account for around 80% of global energy consumption [6], leaving nations vulnerable to supply disruptions and price fluctuations. Global CO_2 emissions increased by 1.5% in 2022 compared to 2021, reaching 36.1 ± 0.3 $GtCO_2$ [7]. This rise was significant, with emissions consuming about 13% to 36% of the remaining carbon budget to limit global warming to 1.5 °C, suggesting that permissible emissions could be depleted within 2 to 7 years with a 67% likelihood [8]. The COVID-19 pandemic caused a record reduction in global carbon emissions in 2020, but emissions rebounded to near pre-pandemic levels in 2021 [9].

1.2 Policies

The Paris Agreement's goals to limit temperature increases are at risk due to current trends, planned infrastructure, and policy commitments. Emissions originate from five sectors: energy systems, industry, buildings, transport, and agriculture, each facing unique challenges in climate change mitigation. Despite efforts to analyze sector-specific emissions trends, overall progress in reducing GHG emissions remains limited, with most sectors experiencing continued growth, especially in emerging regions. The consumption

patterns in developed regions contribute to rising demand for emission-intensive products and services. Efficient practices and low-carbon technologies are offset by increasing demand. Addressing these drivers and adopting integrated policies are crucial to achieving the Paris Agreement's objectives [10]. The policy implications include improving energy efficiency, technology innovation, and implementing measures like carbon taxes and emissions trading schemes are some of the fastest ways to achieve the set objectives in the set time frame. Further, there has also been a shift in emissions dominance from Europe and the US to Asia, particularly China, with the US and Europe now contributing to one-third of global emissions. Qatar exhibits the highest per capita CO_2 emissions due to its oil production, while wealthier countries like the US, Australia, and Canada also have high per capita emissions. In contrast, many Sub-Saharan African countries have low emissions. This data emphasizes the need for collective efforts from major emitters to combat climate change and achieve global climate targets [11].

1.3 Need for Transitioning to Clean Energy

Transitioning to clean energy therefore is an urgent necessity to address these pressing challenges. The switch to clean energy not only mitigates climate change but also brings substantial economic benefits, as the renewable energy sector employed over 12.7 million people worldwide in 2022 [12]. Additionally, embracing clean energy sources ensures energy security, reduces healthcare costs, and promotes long-term sustainability, as renewable resources are virtually inexhaustible. By making this crucial transition a resilient and sustainable future can be built while safeguarding the planet for generations to come.

Renewable energy adoption is crucial in curbing emissions, and the International Renewable Energy Agency (IRENA) estimates that by increasing the share of renewables in the global energy mix to 66% by

2050, cumulative GHG emissions could be reduced by 40-70%. Furthermore, the International Energy Agency (IEA) highlights that a transition to cleaner energy sources can create millions of jobs, with potential employment in the renewable energy sector reaching 42 million by 2050 [13].

1.4 Opportunity

The transition from fossil fuels to clean energy presents a myriad of opportunities, backed by a wealth of data and statistics demonstrating the potential benefits. The options available to switch to clean energy are diverse and promising. Renewable energy reached a share of 29% by the end of year 2020 from 27% in the year 2021. Solar power, for instance, has witnessed remarkable growth, with global installed capacity reaching over 714 gigawatts (GW) by the end of 2020, accounting for 25.5% of the world's total renewable energy capacity. Wind power has also seen significant expansion, surpassing 733 GW of global installed capacity during the same period, contributing 26.2% to the total renewable energy capacity. Hydropower remains a dominant renewable energy source making up 41.3% of the global renewable energy capacity. Biomass and geothermal energy have been making strides as well, with global installed capacities of around 127 GW and 14 GW, respectively [14].

These figures showcase the immense potential of these renewable sources in driving the shift towards cleaner energy alternatives. Additionally, the renewable energy sector has been experiencing substantial investments, with global investments in renewable power capacity amounting to $303.5 billion in 2020 up 2% from 2019 [15]. This increased financial support has further propelled the growth of clean energy technologies worldwide. The investment in renewable energy is expected to be $1.7 trillion in 2023 [16].

1.5 Initiatives Taken for Decarbonization

Decarbonization is a critical process aimed at reducing and ultimately eliminating greenhouse gas emissions, with a primary focus on carbon dioxide (CO_2), across different sectors of the economy. The main goal of decarbonization is to combat the adverse effects of climate change and global warming by shifting away from fossil fuel-based energy sources and embracing low-carbon or carbon-free alternatives. By curbing the release of CO_2 and other greenhouse gases, decarbonization seeks to mitigate the harmful impact of human activities on the environment and create a sustainable, resilient future for generations to come. Through innovative technologies, policy initiatives, and international cooperation, the global community is working towards a cleaner and greener future, fostering the transition to a more sustainable and climate-friendly world. Here are some key things and initiatives taken to achieve decarbonization, supported by data:

- **Renewable Energy Expansion:** Governments and organizations worldwide are investing heavily in renewable energy sources. Renewable energy sources, including hydropower, solar, wind, and bioenergy, accounted for approximately 25.5% of global electricity generation [14]. China, Europe, United States and India led in renewable energy capacity additions, with China alone accounting for 80% of the global growth in renewable capacity. These four markets account for 43% of the global renewable capacity growth [17].
- **Energy Efficiency Improvements:** Energy-efficient buildings have the potential to reduce energy consumption by 50-85% [18]. In recent years the global energy intensity (energy used per unit of GDP) improved by 1.8% annually, however, it must increase to 2.7% per year [19]. Energy-efficient appliances and technologies can significantly reduce energy demand. For instance, LED

lighting consumes up to 75% less energy than traditional incandescent bulbs, resulting in substantial emission reductions [20].

- **Carbon Pricing and Trading:** Implementing carbon pricing mechanisms, such as carbon taxes and emissions trading systems, incentivizes industries and businesses to reduce emissions. By the end of 2021, 64 carbon pricing initiatives have been implemented globally, covering about 22% of global greenhouse gas emissions [21]. The total value of global carbon pricing initiatives reached $53 billion in 2020-2021[22]. The European Union Emissions Trading System (EU ETS) is the largest carbon market globally, covering approximately 40% of the EU's greenhouse gas emissions. Revenues from Carbon taxes and Emissions Trading Systems globally have reached $95 billion [23].
- **Electric Vehicles (EVs):** Encouraging the adoption of electric vehicles and supporting the development of EV infrastructure helps reduce emissions in the transportation sector. 10% of the global car sales were electric in 2021 which is 4 times the cars sold in 2019. Today there are more than 16.5 million electric vehicles on the roads, with countries like China, Norway, the United States, and Europe leading in EV adoption [24].
- **Reforestation and Afforestation:** Asia, Europe and Oceania are on track to reach a key global forest goal of increasing the forest area by 3% by 2030 [25]. The annual rate of deforestation was estimated at 10 million per hectare between 2015-2022 compared to 12 million hectares during 2010-2015. The protected forest area has also reached 726 million hectares by the end of 2020 [25]. The Bonn Challenge, a global initiative to restore 150 million hectares of degraded and deforested land by 2020, has been surpassed, with pledges to restore over 350 million hectares as of 2030 [26].
- **Decentralized Energy Systems:** Promoting decentralized energy systems, such as microgrids and community solar projects, can increase energy resilience and reduce the reliance on centralized

fossil fuel power plants. In 2022, over 268 GW of distributed solar photovoltaic (PV) capacity was installed globally [27]. The rise of community solar projects contributed to the democratization of renewable energy access.

- **Green Building Standards:** Green building practices are estimated to reduce carbon emissions by 84 gigatons by 2050 [28]. The Leadership in Energy and Environmental Design (LEED) certification system, used in over 167 countries, has certified over 100,000 green building projects [29]. Canada certified 248 projects, representing more than 5.3 million gross square meters (GSM) of LEED space [30].
- **Research and Development:** Investing in research and development of clean energy technologies and carbon capture and storage (CCS) techniques is critical in advancing the decarbonization agenda. Globally, public spending on energy research and development grew by 10% to $44 billion in 2022 with 80% devoted to clean energy. Early-stage venture capitalist investment into clean energy startups reached a record high of $6.7 billion in 2022 [31].
- **Transitioning from Coal:** Phasing out coal-fired power plants and replacing them with cleaner energy sources is a significant step in reducing carbon emissions from the energy sector. As of 2021, over 40 countries have announced plans to phase out coal power [32]. The United Kingdom was the first major economy to commit to ending unabated coal-fired electricity generation by 2024 [33].
- **International Agreements:** Participation in international agreements and commitments, such as the Paris Agreement, reinforces global cooperation in tackling climate change and sets targets for emission reductions. The Paris Agreement's goal is to limit global warming to well below 2 degrees Celsius and strive for 1.5 degrees Celsius above pre-industrial levels [34]. The United States, China, and the European Union are among the top emitters that have pledged to achieve net-zero emissions

by or before 2050, covering 76% of global emissions [35]. A total of 194 countries have ratified the Paris Agreement [36].

- **Corporate Sustainability Initiatives:** Over 2,253 companies are committed to setting Science-Based Targets (SBT), out of which 1,171 are committed to set targets while 1,082 have approved targets to align their emissions reduction goals with the Paris Agreement's objectives. Science-Based Targets Initiative (SBTi) with a global reach in over 70 countries and 15 industries today covers a combined market capitalization of $38 trillion [37].
- **Public Awareness and Education:** Raising public awareness about climate change and the importance of decarbonization is vital in garnering support for clean energy initiatives and lifestyle changes. According to a global survey, 87% of Europeans recognize a need to tackle climate change and environmental issues on a priority basis, and 75% think that governments are not doing enough to address it [38].

1.6 Challenges in Achieving Decarbonization

The transition to clean energy and decarbonization entails significant investments. According to the International Renewable Energy Agency (IRENA), to limit global warming to 1.5 degrees Celsius, an estimated annual investment of around $4.4 trillion is needed in the global energy system until 2050 [39]. This includes investments in renewable energy installations, energy storage, grid upgrades, energy efficiency measures, and sustainable transportation systems. While the costs of renewable energy technologies have been steadily declining, financing such a massive transition remains a challenge, particularly for developing countries with limited financial resources. Additionally, the continued presence of fossil fuel subsidies in some regions hinders the competitiveness of renewable energy sources.

Policymakers and governments need to mobilize financial resources and create conducive policy environments to accelerate the shift towards decarbonization and renewable energy adoption. Furthermore, behavioural change and public acceptance are crucial to drive the transition. Surveys show that while most people recognize the urgency of climate change, there remains a gap between awareness and taking concrete actions to reduce carbon footprints. Raising awareness and implementing effective communication strategies are essential to encouraging individuals and communities to embrace sustainable practices and actively participate in the decarbonization journey.

1.7 Decarbonization in Canada

Canada has committed to the Paris Climate Change agreement, aiming to achieve net-zero emissions by 2050. However, significant challenges stand in the way of this goal. Currently, 70% of Canada's energy needs are met by fossil fuels, making it one of the world's top per-capita emitters of green house gases (GHGs). Canada accounts for 2% of global GHGs despite having just 0.5% of the world's population [40]. Wind and solar power, which have falling costs, are underutilized, supplying only 6.5% of Canada's energy demand [41]. To successfully reach its net-zero target, Canada must urgently prioritise the transition to renewable energy sources and significantly increase the adoption of electric vehicles.

To address these challenges and stay on track to reach its 2050 net-zero emissions goal, Canada needs to focus on its shift towards renewable energy and embracing electric vehicles (EVs). While being a signatory of the Paris Agreement is a positive step, the heavy reliance on fossil fuels and high per-capita emissions necessitates urgent action. By investing in and promoting wind and solar power, the country can diversify its energy sources and reduce emissions. Simultaneously, increasing the global market share of electric

passenger vehicles and freight trucks from the current 2% to 30% by 2030 will play a crucial role in curbing emissions from the transportation sector. Meeting these objectives will not only aid in combatting climate change but also position Canada as a leader in sustainable practices and environmental stewardship [40].

By 2021, Canada's major solar energy capacity reached 2,399 MW, showing a growth of 13.6% compared to the previous year's capacity of 2,111 MW. The new major solar power generation installed in 2021 amounted to 288 MW, with most of this growth occurring in Alberta, which added 250 MW. Smaller amounts were added in Saskatchewan (21 MW), Quebec (9.5 MW), Nova Scotia (4.8 MW), Ontario (0.3 MW), Yukon Territory (1.5 MW), and Prince Edward Island (0.1 MW). Notably, the largest solar farm added in 2021 was the Claresholm Solar project in Alberta, with a capacity of 132 MW. These developments indicate a positive trajectory for Canada's solar energy sector, contributing to the country's efforts to transition to cleaner and more sustainable energy sources [41], [42].

1.8 Thermal Energy Storage

Thermal energy storage (TES) is one crucial component in facilitating a seamless transition from fossil fuels to clean energy. TES plays a pivotal role in managing energy supply and demand efficiently, utilizing surplus thermal energy during off-peak periods and releasing it during peak demand hours. The adoption of TES systems is growing rapidly, with a projected installed capacity of 800 GWh by the year 2030 from 234 GWh in 2019 [43]. The global market for TES is expected to reach $8 billion by 2030 from $4.4 billion in 2022 [44], driven by the rising demand for energy storage technologies in conjunction with renewable energy integration. Europe dominates the global thermal energy storage market with 37.2% of the market share with an expected growth of Compound Annual Growth Rate (CAGR) of 8.4% [45]. Sensible heat

storage, latent heat storage, and thermochemical heat storage (TCS) methods are gaining traction in the TES domain, each offering unique advantages in balancing the grid and ensuring a stable power supply.

TCS utilizes thermochemical reactions to store and release thermal energy, making it an attractive solution for large-scale and long-term energy storage applications. One of the main advantages of TCS is its high energy density, allowing for the storage of substantial thermal energy in a compact volume. For example, TCS systems can achieve energy densities up to 420 kWh/m^3 [46], [47], [48] significantly surpassing conventional sensible heat storage methods in which energy densities range from 10-60 kWh/m^3 [49], [46][47], and latent heat storage systems the energy densities of which range from 27-120 kWh/m^3 [48]. This characteristic makes TCS particularly well-suited for storing excess energy from renewable sources, such as solar and wind power, for later use during peak demand or low energy production periods.

Absorbent-based Thermal Energy Storage (ATES) is a form of TCS that has gained a significant momentum as one of the promising solutions for efficiently storing thermal energy for both short and long durations. ATES systems use highly porous adsorbents to desorb and adsorb adsorbate molecules to store and release thermal energy, respectively. Amongst all popular adsorbent-adsorbate pairs the Zeolite 13X-water pair exhibits excellent properties and performance due to its highly porous surface, energy storage density, abundant availability, and non-toxicity. Zeolite 13X can adsorb a significant amount of water vapor after being dried at relatively low temperatures due its naturally strong affinity towards water molecules. It can also be used to store thermal energy that is available over a wide range of temperatures. The research in this thesis aims to contribute to the reduction of greenhouse gas emissions by advancing the performance of adsorbent-based TES systems. The goal is to enhance the performance of TCS systems by developing improved methods of storing low-grade solar and waste heat using Zeolite 13X-water-based ATES systems as an example.

1.9 Goals and Objectives

1.9.1 Goal

The goal of this thesis is to improve the design of adsorption-based thermal energy storage systems powered by solar energy and waste heat.

1.9.2 Objectives

Objective 1: To evaluate the feasibility of zeolite 13X as a storage medium for short-distance mobile thermal energy storage, focusing on its ability to retain thermal energy from a heat source and subsequently release thermal energy after being transported.

Objective 2: To characterize the thermal energy storage density of zeolite 13X in an adsorption bed integrated with a solar thermal collector and compare the effects of using direct irradiation with indirect irradiation to charge the adsorbents.

Objective 3: To understand the influence of combined solar radiation and industrial waste heat charging on the energy storage performance of zeolite 13X adsorption-based thermal energy storage systems.

1.10 Thesis Overview

This thesis is divided into six chapters. Chapter 2 provides a comprehensive analysis of existing studies, research papers, and relevant literature related to the research conducted in this thesis. Specifically, adsorption processes, adsorption systems, adsorbents and adsorbates, adsorption beds, heat sources, solar energy and solar collectors are covered in Chapter 2. At the end of Chapter 2 the status of the research on adsorption-based TES is discussed, the research gaps addressed in this thesis are outlined, and the objectives

of the thesis are stated at the end of Chapter 1. Chapter 3 details the selection of adsorbent-adsorbate pairs. Chapter 4 addresses Objective 1, which is to evaluate the feasibility of using zeolite 13X as a storage medium for short-distance mobile TES. The current state of mobile thermal energy storage (m-TES) with emphasis on the charging of mobile adsorption beds is reviewed. The materials and methods used to conduct experiments wherein adsorbents were charged outside the adsorbent bed are stated prior to presenting an analysis of the results. Chapter 5 presents the outcome of the research conducted to address Objective 2. The main focus of Objective 2 is to conduct experiments to determine whether charging the zeolites directly with solar irradiation, or using a blackened absorber that transfers heat to the zeolite bed yields a higher energy storage density. The methods used are presented and the results show that a blackened absorber can produce a higher energy storage density if it is thermally isolated from the outer walls of the adsorbent bed. The results from the research directed towards achieving Objective 3 are provided in Chapter 6. The third objective of this thesis is to investigate the benefits of charging adsorption-based thermal energy storage systems by charging them using incident solar radiation and industrial waste heat simultaneously. The results show the energy storage density attained when using solar energy and waste-heat simultaneously is greater than the sum of the energy storage densities measured when using solar energy and waste-heat individually to charge the adsorption bed. The conclusions from this research and recommendations for future work are discussed in Chapter 6.

2 Background and Literature Review

2.1 Adsorption Process

Michael Faraday first observed the adsorption phenomenon in 1848. Until the early nineteenth-century adsorption technology advanced slowly in the refrigeration sector. The first significant use of adsorption refrigerators was done on a train which commuted between London and Liverpool from 1940 to 1945 in which a $CaCl_2$-NH_3 based adsorption refrigerator system was installed. However, the advancements in chlorofluorocarbons (CFCs) and hydrochlorofluorocarbons (HCFCs) in the refrigeration sector reduced the interest of researchers in this technology. It was only later, in the early 1970s, when the rising levels of greenhouse gas (GHG) emissions and depletion of the ozone layer drew the attention of the scientific community to explore alternative refrigeration technologies. Since 1992 the solid sorption refrigeration conference, now known as the International Sorption Heat Pump Conference (ISHPC), is catalysing the technological advancements in adsorptive refrigeration technologies [50].

Adsorption is an exothermic thermochemical surface process in which adsorbate particles adhere to the adsorbent surface. The heat released during the process is called the heat of adsorption and is shown in Figure 2.1. The heat of adsorption depends upon the success of adsorption, which on the other hand depends upon the affinity of adsorbate particles towards the adsorbent surface, molecular sizes of the adsorbent and adsorbate; porosity and pore size of adsorbent particles, and experimental conditions including temperature, pressure, and flow rate of the adsorbate particles within the adsorber. The adhesion of adsorbate particles to the adsorbent surface can be purely physical or chemical. If the adsorption is due to the weak van der Wall forces between the adsorbate and adsorbent particles, it is called physisorption, and if the adsorption is due to chemical bonding or ion exchange on the adsorbent surface, it is called chemisorption. Further,

the adsorption can be single layer or multilayer depending upon the selection of adsorbate-adsorbent pairs. Adsorption is a reversible process; during the desorption process the adsorbate particles desorb from the adsorbent, taking the latent heat of vaporization from a heat source as shown in Figure 2.1. The adsorption-desorption cycle is plotted on a pressure-temperature diagram in Figure 2.2; the state of the system moves from point 2 to 3 during the desorption process, and from point 4 to point 1 during the adsorption process.

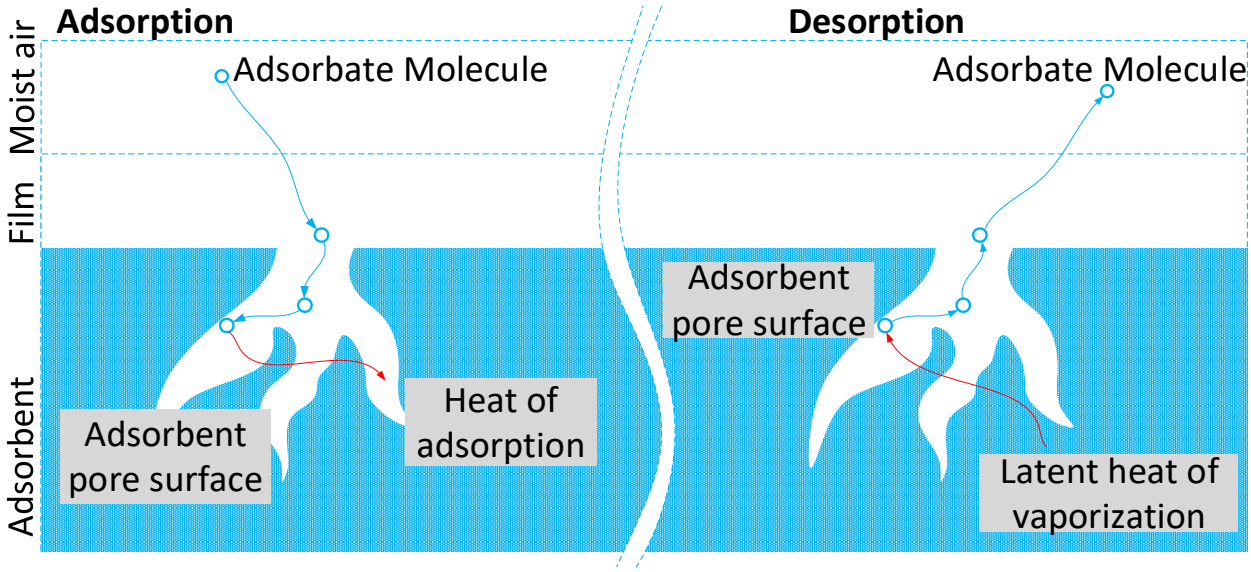

Figure 2.1 Adsorption and desorption phenomenon

The adsorption of adsorbate molecules on the surface of adsorbent involves several steps. The stepwise description of the adsorption process at the molecular level is given below:

1. **Charging of adsorbents:** Adsorbents are charged before the adsorption process begins. Charging involves the desorption of adsorbate molecules present on the adsorbent surfaces. This is typically done by altering the temperature or pressure to favour desorption.

2. **Exposure to adsorbate molecules:** The charged adsorbent is placed inside the adsorption bed and adsorbate molecules, typically entrained in an air stream, enter the adsorption bed.

3. **Diffusion of adsorbate molecules into adsorbent pores:** Depending upon the pore sizes of adsorbents, adsorbate molecules diffuse into the pores of the adsorbent. The structure of the adsorbent provides channels and cages that allow the selective entry of adsorbate molecules based on their size.

4. **Discharging process:** During the discharging process adsorbate molecules are adsorbed onto the active sites within the adsorbent structure. The active sites are locations on the internal surfaces of the adsorbent where interactions, such as weak van der Waals bonding, occur between the adsorbate molecules and the adsorbent.

5. **Molecular Sieving Effect:** The large pores of adsorbents act as a molecular sieve, allowing the adsorption of specific adsorbate molecules while excluding other larger molecules. This molecular sieving effect is a key property of adsorbents and contributes to their selectivity during the adsorption processes.

6. **Formation of a Monolayer:** As more adsorbate molecules are adsorbed the available active sites become occupied and a monolayer of adsorbate molecules forms on the internal surfaces of the adsorbent.

7. **Equilibrium State:** The adsorption process reaches equilibrium when the rate of adsorption equals the rate of desorption. The equilibrium concentration of adsorbents is temperature and pressure dependent. As the adsorbent partial pressure increases and the temperature decreases the adsorbent

becomes saturated, and further exposure to adsorbate molecules does not lead to additional adsorption.

Adsorption based thermochemical energy storage systems often consist of an adsorption bed, an evaporator and a condenser as shown in Figure 2.2b. The adsorption bed is filled with adsorbents and usually acts as both an adsorber and a desorber. Adsorbates cycle through the adsorption bed, condenser and evaporator depending upon the adsorption cycle phase. The thermochemical heat storage process involves an adsorption cycle (illustrated in Figure 2.2a), which comprises two processes, namely the adsorption process and the desorption process. The adsorption cycle can be explained in detail with reference to the Clapeyron diagram shown in Figure 2.2a. During the desorption process a heat source provides thermal energy to bring the adsorption bed up to its regeneration temperature (point 1-2), and the adsorbate molecules desorb from the adsorbent (point 2-3). This process is referred to as charging because the surface of the adsorbent is charged with energy, in the form of high energy surface states, as the adsorbate molecules are desorbed. Once desorption is completed the adsorbate molecules are allowed to undergo isosteric sensible cooling (point 3-4). During the adsorption process, this energy at the surface of the adsorbent is released in the form of heat (point 4-1), as the adsorbate molecules adhere to the adsorbent surface, through a physisorption or chemisorption process. The entire adsorption cycle, comprising the four phases indicated by the bold red arrows in Figure 2.2a, are described in further detail subsequently.

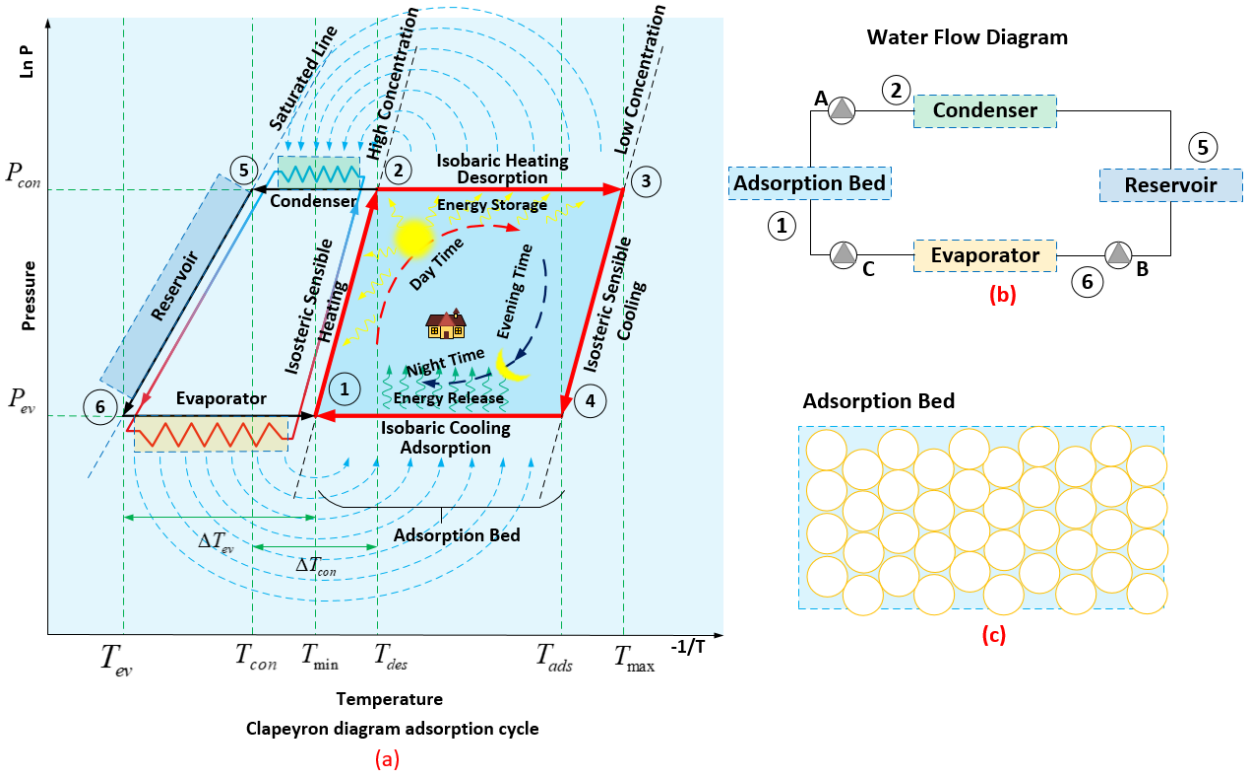

Figure 2.2 a. Clapeyron diagram adsorption cycle, b. components of an adsorption system, c. adsorption bed

Phase 1 (State 1 to 2): At the beginning of this phase, as shown in Figure 2.3, adsorbents are discharged, and have a large quantity of adsorbate molecules on their surface (state 1). The discharged adsorbents are heated sensibly at a constant specific volume (state 1-2) and the temperature increases from T_{min} to T_{des} and the pressure increases from P_{ev} to P_{con}. At point 2, valve A opens when the pressure is equal to the pressure in the condenser and the temperature is equal to the desorption temperature.

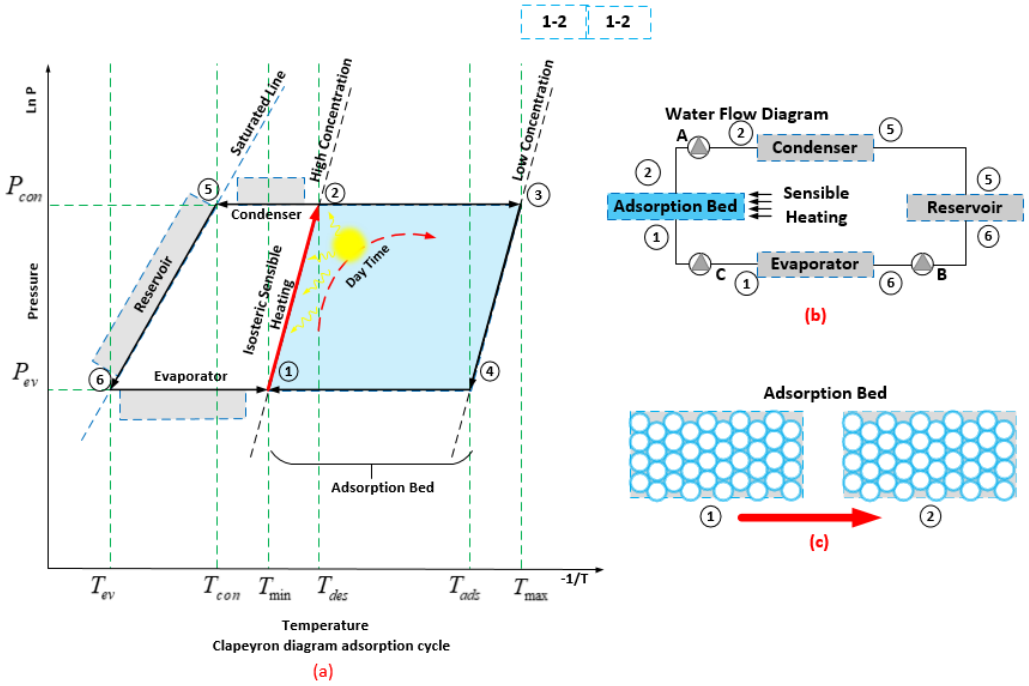

Figure 2.3 a. Phase 1: Isosteric sensible heating b. flow of adsorbate in an adsorption system, c. adsorption bed

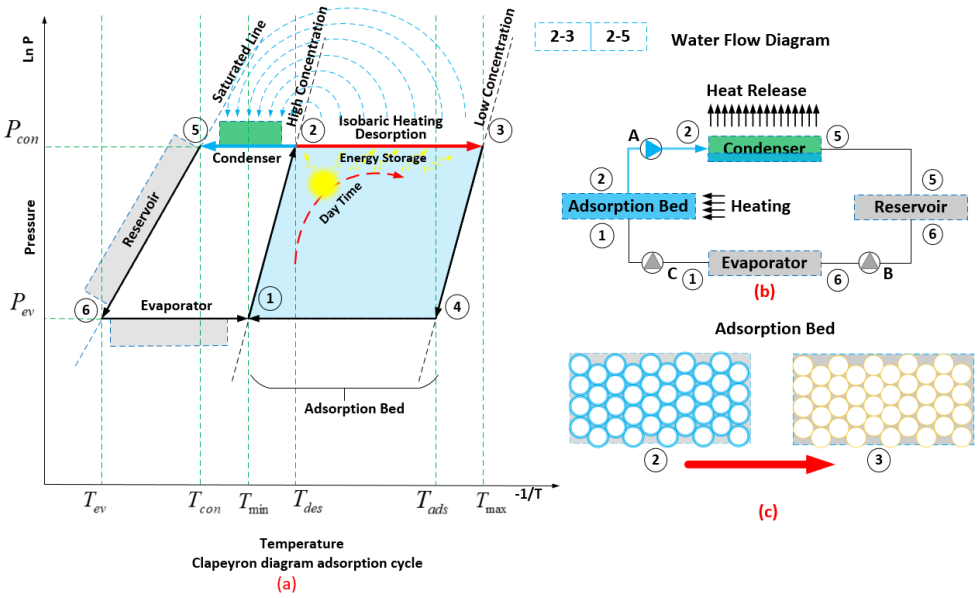

Figure 2.4 a. Phase 2: Isobaric heating (desorption), b. flow of adsorbate in an adsorption system, c. adsorption bed

Phase 2 (state 2 to 3): During this phase, as shown in Figure 2.4, the adsorbents are heated at constant pressure, which is equal to the pressure within the condenser. The state in the adsorption bed moves from a high vapor concentration (state 2) to a low vapor concentration (state 3) on the P-T diagram, as shown in Figure 2.4a, as the temperature of the adsorption bed increases from T_{des} to T_{max}. Desorption occurs, and the adsorbate molecules evaporate from the adsorbents taking the latent heat and condensing within the condenser. The state of the adsorbate molecules moves from point 2 to point 5 on the P-T diagram, as shown in Figure 2.4a, as the heat of condensation is released. The pressure remains constant during this phase, and the temperature of the adsorbates decreases from T_{des} to T_{con}. The concentration of adsorbate molecules in the adsorption bed decreases, and by the end of this phase all the adsorbate molecules are desorbed, and the adsorbents are completely charged.

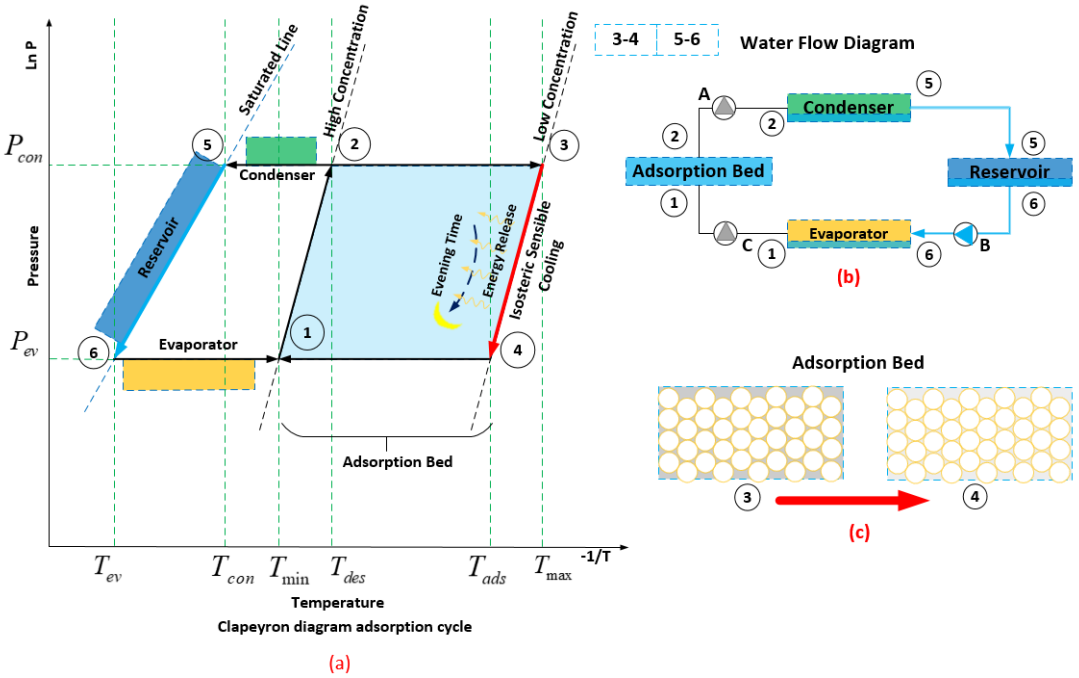

Figure 2.5 a. Phase 3: Isosteric sensible cooling, b. flow of adsorbate in an adsorption system, c. adsorption bed

Phase 3 (State 3 to 4): At the beginning of this phase, as shown in Figure 2.5, adsorbents are completely charged at a temperature T_{max} and pressure P_{con}. During this phase, adsorbents are sensibly cooled as shown in Figure 2.5a (state 3 to 4). The temperature decreases from T_{max} to T_{ads} and the pressure decreases from P_{con} to P_{ev}. At the same time, the adsorbates move from the condenser to the reservoir and cool at constant enthalpy, and subsequently move to the evaporator through valve B as shown in Figure 2.5b (state 5 to 6).

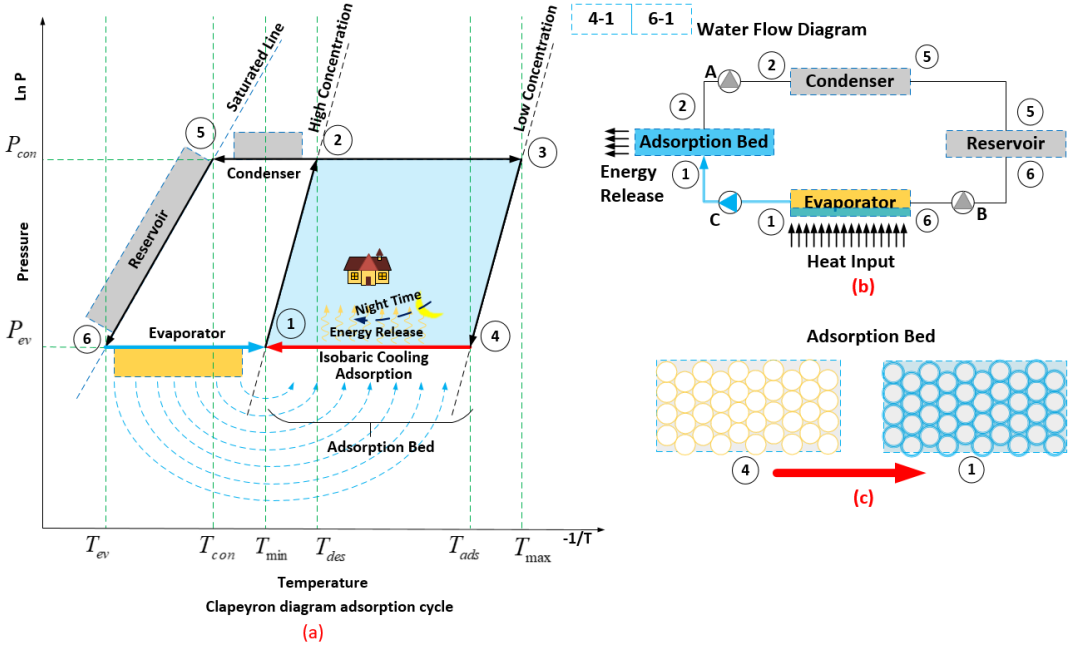

Figure 2.6 a. Phase 4: Isobaric cooling (adsorption), b. flow of adsorbate in an adsorption system, c. adsorption bed

Phase 4 (State 4 to 1): At the beginning of this phase, as shown in Figure 2.6, the adsorbents are completely charged at point 4 with a temperature equal to T_{ads} and pressure equals to P_{ev}. Valve C opens, and the adsorbates evaporate from the evaporator, taking the heat of vaporization from a secondary heat source (state 6 to 1), and adsorbing at the adsorbent surface, releasing the heat of adsorption at a constant specific

volume (state 4 to 1). The pressure remains constant during this phase, and the temperature at the adsorber surface decreases from T_{ads} to T_{min} while the concentration of adsorbates adhered to the surface increases. By the end of this phase, the adsorbents are completely discharged, and the adsorption cycle starts again at phase 1.

During phase 1 (state 1 to 2) and phase 2 (state 2 to 3) of the adsorption cycle, adsorbents take heat from a heat source and becomecharged. The charged adsorbents release the heat of adsorption when brought into contact with moist air. The heat of adsorption released can be utilized in various applications including space heating, while the heat removed from the evaporator can be used for space cooling.

2.2 Physisorption and Chemisorption

The adsorption process involves the interaction and adsorption of adsorbate molecules on the adsorbent surface. This interaction can be purely physical, or chemical. The adsorption is called physisorption if this interaction is purely physical, and chemisorption if this interaction is chemical. Physisorption results in the formation of weak bonds due to weak Van der Waals forces, and chemisorption results in the formation of stronger chemical bonds due to either the electron transfer or sharing between the adsorbate molecules and adsorbent. The classification of an adsorption process as either physisorption or chemisorption is determined by the magnitude of the heat released. Heat released within the range of <40 kJ/mol signifies physisorption, while a range of 40-500 kJ/mol indicates primary chemisorption as the prevailing adsorption mechanism.

Table 2.1 Chemisorption and physisorption

	Chemisorption	Physisorption
Process nature	Irreversible	reversible
Adsorbate	Only if adsorbate forms a chemical bond with the adsorbent surface	Any adsorbate can be adsorbed on the surface
Bonding	Chemical bonds	van der Waals forces
Factors	Adsorption rate is slow at low temperatures	Adsorption rate is slow at low temperatures and increases with an increase in temperature
Activation	Minimum activation energy is needed to start the adsorption process	Does not require energy for activation
Adsorbate layers	Unimolecular layer	Multimolecular layers
Heat of Adsorption	> 500 kJ/mol	< 50 kJ/mol
Coverage	Monolayer or less, site restriction- Titration of active sites	Multilayer- Measurement of surface area
Kinetics	Activation is required	No activation needed
Pores	-	Pores may be filled

2.2.1 Monolayer and Multilayer Adsorption

2.2.1.1 Monolayer Adsorption

In monolayer adsorption, adsorbate molecules arrange themselves in a single layer on the adsorbent surface. This is often considered the initial stage of adsorption. The formation of a monolayer is influenced by factors such as the concentration of adsorbate molecules in the bulk, intermolecular attractions between adsorbate molecules, the affinity of the adsorbent towards the adsorbate, and operating conditions.

2.2.1.2 Multilayer Adsorption

If the adsorbate molecules continue to accumulate beyond a single layer, forming multiple layers on the adsorbent surface, it is referred to as multilayer adsorption. The ability of an adsorbent to accommodate multiple layers depends on factors like the strength of intermolecular forces, the specific surface area of the adsorbent, and the nature of the adsorbate-adsorbent interaction.

2.3 Adsorption System

The adsorber, evaporator and condenser together form an adsorption system. Adsorption systems are designed for a specific purpose which can be to generate a refrigeration effect, to store thermal energy or to provide for space cooling. These systems operate using an adsorption cycle (discussed in the previous section) and use adsorbent-adsorbate working pairs to generate the desired effect. The adsorbent and adsorbate working pairs are selected based on the operating conditions and performance required from the system. The coefficient of performance, specific cooling power, and specific heating power are the predominant high-level parameters used to measure the performance of adsorption-based refrigeration systems while energy storage density and efficiency are the parameters used to measure the performance of adsorption based thermal energy storage systems.

2.4 Heat of Adsorption

Heat is released when adsorbate molecules are adsorbed on the adsorbent surface. This heat is called heat of adsorption. The heat of adsorption is often studied as the integral heat of adsorption, differential heat of

adsorption and isosteric heat of adsorption. The integral heat of adsorption is the total heat released from the beginning of adsorption until its end at a constant temperature, the differential heat of adsorption is the change in integral heat of adsorption with a change in the concentration of adsorbed adsorbate molecules, and the isosteric heat of adsorption is the heat of adsorption defined by the adsorption isosteres and Clausius-Clapeyron relationship. The decrease in entropy of adsorbate molecules upon adsorption is a crucial factor contributing to the exothermic nature of the adsorption process. Entropy is a measure of disorder, and as molecules are adsorbed onto a surface, their freedom of movement is restricted, leading to a decrease in entropy. Similarly, the enthalpy during the adsorption process also is negative and outweighs the negative entropy term especially at higher temperatures such that the overall Gibbs free energy during the adsorption process is negative.

$$\Delta G = \Delta H - T\Delta S \tag{2.1}$$

Conversely, heat is provided to adsorbate molecules when the are desorbed from the adsorbent surface back into the bulk fluid. This heat is known as the heat of desorption and because heat is added during the desorption process, it is an endothermic process.

The heat of adsorption is not constant but depends on environmental conditions which include relative humidity, temperature and pressure. At normal environmental temperatures and pressures, the heat of adsorption can be treated as a function of humidity alone. This implies that the amount of water vapor present in the carrier fluid significantly influences the heat of adsorption.

2.5 Adsorption Equilibrium and Adsorption Kinetics

Adsorption equilibrium, governed by thermodynamics, examines the uptake of adsorbates at equilibrium, elucidating the distribution of molecules between the adsorbent surface and the bulk fluid under specific temperature and pressure conditions. This stage is well-established, employing various adsorption equilibrium isotherms like Langmuir and Freundlich to describe the relationship between adsorbate amount and concentration at equilibrium. On the other hand, adsorption kinetics focuses on the rate of adsorption, dependent on the adsorption mechanism and the steps involved in the process. Kinetic isotherms, derived experimentally by plotting adsorption uptake against time, aid in developing models that describe the adsorption rate. A successful kinetic model not only identifies the rate-limiting mechanism but also allows extrapolation to diverse operating conditions, providing valuable insights for practical applications. Together, equilibrium and kinetics studies contribute to the optimization and design of adsorption processes across various fields, from water treatment to gas separation.

2.5.1 Adsorption Isotherm Types

The International Union of Pure and Applied Chemistry (IUPAC) has classified adsorption isotherms into six distinct types: Type I, Type II, Type III, Type IV, Type V, and Type VI. Each type is characterized by specific features reflecting the nature of the adsorption process.

1. **Type I:** This type of adsorption isotherm is exhibited by microporous adsorbents, this isotherm is indicative of adsorbate uptake largely limited by the size of the adsorbate. It is observed in reversible, physisorption, and the plateau in the isotherm signifies the completion of monolayer adsorption.

2. **Type II:** This type of isotherms is also associated with reversible, physisorption. The completion of monolayer adsorption is marked by the first plateau.
3. **Type III:** Characterized by concave isotherms, Type III is less common and requires reversible adsorption. The presence of adsorbate-adsorbate interactions plays a crucial role in shaping these isotherms.
4. **Type IV:** Featuring a hysteresis loop, Type IV isotherms are linked to mesopores where capillary condensation occurs. The upward curve in the isotherm, deviating from the Type II curve shape, signifies the end of multilayer adsorption and the onset of condensation.
5. **Type V:** Uncommon and observed when adsorbate-adsorbate interactions dominate over adsorbent-adsorbate interactions.
6. **Type VI:** Distinguished by multiple plateaus and upside curves, the number and sharpness of these curves depend on the system and temperature. This type of isotherm is versatile and can exhibit various complexities in the adsorption process [51].

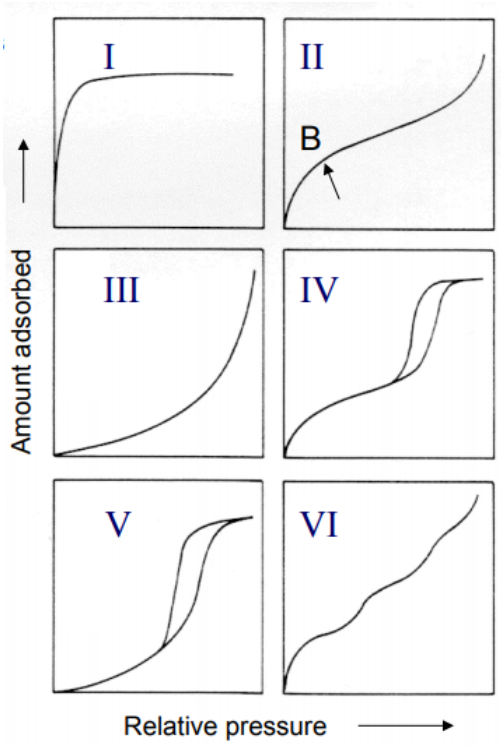

Figure 2.7 Type of adsorption isotherms [51]

2.6 Adsorption Beds

The adsorption bed is the main component of an adsorption cycle or system. In its simplest form, it is a vessel or container filled with or coated with adsorbents. The adsorbents in an adsorption bed release the heat of adsorption during the adsorption phase and receive the heat of desorption during the desorption phase. To extract energy from the adsorption bed or to provide the charging heat to the adsorption bed, the effective heat transfer coefficient of the adsorption bed should be high. However, the heat transfer coefficient is intrinsically low due to the low thermal conductivity for most adsorbents. Moreover, the adsorbate molecules are adsorbed and desorbed on the adsorbent particles in the adsorption bed; therefore,

an adsorption bed essentially should have a high mass transfer coefficient. Also, in adsorption processes the adsorption rate increases with increasing mass transfer rate. It follows that to achieve a highly efficient adsorption process a high mass transfer rate and high mass transfer coefficient are needed. Moreover, the complex thermochemical behavior of adsorption phenomenon, in which adsorbate molecules goes through mass diffusion, film diffusion and pore diffusion before ultimately getting adsorbed to the adsorbent surface, and a continuously varying concentration of adsorbate molecules around adsorbent surface, makes it hard to achieve a high mass transfer coefficient in an adsorption bed. To overcome the challenges associated with a low mass transfer coefficient different adsorbent-adsorbate pairs are used, and to overcome the challenge of low heat transfer, unconsolidated, coated, and consolidated adsorption beds are used.

Unconsolidated adsorption beds are either finned tube, plate type or shell and tube type heat exchangers having a high surface area in contact with the adsorbent particles to facilitate higher heat transfer rates [50]. Various methods have been used in previous studies to increase the heat transfer surface area in adsorption beds which includes mixing of varied sizes of different adsorbents, metal inserts and composite adsorbents with adsorbents. However, the increase in heat transfer in such inserts is often limited by the thermal contact resistance that exists between the surface of these inserts and adsorbent surfaces. Also, an increase in surface area increases the thermal capacity of the adsorption bed which decreases its performance. On the other hand, in coated adsorbers, the adsorbent is coated on the surface of the adsorption bed to increase its overall thermal conductivity. It overcomes the thermal resistance existing between the surfaces in unsolicited adsorption beds. However, to get the same thermal energy storage the total mass of the adsorption bed is significantly higher due to the low amount of adsorbent available for adsorption in adsorption bed. Another

alternative is consolidated adsorption beds, in which binders are used to consolidate the adsorbents to increase the thermal conductivity of adsorption beds.

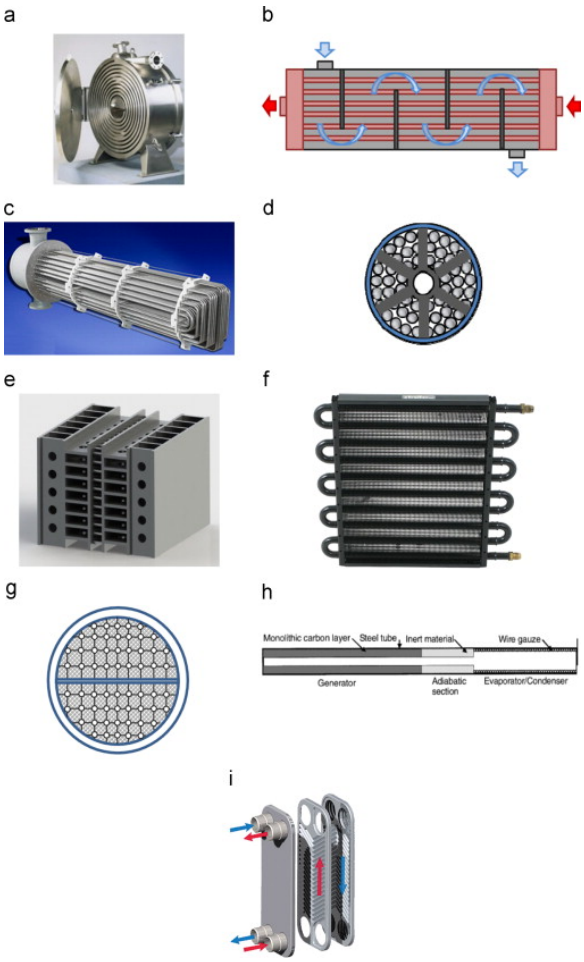

Figure 2.8 Type of adsorption beds a. spiral plate, b. shell and tube, c. hairpin, d. annulus tube, e. plate fin, f. finned tube, g. plate-tube, h. simple tube, and i. plate type adsorbers[52]

Adsorber beds can be divided into nine different categories: spiral plate, shell and tube, hairpin, annulus tube, plate fin, finned tube, plate-tube, simple tube, and plate type adsorbers [52]. Moreover, as the poor thermal conductivity of adsorbers is a big challenge in the performance of adsorbers, adsorbers with fins,

i.e., plate fin and finned tube type adsorbers are widely studied. The plate fin type adsorber beds either hold adsorbents between the fins or are coated with adsorbents coatings to ensure better heat transport [53], [54]. Similarly, finned tube type adsorbers also hold adsorbents either between the fins or are coated with adsorbents coatings, but these adsorbers differ in how the heat transfer fluid carries the heat away from the adsorber for further use. The heat transfer fluid flows either through the finned tubes [55] or flows on the outer side [56].

On the other hand, for plate-tube type adsorbers, tubes can be fixed into big fins to achieve a larger surface area [54], [56], [57], [58], [59]. Another adsorber type is the shell and tube type in which many finned adsorber tubes are placed inside a shell with adsorbents placed between the tubes [60], [61], [62]. Annulus type adsorbers are tubes with internal fins with adsorbents filled inside [63], [64]. Consolidated type adsorbers consolidate the adsorbent into a single shape [65], [66], [67]. Apart from the above adsorbers, there are attempts to use the 3D printing to obtain an optimized adsorbent mesh structure which has better performance than traditional adsorbers [68]. The details on the above discussed adsorption beds can be found in Table 2.2.

Table 2.2 summary on existing adsorption cooling systems having various adsorption beds[52]

Type of adsorption bed	**Working pair**	**Cooling capacity**	**Coefficient of performance**	**Specific cooling power (W/kg)**
Spiral plate	Activated carbon/methanol	31.5 kg ice/day	0.2	2.63 kg ice/kg adsorbent per day
Shell and tube	Activated carbon/methanol	1.7 kW	0.08	7.6
Hairpin	Zeolite/water, activated carbon/methanol	1.44 kW	0.65	23
Annulus tube	Consolidated graphite+zeolite 13X/water	0.213 kW	0.28	38
Plate fin	Silica gel/water	2.8 kW	0.21	26.5
Finned tube	Consolidated activated carbon/ammonia	0.0528 kW	0.061	33

Plate-tube	Activated carbon/ammonia	15.8 kW	0.37	152
Simple tube	Consolidated activated carbon/ammonia	0.042 kW	0.19	550
Plate	Silica gel/water	2336 kJ	0.33	118

2.7 Heat Source

Various heat sources can be used to drive an adsorption cycle. These sources include industrial waste heat, engine waste heat, solar energy, or other sources of thermal energy. Several studies have concentrated on utilizing engine waste heat and very often the engines used in vehicles [69], [70], [71], [72], [73], [74], [75], [76], [77] many of which aimed at powering vehicle air-conditioning systems. Some studies focused on utilizing industrial waste heat [78], [79], [80], [81], [82], [83], [84] for refrigeration systems or heat storage systems. Other studies investigated utilizing solar energy [83], [85], [86], [87], [88], [89], [90], [91], [92], [93], [94], [95] for solar thermal heat storage or to utilize solar energy to generate refrigeration or air-conditioning effects.

2.7.1 Solar Energy

The Sun's surface is incredibly hot and is at a temperature around 5,800 K. It radiates energy in the visible and near-infrared light spectrum. The earth, at a distance of about 150 million kilometers from the Sun, receives a huge amount of solar energy, with an average solar irradiance of about 1361 (W/m^2) at its outer atmosphere. This solar energy arrives at the Earth's surface as a combination of direct and diffuse radiation. Direct solar radiation, arriving in a straight line, can cast distinct shadows, while diffuse radiation scatters through the atmosphere, providing softer illumination even on cloudy days. However, solar energy is

intermittent as it is influenced by the day-night cycle, seasonal variations due to Earth's axial tilt, cloud cover, atmospheric conditions, and the solar zenith angle. To harvest solar energy effectively, technologies like photovoltaic (PV) panels and solar thermal systems have been developed. Solar thermal systems, notably, have gained significant attention in the pursuit of sustainable buildings and renewable energy solutions. This is due to their ability to efficiently capture and store solar energy as heat, which can be used for space heating, water heating, and even electricity generation. One area of research is the design considerations for flat plate and thermal collectors, which are essential components of solar thermal systems [96]. However, the field of adsorption-based thermal energy storage has emerged as a promising technology that could provide an alternative to conventional thermal energy storage methods, [97], [98]. This technology is still in the development stage but shows great potential for sustainable air-conditioning applications.

Further, the adsorbents having a charging temperature below 80°C are needed for using solar energy as a heat source to avoid using costly solar concentrators [63]. The development of new suitable adsorbents having high energy densities and low charging temperatures is in progress [99], [100], [101], but an adsorbent capable of providing high enough energy density to meet the commercial requirements has yet to be found [102].

2.7.2 Industrial Waste Heat

An important and well-known source of thermal energy is industrial waste heat. Industrial waste heat refers to the energy produced as a by-product of various industrial processes, which is typically released into the environment without being harnessed for any useful purpose. Globally, industrial processes contribute

approximately 33% of the total greenhouse gas emissions. Simultaneously, around 70% of the total heat demand stems from the industrial sector. Consequently, industrial processes release industrial waste heat in varying quantities, sometimes reaching up to 50% [103]. This waste heat is generated across a wide range of industries, including manufacturing, power generation, chemical processing, metal refining, cement production, and others, resulting from combustion, manufacturing processes, and chemical reactions.

Depending on its temperature, industrial waste heat can be classified into three categories: low-grade waste heat, medium-grade waste heat, and high-grade waste heat. Waste heat below 230 °C is considered low-grade and is utilized for space heating, water heating, and drying processes. Approximately 15-23% of the total waste heat generated falls into the low-grade category [104]. Waste heat ranging from 230 °C to 650 °C is categorized as medium-grade and finds applications in steam generation, organic Rankine cycle systems, and absorption cooling. Waste heat above 650 °C is referred to as high-grade waste heat, which can be used directly in industrial processes or in combined heat and power cycles [105].

Industrial waste heat is recovered using heat recovery technologies [106]. These technologies can be classified as either active waste heat recovery or passive waste heat recovery. Active waste heat recovery involves the direct utilization of recovered waste heat or its conversion into another form of energy, such as in heat recovery power cycles. On the other hand, passive waste heat recovery involves the collection and storage of waste heat for later use when needed, for example, through thermal energy storage [107].

Numerous passive waste heat recovery technologies exist, including molten salt thermal energy storage, phase change material thermal energy storage, hot water or steam thermal energy storage, underground thermal energy storage, and thermochemical energy storage. Most of these thermal energy storage technologies primarily work with medium- to high-grade waste heat. To utilize low-grade waste heat with these technologies, it is necessary to either upgrade it to medium- or high-grade waste heat or convert it

into another form before utilization [107]. However, thermochemical energy storage has the capability to work with all grades of thermal energy.

Adsorption-based m-TES systems can operate at low- to high-grade heat which makes these suitable for a wide range of residential, commercial, and industrial applications including space heating. These systems are extremely flexible and can be developed and customised to suit the needs of end users. The adsorption-based systems can be developed in various shapes and sizes making these suitable to integrate in modern buildings, facades, and other such infrastructures. These systems considering their reliability, modularity and sustainability can easily complement conventional energy sources to fulfil the needs of end users while reducing carbon footprints and contributing to a greener future.

2.8 Solar Collectors

A common way of harvesting solar energy is using solar collectors, collectors can be used in photovoltaic and solar thermal systems. Solar thermal collectors are used for harvesting solar thermal energy. A properly designed solar collector can play a significant role in harvesting, storing, and delivering heat at the desired temperature. Solar thermal energy in adsorption systems is used either directly or indirectly. The adsorption systems using solar thermal energy indirectly use solar collectors [108] to harvest and supply the charging heat to adsorbers. However, the adsorption systems using solar thermal energy directly, [109], [110], [106] and the solar energy is focused directly on the collector. These collectors can be integrated within the adsorption bed or used as standalone units. Integrating solar collectors within the adsorbent bed enhances heat transfer but also presents challenges in terms of manufacturing and reliability [111]. The systems using parabolic collectors are comparatively very compact and are found to have a better performance and heat

flux densities [109], [112]. There are many types of solar collectors which are widely used in solar thermal harvesting, and some are discussed below:

2.8.1 Flat Plate Collectors

Flat plate collectors are a commonly used type of solar thermal collector in adsorption systems. These collectors are designed to deliver heat at low temperatures and are cost-effective over a long duration. They function as heat exchangers, converting solar radiation into sensible, latent, or thermochemical heat. Depending on the installation location, flat plate collectors can be fixed, tilted, or oriented to maximize their efficiency. Two main categories of flat plate collectors are liquid heaters and air heaters, based on the transfer of thermal energy to either a liquid or air medium [113].

Liquid heater flat plate collectors transfer thermal energy from the collector to a liquid, typically water, while air heater flat plate collectors transfer thermal energy directly to the air. In terms of design, liquid flat plate collectors can be classified into three main types: pipe and fin type, liquid sandwich type, and semi-sandwich type collectors. On the other hand, air flat plate collectors can be categorized as finned plate type, metal matrix type, or corrugated plate with selection surface type collectors [114].

Flat plate collectors play a crucial role in adsorption systems, and their integration can be classified into two types: direct flat plate collector integrated systems and indirect flat plate collector integrated systems. In direct integration, the flat plate collectors form the adsorber, while in indirect integration, the flat plate collectors are separate units fitted to the adsorber. Several studies have been conducted to test and evaluate the performance of solar-driven adsorption systems with flat plate collectors in various climatic conditions.

For example, in Egyptian climatic conditions, a solar-driven adsorption refrigeration system was tested using a 2 m² flat plate solar collector integrated with an adsorption bed as a standalone unit. The system achieved a daily ice production of 27.82 kg using activated carbon-methanol as the adsorbent and adsorbate pairs [115]. In another study, an integrated flat plate collector and adsorption bed were designed for an ice maker, with fins installed to enhance heat transfer. The adsorption bed consisted of two 0.75 m² flat plate collectors, and activated carbon was used as the adsorbent. The system demonstrated effective ice production with proper insulation and solar flux radiation enhancement techniques [116],[117].

Different variations of flat plate collector integration have been explored in various studies. For instance, a double-glazed flat plate collector was integrated with an adsorber for an ice maker, utilizing a matt black painted aluminum alloy absorbing plate and a metallic casing made of stainless-steel wires. Coarse-blue silica gel grains were used as the adsorbent with water as the adsorbate. The collector was tilted at different angles based on seasonal variations, and external flat reflectors were used to enhance performance [118]. Another study employed six black chromium single-glazed flat plate solar thermal collectors connected in series and parallel for a solar-driven adsorption cooling system. The system utilized zeolite 13X/$CaCl_2$-water as the working pair and achieved successful cooling performance in Guangzhou, China [119].

Furthermore, a solar adsorption refrigerator equipped with a flat plate collector was designed to operate with activated carbon adsorbent and methanol adsorbate in Rabat, Morocco, under Mediterranean climatic conditions. The collector was made of copper plates with fins and a stainless-steel wire mesh to ensure proper airflow. The system demonstrated reliable operation even under cloudy and rainy weather conditions [120] [121].

It is worth noting that the performance of flat plate collector-integrated adsorption systems is influenced by factors such as solar intensity and cloud cover. A theoretical and experimental study on a solid flat plate adsorption icemaker revealed that ice formation varied significantly with cloud cover, and prolonged cloud cover lasting more than three hours prevented ice formation [122].

2.8.2 Tube-Type Flat Plate Collectors

A tube-type flat plate collector is designed and developed for water heating and ice-making. 28 stainless still tubes of 50x1x750 mm^3 size are filled with activated carbon adsorbent. Water is used as the adsorbate. A $3m^2$ vacuum heat pipe solar collector is simulated using a 1500 W electric heater in the hybrid system [123] An evacuated tube solar collector is simulated in TRNSYS 16 simulation software for hybrid adsorption desalination and cooling system for Egyptian climatic conditions [124]. A flat plate solar collector is developed for a solar adsorption ice maker system. The acrylic collector is fitted with ten black-painted absorber copper tubes, each containing a stainless-steel tube to facilitate the methanol flow. The annular spaces between stainless-steel and copper tubes are filled with AquaSorb 2000. The collector is covered on top with a glass cover. The acrylic collector is placed in a wooden box to minimise heat loss. The collector is inclined at an angle of 27°C for maximising sun exposure in Egyptian geographic conditions [125]. An evacuated heat pipe collector is designed for a solar adsorption chiller. Heat pipes in the collector transfer heat from incident solar radiation to the adsorption bed. Water is used as a heat transfer fluid. A thermal switch controls the heat transfer to the adsorption bed and its storage on requirement [126]. Another evacuated tube-type solid collector is developed for solid adsorption solar refrigeration. The collector box is made with a 22G galvanised steel sheet plate painted with black oil paint. Six steel pipes are having a coaxial perforated inner tube. The annular space between the steel pipes and perforated inner

tubes is filled with 1.4 kg of activated carbon AC-35 supplied by CECA, France. The top part of the collector is fitted with clear plane glass. The collector box is insulated with a 95 mm thick Styrofoam chip and a 5 mm thick top covering the asbestos ceiling board [127],[128]. Flat-plate vacuum tube solar collectors having an efficiency of 28.4% are integrated into a two-bed solar adsorption chiller. Silica gel and water are used as adsorbents and adsorbates. All the collectors are installed at 20°C [129]. A theoretical and experimental study is conducted on a solar-driven adsorption desalination-cooling system (ADC) designed for Egyptian climatic conditions. The system works with silica gel adsorbent and water adsorbate. The collector uses an evacuated tube with a total surface area of 4.5 m^2. The system is fitted with two fin tube-type adsorption beds heat exchangers [130] A tubular flat plate collector is designed for a solar adsorption refrigerator. The collector is integrated with 20 stainless steel 5 cm outer diameter tubes containing activated carbon adsorbent in granular form. The tubes are coated on the outer side with selective paint. A coaxial perforated inner pipe enables the flow of methanol to the adsorbent to facilitate adsorption. The collector is covered with a plane glass cover [131]. An evacuated tube collector is used with an adsorption-based chiller having a cooling capacity of 10 kW. The system works on zeolite-water as the adsorbent-adsorbate pair. To enhance the performance of the solar collectors and a risk-free operation, a propylene glycol solution is used as the working medium [39]. A flat plate collector is designed for a solar absorption refrigerator. The collector is fitted with cylindrical tubes having external horizontal fins. The tubes are filled with activated carbon adsorbent and are designed to allow the adsorbate flow. Plain glass covers the collector on top, with all other sides insulated properly [132].

2.8.3 Concentrating Collectors

Concentrating collectors are high-temperature range collectors designed to intercept the directly incident solar radiation over a large area and focus on a small absorber area. These collectors are fitted with lenses and mirrors to direct solar radiation onto the absorber. These collectors have a complex structure often fitted with a mechanism to track sun movements to ensure the maximum exposure to the sun for the maximum performance of the collector. Concentrating collectors can be classified into two types: line-focused and the other point focused.

Line-focused concentrating collectors have a parabolic cross-section and are fitted with a tube at the concentration point. A heat transfer fluid flows through the pipe. The temperature of heat transfer fluid increases gradually as it passes from one end of the pipe to the other, absorbing concentrated solar radiation from concentrators. These concentrators have high efficiency and can reach up to 1000 °C. Parabolic collectors are an example of line-focused collectors.

The point-focused concentrating collectors focus the incident solar radiations onto an absorber placed at the concentration point. Parabolic dishes, power towers and lens concentrators are examples of point-focused concentrator collectors. Parabolic trough collectors are dish collectors fitted with mirror reflectors and an absorber at the focal point. These collectors often use a dual-axis sun movement tracker to achieve maximum exposure to the sun [113] [114].

2.8.4 Compound Parabolic Concentrators

A numerical model is developed using a parabolic trough collector and an annular heat pipe in a solar adsorption cooling machine. Parabolic trough collectors, when coupled with a heat pipe, are found to be

more efficient than flat plate collectors [133]. Two compound parabolic type collectors were developed for an adsorption chiller. Two 70 cm copper pipes are used as an adsorbent bed. The adsorption beds are placed at the focal point of the collectors. Activated carbon is used as an adsorbent and methanol as an adsorbate [134]. Another refrigerator is designed using a compound parabolic concentrator (CPC) having a tubular design for Burgo, Spain. The collector uses activated carbon, CNR115 from NORIT adsorbents with a methanol adsorbate. The copper tubes of the collectors are covered with MIRO THERM selective sheet manufactured by ALANOD and have a solar absorptance of 0.94 ad thermal emittance of 0.05. About 9 kg of water per m^2 area was chilled from 23 C° to 2 °C in a single cycle [135].

A compound parabolic concentrating solar collector is designed for an adsorption refrigerator. 2.5 kg of activated charcoal, 207E3 adsorbent is packed in copper tubes in the collector, having a concentration ratio of 3.9 and an aperture area of 2.0 m^2. The refrigerator is designed to produce 1 kg of ice with a coefficient of performance of 0.02 [136] A double-glazed flat plate solar collector having cylindrical tubes working as both adsorber and solar collector are used [137]. A theoretical study focuses on designing a double-pass flat photovoltaic thermal compound parabolic concentrating (CPC) solar collector. The CPC concentrates the light on the photovoltaic cells and the fins on the back and transfers the heat to the air [138]. A compound parabolic concentrator fitted with four finned tubes is designed for solar adsorption refrigeration. A CFD analysis compares the collectors with and without fins [139]. A parabolic trough collector having a surface area of 36 m^2 is designed for solar-driven adsorption ice-making system. The system works with $CaCl_2$ + activated carbon-ammonia adsorbent-adsorbate pair. 30 kg of adsorbent is used in experiments to produce 50 kg of ice per day [140]. A simulation study is conducted with a compound parabolic concentrator (CPC) having wings angled towards the surface azimuth angle for a solar adsorption refrigeration system for Tokyo, Japan. The CPC is divided into three parts, and the tilt and bending angles are optimised by

optimising the energy absorbed at the CPC adsorber for a sunny day each month. Activated carbon fibre and ethanol are used as adsorbent and adsorbate pairs. The collector provides an effective temperature for a longer period than the conventional liner CPC [141]. A parabolic dish-type collector is tested for charging various adsorbents, silica gel, activated alumina, and charcoal. The circular dish collector has 40 segments of anodised aluminium with an outer ring frame of mild steel. The tracking is done manually. A wire mesh container is used to hold the adsorbents at the focal point of the dish. The dish collector is found to have effectively charged the adsorbents during the experiments [142].

2.8.5 Hybrid Systems

There are some hybrid systems developed by integrating several renewable energy technologies into a single system. PVT solar collectors are integrated into a hybrid biomass + solar + wind-powered cascade adsorption-compression refrigeration system working with silica gel and water pair [133]. A dynamic simulation study is conducted on a solar-driven hybrid adsorption-compression cooling system. Two cases are studied, first with only a solar thermal collector and the other with a hybrid setup with solar thermal and on-grid monocrystalline-photovoltaic collectors [144]. The hybrid solar heating and cooling systems working on absorption and adsorption chillers are designed and modelled for Europe. Four different buildings including office and residential spaces, located in different European weather zones are considered for the study. The modelled solar poly generation systems simultaneously produce electricity, space heating and cooling, and domestic hot water; electricity is self-consumed or delivered to the electrical grid. The systems considered to use the flat plate and dish concentrating photovoltaic/thermal solar collectors with a combination of a single effect absorption chiller and two different kinds of adsorption chillers (with high and low activation temperatures). The concentrating Photovoltaic/Thermal (CPVT) solar

collectors are found to perform better under high beam solar radiations however the glazed or low-E glass flat-plate Photovoltaic/Thermal (PVT) technologies are found to perform best under poor beam solar radiations [145].

Table 2.3 Examples of adsorption-based solar thermal systems

Application	Adsorbent-Adsorbate pair	Collector type	Amount of adsorbent	Collector Size	Reference
Cooling	Activated carbon-methanol	Flat plate collector with two grass covers	50 kg	2 m^2 (2m x 1m)	[115]
Ice maker	Activated carbon-water	Flat plate collector with fins	22 kg x 2	0.75 m^2	[116], [117]
Water heater and Ice maker	Activated carbon-water	Tube type flat collector	22 kg	2 m^2	[123]
Ice maker	Silica gel-water	Double-glazed flat plate collector	3.7 kg	0.64 m^2 (0.8 m x 0.8 m)	[118]
Ice maker	Activated carbon-methanol Zeolite-water	Flat plate collector with fins	103-114 kg A.C.	1.5 m^2	[146]
Adsorption desalination-cooling system	Silica gel-water	Evacuated tube solar collector	13.5 kg	6 m^2	[124]
Solar refrigerator	Silica gel- water	Double-glazed flat plate collector	3.7 kg	0.36 m^2 (0.604 m x 0.604 m)	[147]
Cascaded adsorption-compression refrigeration systems	Silica gel-water	PVT collectors (6)	-	1.64 m^2	[143]
Hybrid adsorption-compression cooling system	Silica gel-water	Evacuated tube solar collector Monocrystalline-photovoltaic collectors	47 kg	56.8 m^2 (20 m × 2.84 m) (ECT) 6 m^2 (6m x 1 m) (mono-PV)	[144]
Solar adsorption cooling machine	Activated carbon-ammonia	Parabolic trough collector coupled with heat pipe	-	-	[133]
Solar adsorption ice maker system	AquaSorb-methanol	Evacuated tube solar collector	10 kg (1 x 10)	0.8 m^2	[125]
Solar adsorption chiller	Activated carbon-ammonia	Heat pipe type solar collector	1 kg	1 m^2	[126]

solid adsorption solar refrigerator	Activated carbon-methanol	Evacuated tube solar collector	8.4 kg	1.2 m^2	[127], [128]
Solar adsorption chiller	Nano-activated carbon-methanol	Compound parabolic collector	0.4 g	0.08 m^2	[134]
Solar adsorption refrigeration	Activated carbon-methanol	Compound parabolic concentrator (CPC)	2.05 kg per finned tube 2.23 kg per smooth tube	-	[139]
Solar adsorption chiller	Silica gel-water	Flat-plate vacuum tube solar collectors	62.64 kg	108.5 m^2	[129]
Solar adsorption cooling system	Zeolite 13X/$CaCl_2$ composite adsorbent-water	Single-glazed flat plate solar collectors	5.6 kg	12 m^2 (6 x 2 m^2)	[119]
Solar adsorption refrigerator	Silica gel-water	Double-glazed flat plate solar collector	78.8 kg	2 m^2	[137]
Adsorption refrigerator	Charcoal/207E3-methanol	Compound parabolic concentrating solar collector (CPC)	2.5 kg	-	[136]
Solar adsorption refrigerator	Activated carbon-methanol	Compound parabolic concentrating solar collector (CPC)	7.6 kg	-	[135]
Solar solid adsorption refrigeration	-	Flat plate collector	-	-	[122]
Solar adsorption refrigerator	Activated carbon AC35-methanol	Flate plate collector with fins	14.5 kg	0.051 m^2	[120], [121]
Solar-driven adsorption desalination-cooling system	Silica gel-water	Evacuated tube solar collector (ETSC)	13.5 kg	4.5 m^2	[130]
Solar adsorption refrigerator	Activated carbon–methanol	Flat plate tubular collector	-	-	[131]
Solar adsorption refrigerator	Activated carbon–ammonia	Flat plate collector with cylindrical tubes with external fin	-	-	[132]
Solar adsorption refrigeration	Activated carbon-methanol	Flat plate compound parabolic concentrator (CPC) collector	-	-	[139]
Solar adsorption chiller	Zeolite- water	Evacuated tube solar collector	-	40 m^2	[148]
Solar Adsorption Refrigeration System	Activated carbon fibre (ACF, adsorber)-ethanol	Compound parabolic concentrator (CPC)	-	-	[141]
-	silica gel, activated alumina, and activated charcoal-water	Dish type collector	2 kg	-	[142]

Solar-driven adsorption ice-making system	$CaCl_2$ + activated carbon-ammonia	Parabolic trough collector	30 kg	36 m^2	[140]
Solar heating and cooling systems by absorption and adsorption chillers	-	Flat plate and dish concentrating photovoltaic/thermal solar collectors	-	-	[145]

Amongst all collectors, flat plate collectors are widely used in adsorption systems for solar thermal energy harvesting. These collectors can be categorized as liquid heaters or air heaters, based on the medium through which thermal energy is transferred. Integration of flat plate collectors in adsorption systems can be direct or indirect, depending on their configuration with the adsorber. Numerous studies have investigated the performance of flat plate collector-integrated adsorption systems in different climatic conditions, showcasing their potential for sustainable cooling and ice-making applications. Further research and development in this area can contribute to the advancement and optimization of solar adsorption technologies. Flat plate collectors do not require costly optical components or trackers for concentrating solar energy. Considering these advantages, combined with the fact that these collectors are inexpensive, require low maintenance, and are comparatively easy to design and fabricate, the research presented in this thesis focuses on integrating adsorbent beds into solar collectors with a flat-plate configuration.

2.9 Mobile Thermal Energy Storage

Mobile Thermal Energy Storage (m-TES) refers to the storage of thermal energy in a portable and mobile system. It involves capturing and storing excess or waste heat generated from various sources, such as industrial processes, power generation, or renewable energy systems. The stored heat can then be transported and utilized at a different location or time when heat demand is high, providing flexibility and

efficiency in thermal energy management. m-TES technologies offer advantages such as flexibility, efficient energy utilization, and the ability to transport heat to locations where it is needed. These technologies contribute to the overall efficiency and sustainability of energy systems by capturing and utilizing waste heat, reducing energy waste, and providing an on-demand heat supply. Ongoing research and development in mobile heat storage aim to improve these systems' efficiency, capacity, and reliability to meet the growing demand for portable thermal energy solutions.

One such m-TES technology is adsorption-based mobile thermal energy storage. Adsorption-based m-TES systems have the potential to revolutionize the way thermal energy is harvested and utilized, just like how solar photovoltaics has revolutionized electricity generation. These systems leverage the adsorption technology to store and release heat. These systems utilize adsorbent materials that can adsorb the adsorbate molecules, retain these molecules, and can desorb these on exposure to thermal energy. During desorption, these materials get charged with thermal energy and store it indefinitely without loss and release this stored thermal energy on the exposure to adsorbate molecules during adsorption.

2.10 Summary of Literature

This literature review delves into the well-established and extensively researched adsorption process for thermochemical energy storage, investigating its fundamental principles, recent advancements, adsorption systems, heat of adsorption, adsorbents, and its applicability in thermal energy storage contexts. Despite considerable progress, a noticeable gap persists in the development of compact adsorption-based solutions suitable for domestic and mobile thermal energy storage applications. While multiple heat sources have been explored for adsorbent charging, the direct utilization of solar radiation remains a relatively

unexplored avenue. Although stationary adsorption systems predominate, the emergence of mobile thermal energy storage setups introduces an innovative dimension. In summary, this field offers ongoing prospects for innovative advancements, spanning compact applications, solar-driven charging, and synergistic integration of energy sources, with both stationary and mobile systems contributing to the evolving landscape.

3 Adsorbent-Adsorbate Pair Selection for Thermal Energy Storage

3.1 Chapter Overview

This chapter focuses on the selection of suitable adsorbate-adsorbent pairs for thermal heat storage applications. It begins with a comprehensive introduction to adsorbents, covering factors influencing their performance, key characteristics, and methods for physical and thermal characterization, followed by an exploration of selection criteria. Subsequently, attention is directed towards understanding adsorbent-adsorbate pairs, setting the stage for a case study involving a four-person house located in Toronto, Canada. This case study aims to ascertain the feasibility of utilizing adsorbent-based thermal energy storage (TES) to meet energy requirements at minimal cost. Various adsorbents, namely silica gel, activated carbon, activated aluminum, zeolite 4A, zeolite 5A, and zeolite 13X, are shortlisted for the study, with methanol and water as adsorbates. The latter part of this chapter conducts a review of Life Cycle Assessment (LCA) studies from literature to evaluate the environmental impacts associated with the selected adsorbents. Special emphasis is placed on assessing the Global Warming Potential (GWP) of TES systems employing different adsorbate-adsorbent pairs. Based on the selection criteria, and outcomes from the case study and review of LCA studies, zeolite 13 X and water are selected as the adsorbent-adsorbate pair. The material properties and characteristics specific to zeolite 13 X are also provided in this chapter.

3.2 Adsorbents

Adsorbents are highly porous materials with a high surface area and, depending upon the pore diameter and polarization, adsorb a variety of adsorbates. Adsorbents should have excellent thermal stability, excellent

thermal conductivity, low costs, and high reversibility to desorb the adsorbed adsorbates. Adsorbents can be categorized into physical adsorbents (e.g. zeolites, silica gel, activated carbon) [89], [149], chemical adsorbents (metal chlorides, metal hydrides and metal oxides) [150], and composite adsorbents which are often prepared by mixing, impregnation or consolidation of multiple adsorbents (metallic inserts or binders) [101], [151], [152], [153], [154], [155], [156], [157], [158], [159], [160], [161].

Adsorbents interact with adsorbate molecules in several ways depending on the surrounding conditions, such as heat, pressure and competing molecules. Forces or interaction factors that influence the adsorption of adsorbate molecules on the adsorbent surface are summarized in Table 3.1.

Table 3.1 Weak intermolecular interactions

Forces	Strength (kJ/mol)	Distance between adsorbent and adsorbate molecules (nm)	Comment
Van der Waals	0.4-4.0	0.3-0.6	Weakest interaction, controls molecular orientation
Hydrogen bonds	12-30	0.3	Strong interaction with polar and protic molecules
Ionic interactions	20	0.25	Interaction with ionizable groups of molecules, driven by pH
Hydrophobic interactions	< 40	varies	Strong interaction with molecules having aromatic group of alkyl chains

3.2.1 Physical Characterization of Adsorbents

The structure, morphology and surface features of the adsorbents can be characterized at different length scales; microscopic (< 2 nm), mesoscopic (2-50 nm) and macroscopic (>50 nm). On the microscopic length scales the textural characteristics of adsorbents (micropore sizes, pore size distribution [157], total pore volume [101], [152], [156], [157], [162] and incremental pore volume [157]) and surface characteristics

such as the surface structure and surface area [101], [152], [156], [157], [162]) are studied. On the mesoscopic length scales, the effect of adsorbent porosity [162], shape and sizes are studied. Moreover, on the macroscopic length scales the adsorbent bed configuration (shape and size) is studied.

Adsorption capacity, adsorption rate, and heat of adsorption, which are determined by plotting adsorption isotherms in an adsorption experiment, are also utilized for the characterization of adsorbents. Isotherms plot the amount of adsorbate adsorbed on the adsorbent surface as a function of pressure at a constant temperature. Freundlich, Langmuir and BET isotherms are now well-accepted to study the adsorption phenomenon. There are two methods which can be used to measure the adsorption isotherms: volumetric and gravimetric methods. The volumetric approach is used when the adsorbent volume in the adsorber is small, and the volume of which is possible to measure. The adsorption experiment in volumetric approach is conducted at constant pressure conditions. The gravimetric approach is used when the adsorber has a large amount of adsorbent, and the weight of which is possible to obtain in real time to obtain the adsorbate uptake. The gravimetric approach-based adsorption system is designed to measure the adsorption rate under controlled temperature and pressure conditions. The system can measure the performance of adsorbers with different sizes and configurations.

The apparatuses used to study adsorption and desorption processes generally have a cylindrical adsorber bed filled with a known volume of adsorbent, and the adsorbate is supplied under high temperature or pressure from an evaporator depending on whether the adsorption process is temperature swing or pressure swing [163], [164]. There are some apparatuses which use two different vessels maintained at constant temperature; one functioning as an evaporator and condenser while the other is used as a measuring chamber in which a known volume of adsorbent is placed on a load cell or electronic balance to measure the weight change during the adsorption experiment [165], [166]. Other apparatuses that operate using a temperature

swing consist of a constant volume adsorption system with two vessels; one acting as the water vessel and the other as a measuring unit to characterize the adsorbents [167], [168]. The experiment can be used to plot adsorption isotherms, to study transient temperature and pressure during the experiment, and to measure the adsorption capacity. There are many different apparatus designs discussed in the literature to characterize the adsorbents, and a standardized testing procedure has not yet been developed. Consequently, when comparing values reported in the literature for different adsorbents, the differing experimental conditions must be taken into consideration [155], [169], [170], [171], [172], [173], [174], [175], [176]. Also, with the exception of one adsorption system designed and fabricated by Mohammed et al. to measure adsorption kinetics[177], adsorption systems reported in the literature cannot be used to study adsorbers with and without coatings. Thus, a standard experimental setup for characterizing both adsorbents and adsorbers is lacking.

The energy density of an adsorption system can be measured by carrying out a thermal energy storage experiment using adsorbent materials. Various adsorbents have been tested for energy density in several experiments using a stainless-steel tube adsorption bed in a thermal energy storage adsorption system [88], [89], [178]. The adsorption capacity and adsorption rates of adsorbents are measured in a thermogravimetric study in which a known amount of adsorbent is made to undergo adsorption under controlled temperature and pressure conditions to obtain the adsorption kinetic data and weight change [101].

One common drawback of most adsorbents and adsorbent beds is poor thermal conductivity. The low thermal conductivity of adsorbent beds is due to the low thermal conductivity of adsorbent particles (0.1-0.8 W/mK) [179], high thermal contact resistances between adjacent adsorbent particles [180] and, adsorbent and adsorption bed heat exchanger surfaces [181], and the porosity of adsorbent beds [182]. High thermal contact resistances are usually responsible for the low thermal conductivity of adsorbents. It follows

that thermal conductivity is an important parameter to characterize the adsorbents. A guarded-hot plate apparatus [158], [183], transient plane source (TPS) [154], or gravimetric large pressure jump (GLAP) apparatus are used to measure the thermal conductivity of adsorbents [99].

3.2.2 Adsorbent-Adsorbate Pairs

Adsorbent-adsorbate pairs form a crucial component in an adsorption based thermal energy storage system, and it is important to select the right adsorbent-adsorbate pair. Tailored to specific applications, adsorbent-adsorbate pairs presents a wide range of possibilities. Silica gel and zeolites, proficient at adsorbing water vapor, provide reliable options, while activated carbon and metal-organic frameworks (MOFs) excel in capturing organic compounds and gases like methane, hydrogen, and carbon dioxide. Specific substances find affinity with calcium chloride and ammonia-based adsorbents, whereas metal hydrides efficiently store hydrogen gas. The choice of an optimal pair hinges on crucial factors like operating conditions and the desired energy storage capacity. While many different adsorbates are available for various applications, the most commonly used are water, ammonia, methanol, and ethanol [184].

Silica gel, zeolites, activated carbons and composite adsorbents are the commonly utilized adsorbents. Silica gel, known for its low cost and very low charging temperature (below 100 °C) [185] is widely employed. Zeolites belong to a family of porous adsorbents that exhibit a very high surface area and a very high affinity for water. However, the temperature required to completely charge these materials can be very high (up to 350 °C). Their excellent hydrothermal stabilities make these a good choice for long-term energy storage [186]. Activated carbons are carbon-based adsorbents having a very high surface area [89], [186]. These are widely used with methanol, ethanol and ammonia but can be used with water adsorbates but their affinity to water is comparatively limited [187]. Composite adsorbents are hybrid adsorbents developed to enhance the performance of natural adsorbents. These have an excellent energy density and heat of

adsorption at comparatively lower charging temperatures. The key thermophysical properties of these adsorbents are summarized in Table 3.2 [186]. Thermodynamic properties such as molecular weight, critical temperature, critical pressure, density and specific heat of some selective adsorbates are given in Table 3.3.

Table 3.2 Properties of adsorbents [186]

	Silica Gel	Zeolites	Activated Carbons	Composites
Adsorption heat (kJ/kg)	160-180	50-300	45-900	50-250
Charging temperature (°C)	50-80	70-350	80-200	60-90
Energy density (kg/m^3)	650-700	650-900	700-750	300-600
Specific heat (kJ/kgK)	0.8-0.9	0.85-0.95	0.8-1.5	0.95-1.05
Thermal conductivity (W/mK)	0.15-0.20	0.15-0.25	0.15-0.75	0.15-0.30
Adsorbate	Water	Water	Methanol, ethanol and ammonia	Water, methanol, ethanol
Adsorbate uptake (g/g)	0.03-0.10	Up to 0.2	0.15-0.60	Up to 0.8

Table 3.3 Thermodynamic properties of adsorbates for adsorption cooling and heating

	Mol wt.	**Critical temp.**	**Critical pressure**	**Density**	**Specific heat**
	g/ mol	**K**	**kPa**	**Mol/m**	**kJ/mol.K**
Methanol	32.042	512.64	8140	8547	0.061
Ethanol	46.069	513.92	6120	5952	0.098
Ammonia	17.031	405.65	11300	13889	0.038

Water	18.015	647.3	22048	17857	0.037

3.3 Adsorbent Selection Criteria

The performance of adsorbents is based on parameters such as the heat of adsorption, charging temperature, energy density, specific heat, thermal conductivity, and adsorption capacity. These parameters are defined in Table 3.4.

Table 3.4 Various quantities used to select adsorbent-adsorbate pair for an adsorption system

Quantity	Unit	Definition
Heat of Adsorption	kJ/kg	It is defined as the amount of heat released on the adsorption of adsorbate onto the surface of adsorbent.
Charging Temperature	°C	It is the temperature at which adsorbents are fully charged with energy.
Energy Density	kJ/m^3	It is the amount of energy stored in a system per unit volume of adsorbent.
Specific Energy Density	kJ/kg	It is the amount of energy stored in a given system or region of space per unit mass.
Specific Heat	kJ/kg ·K	It is the amount of heat required to raise the temperature of one gram of a substance by one degree Celsius.
Thermal Conductivity	W/m·K	It is the ability of a material to conduct heat
Adsorption Capacity	g/g	It is the ratio of weight of adsorbate molecules adsorbed to the total weight of the adsorbent.

The selection of the right adsorbent for any specific application is cruicial for optimizing thermal energy storage systems. The ideal adsorbent boasts a strong adsorption affinity towards the selected adsorbate molecules for maximizing the storage effectiveness. A high surface area provides more binding sites, enhancing the performance of adsorbents. Additionally, a heat of adsorption translates to effcient thermal energy storage and release during the adsorption/desorption process. Furtehrmore, high thermal

conductivity ensures effective heat flow within the adsorbent material. For system longevity, a long operational life is essential. To improve overall system efficiency, a low charging temperature is desirable. Chemical and thermal stabilities are crucial to maintaining sstem reliability by preventing degradation. From a cost perspective, affordability is key for widespread adoption of this technology. The adsorbent material shouold also be non-toxic to safeguard human health and the environment. Finally, easy availability and minimal processiing requirements before implementation furtehr promote the practicality of this technology. Adsorbents with attributes such as inflammability, non-explosiveness, non-corrosiveness, possessing substantial gravimetric and volumetric storage capacities, and high thermal diffusivities are generally preferred.

3.4 Viability Study of Adsorbents Based Beds for Domestic Energy Needs- A Toronto Case Study

This case study focuses on evaluating the feasibility of employing adsorbent-based beds to meet the heating requirements of a typical residential home located in Toronto, Canada. By investigating different adsorbate-adsorbent pairs, this study aims to assess the effectiveness of adsorption technology in capturing and storing solar energy during the day for subsequent heating purposes. The average size of a residence with four occupants is around 200 m^2 [188] with the overall energy requirements of 130 GJ yearly, or 0.36 GJ daily, by Statistics Canada [42], and it is assumed that 63% of this energy is used for spatial heating [189]. Thus, it is assumed that 0.23 GJ is required for spatial heating, which is much less than the average solar irradiance (1.6 GJ) estimated to be incident on a residential home in Toronto over the months from November to March [190]. Various adsorbate-adsorbent pairs comprising seven adsorbents (charcoal, silica gel, activated

alumina, zeolie-4A, -5A, and -13X) with water and methanol as the adsorbates are considered. The thermochemical properties of adsorbate-adsorbent pairs are listed in Table 3.5. Selected thermochemical properties from Table 3.5 are plotted in Figures 3.1 and 3.2.

Table 3.5 Thermochemical properties of adsorbent–adsorbate pairs [191]

Material	Adsorbate	Maximum adsorbate capacity	Heat of adsorption (Average)	Adsorbent specific heat	Net heat of adsorption per mass of adsorbent	Net heat of adsorption per volume of adsorbent	Volume of adsorbent required*	Net adsorbent required*	Amount of adsorbate required*	Total mass of system required*
		$kg_{adsorbate}/kg_{adsorbent}$	kJ	$kJ\ kg^{-1}\ K^{-1}$	$kJ/kg_{adsorbent}$	kJ/m^3	m^3	kg	kg	kg
Charcoal	**Water**	0.4	2320	1.09	928	445,440	0.81	387.93	155.17	543.10
Silica gel	**Water**	0.37	2560	0.88	947.2	634,624	0.57	380.07	140.63	520.69
Activated alumina	**Water**	0.19	2480	1	471.2	461776	0.78	764.01	145.16	909.17
Zeolite 4A	**Water**	0.22	4410	1.05	970.2	756,756	0.48	371.06	81.63	452.69
Zeolite 5A	**Water**	0.22	4180	1.05	919.6	625,328	0.58	391.47	86.12	477.60
Zeolite 13 X	**Water**	0.3	4410	0.92	1323	793,800	0.45	272.11	81.63	353.74
Active carbon	**Methanol**	0.32	1400	0.9	448	-	-	-	-	-
Zeolite 4A	**Methanol**	0.16	2300	1.05	368	287,040	1.25	978.26	156.52	1134.78
Zeolite 5A	**Methanol**	0.17	2300	1.05	391	265,880	1.35	920.72	156.52	1077.24
Zeolite 13 X	**Methanol**	0.2	2400	0.92	480	288,000	1.25	750.00	150.00	900.00

- These are the values required to store thermal energy to provide for a home with four occupants for one day [190].

The maximum adsorbate capacity (Figure 3.1a) for the adsorbate-adsorbent pairs varies from 0.16-0.4 $kg_{adsorbate}/kg_{adsorbent}$, with the charcoal-water and silica gel-water pairs having the maximum at 0.4 and 0.37 $kg_{adsorbate}/kg_{adsorbent}$, followed by activated carbon-methanol at 0.32 $kg_{adsorbate}/kg_{adsorbent}$. The maximum

adsorbate capacity of Zeolite 13X is 0.3 $kg_{adsorbate}/kg_{adsorbent}$. The heat of adsorption of zeolite 13X on a mass and volume basis is 1323 $kJ/kg_{adsorbent}$ and 793,800 kJ/m^3, respectively, which are the highest values of all pairs considered. The heat of adsorption is essentially an indicator of how much thermal energy can be stored using the pair, and here zeolite 4A-water and zeolite 13X-water emerge as promising pairs with an energy capacity per mass of adsorbate of 4410 $kJ/kg_{adsorbent}$, which is maximum amongst all pairs considered.

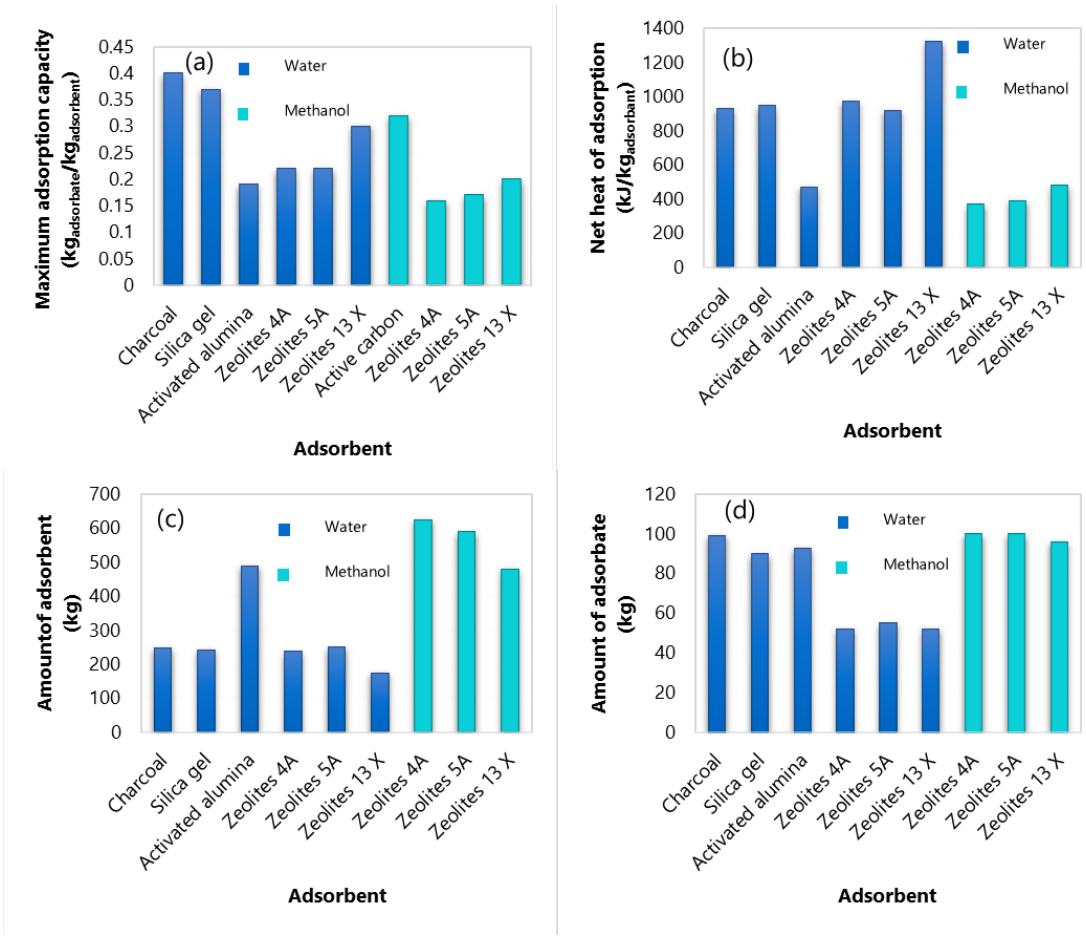

Figure 3.1 a) Maximum adsorption capacity of various adsorbents, b) Heat of adsorption generated with one kilogram of various adsorbents, c) Amount of adsorbents needed to meet the energy requirements of house of four in Canada , and d) Amount of adsorbate needed to meet the energy requirements of house of four in Canada.

Table 3.5 also presents the details on the net heat of adsorption (plotted in Figure 3.1b) which can be obtained from one kilogram of adsorbent. Here the zeolite 4A-water and zeolite 13X-water pairs have a heat of adsorption of 970.2 and 1323 $kJ/kg_{adsorbent}$, respectively, which are the maximum amongst all pairs under consideration. Also, zeolite 4A-water and zeolite 13X-water pairs have the minimum mass of adsorbent (Figure 3.1c) and adsorbate (Figure 3.1d) needed to satisfy the energy demands.

The total mass of the of the adsorption system (Figure 3.2a), including both adsorbent and adsorbate, needed to meet the energy requirements when zeolite 4A-water and zeolite 13X-water are used is 452.6 and 353.7 kg, respectively. The total volume of adsorbents (Figure 3.2c) needed to meet the set energy requirements when using the zeolite 4A-water pair is 0.48 m^3 and that for when the zeolite 13X-water pair is used is 0.45 m^3, which are significantly lower than when the zeolite 5A-methanol pair is used, which is 1.35 m^3. The total cost of the adsorbents in the discussion is shown in Figure 3.2d which is reasonable considering the possible thermal energy storage.

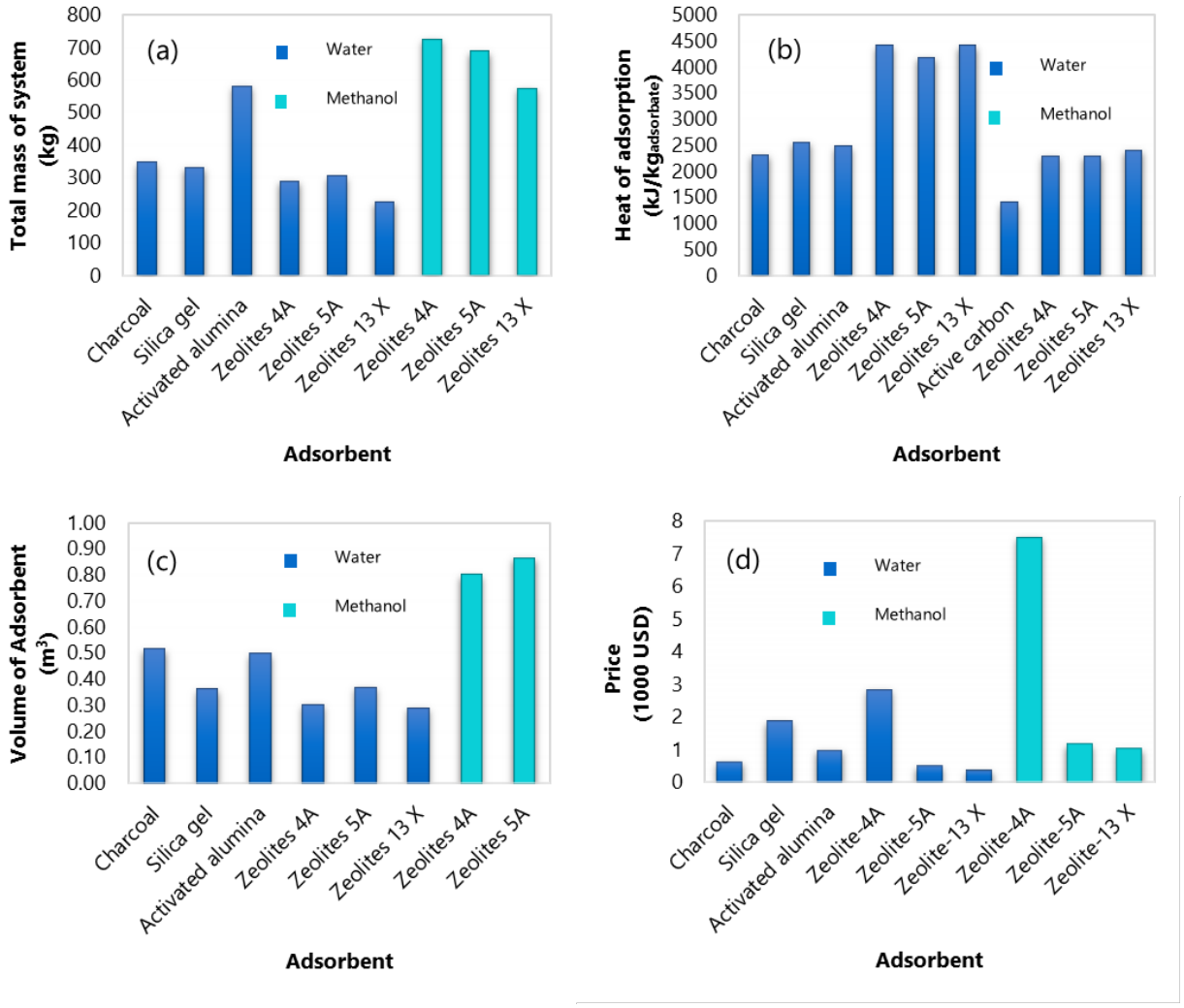

Figure 3.2 a) Total mass of system (adsorbent and adsorbate) to meet the energy requirements of house of four in Canada, b) Net Heat of adsorption of various adsorbents, c) Volume of adsorbents needed to meet the energy requirements of house of four in Canada, and d) Costs of various adsorbents

3.5 Life Cycle Assessment of Adsorbents

The criteria guiding the selection of TES materials predominantly revolves around their thermophysical properties. Materials with attributes such as non-toxicity, inflammability, non-explosiveness, non-corrosiveness, possessing substantial gravimetric and volumetric storage capacities, and high thermal diffusivities are generally preferred. Furthermore, cost-effectiveness, availability, stability, extended service life, and cyclic durability are highly desirable attributes of TES materials. Regardless of the operational efficiency of a TES material, its environmental compatibility is of paramount importance. The realization of the core objectives of harnessing solar energy and efficiently recovering waste heat hinges on the eco-friendliness of the materials employed. Consequently, a comprehensive life cycle assessment is imperative to thoroughly evaluate these materials for their environmental impact over the entire lifespan of the system. Therefore, this part of study undertakes a comparative study of environmental impact associated with thermal energy storage materials from literature with a primary focus on comparing these materials based on their total greenhouse gas emissions per kilowatt-hour (kWh) of stored energy. The analysis encompasses Silica gel, SAPO-34, Zeolite 13X, CAU-10-H, AI-Fumarate and activated carbon employed in the thermochemical based thermal energy storage aiming to pinpoint the most environmentally friendly options. Here below, a general introduction to Life Cycle Assessment (LCA) is provided followed by a discussion on LCA studies focused specifically on adsorption based thermochemical energy storage.

3.5.1 Life Cycle Assessment

The life cycle of a product represents a comprehensive journey that encompasses the progression of raw materials from their initial extraction phase through various transformative processes occurring under

diverse conditions within multiple systems. This journey culminates in the creation of the finished product, which is subsequently transported, distributed, utilized, maintained, recycled, and ultimately disposed of at the end of its service life. Each of these phases, spanning from the initial raw material extraction to final disposal, exerts a discernible impact on both the environment and human health. In response to this, LCA emerges as a systematic and holistic methodology employed for the assessment and quantification of the environmental implications associated with materials, processes, systems, and products throughout their entire life cycle. The methodological framework for conducting a LCA study is well-established and follows the guidelines outlined in ISO 14040 and ISO 14044. This structured methodology comprises four essential phases: goal and scope definition, inventory analysis, impact assessment, and interpretation (Figure 3.3) [192].

The environmental impacts from various activities during the life cycle of a product on air, water and soil are studied in various environmental impact categories e.g., Global Warming Potential (GWP), Acidification Potential (AP), Eutrophication Potential (EP) and Photochemical Ozone Creation Potential (POCP) etc. GWP describes the emission of greenhouse gases in air which increases the solar heat absorption in earth atmosphere which on the other hand causes an increase in average global temperature.

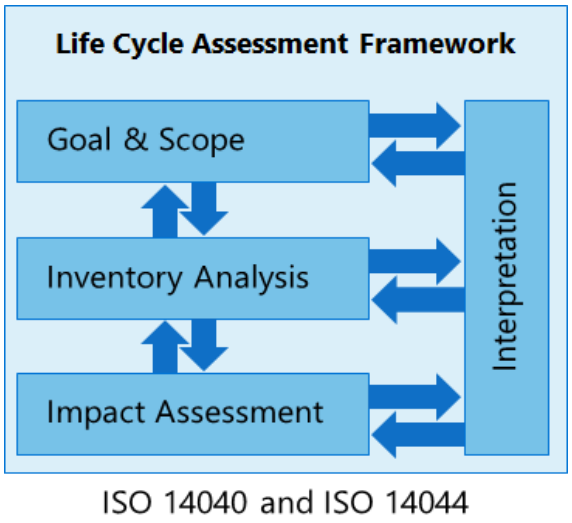

Figure 3.3 Life Cycle Assessment (LCA) framework

3.5.2 LCA studies focused on Thermochemical Energy Storage

A LCA study by Nienborg et. al. compared the GWPs of materials used in absorption and adsorption based thermal energy storage technologies. The GWPs of Silica gel, zeolite 13X, SAPO-34, CAU-10-H and Al-Fumarate are compared. The setup simulates a closed sorption thermal energy storage system using a coated copper tube-fin heat exchanger having three vertical tube rows to assess the performance of adsorbents at near-vacuum conditions. Water acts as the adsorbate, and a combined condenser and evaporator simplifies the design. The total volume of the heat exchanger considers the volume of the finned tubes is around 1.59 x 10^{-3} m^3 and an additional 20% for headers and bends. The entire system is sealed in a stainless-steel containment. The sorption cycle is kept less than 30 minutes. The results for four scenarios are presented. In the first two scenarios, adsorption occurs at 35 °C and 55 °C, which corresponds to underfloor and radiator heating systems, respectively. Desorption occurs at 90 °C and 120 °C for these scenarios. In all scenarios, the condensation and evaporation temperatures were fixed at 20 °C and 10 °C, respectively.

SAPO-34 while having the best heating capacity amongst all, was found to have the highest GWP [193]. In another study by Nienborg et. al., Al-Fumarate is found to have the highest GWP when compared with the GWPs of silica gel, zeolite 13X and SAPO-34 using GaBi software [194]. Furthermore, a Solar Thermal Adsorption Refrigerator prototype demonstrated the ability to achieve temperatures between 20°C and 80°C on the external wall of a vacuum tube using ethanol and activated carbon, both readily available and environmentally friendly materials. The results indicated significant life cycle environmental benefits associated with STAR compared to a conventional refrigerator. This assessment employed the "TRACI" tool developed by the U.S. Environmental Protection Agency [195]. A separate study by Denzinger et. al. offered a comprehensive method for performing a LCA while emphasizing the studied materials' global warming potential (GWP) and their thermochemical properties. This method involved a three-part analysis: material level, component level, and concept level. The material level analysis followed the EN15804 standard, focusing on the amount of thermal energy stored per kilogram of material. The component level analysis used the functional unit of 1 kWh of delivered thermal energy which includes loses during charging, storage, and discharge losses. The building level analysis adhered to the EN15643-1 standard for the functional unit. The chosen system boundary followed a cradle-to-gate approach, as defined by the EN15978 standard. The Speicher-LCA tool was utilized for the LCA analysis [196]. Figure 3.4 and Table 3.6 presents this comparative data in detail, wherein all values have been converted to units of Kg CO_2-eq/kwh in order to make a comparison. The standard error of the mean for the GWP values reported in the literature were determined and the error bars in Figure 3.4 represent 95% confidence intervals.

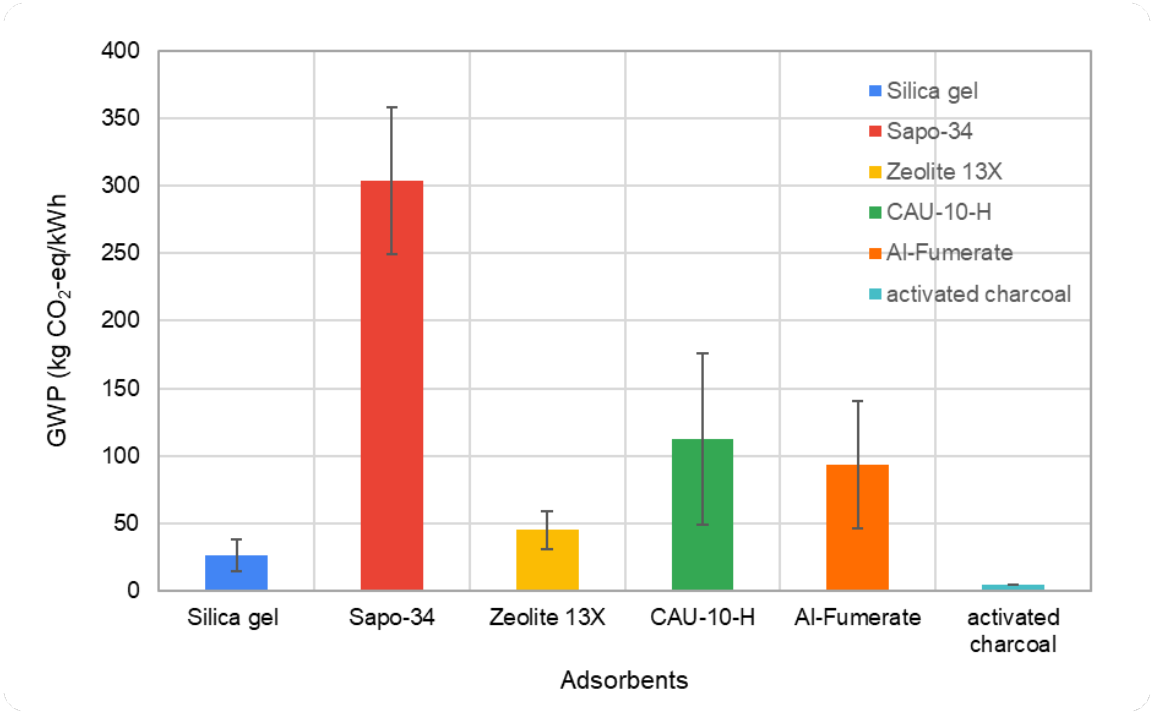

Figure 3.4 Global Warming Potential (GWP) from the studied adsorbents

Table 3.6 GWP data for various adsorbents

Adsorbent	Life cycle boundary	Operating temperature range (°C)	Functional Unit	Global warming potential per energy stored ($KgCO_{2e}$/kWh)	Reference
Silica gel	Cradle to Grave	55-120	1 m^3 Storage	54.0	[193]
Silica gel		35-120	1 m^3 Storage	7.2	
Silica gel		55-90	1 m^3 Storage	72.0	
Silica gel		35-90	1 m^3 Storage	7.2	
Sapo-34		55-120	1 m^3 Storage	378.0	
Sapo-34		35-120	1 m^3 Storage	216.0	
Sapo-34		55-90	1 m^3 Storage	540.0	
Sapo-34		35-90	1 m^3 Storage	252.0	
Zeolite 13X		55-120	1 m^3 Storage	50.4	

Zeolite 13X		35-120	1 m^3 Storage	36.0	
Zeolite 13X		55 -90	1 m^3 Storage	108.0	
Zeolite 13X		35 -90	1 m^3 Storage	46.8	
CAU-10-H		55 -120	1 m^3 Storage	162.0	
CAU-10-H		35 -120	1 m^3 Storage	9.0	
CAU-10-H		55 -90	1 m^3 Storage	270.0	
CAU-10-H		35 -90	1 m^3 Storage	9.0	
Al-Fumerate		55 -120	1 m^3 Storage	180.0	
Al-Fumerate		35 -120	1 m^3 Storage	36.0	
Al-Fumerate		55 -90	1 m^3 Storage	288.0	
Al-Fumerate		35 -90	1 m^3 Storage	36.0	
Silica gel	Material Production		kg CO_{2e}/kg	8.7	[194]
Zeolite 13X			kg CO_{2e}/kg	14.9	
Sapo-34			kg CO_{2e}/kg	253.8	
Al-Fumerate			kg CO_{2e}/kg	10.3	
System: The Solar Thermal Adsorption Refrigerator (STAR) prototype using granular **activated charcoal**	Cradle to Grave	4°C-22	KJ per cycle	4.8	[195]
Silica gel	Cradle to Grave		1 kWh of TES	8.7	[196]
Zeolite 13X			1 kWh of TES	13.8	
SAPO-34			1 kWh of TES	181.2	
Al-Fumerate			1 kWh of TES	10.3	

3.6 Selected Adsorbent-Adsorbate Pair

It is evident from both the case study and comparative LCA study that zeolite 13X-water pair is an outperformer. It has the highest heat of adsorption of 4410 kJ/$kg_{adsorbent}$, and specific heat of 4410 kJ/kg. K between all the adsorbents considered. Also, it requires only 81.63 kg of water with 272.11 kg of zeolite 13X to meet the space heating requirements of the house under consideration in Section 3.4 which are the lowest amongst all adsorbent-adsorbate pairs under consideration. The GWP of zeolite 13X and silica gel are 45 kg CO_2-eq/kWh and 26.31 kg CO_2-eq/kWh, respectively. The GWP of 45 CO_2-eq/kWh for zeolite 13X makes it a good choice to be used in TES applications in comparison to Sapo-34, CAU-10-H and Al-Fumerate for which GWP are 303.56 kg CO_2-eq/kWh, 112.49 kg CO_2-eq/kWh and 93.45 kg CO_2-eq/kWh respectively.

Based on the findings presented in this chapter zeolites have emerged as suitable adsorbents for thermal energy storage applications. However, to fully appreciate the unique properties of zeolites, a foundational understanding of zeolites themselves is necessary. The following section presents a brief introduction to zeolites.

3.7 Zeolites

The exploration of natural zeolites can be traced back to the work of the Swedish mineralogist, Freiherr Axel Fredrick Cronstedt (1722-1765). Cronstedt made his discovery in 1756 while researching in a Swedish copper mine. He noticed that the minerals he studied puffed up when heated with a blow-pipe flame, leading him to name them "ze”lites," derived from the Greek“wor”s "zeo" (to boi“) and ”lithos" (stone) [197], [198]. Throughout history, around 50 natural zeolites have been discovered, with some being used by

ancient civilizations for various purposes, including construction. Zeolite crystals, often found in basaltic and volcanic rock cavities, have long fascinated rock collectors and geologists. Initially, their limited use and rarity hindered their widespread commercial use. However, the late 1940s marked a pivotal era with major geological findings, revealing significant sedimentary deposits of natural zeolites worldwide. This breakthrough heightened interest in their scientific study and practical uses [199].

Natural zeolites are aluminosilicate materials enriched with hydration. Their primary building units consist of Si and Al oxide tetrahedra, intricately connected by oxygen ions to form both two-dimensional and three-dimensional secondary units. These zeolites contain channels and cavities within their network, accommodating hydrated alkali and alkaline earth metal ions, which maintain electrical balance. Zeolites are known for their exceptional hydrating and dehydrating properties, which have been key in understanding their physical and chemical properties. While natural zeolites form in low-temperature geological environments, synthetic zeolites are produced in labs through hydrothermal synthesis [200]. The synthetic mordenite displays larger pores compared to its natural counterpart. The continuous synthesis and exploration of zeolites underscore their significance in both scientific research and industrial applications.

During hydrothermal synthesis, specific chemicals “alled "te”plates" or structure-directing agents guide the organization of SBUs into tertiary or composite building units. The resulting crystal zeolite takes a polyhedral shape with Si-O-Al bonds. Controlling kinetic processes is crucial, as many zeolites formed this way are metastable [200], [201].

"The Atlas of Ze”lites," published in 2001, details 176 unique zeolite framework types. Only six natural zeolites are found abundantly worldwide: analcime, chabazite, clinoptilolite, erionite, mordenite, and phillipsite [202].

These crystalline aluminosilicates, found in minerals like clinoptilolite and garronite, are highly resistant and thermally stable. In contrast, synthetic zeolites (e.g., types A, P, X, Y) are used as sorbents, catalysts, and ion exchange materials, with properties tailored by controlling the silica-alumina ratio. Zeolite crystals are complex in structure and effective in molecular sieving, playing key roles in selective separation and as acid catalysts in petroleum refining. The evolution of zeolite synthesis, with over 200 types, and their use in heterogeneous catalysis underline their versatility and significance.

Zeolites have a general formula of $(MAlO_2)(SiO_2)_x(H_2O)_y$ with M^+ usually being H^+ or Na^+, and x and y are the number of molecules. Their cage-like tetrahedral structures make them ideal for adsorption applications. With a high surface area due to their porosity, zeolites are effective in air purification, carbon capture, catalysis, and thermal energy storage.

The International Zeolite Association (IZA) has established a nomenclature system for both natural and synthetic zeolites, using a three-letter code for each framework type. Notable types include Zeolite A (LTA), Zeolite X (FAU), and Mordenite (MOR). Zeolite A was one of the first synthetic zeolites, Zeolite X and Y are known for large pores and catalytic use, and Mordenite is noted for its fibrous crystals. Other important types are Clinoptilolite, Chabazite, Erionite, Phillipsite, and Analcime, see Table 3.7. Faujasite is a general term for faujasite-type zeolites, including X and Y.

Table 3.7 Type of zeolites [203], [204].

Type	Framework	Discription
Zeolite A	LTA	Linde Type A, one of the earliest synthetic zeolites.
Zeolite X	FAU	Faujasite, known for its large pores and used in various industrial applications.

Zeolite Y	FAU	Another faujasite type with a high silicon-to-aluminum ratio, widely used as a catalyst.
Mordenite	MOR	Known for its fibrous crystals and used as a catalyst.
Clinoptilolite	HEU	Heulandite, commonly found in natural deposits and used for ion exchange.
Chabazite	CHA	Has a unique cage-like structure and is used in catalysis.
Erionite	ERI	Known for its fibrous crystals,'but it's a health concern due to its association with respiratory diseases.
Phillipsite	PHI	Contains large cavities and is used in catalysis.
Analcime	ANA	Known for its cubic crystals and is found in volcanic rocks.
Faujasite	FAU	General term for faujasite-type zeolites, including types X and Y

3.7.1 Zeolite 13X

Considering the adsorption of water on zeolite 13X is purely physisorption in nature, zeolite 13X and water are used as the adsorbent and adsorbate, respectively, for all experiments performed in this work because of their high ESD, high porosity and surface area, non-toxicity, and availability. Furthermore, during the recharging phase water can be delivered to the zeolite 13X beads by passing air through the adsorbent bed; the water vapor in the air is adsorbed as air flows through the adsorbent bed. Notably, when the adsorbate is water, Zeolite 13 X has a higher net heat of adsorption than other adsorbents such as silica gel, activated alumina, zeolite 4A, and zeolite 5A, which reduces the volume of adsorbent required for TES applications. Furthermore, there have been numerous studies reported in the literature which show zeolite 13 X yields good results in adsorbent-based thermal energy storage systems. Some of the Zeolite 13X characteristics that makes it one of the most popular adsorbents in thermal energy storage applications are:

- **Surface area:** Zeolite 13X is a high surface area adsorbent. Its surface area varies from 600-800 m^2/g.

- **Pore size:** The cage like tetrahedral structure of Zeolite 13X offers a uniform pore size with a pore diameter of approximately 1 nm which is suitable for adsorbing larger molecules.

- **Adsorption Capacity:** Zeolite 13X has a high adsorption capacity for larger molecules like water (26 g per 100 g of water [205]), and carbon dioxide (3.2-5.1 mmol/g [206]).

- **Selectivity:** Due to its larger cage size structure Zeolite 13X adsorbs large molecules while allowing the smaller molecules to pass through it which is why it is a very popular adsorbent for filtration applications.

- **Thermal Stability:** Zeolite 13X has a charging temperature of up to 350 °C which makes it thermally stable at elevated temperatures in comparison to other popular adsorbents.

- **Chemical Stability:** It does not chemically react with water, methanol and ethenol due to which it is widely used as a catalyst in various industrial applications.

- **Water Adsorption:** Zeolite 13X has a high adsorption affinity for water molecules due to which it is popular in water filtration, atmospheric water capture, and thermal energy storage applications. An experiment study demonstrated that the water adsorption capacity of zeolite 13X is 23%, 21% and 19% (kg/kg) when the discharging temperature was 35, 45 and 60 °C and the adsorbents were charged at 90°C. Adsorption capacity increased to 24% on increasing the adsorption temperature to 150°C [207].

The specifications of the zeolite 13X used in the experiments within this dissertation are given below in Table 3.8.

Table 3.8 Zeolite 13X specifications [208]

Product Name	Molecular sieves, 13X, 3-5mm (0.12-0.20in) beads, Thermo Scientific Chemicals
Catalog Number	L06085.30
CAS	63231-69-6
IUPAC Name	Molecular sieves 13X
MDL Number	MFCD00131613
Appearance (Color)	White to cream to pale brown
Comment	Tapped bulk densi–y 600 - 725 g/L
Particle Size	Oversize: ≤5.0% @ >4.75mm (4 mesh)
Comment	CO_2 adsorption: ≥11.5% (45mbar, 25°C)
Particle Size	Undersize: ≤5.0% @ <2.36mm (8 mesh)
Form	Beads
Residual water	≤1.5% (550°C, 2h)
Chemical Stability	Hygroscopic

Zeolite 13X is a Faujasite (FAU) type of zeolite adsorbent. It is known for its high adsorption affinity towards larger adsorbate molecules e.g., nitrogen, carbon dioxide, oxygen and water, and it is widely used in many industrial applications. Some of the applications of Zeolite 13X are drying and purification, carbon dioxide capture and separation, air separation, atmospheric water capture and thermal energy storage [209], [210].

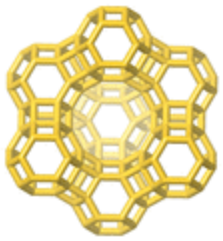

Figure 3.5 Structure diagram of zeolite 13X [209].

A synthetic zeolite can be synthesized using the alkali fusion method [211].

Step 1 Prepare the mixture: Prepare a homogeneous mixture of waste porcelain powder and NaOH powder in a ratio of 10:12 (weight ratio).

Step 2 Heating in a nickel crucible: Heat the mixture in a nickel crucible in the air at 600 °C for 6 hours. This process is referred to as alkali fusion and involves the reaction between the porcelain and sodium hydroxide.

Step 3 Cooling down: Allow the fused material to cool down to room temperature. The material obtained after cooling is referred to as the fused material.

Step 4 Preparation of suspension: Add 0.5 g of the fused material to 2 mL of distilled water.

Step 5 Aging process: Allow the mixture to age with vigorous agitation using a reciprocal shaker at room temperature for 24 hours. This aging step promotes the formation and growth of zeolite crystals

Step 6 Heating in water bath: Heat the aged material in a water bath at 80 °C for 12 hours. This step further promotes crystallization and the formation of zeolite structures.

Step 7 Product formation: The material obtained after the heating process is considered the final product. This product likely contains Zeolite 13X crystals.

Step 8 Filtration: Filter the aged material and the final product to separate the solid zeolite material from the liquid.

Step 9 Washing: Wash the filtered material with distilled water to remove any impurities or residual reactants.

Step 10 Drying: Dry the washed material in a drying oven at 60 °C overnight. The drying process ensures that the zeolite crystals are in a stable form and ready for use or further characterization.

4 The Evaluation of Zeolite 13X Adsorbent as a Storage Medium for Short-Distance Mobile Thermal Energy Storage

4.1 Chapter Overview

The utilization of the water-zeolite pair as an adsorbate-adsorbent system has garnered significant attention in the realm of thermochemical energy storage, offering great potential for various applications. Despite promising results in laboratory settings, widespread implementation of this technology has yet to be realized. Recent advancements in mobile thermal energy storage (m-TES) employing thermochemical materials have opened new avenues for enhancing the practicality and cost-effectiveness of solar thermal energy harnessing and waste heat recovery. The experimental work conducted in this chapter delves into the feasibility of storing thermal energy in zeolites, charged externally to the heat recovery reactor, and discusses the potential applications of externally charged zeolites for m-TES over short distances, shedding light on their practicality and significance in advancing the field of mobile thermal energy storage. The findings reveal that zeolites charged at 200°C and subsequently stored outside the discharging unit exhibit an impressive energy storage density (ESD) exceeding 110 kWh/m³ under conditions of 0.45 m/s air flow velocity (flow rate 0.00059 m^3/s) and 60% relative humidity during zeolite discharging. These ESD values are comparable to previously reported values in the literature. Moreover, ESD values of 24.0 kWh/m³ were achieved by charging zeolite beads contained within packed transportable tubes constructed from stainless steel mesh.

4.2 Introduction

Up to 50% of the energy consumed in industry is ultimately lost as industrial waste heat (IWH), [212], [213] causing unnecessary greenhouse gas emissions and increased costs. Recently, there has been a significant amount of research focused on industrial waste heat recovery (IWHR), including advancements in heat exchangers, thermoelectric generators, and the organic Rankine cycle [214], [215]. However, presently IWHR is not implemented commercially on a large scale and the vast majority of IWH remains underutilized [216], [217]. Barriers to recuperating IWH include owners' reluctance to risk economic losses and disturbances in daily operation, capital costs, and challenges with matching IWH supply with heat demands [218]. Regarding the latter point, the importance of integrating thermal energy storage (TES) in IWHR processes to facilitate load matching and to prevent disruptions due to intermittently supplied IWH has been recognized [219].

Thermal energy can be stored using sensible heat storage (SHS), latent heat storage (LHS), or thermochemical heat storage (THS). Among these options, THS materials offer advantages due to their high energy storage density (ESD), which is roughly an order of magnitude greater than that of SHS materials, and often double that of LHS materials [220]. In particular, using the heat of adsorption of water on zeolites to store thermal energy has shown promising results [221], [222]. Zeolites can be “charged” by heating and drying and thermal energy can be recovered at a later time by exposing the dried zeolites to moist air during a “discharging” phase.

TES using zeolites has been investigated extensively. Hongois et. al. measured an energy density of 166 kWh/m^3 for a zeolite-$MgSO_4$ composite comprising 10 to 25 wt% of $MgSO_4$ [223] Johannes et. al. designed an open thermal energy storage system to supply 2 kW of heat power over 2h to reduce peak electric loads in a single-family house. This TES system contained two packed bed reactors, each with 40 kg of zeolite

NaX. Measurements showed the system could provide a constant power of 2.25 kW for over two hours, and was thus able to satisfy the design requirements [224]. Tatsidjodoung et. al. built a prototype TES system that was designed to provide space heating for a modern family house. The reactor consisted of two cylindrical vessels, each with a volume of 140 L, a diameter of 72 cm, and a height of 20 cm. In their experiments, a zeolite 13X/H_2O reactive pair was charged using a stream of hot air with temperatures and flow rates of 120–180 °C, and 120–180 m^3/h, respectively. Their results demonstrated that average air temperature rises of 38 °C could be achieved over a duration of about 8 hours, significantly increasing the fraction of energy consumption supplied by solar energy in a house [225]. Mette et. al. proposed a new strategy to regenerate zeolite 4A for applications in TES systems. They used a two-stage process in which air was first dried using zeolites. This dried air was then heated to 130 °C and used to regenerate zeolites to store thermal energy. Their experiment results showed that air with a water vapor pressure of 1.5 mbar and a temperature of 130 °C was more effective for recharging zeolites than air at a temperature of 180 °C and a pressure of 10 mbar [226]. Lim et. al. constructed a TES system in which the adsorbents were housed in a 400 mm long stainless-steel pipe with a 159.6 mm diameter. In their experiments, zeolite 13X and zeolite 4A were dried at 350 °C and 450 °C, respectively. The system was under vacuum during the experiments, and the measured ESD for zeolite 13X was 233. 8 MJ/m^3, while that of zeolite 4A was 218.6 MJ/m^3 [227].

In the vast majority of research reported to date, the charging process involves supplying heated air to stationary zeolites housed in an adsorption bed. This approach can be disadvantageous for Industrial Waste Heat Recovery (IWHR) due to the extensive hardware required, such as heat exchangers, piping, and fans, to transport air from the heat source to the adsorption bed. These requirements increase capital costs, consume space, and maintenance needs throughout the life of the IWHR system. Alternatively, mobile TES

(m-TES) systems are being developed to enhance flexibility in connecting heat supply with demand. While most m-TES systems for waste heat recovery have primarily focused on using phase change materials for Latent Heat Storage (LHS) [228], it is crucial for m-TES systems to possess a high Energy Storage Density (ESD). For instance, in a techno-economic analysis, Shehadeh et al. determined that the minimum system-level ESD required to make m-TES competitive with other low-carbon energy sources ranged from 0.3 to 0.4 MJ/kg, depending on whether a diesel-powered or electric truck was used to transport the zeolite [229]. Further, Fujii et. al. conducted a prospective life cycle assessment for the design of m-TES systems and their results emphasized that, for truck transport, the ESD must increase as the transport distance increases to achieve a reduction in greenhouse gas emissions [230].

To achieve a high ESD, THS materials, such as the zeolite-water pair, are better suited for m-TES. Krönauer et. al. constructed and tested a storage container that housed 14 tons of zeolite for mobile heat storage. The zeolite was charged using hot air at a temperature of 130 °C from a waste incineration plant and transported 7 km by truck to provide heat for an industrial drying process. The storage capacity was 2.3 MWh, and it was estimated that each trip avoided 616 kg of CO_2 emissions [231]. However, apart from this work by Krönauer et. al., limited research has been conducted on utilizing zeolites for m-TES.

In this chapter, the potential of charging and storing zeolites outside of an adsorption bed and subsequently loading them into a reactor to be discharged to recover heat is evaluated. The subtle difference between charging zeolites in a location external to the adsorption bed, rather than by flowing hot air through an adsorption bed packed with zeolites, can have significant implications for IWHR and for storing solar energy. For example, concentrated solar radiation and industrial equipment and processes that generate suitable heat, such as drying and baking ovens, steam boilers, glass melting, and various chemical processes can be used to charge zeolites housed in lightweight containers. These containers could then be transported,

via a fuel cell or battery-powered forklift [232], from different locations in an industrial facility or complex and stored near a single discharging unit to be used when heat is in demand. m-TES systems designed for heat recovery over short distances can reduce the hardware needed to pipe heat from multiple sources thereby improving the economic feasibility of IWHR throughout an industrial complex while also reducing thermal losses. The objective of this work is to compare the ESD of zeolites charged and stored externally to the adsorption bed with the ESD of zeolites reported in the literature. Our results show that the ESD of zeolites charged in an oven at 200 °C and stored external to the discharging unit can exceed 110 kWh/m^3 when the flow rate and relative humidity of the air used to discharge the zeolites are 0.45 m/s (flow rate 0.00059 m^3/s) and 60%, respectively, which is comparable with ESD values reported for zeolites in the literature.

4.3 Materials and Methods

4.3.1 Materials

The adsorbent used in this study was Zeolite 13X (CAS No: 63231-69-6), which came in the form of spherical beads supplied by Alfa Aesar. These beads have a size of 3 mm, a density of 688 kg/m^3, and a surface area of 585 m^2/g. Distilled water was employed as the adsorbate. The adsorbate was kept at room temperature before filling it in a humidifier reservoir.

4.3.2 Experimental Setup

The experimental setup is depicted in Figure 4.1, with its central component being the test section housing the adsorption bed. The zeolite beads are contained within this adsorption bed, which has dimensions of 120 mm in length, 80 mm in width, and 40 mm in height and a volume of 0.384 L. This is comparable to the volume of reactors reported in Table 4.1 which range from 9 mL to 70 L. The walls of the adsorption bed are constructed from rigid foam insulation boards, specifically 25.4 mm (1-inch) thick Owens Corning FOAMULAR C-300 XPS boards. The zeolites are held in place by metal meshes located near the inlet and outlet of the adsorption bed to secure the zeolites in place. Within the adsorption bed, seven T-type thermocouples (Omega TMQSS-020G-6) are strategically placed. Five of these thermocouples, denoted as T_1 through T_5, are positioned at the center of the adsorption bed at distances of 27 mm, 53 mm, 80 mm, 107 mm, and 133 mm, measured from the inlet. Another thermocouple, labeled as T_I is situated upstream from the zeolite beads near the inlet, while an additional thermocouple, referred to as T_o, is located downstream from the zeolite beads near the outlet of the adsorption bed. For the measurement of relative humidity at the inlet and outlet of the adsorption bed, two hygrometers (HTM2500LF from TE Connectivity) are employed. These hygrometers are positioned as indicated in Figure 4.1, with RH_i denoting the one at the inlet and RH_o denoting the one at the outlet. Temperature and humidity measurements are acquired using an Agilent 34970a data acquisition system. During the storage period, the zeolite beads in the adsorption bed are isolated by closing valves V_3 and V_4. Two flanges, located just upstream from V_3 and just downstream from V_4, facilitating the removal of the adsorption bed from the system to simplify the loading and unloading of the zeolite beads.

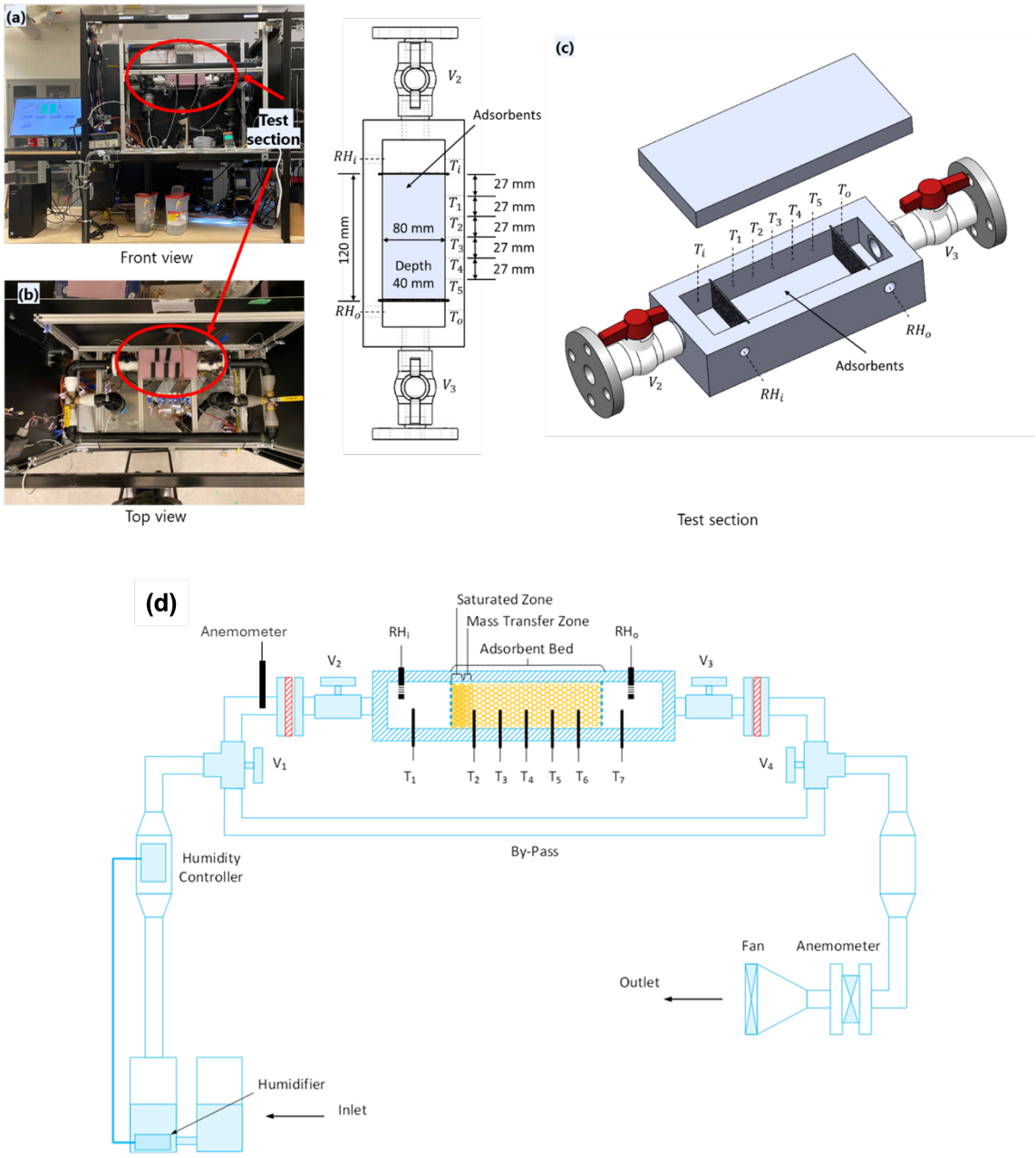

Figure 4.1 (a) Front view of experiment setup; (b) top view of experiment setup; (c) a schematic of the test section; (d) a schematic of the adsorption bed illustrating the locations of the thermocouples, valves, and hygrometers

A container filled with distilled water and equipped with two ultrasonic mist makers (AGPTEK Aluminum Mini Mist Maker) is positioned near the inlet of the reactor to provide humidified air. To regulate humidity, a programmable humidity controller (Auber Instruments, HD220) is placed 500 mm away from the humidifier. During the humidity stabilization phase, two three-way valves (V_1 and V_2) are employed to direct air through the bypass. At the commencement of the discharging phase, Valves V_1 and V_2 are switched to redirect air through the adsorption bed. The airflow within the system is controlled using a DC-axial fan (EBM-PAPST, 24V), located at the system's outlet. Throughout the system, air flows through ABS piping with an inner diameter of 4.1 cm and an outer diameter of 4.8 cm. To measure air velocity, a hot-wire anemometer (Testo 405i) is utilized upstream from the adsorption bed.

4.4 Experimental Procedure

4.4.1 Charging Phase

Experiments were conducted using loose zeolite 13X beads contained within steel mesh tubes to facilitate their transport.

Loose zeolite beads: The zeolite beads were placed in glass beakers to charge for 2 h in a Thermo Scientific Heratherm Oven (OGS60) at different temperatures (50, 100, 150, and 200 °C). When the adsorbents were removed from the oven, the beakers were immediately sealed using aluminum foil and then left overnight to cool to room temperature overnight.

Zeolite beads contained within steel mesh tubes: Zeolite beads were packed into tubes that were fabricated using stainless steel wire mesh and secured with metal clamps. In practice, these tubes could be positioned near various sources of industrial waste heat to charge the Zeolite 13X. And then readily transported to an

adsorption bed at a centralized location to be discharged when heat recovery is needed. The wire mesh had an aperture of 1.6 mm, and the mesh tubes comfortably accommodated the zeolite beads, which have a diameter of 3 mm. The mesh tubes themselves had a diameter of 40 mm and a length of 115 mm. Wire mesh was attached inside both ends of the tube, and the section of the tube occupied by the zeolite beads was 100 mm in length. The mesh tube diameter was chosen to precisely fit the 40 mm depth of adsorbent bed in the test section (Figure 4.1a). The mesh tubes containing the Zeolite 13X were charged at 200 °C for 2 h and then transferred to a container, which was subsequently sealed. Charging times for lab-scale adsorption-based TES experiments reported in the literature vary between 1.5 h [233] and 8 h [234] For the experiments in Chapter 4 the charging time was set to 2 h. This comparatively shorter charging time is advantageous for transferring more heat in mobile TES systems. The flow rate used in this study ranges from 0.00046 - 0.00059 m^3/s which ate comparable to the flowrates reported in the literature (see Table 4.1). These sealed containers with the zeolite-filled mesh tubes were stored overnight before being moved to the adsorption bed within the experimental setup the following day. Figure 4.2a displays the adsorption bed filled with Zeolite 13X, while Figure 4.2b shows an image of the adsorption bed filled with zeolite beads packed into the mesh tubes.

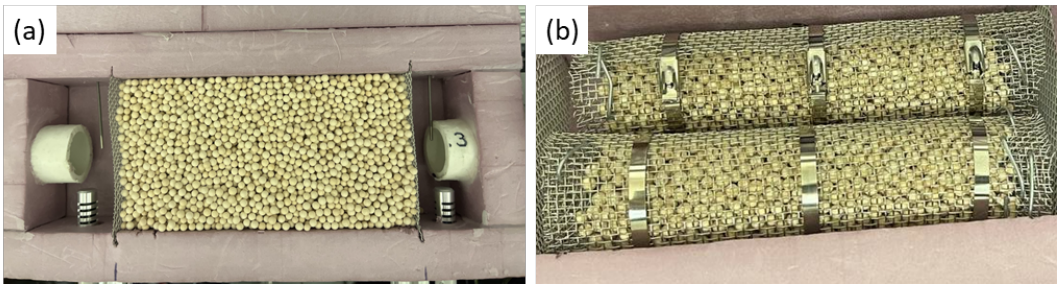

Figure 4.2 (a) The adsorption bed packed with zeolite beads (b) Stainless steel wire mesh tubes packed with Zeolite 13X.

4.4.2 Discharging Phase

After cooling to room temperature, the charged zeolite beads were carefully placed into the adsorption bed while valves V_2 and V_3 were closed. The thermocouples and hygrometers were then installed in their appropriate positions in the test section. Subsequently, the lid of the adsorption bed was closed using clamps and the adsorbent bed was connected to the rest of the experimental set-up using the flanges located at the outer edges of the test section, as illustrated in Figure 4.1b. Before commencing the discharging phase, V_1 and V_4 were adjusted to direct air through the bypass. The humidifier reservoir is filled with distilled water at room temperature, and the humidity controller is set to the desired humidity level. The fan at the system's outlet is turned on to initiate airflow through the system.

Once the velocity and humidity of the air flowing through the bypass stabilized, valves V_1 and V_4 are adjusted to allow the air pass through the test section. The inlet temperature and relative humidity level of the moist air flowing into the adsorption bed are recorded using thermocouple T_i and hygrometer RH_i. Airflow measurements taken using the Extech SDL300 metal vane thermos-anemometer were found to be much higher than that flowing through the test section. To measure the airflow through the adsorption bed a hot-wire anemometer (Testo 405i) was used just upstream from the inlet of the test section as shown in Figure 4.1a. The water vapor suspended in the moist air is adsorbed by the zeolite beads, and the heat of adsorption is generated. The heat of adsorption increases the temperatures of the zeolite beads and of the air within the adsorption bed, which are measured using thermocouples T_1-T_5. The relative humidity of the air flowing through the adsorbent bed decreases as water vapor in the air is adsorbed by the zeolite beads. The relative humidity of the air exiting the adsorption bed is measured using hygrometer RH_o. As the discharging phase continues, the capacity for the zeolite beads to adsorb water diminishes, and the heat generated in the adsorption bed gradually decreases to zero. When the temperature of the adsorption bed

returns to that of the inlet, the discharging phase is completed, and valves V_1 and V_4 are set to direct airflow through the bypass. The humidifiers and fan are turned off and the test section is removed.

4.4.3 Calculating the Energy Storage Density

The ESD, which is the thermal energy retrieved by the air flowing through the adsorption bed during the discharging phase, is calculated using Equation (4.1)

$$\mathrm{ESD} = \frac{1}{V_{ads}} \int \dot{m} \cdot Cp_{ma} \cdot \Delta T \cdot dt \qquad (4.1)$$

where V_{ads} is the volume of the adsorption bed, $\dot{m}$ is the mass flow rate of the air through the adsorption bed, Cp_{ma} is the heat capacity of the moist air exiting the adsorption bed, and ΔT is the difference between the air temperatures at the outlet and inlet of the adsorption bed. The integral is carried out over the first 2.5 h of the discharging phase.

The heat capacity of the air exiting the adsorption bed is taken as the sum of the heat capacity of the dry air and the water vapor within the air and is calculated using

$$C_{p_{ma}} = C_{p_{air}} + x \cdot C_{p_{wv}} \qquad (4.2)$$

where x is the humidity ratio. The specific heat capacities of the air and water vapour are taken to be $C_{p_{air}}$= 1.006 kJ/kg·K and $C_{p_{wv}}$ = 1.84 kJ/kg·K. The humidity ratio is calculated using:[235]

$$x = 0.622 \cdot \left(\frac{RH_o \cdot (P_{wv})_{sat}}{1 - (RH_o \cdot (P_{wv})_{sat})} \right) \qquad (4.3)$$

where RH_o is the relative humidity at the outlet of the adsorption bed and the partial pressure of water vapour in moist air is calculated using as: [236]

$$(P_{wv})_{sat} = 0.611 \cdot e^{\left(\frac{17.27*T_o}{T_o+237.3}\right)} . \quad (4.4)$$

4.5 Results and Discussion

The impact of charging temperature on the measured temperature-time profiles is depicted in Figure 4.3. In this experiment, the zeolites were charged for 2 h and subsequently discharged with an air flow velocity of 0.35 m/s (flow rate 0.00046 m^3/s). For the case when the zeolite beads were packed in the steel mesh tube the flow rate was measured to be 0.4 m/s (flow rate 0.00053 m^3/s). As anticipated, the charging temperature exerts a significant influence on the heat generated during the discharging phase. Specifically, at the location of the first thermocouple, T_1, within the adsorption bed, the temperature rise is 2.4, 5.0, 17.1, and 33.7 °C when the charging temperature is set to 50, 100, 150, and 200 °C, respectively.

In all experiments depicted in Figure 4.3, the temperature raise occurs successively from positions near the inlet to those near the outlet of the reactor. In other words, the temperature at T_1 increases first, followed by the temperature at T_2 and so on. When humid air enters the adsorption bed water vapor is initially adsorbed by the charged zeolite near the inlet of the reactor. As the discharging phase progresses, the region where adsorption primarily occurs gradually shifts toward the outlet of the reactor, and the temperature at T_1 begins to decrease while adsorption continues downstream. For instance, the temperature raise at T_5 persists for a longer period and exhibits a broader profile compared to that at T_1 in all experiments.

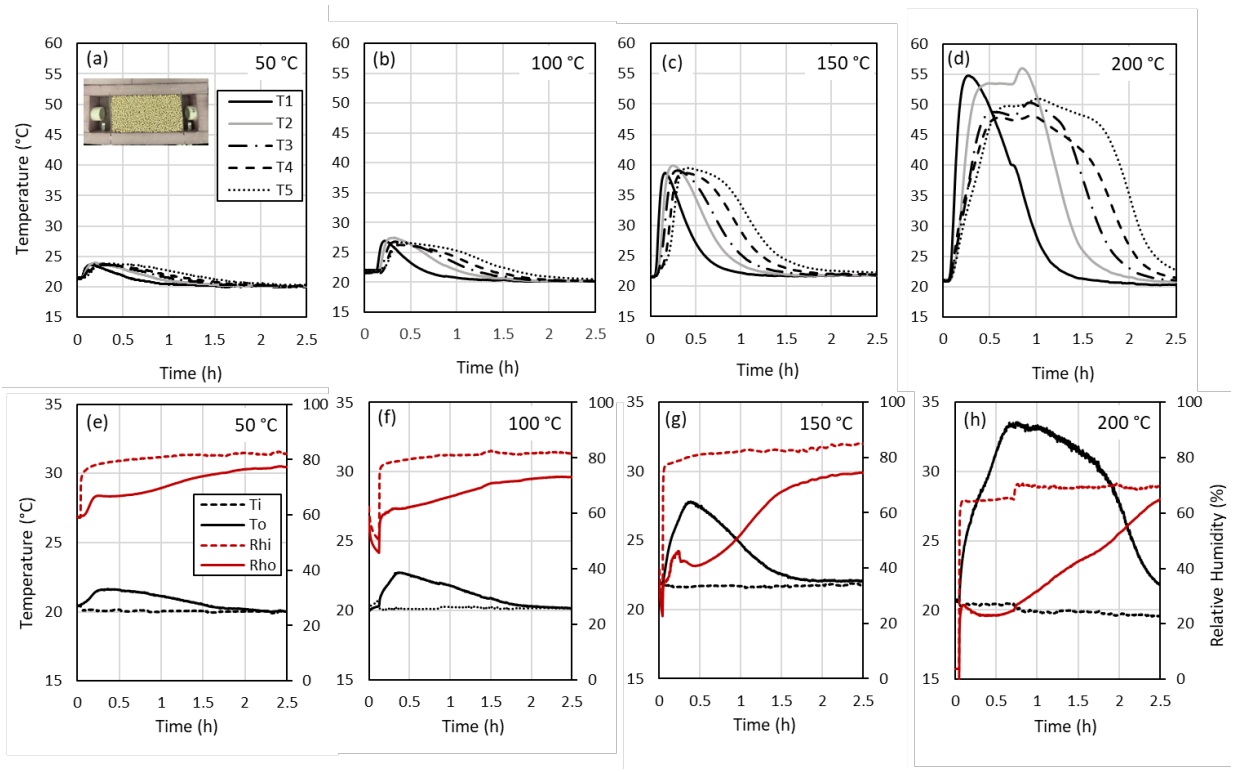

Figure 4.3 The temperature at thermocouple positions T_1 – T_5 as a function of time during the discharging phase when the Zeolite 13X were charged at (a) 50 ° C, (b) 100 ° C, (c) 150 °C, and (d) 200 °C. The inlet and outlet temperatures and relative humidities plotted as a function of time during the discharging phase when the Zeolite 13X were charged at (e) 50 ° C, (f) 100 ° C, (g) 150 °C, and (h) 200 °C. The air flow velocity during the discharging phase was 0.35 m/s.

The inlet and outlet temperatures, measured during the discharging phase for the different charging temperatures, are represented by the dashed and solid black lines, respectively, in Figures 4.3e -3h. The inlet temperature remains constant across all experiments, while the outlet temperature begins to increase at the start of the discharging phase, reaches its peaks when the temperature lift is at a maximum, and then gradually decreases at a slower rate. The temperature lift at the outlet, when the charging temperature is set to 50, 100, 150, and 200 °C is 1.2, 2.8, 6.0, and 12.9 °C, respectively. Temperature distribution at different positions at different times in the adsorbent bed during the discharging phase is shown in Figure 8.5a-d.

The relative humidity at the inlet and outlet of the adsorption bed during the discharging phase is shown as the dashed and solid red lines, respectively, in Figures 4.3e-3h. At the commencement of the experiments there is a substantial disparity between the relative humidities at the inlet and outlet of the adsorption bed. For example, for the case when the zeolite was charged at 50 °C, at the start of the discharging phase the RH at the inlet and outlet of the adsorption bed differs by approximately 20% (e.g. the RH is about 60% at the inlet and about 80% at the outlet). However, by the end of the discharging phase the RH at the inlet and outlet are within 5% of each other. The difference in RH between the inlet and outlet of the adsorption bed measured near the beginning of the discharging phase increases as the charging temperature increases. This is as expected because zeolites adsorb a greater amount of water from the air passing through the adsorption bed when they have been charged at a higher temperature. It can also be noted that the difference between the humidity at the inlet and outlet appears to be less when the results are plotted in terms of absolute instead of relative humidities. Figure 4.3 is plotted in terms of the absolute humidity, instead of the relative humidity, in Figures 8.1 in the appendix. A visible difference when plotting the results in terms of absolute humidity instead of relative humidity is that there appears to be a larger difference between the humidities at the inlet and outlet of the adsorption bed during the discharging phase when the relative humidity scale is used. This occurs when the outlet is at a higher temperature than the inlet because for a given amount of water vapor the relative humidity decreases with increasing temperature (the results shown in Figures 4.4 and 4.5 are also plotted as Figures 8.2 and 8.3 in the appendix in terms of absolute humidity instead of relative humidity).

The results for the experiments in which the zeolites were charged for 2 h at 200 °C and then discharged using different flow velocities of 0.35, 0.4 and 0.45 m/s (flow rates 0.00046, 0.00053, and 0.00059 m^3/s respectively) are presented in Figure 4.4. As depicted in Figures 4.4a – 4c, similar to the case for Figure

4.3, the temperature increase within the adsorption bed occurs progressively from the adsorbents near the inlet of the reactor, at T_1, to the adsorbents close to the outlet of the reactor, at T_5. The inlet and outlet temperatures and relative humidities when the flow velocities are 0.35, 0.4 and 0.45 m/s (flow rates 0.00046, 0.00053, and 0.00059 m^3/s respectively) are shown in Figures 4.4d – f, respectively. Consistent with the results shown in Figure 4.3, the inlet temperature remains relatively constant while the outlet temperature increases to a maximum value during the discharging phase, and then gradually decreases to the temperature at the inlet as the discharging phase progresses. Based on the results in Figure 4.4d-f there is no apparent correlation between the outlet temperature and the airflow velocity. This is in contrast to results reported by Lefebvre et al. who reported that the maximum outlet temperature decreases with increasing flow rate [237]. They also reported the outlet temperature peak broadens as the flow rate decreases because adsorption occurs at a reduced rate over a longer duration. The reason these effects were not observed in Figure 4.4d-f may be due to the narrow range of airflow velocities investigated and experimental variations. In Figure 4.4d-f the highest airflow rate was about 30% more than the lowest airflow rate (0.45 m/s as compared to 0.35 m/s) whereas in the study by Lefebvre et al the highest airflow rate was four times larger than that of the lowest airflow velocity. The temperature distribution at different positions at different times in the adsorbent bed during the discharging phase is shown in Figure 8.4a-c.

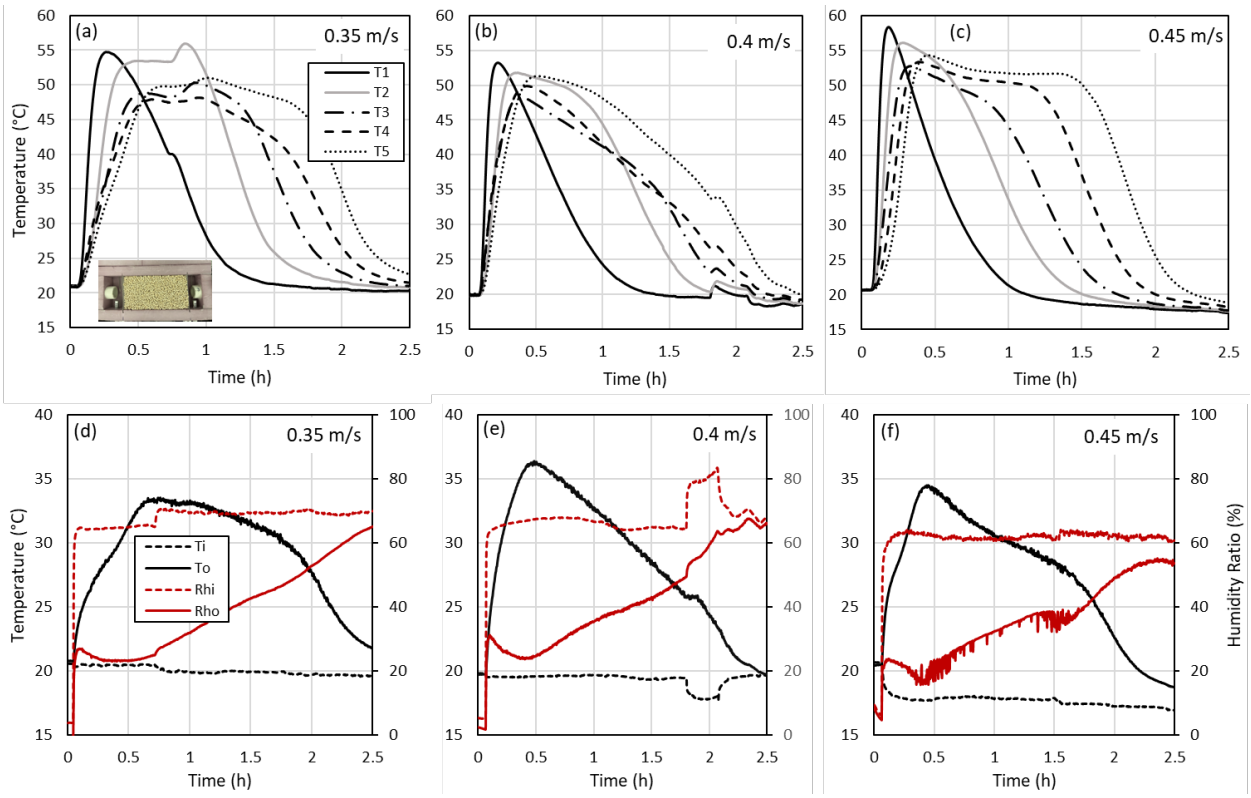

Figure 4.4 The temperature at thermocouple positions T_ - T_5 as a function of time during the discharging phase when the Zeolite 13X were charged at 200 °C and the air flow velocity is (a) 0.35 m/s, (b) 0.4 m/s, and (c) 0.45 m/s. The inlet and outlet temperatures and relative humidities plotted as a function of time during the discharging phase when the Zeolite 13X were charged at 200 °C and the air flow velocity during the discharging phase is (d) 0.35 m/I€ 0.4 m/s, and (f) 0.45 m/s.

For the results shown in Figures 4.4d-4f the difference between the RH at the inlet and outlet is approximately 40% at the beginning of the discharging phase. As expected, the RH at the outlet increases and approaches that near the inlet as the discharging phase continues and the zeolite becomes saturated with adsorbed water. There is a sharp increase in the inlet RH at the 2 h mark of the discharging phase for the case when the flow velocity is 0.4 m/s (flow rate 0.00053 m^3/s). This is attributed to an increase in relative

humidity of the air entering the reactor, which may have occurred if the water reservoir near the inlet of the reactor was disturbed. Moreover, the two ultrasonic mist makers (AGPTEK Aluminum Mini Mist Maker), which add humidity to the air intermittently, could have contributed to variations to the relative humidity during the experiments despite using a humidity controller. The temperature of the air flowing through the adsorption bed also rose abruptly just before the 2 h mark in Figure 4.4e due to the sudden increase in relative humidity. However, it's worth noting that the small changes in temperature measured during the experiment did not have a significant impact on the ESD value determined. The absolute humidity at inlet and outlet of the adsorbent bed during the discharging phase is shown as the dashed and solid red lines, respectively, in Figures 8.2e-3h.

The ESD of the Zeolite 13X is shown with respect to their charging temperatures in Figure 4.5a. The ESD at the charging temperature of 50 °C is 6.37 ± 2.1 kWh/m^3 (9.27 ± 2 Wh/kg) and at 100 °C is 8.28 ± 2.3 kWh/m^3 (13.43 ± 2 Wh/kg). The charging temperature has a significant effect on the ESD, and the benefits of charging at temperatures above 150 °C is apparent. Specifically, the ESD increases from 20.5 ± 3 kWh/m^3 (29.9 ± 3 Wh/kg) to 83.05 ± 4.2 kWh/m^3 (120.72 ± 4.2 Wh/kg) when the charging temperature increases from 150 to 200 °C. The error on these values was determined using the error propagation method. The error in the temperature measurements using the T-type thermocouples is ±0.1°C. The specific heat of air was assumed to be 1.000 ± 0.015 kJ/kg·K. The specific heat of water vapour was assumed to be 1.996 ± 0.030 kJ/kg K. The error in the airflow velocity measurements is ± 0.05 m/s.

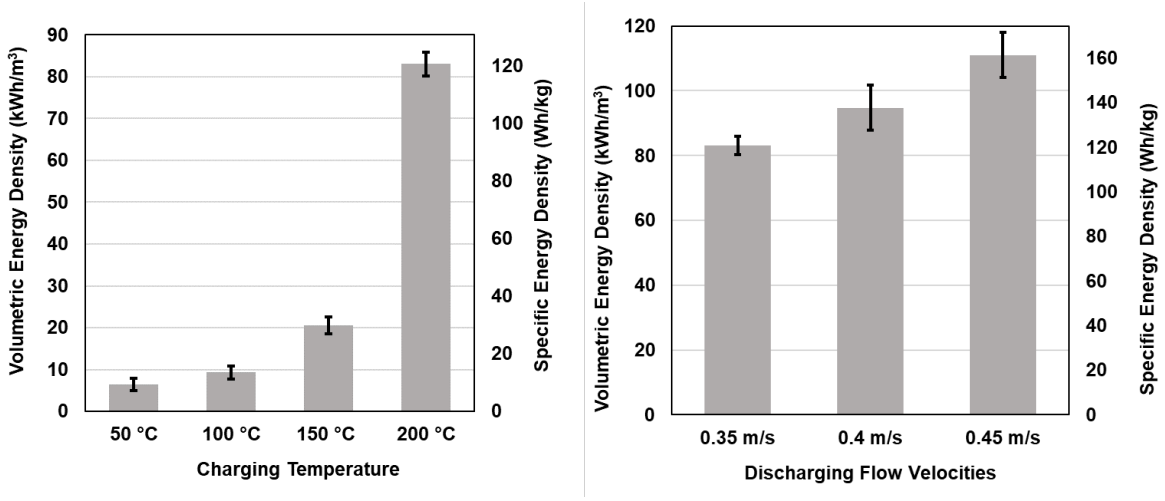

Figure 4.5 The volumetric and specific energy density of the thermal energy recovered from the Zeolite when the it was charged at (a) different temperatures and when the air flow velocity was 0.35 m/s during the discharging phase, and (b) when the charging temperature was 200 °C and the air flow velocity was varied during the discharging phase.

The ESD for Zeolite 13X charged at 200 °C for 2 h is shown in Figure 4.5b for different airflow rates during the discharging phase. The ESDs at a flow velocity of 0.35 m/s (flow rate 0.00046 m^3/s) and 0.4 m/s (flow rate 0.00053m^3/s) are 83.05 ± 4 kWh/m^3 (120.7 ± 4.1 Wh/kg) and 94.7 ± 10 kWh/m^3 (137.7 ± 10 Wh/kg) respectively. As shown in Figure 4.4e, the relative humidity at the inlet increased while the inlet temperature decreased over the time period of 1.7 to 2.1 h during the experiment. To check the effects of this change in RH on the ESD the variation in the inlet temperature was removed (by extrapolating the inlet temperature such that it was at a constant value of almost 20 °C for the entire duration of the experiment) and the ESD was recalculated. With this adjustment the ESD decreased slightly from 94.7 kWh/m^3 to 92.8 kWh/m^3, showing the increase in RH caused the ESD to increase by just ~ 2%. The ESD increases with increasing flow velocity, reaching a maximum of 111.04 ± 10 kWh/m^3 (161.4 ± 10 Wh/kg) at an airflow velocity of 0.45 m/s (flow rate 0.00059 m^3/s). The ESD increases with increasing flow velocity is attributed to a greater

amount of heat lost to the surroundings that occurs as the duration of the discharging phase increases [236]. In other work D. Dicaire et al. have reported that the ESD is independent of airflow rate in a highly insulated adsorption bed [238]. [239]

In Figure 4.6a, the temperature at thermocouple positions T_1 – T_5 are plotted as a function of time during the discharging phase, considering the scenario where the zeolite beads were enclosed within stainless steel mesh tubes. Correspondingly, temperatures and RH at the inlet and outlet of the adsorption bed are presented in Figure 4.6b. The temperature within the adsorption bed at T1-T5 increased to a maximum of about 32 to 34 °C after around 30 minutes into the discharging phase.

In contrast to Figures 4.3 and 4.4, where the temperatures at T1-T5 peak at different times when the zeolite beads are placed directly within the adsorption bed without the stainless steel mesh tubing, there was not much variation between the temperatures at T1-T5 when the zeolites are housed within the stainless steel mesh tubes. This phenomenon can be attributed to improved airflow through the adsorption bed when the zeolite beads are contained within the mesh tubes. With the zeolite beads in the mesh tubes, there is room for the humid air flowing through the adsorption bed to interact with the zeolite beads at various points along the length of the mesh tube. On the other hand, when the zeolite beads are packed directly into the adsorption bed, the humid air flowing through the reactor initially contacts the zeolite 13X near the inlet and progressively interacts with points closer to the outlet.

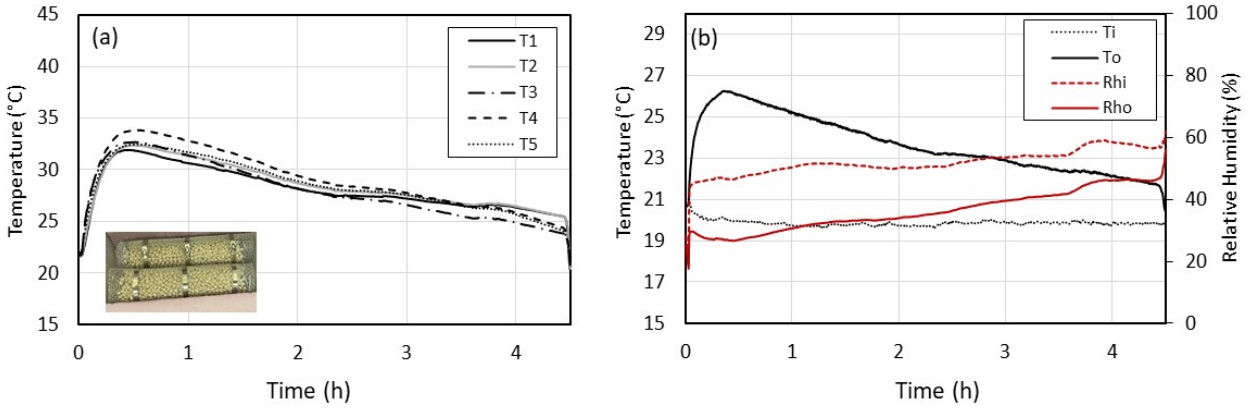

Figure 4.6 (a) Temperature profiles at thermocouple positions T_1 – T_5 as a function of time during the discharging phase when the Zeolite 13X were housed within tubes made from stainless steel mesh; (b) Corresponding inlet and outlet temperatures along with relative humidities plotted as a function of time during the discharging phase.

As indicated in Figure 4.6b, the outlet temperature increased from 20 °C to about 26 °C. This temperature increase is modest compared to the outlet temperature rise observed in some experiments where the zeolites were packed into the adsorption bed without the stainless steel mesh (for instance, the outlet temperature increases to over 35°C in Figure 4.4e). While the outlet temperature increase is relatively small for the case when the zeolites are stored in mesh tubing, it is also noted that it takes longer for the outlet temperature to return to the temperature at the inlet. As illustrated in Figure 4.6b, the outlet temperature is still elevated in comparison to the inlet temperature after 4.5 h. This is attributed to the fact that there is less air contact with the zeolite beads when they are stored within the mesh tubes. In other words, a portion of the humid air flowing through the adsorption bed can bypass the zeolite beads by flowing through the open spaces surrounding the tubes. On the contrary, when the adsorption bed is packed with zeolite beads (without the tubes) the humid air flowing through the adsorption bed is forced to pass through the smaller space between the beads, thereby increasing adsorption and accelerating the amount of heat generated during the

discharging phase. The average ESD when the zeolites were housed within the mesh tube for two experiments with a 4.5 h discharging phase is 24.0 kWh/m^3. Temperature distribution at different positions at different times in the adsorbent bed during the discharging phase is shown in Figure 8.6, and the absolute humidity at inlet and outlet of the adsorbent bed during the discharging phase is shown as the dashed and solid red lines, respectively, in Figures 8.3b.

4.5.1 Comparison to Literature

Using zeolites for thermochemical energy storage has been investigated under different charging and discharging conditions in a variety of reactor configurations in the literature. Examples of ESD values reported in the literature from different experiments are provided in Table 4.1. In viewing the results in Table 4.1 it should be noted that the ESD depends on many factors including the charging and discharging conditions, the size of the reactor, the insulation and heat losses from the reactor, and the flow rate used during the discharging process. The ESD also depends on the composition of the zeolite used. For example, Casey et. al. measured the ESD of different Na zeolite samples, wherein Na had been exchanged with different ions and the mesoporous structure was impregnated with hygroscopic salts. Their results showed the ESD depends on the composition of the zeolite and that the inclusion of hygroscopic salts increases the ESD [239].

Excluding the results from this work, the ESD attained using zeolites ranges from 25.8 to 200 kWh/m^3. The ESD of 25.8 kWh/m^3 was measured for a zeolite 13x sample in a packed bed adsorption column with a length and volume of 6.9 cm and 62.8 cm^3, respectively [240]. The ESD of 200 kWh/m^3 was achieved

using a hybrid activated alumina and zeolite 13x in a packed cylindrical column with a volume of 9.04 mL and regeneration temperature of 250 °C [22].

As can be noted in Table 4.1, the ESD measured in this work is generally lower than that reported in the literature. For example, the largest ESD reported in the literature for pure zeolite 13x, which is the adsorbent used in this study, was 198 kWh/m^3 for the case of a packed bed reactor with a volume of 250 L comprising four 62.5 L segments and a charging temperature of 190 °C [241]. In comparison, in this work when the charging temperature is 200 °C the ESD ranged between 82.9 and 110.9 kWh/m^3 depending on the discharging flow rate. Furthermore, the ESD measured in this work for the cases when the charging temperature was 150 °C or less was much lower than that reported in the literature. For example, the ESD measured in this work was 20.5 kWh/m^3 when the charging temperature was 150 °C, whereas an ESD of 25.79 kWh/m^3 was measured when the charging temperature was 120 °C and the relative humidity was 50%.

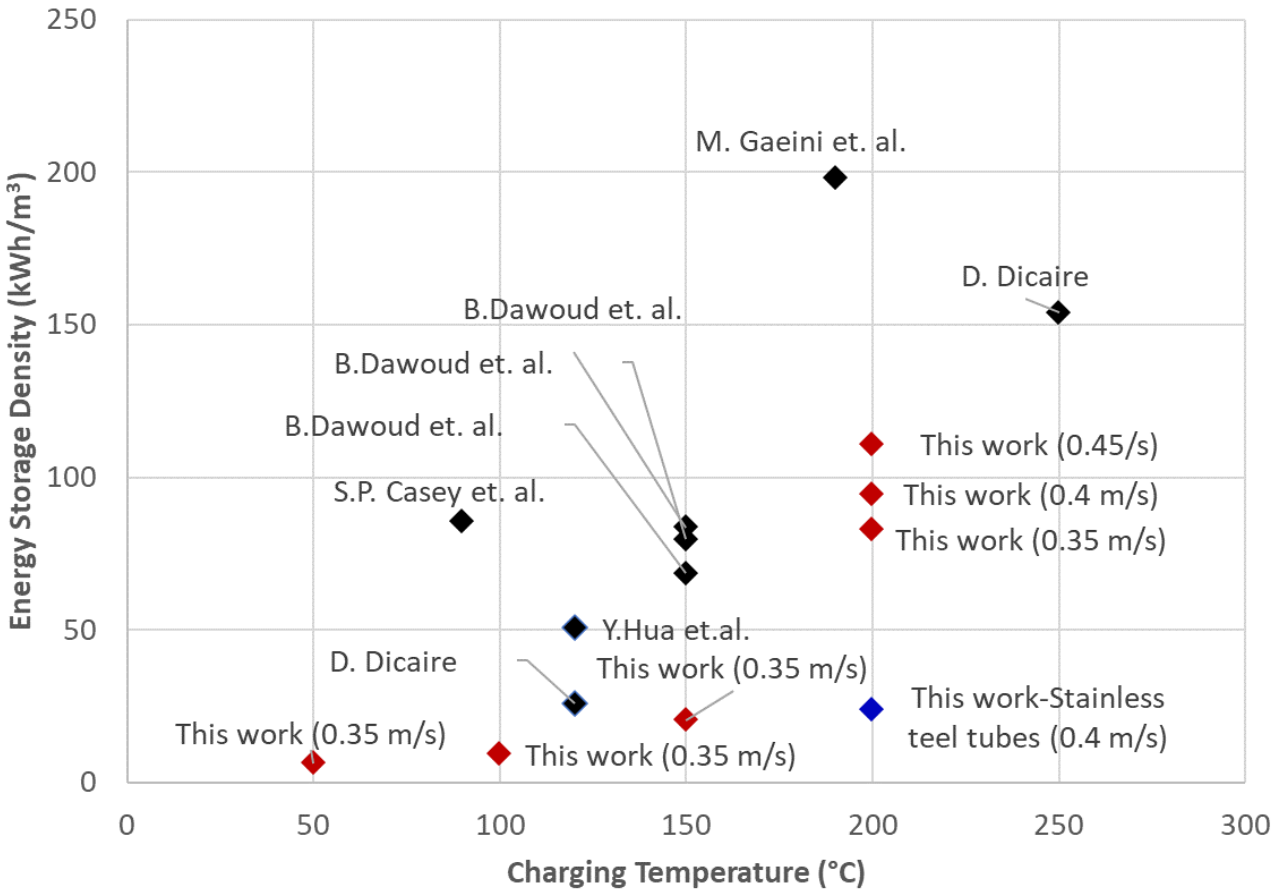

Figure 4.7 Energy storage density of zeolite 13X from this work compared with the reported values in literature.

Despite that the ESD measured in this work is typically lower than that reported in the literature, the ESD values achieved when the charging temperature is 200 °C are still significant. For example, an ESD over 110 kWh/m^3 was achieved when the discharge airflow velocity was 0.45 m/s (flow rate 0.00059 m^3/s). In comparison, the ESD when using water as a storage medium is about 70 kWh/m^3 for a temperature difference of 60 °C [242]. Furthermore, energy can be stored using zeolites for as long as required whereas as water gradually transfers heat to its surroundings. These results show the potential of charging zeolites in lightweight containers at distributed point sources at a temperature of 200 °C, and then transporting and

storing the charged zeolites to a reactor with an adsorbent bed at a central location where the heat can be recovered and utilized.

Table 4.1 Energy storage densities of Zeolite 13X reported in the literature

System Description	Adsorbent	Charging	Discharging	Energy Storage Density (kWh/m^3)	Ref
- Comprises an adsorber/desorber unit and a condenser/evaporator unit - The adsorber/desorber contains 13.2 kg of zeolite	Zeolite 13X	- Flow rate is 2 L/min - Inlet air is at 150 °C	- Flow rate is 0.5 L/min	68.53	[243]
			- Flow rate is 1 L/min	79.71	
			- Flow rate is 2 L/min	83.53	
- Lab-scale flow reactor with 200 g of sample in the adsorption bed	Zeolite-$MgSO_4$ composite		- Flow rate is 8 L/min - RH is 50%	166	[244]
- Cylindrical packed column with a volume of 62.76 mL holding ~55 g of adsorbent	AA13X (hybrid)	- Charged at 250 °C	- Flow rate is 24 L/min - 100 % RH	197	[245]
- Packed cylindrical column with a length of 10 cm and volume of 9.04 mL	Zeolite 13X	- Hot air at 250 °C is blown through the column - 8 h charging time	- Flow rate is 8 L/min - 100 % RH	153.9	[236]
	NaLSX			146.6	
	AA/13X hybrid			160.6	
	AA/13X hybrid		- Flow rate is 24 L/min - 100 % RH	200	
- Rectangular shaped reactor (500 mm x 250 mm x 200 mm) with a sloping roof	Zeolite 13X	- Charged at 90 °C		85.7	[246]
- Packed bed with 41 kg of zeolite	Zeolite 5A	- Charged at 103 °C	- Adsorber inlet temperature is 20 °C	47.2	[247]
- A revolving cylindrical drum (diameter 700 mm, depth 300 mm) filled with 70 L of granular storage material	Zeolite 4A	- Charged at 180 °C	- Humidified inlet air at 25 °C and a flow rate of 140 m^3/h	148	[248]
	Zeolite Na-MSX	- Charged at 230 °C		154	
- Closed sorption storage system with two insulated tanks filled with 1 m^3 of zeolite	Zeolite 13XBF	- Charged at 180 °C	- Constant evaporation temperature of 20 °C.	178	[249]
- A 250 L packed bed reactor comprising four 62.5 L segments	Zeolite 13X	- Flow rate is 33 g/s - Charged at 190 °C	- Flow rate is 50 g/s	198	[241]

- Packed bed adsorption column with a length of 6.9 cm, diameter of 3.4 cm, and volume of 62.8 cm^3	Zeolite 13X	- Charged at 120 °C - RH is 2%	- Flow rate is 24 SLM - RH is 50%	25.79	[240]
			- Flow rate is 24 SLM - RH is 90%	50.66	
- Adsorbents are charged in an oven and stored outside the reactor over night before being loaded into and adsorption bed with a length, width, and height of 120 mm, 80 mm, and 40 mm, respectively	Zeolite 13X	- Charged at 50 °C	- Flow velocity is 0.35 m/s (flow rate 0.00046 m^3/s)	6.37	This work
		- Charged at 100 °C		9.27	
		- Charged at 150 °C		20.5	
		- Charged at 200 °C		82.9	
		- Charged at 200 °C	- Flow velocity is 0.4 m/s (flow rate 0.00053 m^3/s)	94.6	
		- Charged at 200 °C	- Flow velocity is 0.45 m/s (flow rate 0.00059 m^3/s)	110.9	

4.5.2 Short-Distance Thermal Energy Transport

In practice, Zeolite beads could be charged using waste heat from multiple heat sources at an industrial complex such as exhaust streams from reciprocating engines and steam boilers, which have temperatures in excess of 230 °C [215], [250], [251].The charged zeolites could then be transported to an adsorption bed at a centralized location to be discharged to recover the heat. Considering the results in this work, ESDs of 24.0 kWh/m^3 and 110.9 kWh/m^3 were attained when the zeolites were charged at 200 °C for 2 h with and without using the mesh tubes, respectively. Assuming the zeolites used to collect waste heat have a volume of 0.1 m^3, the amount of heat that could be stored over one day per waste heat source (by charging zeolites for 2 hours 12 times) would be 133.1 kWh/m^3 or 28.8 kWh/m^3, using ESD values of 110.9 kWh/m^3 and 24.0 kWh/m^3, respectively. The charged zeolites could be collected from multiple waste heat sources and

transported to an adsorption bed. As shown in Figure 4.8, three waste heat sources (charging zeolites with a volume of 0.1 m^3 each for two hours) could supply two adsorption beds with a total volume of 3.6 m^3. Two adsorption beds could be used such that one could be used to run the discharging process while the other is used to collect and store charged zeolites. Based on the results from this work, 200 kWh of heat could be generated every 12 h. In comparison, and as discussed earlier in chapter 3, heating the average residential house in Canada requires about 40 kWh/day. Furthermore, the ESD values reported in this work can be increased through further optimisation of the size and geometry of the mesh tubes and adsorption bed. Further, the breakeven distance up to which adsorption based thermal energy storage would be reasonable is presented in section 8.1.3.

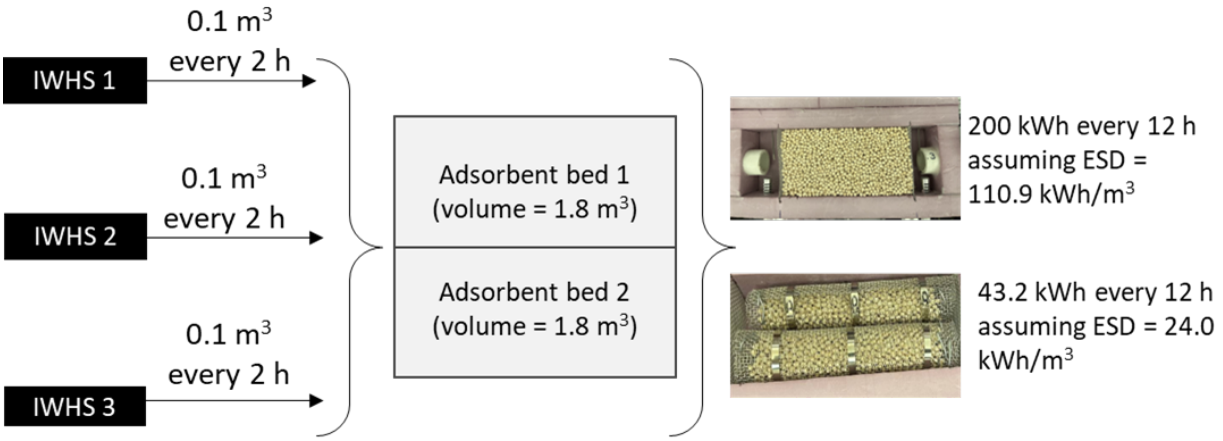

Figure 4.8 A hypothetical scenario based on the results from this work wherein zeolite beads are charged at three different industrial waste heat sources (IWHS) and then transported to an adsorbent bed with two compartments that each have a volume of 1.8 m^3. Thermal energy can be discharged from the adsorbent bed at a rate of 200 kWh and 43.2 kWh every 12 hours if the energy storage density (ESD) is 24.0 kWh/m^3 and 24.0 kWh/m^3, respectively.

In the literature only a limited amount of research wherein thermochemical heat storage materials are transported over short distances has been reported to date, and further development in this area is warranted.

For example, in one related study Mette et. al. proposed an external reactor design wherein the adsorbent reservoir was separated from the reactor. The proposed reactor had a 20 L compartment with funnels at its top and bottom. Charged zeolite entered the top funnel and was discharged in the compartment to generate heat prior to exiting the compartment through the bottom funnel. The results from numerical analysis conducted using Comsol showed that for an airflow rate of 200 kg/h the heat generated from discharging the zeolites increases the air temperature by 26 K [252]. Further research is warranted to determine if externally charged zeolites should be discharged in a centralized adsorption bed using a batch or flow-through process.

Further research is also needed to determine an optimal configuration for the reactor, comprising the adsorbent bed, that would be used to discharge the transported zeolites. In one study Weber et. al. built a seasonal TES system for a living space with a floor area of 43 m^2. The store comprised 4.3 m^3 of zeolite material which segmented into four quadrants with each quadrant partitioned into six segments. The thermal performance of the sorption store was improved by partitioning it into segments because discharging smaller amounts of zeolite at a time reduced the pressure drop across the adsorption bed. Furthermore, for a given amount of charged zeolite, more heat can be delivered and quicker because the reduced mass of the adsorption bed lowers its heat capacity [253]. Considering the results from this work, an optimal configuration may be to segment the zeolites into partitioned containers at the centralized reactor used for the discharging process. This work demonstrated that zeolites can be packed into stainless steel mesh tubes that can be transferred between industrial waste heat sources and an adsorption bed where they can be discharged. In practice, the zeolites beads could be contained in mesh containers of different shapes and sizes. Modular segmented containers could be used to transport zeolites between the heat source and the reactor where discharging will occur. The performance of the discharging process would also depend on

the size of the segmented containers. For example, Lass-Seyoum et. al. investigated storing thermal energy using zeolites in adsorbent beds of different sizes (1.5 L, 15 L and 750 L) and their results showed a larger heat storage capacity was achieved for the adsorbent bed with a volume of 15 L. Furthermore, the maximum specific heat power delivered from the TES systems was measured to be 240, 66, and 50 W/kg when the adsorbent bed was 1.5, 15, and 750 L, respectively [254].

4.6 Conclusion

In this chapter the potential of storing thermal energy using water and zeolites as an adsorbent-adsorbate pair for mobile TES applications was investigated. The approach involved charging zeolites through heating in an oven and storing them externally from the reactor used for the thermal energy recovery process. This method of charging and storing zeolites outside the discharging unit holds practical implications for mobile heat storage applications. The results derived from the experiments conducted in this research reveal that the Energy Storage Density (ESD) of zeolites, charged in an oven at 200°C and stored externally, can exceed 110 kWh/m3 when the air flow velocity and relative humidity during the discharging phase are set at 0.45 m/s (flow rate 0.00059 m^3/s) and 60%, respectively. These ESD values, as observed in this work, are on par with values reported in the literature for experiments where zeolites remained permanently within the adsorption/desorption bed throughout both the charging and discharging phases of the Thermal Energy Storage (TES) cycle. The findings reported herein indicate the necessity for further research into TES systems that facilitate short-distance mobile heat storage. Future investigations will concentrate on optimizing the configuration of the discharging reactor, as well as exploring the use of modular and portable segmented containers for the transportation of zeolites between heat sources of varying temperatures and the discharging reactor. In summary, the results obtained thus far underscore the potential for the

development of TES systems that support the collection of waste and solar heat from multiple sources located within a shared facility or complex. These advancements hold promise for more efficient and versatile heat storage solutions, with far-reaching applications in renewable energy utilization and waste heat recovery.

5 An Experimental Comparison of Thermal Energy Storage in Directly and Indirectly Radiated Adsorbent Beds integrated with Solar Thermal Collectors.

5.1 Chapter Overview

Adsorbents heated using solar energy can be used to achieve thermal energy storage and sorption refrigeration with low environmental impacts. This research compares two different methods of heating adsorbents with solar energy to store thermal energy: (1) by exposing the adsorbents to incident light transmitted through a solar collector window, and (2) by heating a highly absorbing solar collector cover, and then transferring the heat from this solar absorber to adsorbents located beneath it. To carry out this comparison experiments are conducted for three cases of adsorbent beds using zeolite 13X and water as the adsorbent-adsorbate pair. In the first case, the top of the adsorbent bed is a polycarbonate sheet, and the zeolites are heated directly by solar-simulated light transmitted through this sheet. In the context of this study, radiation emitted by the solar lamps that is directly incident onto the zeolite 13X after traversing through the window of the adsorbent bed is referred to as direct radiation. Direct radiation adsorbed by the Zeolite 13X beads at the top of the adsorption bed is converted to heat, which elevates the temperature of the adsorption bed. In the second case a blackened aluminum sheet is placed beneath the polycarbonate window, to generate heat by absorbing incident light. In this configuration the adsorption bed is indirectly radiated, as its temperature increases when heat is transferred to it from the radiated aluminum sheet. Similarly to the second case, the adsorption bed is also indirectly radiated for the third case. However, for the third case the blackened aluminum absorber is placed directly on top of the zeolite 13X beads and the

absorber is isolated from the walls of the reactor to avoid heat losses. The outcomes reveal an energy storage density (ESD) of 43.6 kWh/m3 (63.4 Wh/kg) when light is directly incident onto the Zeolite 13X and an ESD of 33.3 kWh/m3 (48.4 Wh/kg) when light is incident onto a blackened absorber plate that transfers heat to Zeolite beads residing beneath it. However, ESD values were improved to 48.9 kWh/m3 (71.0 Wh/kg) for the third case when the blackened absorber plate was thermally insulated from the walls of the adsorbent bed. These results demonstrate the importance of an optimal absorber arrangement in enhancing the adsorption process for the purpose of elevating energy storage densities.

5.2 Introduction

Solar radiation provides the Earth with 173 PW of power, which is more than 10,000 times the global anthropogenic rate of energy consumption [255], [256]. Solar radiation can be converted to electric power, thermal energy, and cooling power using refrigeration cycles. Recently, there has been much interest in researching adsorbents for solar thermal energy storage (TES) systems. In these systems, solar thermal energy is used to "charge" an adsorbent by heating it to desorb an adsorbate from its surface. In TES systems, the charged adsorbate can be stored indefinitely until heat is required. The heat of adsorption is retrieved during a "discharging" phase when the adsorbate is allowed to come into contact with the adsorbent [257]. Solar-powered TES systems can be used to provide space heating when sunlight is unavailable. For example, using water as the absorbate, Z. Zeng et. al. investigated a Trombe-wall (T-wall) comprising a moisture-based adsorption thermal battery. In this configuration, adsorbents within the T-wall are charged with sunlight during the day and heat is released at night by flowing moist air through the T-wall [258].

A key component in adsorbent-based solar-powered TES systems is the solar collector [259], [260]. In most systems the solar collector is separate from the adsorbent bed; a fluid is heated in the collector and transferred to a heat exchanger within the adsorbent bed [224], [261]. However, in some cases the adsorbent bed is integrated with the solar collector. This integrated approach, wherein the adsorbent bed functions as the solar collector, is advantageous because it enables a high heat transfer rate to the adsorbent and minimizes thermal losses [262], [263]. Moreover, the adsorbents within an integrated collector may be heated with solar energy directly or indirectly. When the adsorbents are heated directly the adsorbent bed has one or more transparent windows that transmit sunlight which is then directly incident onto the adsorbents. When the adsorbents are heated indirectly, they are housed within a container that has a surface on its top side that is highly absorptive towards solar energy. Most integrated solar collectors for adsorption-based systems are heated indirectly. However, for some research on solar-powered adsorption refrigeration cycles the adsorbent beds were directly radiated. For example, Ambarita et. al. investigated the performance of an adsorption refrigeration cycle with activated carbon and alumina as the adsorbents. In their experiments, a 0.5 m x 0.5 m flat plate collector with two glass covers contained 6 kg of adsorbent. A coefficient of performance (COP) of 0.074 was achieved when activated carbon and methanol were used as the adsorbent and adsorbate, respectively [264]. Zeng et.al integrated $CaCl_2$-based fibre brick with ink (ICFB) adsorbent with a honeycomb design to a Trombe wall which was illuminated by direct sunlight during the day to charge the adsorbents and discharged during the night by exposing the adsorbents to moisture. The prototype system achieved an energy storage density of $92\ kWh/m^3$ [265]. Li et. al. used a solar collector with a glass cover and an area of 1.5 m^2 to make an adsorption refrigeration ice maker. The ice maker, which employed an activated carbon-methanol pair, generated 7 – 10 kg of ice after receiving 28 – 30 MJ of incident solar radiation [266]. Sitorus et. al. analyzed the performance of a solar adsorption refrigeration system that used activated carbon from coconut shells and methanol as the working pair. The

system had a flat plate solar collector with an area of 0.25 m^2 comprising 6.5 kg of adsorbents. The collector had two plain glass covers with a thickness of 3 mm separated by a 2 cm air gap. A maximum COP of 0.1276 was obtained when the daily global irradiance was 3.918 kWh/m^2[267].

While directly and indirectly heated adsorbent beds integrated with solar collectors have been studied in the literature, little work has been done to investigate which provides better performance for charging adsorbents and for achieving high TES densities. In the case of indirect absorption, the surface of the solar collector containing the adsorbents can be blackened with a coating to achieve high solar absorptivity and high heat gains. On the other hand, for the direct approach, sunlight is absorbed by the adsorbent, providing an opportunity to minimize heat losses. The objective of this work is to compare the energy storage density achieved in TES systems with different integrated solar collector configurations that are heated directly or indirectly using solar-simulated light. Such a comparison has not yet been reported in the literature. Herein we determine which configuration achieves the greatest energy storage density by elevating the temperature of adsorbents within the solar collector to the greatest extent.

Zeolite 13X and water are used as the adsorbent-adsorbate pair and three different cases of integrated solar collector configurations are considered. In the first case, the top of the adsorbent bed is a polycarbonate sheet and the zeolite 13X is heated directly by solar-simulated light transmitted through this sheet. In the second case, a blackened aluminum sheet is placed beneath the polycarbonate sheet. This aluminum sheet generates heat when it absorbs incident light. The Zeolite 13X beads are heated indirectly as heat is transferred from the aluminum sheet. For the third case, the blackened aluminum absorber is placed directly on top of the zeolite beads and the absorber is isolated from the walls of the reactor to avoid heat losses. The results reveal the energy storage density (ESD) attained using the directly irradiated configuration is

larger than that for the case wherein the blackened aluminum plate is used to indirectly heat the adsorbent bed. However, the largest ESD is achieved in the case of the isolated absorber.

5.3 Methods

5.3.1 Methods used to Measure the Reflectance and Transmittance

The reflectance of the aluminum absorber and packed zeolites were measured using a UV-2600i UV-Vis Spectrometer by Shimadzu LabSolutions. The reflectance and transmittance of the polycarbonate sheet employed as the window of the adsorbent bed were also measured using this instrument. Samples sized at 2 x 2 cm^2 were employed for the analysis.

5.3.2 Methods used to Measure the Thermal Conductivity

The thermal conductivity of packed Zeolite 13X beads is measured using a modified variant of the steady state guarded hot plate technique (Figure 5.2), as outlined in references [268], [269]. This apparatus comprises two distinct sides: one functions as the source of heat, while the other acts as the heat sink. The Zeolite 13X beads are positioned between these two plates, and their thermal conductivity is gauged via electrical means. In this process, controlled heat input is applied to the sample, which subsequently conducts through the sample. The heat then travels to a heat sink that is maintained at a consistent temperature. By measuring the temperature difference between the heat source and the heat sink, the heat resistance of the Zeolite 13X sample is determined which is then used to calculate the material's thermal conductivity.

Zeolite 13X beads of size 3 mm are placed in two different 3-D printed frames of size 40 mm x 40 mm x 7 mm and 40 mm x 40 mm x 10 mm (Figure 5.1) are used for thermal conductivity measurements.

Figure 5.1 Zeolite 13X samples placed inside 3D printed Polylactic Acid (PLA) frames.

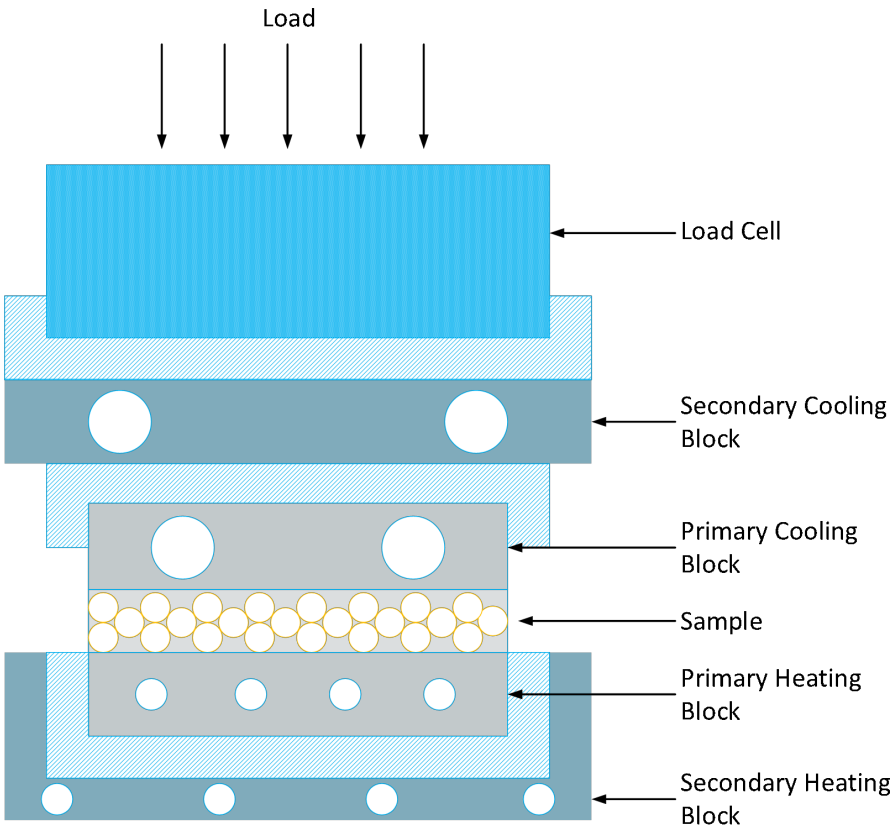

Figure 5.2 Schematic diagram of hot plate apparatus for thermal conductivity measurements.

5.3.3 Experimental Methods

A lab-scale adsorption bed, with dimensions of 90 x 90 x 50 mm^3 as shown in Figure 5.3a and b, was used to conduct experiments. The top side of the adsorption bed is covered with a 6 mm thick Lexan polycarbonate sheet. To facilitate the airflow, a SharkBite 12.7 mm PEX-A pipe (model UA60W100) is installed in the adsorption bed, with an internal diameter of 11.85 mm and an outer diameter of 15.85 mm at the inlet and outlet positions. The airflow through the bed is controlled by two Dahl 12.7 mm valves (model 521-13-13-BAG-HD) located at the inlet and outlet. A Winsinn 40mm 24V fan, positioned at the outlet of the adsorption bed, generates an airflow rate of 1.6 x 10^{-4} m^3/s measured by a Testo 405i flow meter throughout the charging and discharging phases. For temperature measurements, the adsorption bed is equipped with six K-Type thermocouples. Four of these thermocouples are positioned at the center of the adsorption bed, at depths of 5, 15, 25, and 35 mm from the polycarbonate sheet. These thermocouples are aligned vertically to analyze the heat penetration within the adsorption bed resulting from the solar-simulated light coming from the top of the bed. Additionally, one thermocouple is located at the inlet and another at the outlet of the adsorption bed. The adsorption bed is filled with Zeolite 13X beads (chemical compound 63231-69-6) supplied by Alfa Aesar, which consists of beads with a size of 3 mm. Zeolite 13X and water were used as the adsorbent and adsorbate, respectively, because of their high ESD, high porosity and surface area, non-toxicity, and availability. Furthermore, during the recharging phase water can be delivered to the zeolite 13X beads by passing air through the adsorbent bed; the water vapor in the air is adsorbed as air flows through the adsorbent bed. Notably, when the adsorbate is water, Zeolite 13 X has a higher net heat of adsorption than other adsorbents such as silica gel, activated alumina, zeolite 4A, and zeolite 5A, which reduces the volume of adsorbent required for TES applications [190]. Furthermore, there

have been numerous studies reported in the literature which show zeolite 13 X yields good results in adsorbent-based thermal energy storage systems [270], [271].

Each experiment consists of three distinct phases: a charging phase, a storage phase, and a discharging phase. Initially, two cases were compared wherein the adsorbent beds were directly and indirectly radiated with solar-simulated radiation. In Case 1 the light is directly incident onto the top surface of the zeolite 13X beads after it is transmitted through the polycarbonate sheet. For Case 2 an aluminum absorber is placed on top of the zeolite beads. This aluminum absorber, which has an upper surface area of 95 x 95 mm^2, is referred to as a full absorber because it extends across the entire upper surface of the adsorbent bed, including the upper edges of the walls of the adsorbent bed. The top side of this absorber is coated with matte black paint.

Experiments were conducted under a light intensity of 128.8 mW/cm^2. The light was generated using two 1000 W metal halide bulbs (Sunmaster FULL NOVA) and was measured using a ThorLabs S401C Thermal Power Sensor. During the charging phase, which is 8 hours, the air flow through the adsorbent bed remains on. Upon completion of the charging phase the light source is switched off, and the inlet and outlet valves are closed. The storage phase follows the charging phase and has a fixed duration of 16 hours for all experiments. During this phase, the inlet and outlet valves remain closed. At the end of the storage phase, the charging phase is initiated by opening the inlet and outlet valves and turning on the fan to enable airflow through the reactor. Charging times are selected to represent roughly the availability of sun on a normal day which is about a maximum of approximately 8 h. Storage times of 16 h are selected to ensure that adsorbents get sufficient time to reach room temperature and the time is long enough to see the temperature variation (if any) during the storage period. Furthermore, a duration of 16 h is long enough for the thermal energy to be stored overnight. The water vapour in the humid air entering the reactor acts as the adsorbate.

Heat is generated when water is adsorbed by the Zeolite 13X during the discharging phase, which continues for 8 hours or longer until the Zeolite 13X beads in the adsorption bed are discharged.

As will be discussed in more detail in the results section, the experimental results show that the directly radiated zeolite 13X (Case 1) has a higher energy storage density than the indirectly irradiated adsorber (Case 2). This was unexpected because the reflectance from the zeolite 13X beads is much higher than that of the aluminum absorber (as shown in Figure 5.4 the reflectance from the aluminum absorber is about 5% from 200 nm to 1400 nm, whereas the reflectance from the zeolite 13X beads surpasses 60% over a large range portion of this spectral range). Due to the significantly larger reflectance from the zeolite 13X beads, a large portion of the incident light energy is lost, and one might expect the zeolite 13X beads will not be heated to the same extent as for the case when the aluminum absorber is present. In other words, since the aluminum absorber has minimal reflection losses (and is highly absorbing over a broad spectral range) one might expect that the energy storage density for Case 2 would be greater than that for Case 1, although the opposite was observed from our experimental results. Based on these unexpected results for Cases 1 and 2, it was decided to investigate a third case wherein the size of the aluminum absorber was reduced to 85 x 85 mm^2. Similarly to the full absorber, this absorber is also made of a 0.5 mm thick aluminum sheet resting on top of the zeolite 13X. The top side of this absorber is also coated with matte black paint. However, the important difference for Case 3 is that the aluminum absorber does not contact the aluminum sidewalls of the adsorption bed. It follows that there is a large thermal resistance between the aluminum absorber and its surroundings, and for this reason, it is referred to herein as the “isolated absorber”. The testing conditions for testing Case 3 are identical to those for Cases 1 and 2. Additionally, for Case 3 a series of tests were carried out wherein the charging time was set to 2, 4, 6, and 8 h. A flow chart detailing the experimental cases is shown as Figure 5.3c.

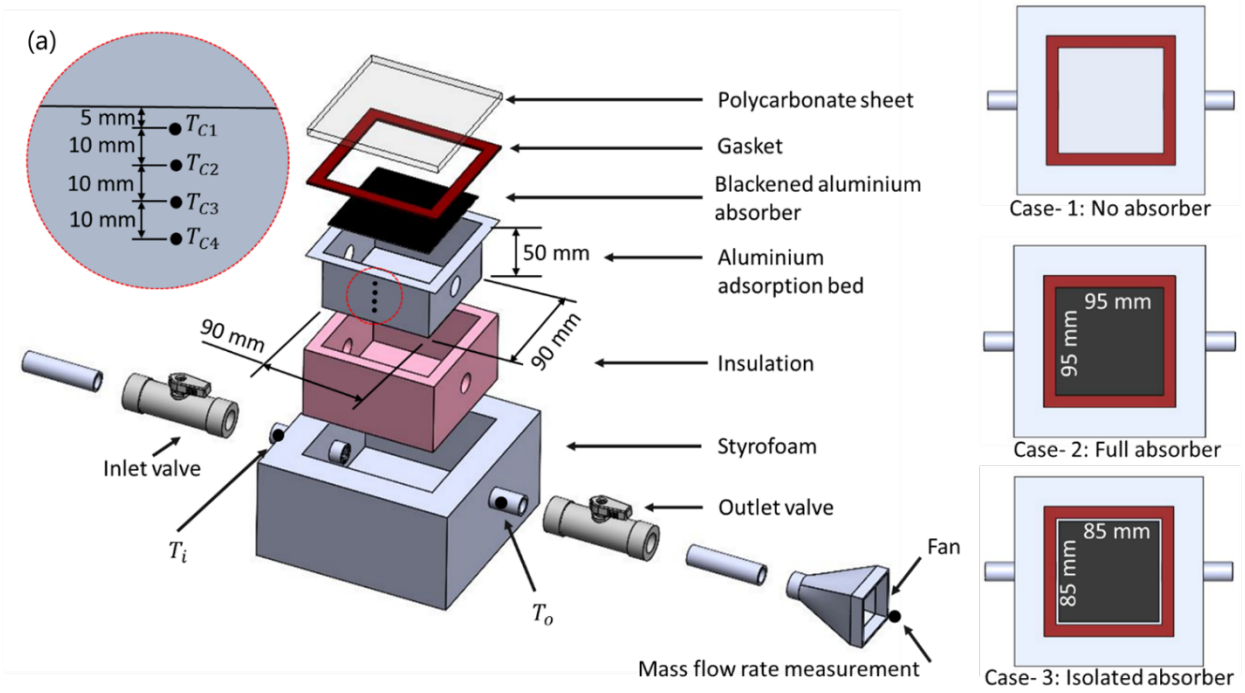
(a)
5 mm
10 mm
10 mm
10 mm
T_{C1}
T_{C2}
T_{C3}
T_{C4}
Polycarbonate sheet
Gasket
Blackened aluminium absorber
50 mm
Aluminium adsorption bed
90 mm
90 mm
Insulation
Styrofoam
Inlet valve
Outlet valve
T_i
T_o
Fan
Mass flow rate measurement
Case- 1: No absorber
95 mm
95 mm
Case- 2: Full absorber
85 mm
85 mm
Case- 3: Isolated absorber

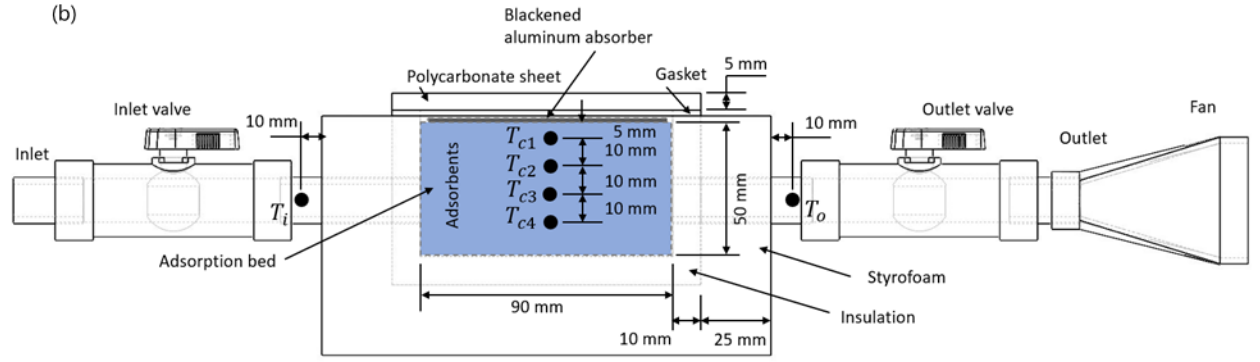
(b)
Blackened aluminum absorber
Polycarbonate sheet
Gasket
5 mm
Inlet valve
10 mm
Outlet valve
Fan
Inlet
Outlet
T_{c1}
T_{c2}
T_{c3}
T_{c4}
5 mm
10 mm
10 mm
10 mm
Adsorbents
50 mm
T_i
T_o
Adsorption bed
Styrofoam
Insulation
90 mm
10 mm
25 mm

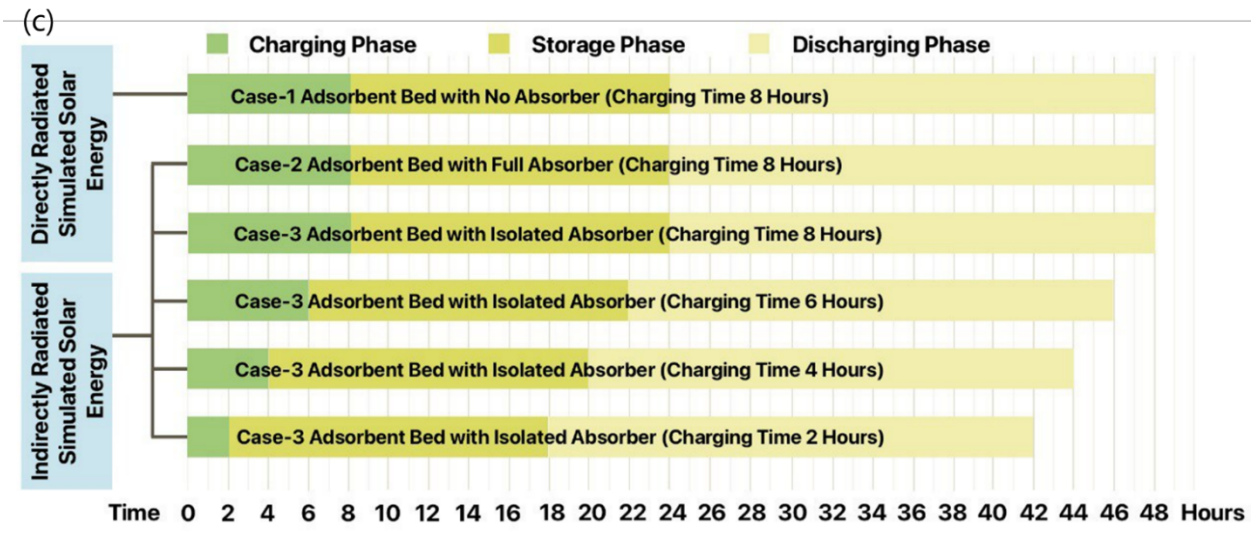

Figure 5.3 a) Diagram of the adsorbent bed and reactor used to conduct the TES experiments. The zeolite adsorbents reside within the aluminum adsorption bed. b) Cross-section of the test section with the region occupied by the adsorbents shaded Blue. c) Flow chart showing the experimental cases.[266]

5.3.4 Methods used to Estimate the Energy Storage Density

The energy storage density (ESD), which can be calculated using Equation (5.1), quantifies the thermal energy retrieved by the air flowing through the adsorption bed during the discharging phase:

$$\mathrm{ESD} = \frac{1}{V_{ads}} \int \dot{m} \cdot Cp_{ma} \cdot \Delta T \cdot dt \qquad (5.1)$$

In Equation (1), V_{ads} represents the volume of the adsorption bed, $\dot{m}$ is the mass flow rate of the air through the adsorption bed, Cp_{ma} is the heat capacity of the moist air exiting the adsorption bed, and ΔT is the temperature difference between the air at the outlet and inlet of the adsorption bed, and the integral is carried out over the first 24 hours of the discharging phase.

The heat capacity of the air exiting the adsorption bed, Cp_{ma}, is determined by the sum of the heat capacity of the dry air and the water vapor within the air. It can be calculated using Equation (5.2):

$$C_{p_{ma}} = C_{p_{air}} + x \cdot C_{p_{wv}} \quad (5.2)$$

In Equation (5.2), $C_{p_{air}}$ represents the specific heat capacity of dry air (taken as 1.006 kJ/kg·K.), $C_{p_{wv}}$ is the specific heat capacity of water vapor (taken as 1.84 kJ/kg·K), and x is the humidity ratio.

The humidity ratio, x, can be calculated using Equation (5.3):

$$x = 0.622 \cdot \left(\frac{RH_o \cdot (P_{wv})_{sat}}{1-(RH_o \cdot (P_{wv})_{sat})}\right) \quad (5.3)$$

In Equation (5.3), RH_o represents the relative humidity at the outlet of the adsorption bed, and $(P_{wv})_{sat}$ is the partial pressure of water vapor in moist air, which is calculated using:

$$(P_{wv})_{sat} = 0.611 \cdot e^{\left(\frac{17.27 * T_o}{T_o + 237.3}\right)} . \quad (5.4)$$

In Equation (5.4), T_o represents the temperature in degrees Celsius at the outlet of the adsorption bed.

The energy storage efficiency (η) is calculated using:

$$\eta = \frac{ESD}{\text{Energy Input}} \quad (5.5)$$

5.4 Results and Discussion

5.4.1 Reflectance and Transmittance

The reflectance spectra of the aluminum absorber, packed zeolite 13X beads, and polycarbonate cover are shown in Figure 5.4a. The transmittance of the polycarbonate cover is shown in Figure 5.4b. The reflectance of the blackened aluminum absorber is about ~ 5%, demonstrating that it can effectively absorb incident light. On the other hand, the reflectivity of the Zeolite 13X beads reaches as high as 60% over a broad wavelength range, revealing that there are significant optical losses when the zeolite is directly irradiated.

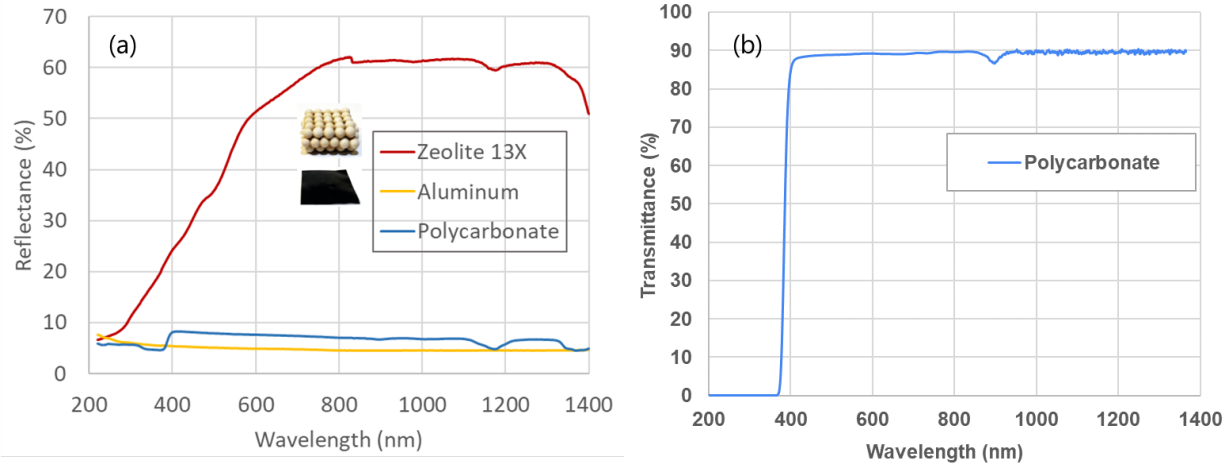

Figure 5.4 a) Reflectance of Aluminum, Zeolite 13X and Polycarbonate, b) Transmittance of Polycarbonate

5.4.2 Thermal Conductivity Measurements

As shown in Table 5.1, the thermal conductivity of Zeolite 13X beads with 3-D printed frames of size 40 mm x 40 mm x 7 mm and 40 mm x 40 mm x 10 mm was measured to be 0.12 W/mK and 0.13 W/mK, respectively.

Table 5.1 Thermal conductivity measurements of Zeolite 13X

Adsorbent	**Sample size (mm^3)**	**Average temperature (°C)**	**Effective thermal conductivity (W/m·K)**
Zeolite 13X	40 x 40 x 7	22.39	0.12
Zeolite 13X	40 x 40 x 10	23.87	0.13

5.4.3 Experimental Results

The pressure drop across the adsorption bed during the experiments as measured with a EHDIS CR410 digital monometer is found is 110 Pa when the airflow speed 0.08 m/s, which is small and is in accordance with the values reported in the literature [272]. The temperature profiles for the adsorbent beds as a function of time for the three cases when the incident light intensity is 128.8 mW/cm^2 are plotted in Figure 5.5. The temperature profile of the adsorbent bed for Case 1, wherein the absorber is absent, is depicted in Figure 5.5a. At the end of the 8-hour charging phase, the thermocouple near the top of the bed (T_1) reaches a temperature of 117.6 °C, while the thermocouple near the bottom (T_4) reaches 82.2 °C. The large drop in temperature between the top of the adsorbent bed at T_1 and the bottom of the adsorbent bed at T_4 are attributed to the low thermal conductivity of the Zeolite 13 X, which is provided in Table 5.1. Figure 5.5d presents the inlet and outlet temperatures for Case 1. At the end of the charging phase the inlet temperature increases to 49.1 °C, while the outlet temperature reaches 86.5 °C. The temperature in the adsorbent bed, and at the inlet and outlet, decrease to room temperature and then remain at this temperature during the 16-hour storage period. At the 24-hour mark of the experiment, the discharging phase begins as the inlet and outlet valves are opened, and air is flown through the adsorbent bed. As shown in Figure 5.5d, the temperature of the air flowing through the adsorption bed for Case 1 increases from 22.3 °C at the inlet to

31.4 °C at the outlet. Thus, the temperature of the air flowing through the adsorption bed increases by 9.1 °C.

For Case 2 (Figure 5.5b), the temperature in the adsorbent bed rapidly increases when the lights are turned on at the beginning of the experiment. The uppermost thermocouple (T_1) reaches 83.9 °C at the end of the 8-hour charging phase. The thermocouple closest to the bottom of the adsorption bed (T_4) reaches a maximum temperature of 76.3 °C during the charging phase.

Figure 5.5e shows the inlet and outlet temperatures for Case 2. During the charging phase, the inlet temperature increases to around 48.7 °C, while the outlet temperature reaches 82 °C. As shown in Figure 5.5b, the temperature inside the adsorption bed rises to approximately 39.2 °C during the discharging phase, with consistent temperatures observed at different heights within the bed. Additionally, Figure 5.5e demonstrates that the air entering the reactor through the inlet remains at room temperature during the discharging phase, while the air temperature at the outlet increases by 11.3 °C compared to the inlet temperature (from 21.6 at the inlet to 32.9 °C at the outlet). As the discharging phase progresses, the temperature at the outlet gradually decreases until it reaches the inlet temperature.

The temperature profile of the adsorption bed for Case 3, where an isolated absorber is used, is presented in Figure 5.5c. Upon completion of the 8-hour charging phase, the thermocouple placed near the top of the bed (T_1) reaches 121.4 °C, while the thermocouple near the bottom (T_4) reaches 84.1 °C. Figure 5.5f shows the outlet temperature during the charging phase, which reaches 91.6 °C. The inlet temperature during the charging phase for Case 3 reaches 50.7 °C. Throughout the storage phase, which extends from the 8-hour mark to the 24-hour mark, the adsorption bed, inlet, and outlet cool to and remain at room temperature. During the discharging phase, the temperature of the air flowing through the reactor increases from 21.6 °C at the inlet to 34.4 °C at the outlet. Thus, the maximum temperature increases of the air flowing through

the adsorption bed for Case 3 is 12.8 °C. By the time the discharging phase is completed, the outlet temperature decreases to that of the inlet temperature. The temperatures at T_1 and T_4 and the maximum increase in the temperature of the air flowing through the adsorption bed during the discharging phase (denoted as ΔT_{max}) for the results shown in Figure 5.5 are summarized in Table 5.2. Reproducibility of results is shown in Figure 8.8, and Table 8.2. Also, the temperature distribution in the adsorbent bed at different position during the experiment is shown in figures 8.11-8.13. The estimated temperatures of top surfaces in Case 1, Case 2 and Case 3 are 137.2 °C, 90.8 °C and 144.8 °C respectively.

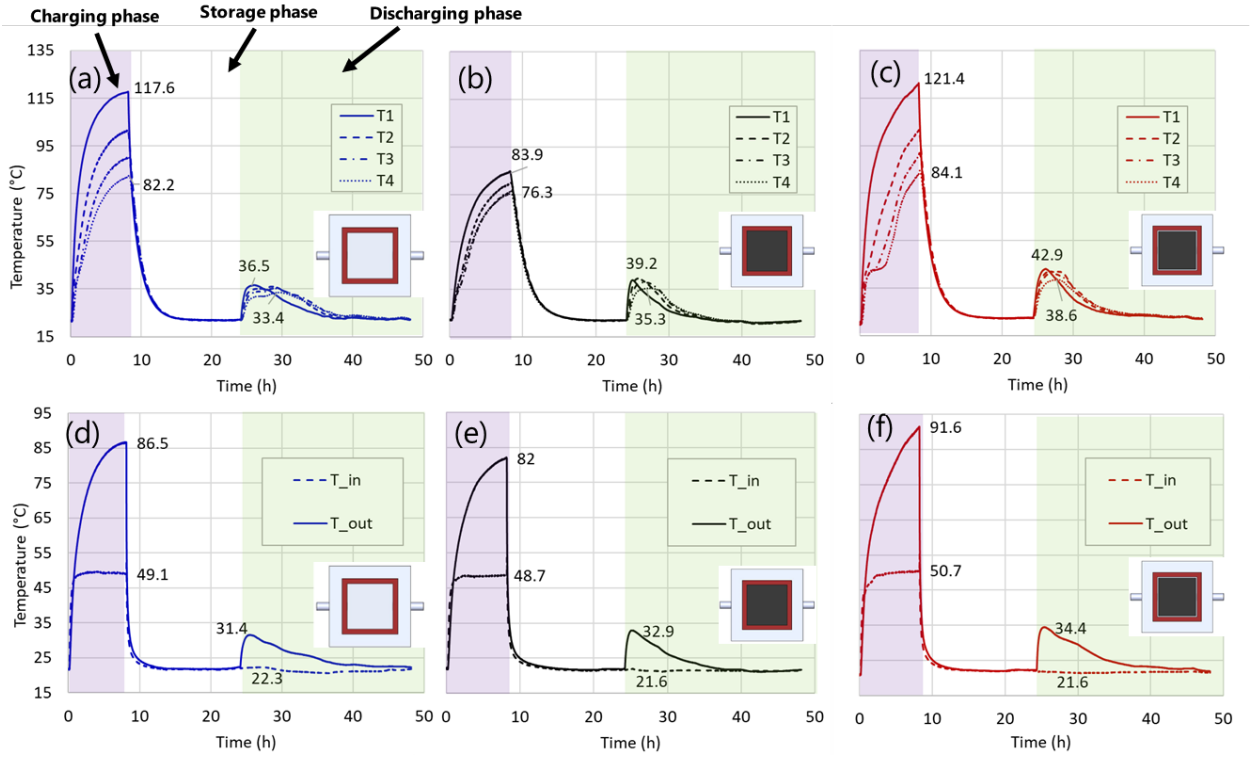

Figure 5.5 Temperature profiles during the charging, storage and discharging phases for (a) Case 1 with no absorber, (b) Case 2 with a full absorber, and (c) Case 3 when there is an isolated absorber. The inlet and outlet temperatures during the charging, storage and discharging phases for (d) Case 1, (e) Case 2, and (f) Case 3.

Table 5.2 Summary of results from Figure 3

Case	Light intensity (mW/cm^2)	Charging time (h)	T1 upon completion of the charging phase (°C)	T4 upon completion of the charging phase (°C)	ΔT_{max} during the discharging phase (°C)
1	128.8	8	117.6	82.2	9.1
2	128.8	8	83.9	76.3	11.3
3	128.8	8	121.4	84.1	12.8

The effects of altering the charging time on the temperature profiles in the adsorption bed and at the inlet and outlet for Case 3 is shown in Figure 5.6. Specifically, the temperature profile of the adsorbent bed when the duration of the charging time is 2, 4, 6, and 8 hours and the light intensity is 128.8 mW/cm^2 are shown in Figures 5.6a-d. As expected, the temperature in the adsorption bed and the maximum increase in the temperature of the air flowing through the adsorption bed during the discharging phase increase as the charging time increases. The temperatures at T_1 and T_4 and the maximum increase in temperature of the air flowing through the adsorption bed during the discharging phase (denoted as ΔT_{max}) for the results shown

in Figure 5.6e-f are summarized in Table 5.3. The temperature distribution in the adsorbent bed at different position during the experiment is shown in Figure 8.14.

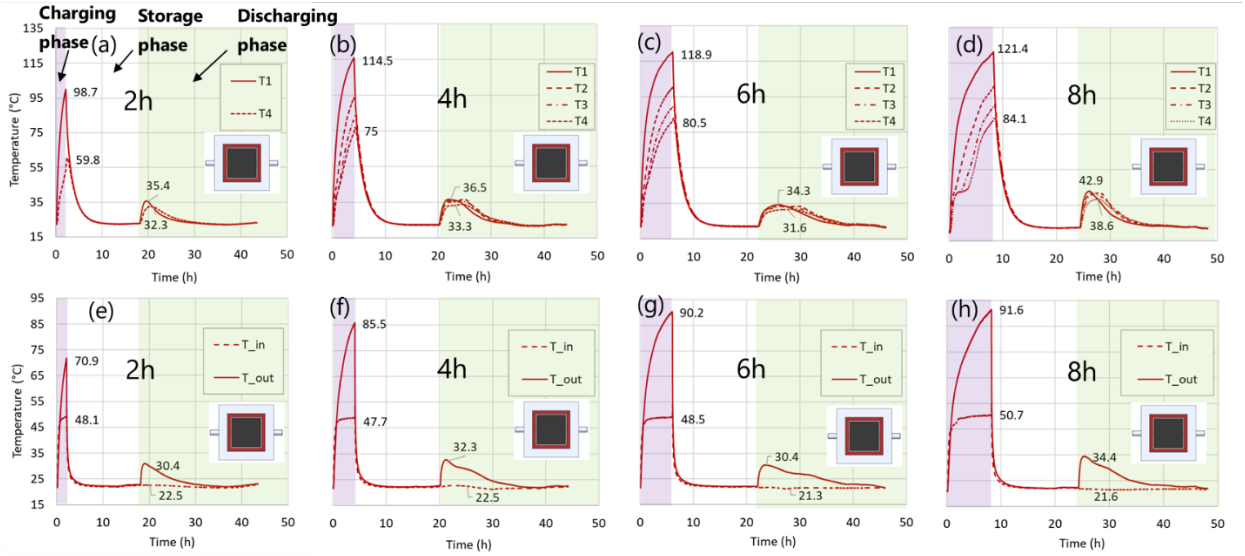

Figure 5.6 Temperature change during the charging, storage and discharging periods for case 3 with an isolated absorber when charging times are 2 h (a), 4 h (b), 6 h (c) and 8 h (d). The inlet and outlet temperatures during the charging, storage and discharging phases for case 3 when charging times are 2 hours (e), 4 hours (f), 6 hours (g) and 8 hours (h).

Table 5.3 Thermal conductivity measurements of Zeolite 13X

Case	Light intensity (mW/cm^2)	Charging time (h)	T1 upon completion of the charging phase (°C)	T4 upon completion of the charging phase (°C)	ΔT_{max} during the discharging phase (°C)
3	128.8	2	98.7	59.8	7.9
3	128.8	4	114.5	75.0	9.8

3	128.8	6	118.9	80.5	9.1
3	128.8	8	121.4	84.1	12.8

5.4.4 Energy Density

The energy storage densities (ESD) for Cases 1, 2, and 3 are presented in Figure 5.7. For Case 1, wherein the adsorption bed does not have a blackened aluminum absorber, the ESD is 44.6 ± 7.7 kWh/m^3 (64.8 ± 7.7 Wh/kg). For Case 2, where the adsorption bed is fitted with a full absorber, the ESD is 35.0 ± 7.7 kWh/m^3 (50.9 ± 7.7 Wh/kg). On the other hand, for Case 3, which features the isolated absorber, the ESD is 49.3 ± 7.7 kWh/m^3 (71.7 ± 7.7 Wh/kg). The error on these values was determined using the error propagation method. The error in the temperature measurements using the K-type thermocouples is ±0.8 °C. The specific heat of air was assumed to be 1.000 ± 0.015 kJ/kg·K. The specific heat of water vapour was assumed to be 1.996 ± 0.030 kJ/kg K. The error in the airflow velocity measurements is ± 0.05 m/s.

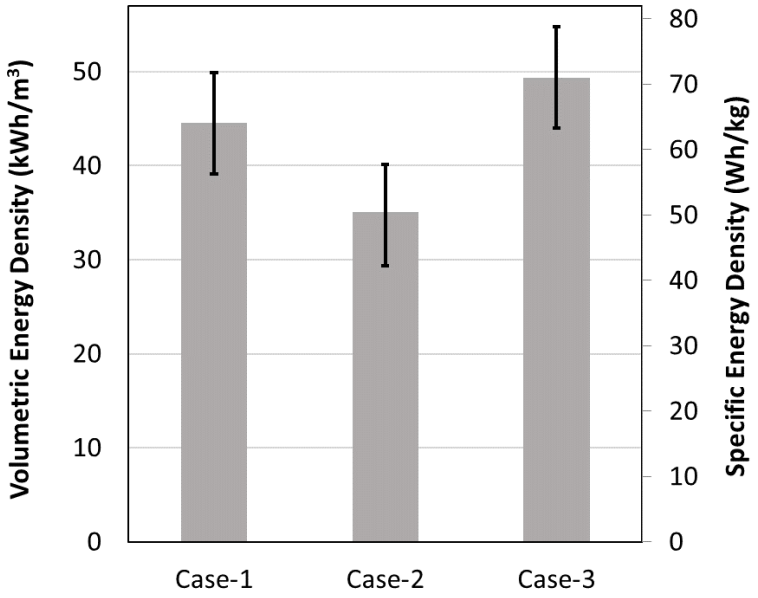

Figure 5.7 The volumetric and specific energy density of the thermal energy recovered from the zeolite when it was charged with no absorber (Case 1), with a full absorber (Case 2), and with an isolated absorber (Case 3).

It is interesting to note the ESD is larger for the directly radiated zeolites (Case 1) than the ESD attained when the full aluminum absorber was used. As shown in Figure 5.2a the reflection losses are much higher at the bare zeolite surface as compared to the reflection losses for the aluminum absorber. Particularly, the ESD for Case 3 is significantly higher than the ESD values achieved for Case 2 and slightly higher than the ESD values observed in Case 1. We also calculated the energy storage efficiency (defined herein as the ESD divided by the amount of light energy incident onto the adsorption bed during the charging phase) for the results reported in Figure 5.7. The energy storage efficiency is 21.2% for Case 1, 16.2% for Case 2, and 23.7% for Case 3. The lower ESD value for Case 2 is attributed to heat loss through the aluminum absorber to the sidewalls of the adsorbent bed. The aluminum sidewalls conduct heat, a portion of which moves in the direction of the adsorption bed outlet, which contributes to heat losses and ultimately lower charging

temperatures within the adsorption bed. Notably, for Case 2 (no absorber) the only mode of heat transfer to sidewalls is through the air or through the zeolite 13X, which both have a high resistance to heat transfer as compared to the aluminum sheet. That is, the difference between Cases 2 and 3 is that there is a 2.5 mm gap between the absorber plate and the sidewalls of the adsorption bed for Case 3, whereas the aluminum plate is in contact with the sidewalls for Case 3. The thermal resistance across this gap for the Zeolite 13X is 4.9 K/W (given the width is 0.09 m and the height is 0.05 m). The thermal resistance across this gap for Case 3, when the aluminum absorber is present, is 0.25 K/W (given the width of the absorber is 0.085 m and its height is 0.0005 m). The thermal resistance through the air is 220 W/K (given its height is 0.005 m and its width is 0.009 m). Thus, the thermal resistance through the aluminum absorber is much less (more than an order of magnitude less) than that of the air or zeolite 13 X. The estimate for the thermal resistance through the air did not account for the movement of the air flow or heat transfer to the air ($h \sim 12$ W/m^2·K). Nevertheless, resistance to heat conduction through the aluminum plate is much lower than that through the air (220 W/K vs 0.25 W/K) such that these factors would not alter the consideration that heat conduction through the aluminum absorber is dominant.

Figure 5.8 shows the ESD in the adsorbent bed for Case 3, in which the adsorbent bed is equipped with an isolated absorber, when the charging time is 2, 4, 6 and 8 h. When the charging period is set at 2 h, the ESD is determined to be 9.1 ± 7.7 kWh/m^3 (13.2 ± 7.7 Wh/kg). For a 4-hour charging time, the ESD substantially increases to 21.3 ± 7.7 kWh/m^3 (30.9 ± 7.7 Wh/kg). A higher ESD value of 38.4 ± 7.7 kWh/m^3 (55.8 ± 7.7 Wh/kg) is obtained with a 6-hour charging duration. Lastly, for an 8-hour charging time, the ESD reaches 49.3 ± 7.7 kWh/m^3 (71.7 ± 7.7 Wh/kg). The energy storage efficiencies for the results reported in Figure 5.8 were calculated to be 17.7% when the charging time was 2 h, 20.6% when the charging time was 4 h, 24.8 % when the charging time was 6 h, and 23.7% when the charging time was 8 h. Thus, the highest

energy storage efficiency was measured for Case 3 when the charging time was 6 h. When the charging time is lower (2 h or 4 h) the adsorbents are heated to a lower temperature, and the ESD is lower, resulting in a lower energy storage efficiency. On the other hand, when the charging time is higher (8 h) the adsorbents are heated to a higher temperature for a longer duration, and the ESD is higher than when the charging period is 6 h. However, the incident light energy received over the 8 h charging phase is significantly higher than that received over the 6 h charging phase, and as a result the energy storage efficiency is lower when the charging time is 8 h as compared to when it is 6 h.

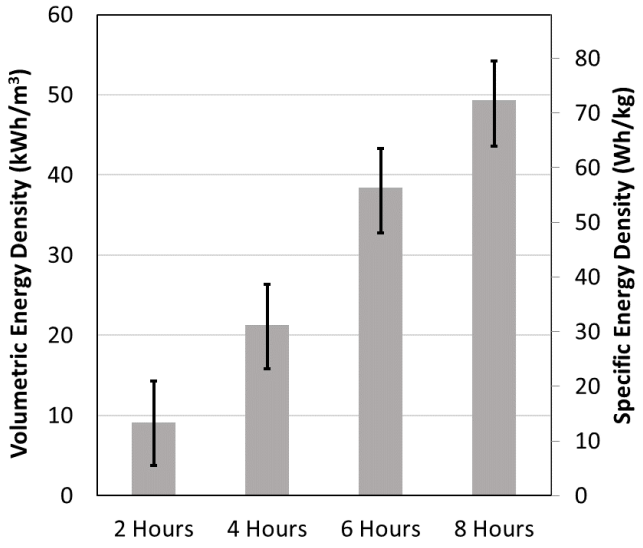

Figure 5.8 The volumetric and specific energy density for Case 3, wherein an isolated absorber is used, when the charging time is 2, 4, 6, and 8 h.

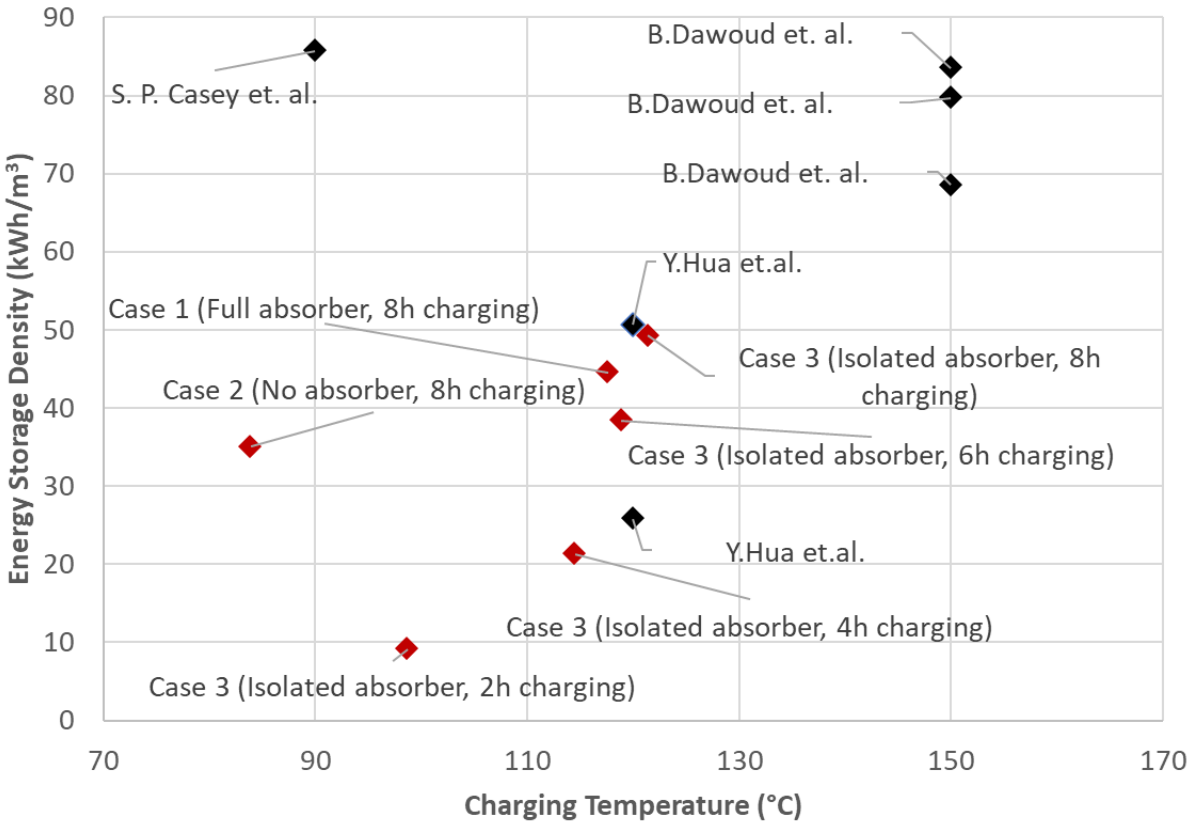

Figure 5.9 The energy storage density for the experiments reported in this work (red diamonds) compared to energy storage densities reported in the literature for zeolite 13X (black diamonds) for different charging temperatures.

The energy storage densities measured in this work are compared to those reported in the literature for zeolite 13X in Figure 5.9 for different charging temperatures. The ESD depends on several factors, including charging and discharging conditions, the size and geometry of the adsorbent bed, insulation effectiveness, heat losses, and the flow rate employed during the discharging process. It should be noted these factors were not similar to the results compared in Figure 5.9. The ESD of 85.7 kWh/m^3 was measured when zeolite 13X was charged at 90 °C in a rectangular-shaped reactor (500 mm x 250 mm x 200 mm) with a sloping roof [273]. The ESD values of 68.5, 79.7 and 83.5 reported by Dawoud et. al. are for a

system comprising an adsorber/desorber unit with 13.2 kg of zeolite 13X adsorbent with 0.5, 1 and 2 L/min flow rates, respectively [274]. The ESD values of 25.8 and 50.7 kWh/m^3 reported by Hua et. al. were measured when the flow rate during the discharging phase was 24 L/min and the relative humidity was 50% and 90%, respectively. For these experiments, the zeolite 13X resided in a packed bed adsorbent column with a volume of 62.8 cm^3 and the regeneration temperature was 120 °C [240].

As can be noted in Figure 5.9, the largest ESD value reported in this work with zeolite 13X is 49.3 kWh/m^3 for Case 3, when the adsorbent bed is fitted with an isolated absorber and the adsorbents are charged for 8h. The highest temperature in the adsorption bed during the charging phase for this case was 121.4 °C. When the charging time was 4 h for Case 3 the highest temperature the adsorbent bed reached was 114.5 °C and the ESD was 21.3 kWh/m^3. Thus, an increase in ESD for Case 3 from 21.3 kWh/m^3 to 49.3 kWh/m^3 was observed when the charging time was increased from 4 to 8 h, which resulted in an increase in the maximum charging temperature from 114.5 to 121.4 °C. As shown in Figure 5.9, this range in ESD values is comparable to those reported in the literature at a charging temperature of 120 °C. Furthermore, Figure 5.9 also shows the trend wherein the ESD values reported in this work increase with temperature is in good agreement with this trend observed for the data reported in the literature. Moreover, based on the results in Figure 5.9 it is expected that higher ESD values can be achieved in future work by concentrating solar radiation onto the isolated absorber to increase the charging temperature of the zeolite 13X beads. It can also be noted that the thermally isolated solar absorber implemented in this work (Case 3) can be used on adsorption beds of different sizes. That is, the adsorption bed and solar adsorber could be scaled to any size in practice. As one example, we speculate that the isolated solar absorber could be applied in the concept of the solar-based adsorption thermal battery reported by Zeng et. al. [265]. In this application the area of the solar absorber would be slightly less than that of the surface are of the Trombe wall such that it is in

contact with the adsorbents, but insulated from other solid components of the wall to prevent unwanted heat losses. Moreover, a case study about using adsorption-based TES rooftop panels to supply heated air to building ventilation systems is provided in the appendix (Section 8.2 Supplementary Material for Chapter 5).

5.5 Conclusion

In this work, experiments were conducted to compare the energy storage densities achieved when using two different methods of heating zeolite 13X adsorbents with solar-simulated light. In the first method, the adsorbents were directly irradiated by exposing them to incident light transmitted through a solar collector window. In the second method, the adsorbents were heated indirectly by illuminating a solar absorber with incident solar simulated light. This blackened aluminum solar absorber is heated by the incoming light and transfers heat to the adsorbents located beneath its bottom surface. Three different cases were investigated: one with an aluminum absorber, another with an isolated aluminum absorber, and a third with no absorber. The isolated absorber rested on top of the zeolite 13X adsorbents and was not in contact with any other components of the adsorbent bed. As a result, there is a high thermal resistance between the isolated absorber and its surroundings. Interestingly, a higher energy storage density was achieved when no absorber was present (44.5 ± 7.7 kWh/m^3) as compared to the case when an aluminum absorber was used (35.0 ± 7.7 kWh/m^3) despite that the reflection losses were very high when the aluminum absorber was not present. The reason for the poor performance in the case of the aluminum absorber is conductive heat transfer loss to the walls of the adsorption bed. When the aluminum absorber was thermally isolated the energy storage density increased to 49.34 ± 7.75 kWh/m^3. These results demonstrate the importance of minimizing the loss of thermal energy from the absorber to the walls of the adsorbent bed. Ideally, thermal energy from the

absorber should be transferred solely to the underlying adsorbents during the charging phase. It was also observed that the energy storage density increased with increasing charging time. For the case of the isolated absorber, as the charging time increased from 2 to 4 to 6 to 8 h the energy storage density increased from 9.11 ± 7.71 kWh/m^3 (13.24 ± 7.71 Wh/kg) to 21.3 ± 7.74 kWh/m^3 (30.9 ± 7.74Wh/kg) to 38.4 ± 7.74 kWh/m^3 (55.8 ± 7.75 Wh/kg) to 49.3 ± 7.75 kWh/m^3 (71.7 ± 7.75 Wh/kg), respectively. The values obtained for the ESD provide important insights into the energy storage capabilities of the respective cases and can guide further optimization efforts in the design and operation of adsorption-based TES systems. Further, these findings suggest that the use of an isolated absorber with blackened aluminum in the adsorption bed enhances the efficiency of solar-driven energy storage. It allows for greater heat absorption and retention within the bed, resulting in a higher ESD. This outcome highlights the potential of this configuration for improving the performance of TES systems. Future work will involve the extension of heating fins from the bottom side of the isolated absorber into the absorbent bed to increase heat transfer rates and achieve more uniform heating throughout the adsorbent bed. Further, tests may be performed using concentrated solar to elevate the temperature of the adsorbent and increase the ESD.

6 Enhanced Energy Storage Density in Thermal Energy Storage Systems Simultaneously Heated with Solar Radiation and Industrial Waste Heat

6.1 Chapter Overview

Adsorbent-based thermal energy storage (ATES) systems can provide high energy storage densities for long durations. However, abundantly available thermal energy sources, such as industrial waste heat and solar energy, do not generally provide enough heat to effectively charge ATES systems. Herein experiments are performed to investigate the benefits of using simulated solar radiation and waste heat simultaneously to charge zeolite 13X for ATES applications. The energy storage density (ESD) for three cases is determined: 1) When the adsorption bed is heated with simulated solar radiation alone, 2) when the adsorption bed is heated using simulated waste heat alone, and 3) when the adsorption bed is heated using simulated solar radiation and waste heat simultaneously. Results show that when simulated solar radiation is the sole source of thermal energy, the ESD is 5.6 kWh/m^3. When the adsorbent bed is charged using waste heat the ESD is 7.6 kWh/m^3. However, when both solar-simulated radiation and waste heat are used simultaneously to charge the adsorbent bed the ESD is 18.9 kWh/m^3. The results show that using both solar and waste heat at the same time to charge the adsorbent bed is a promising strategy for improving the performance of ATES systems.

6.2 Introduction

The pursuit of sustainable energy solutions has become an urgent imperative in the face of global challenges such as climate change and escalating energy demands. As the world navigates the complexities of transitioning towards a carbon-neutral future, the role of thermal energy storage (TES) emerges as a crucial technology for addressing the intermittency of renewable energy sources and for achieving both environmental sustainability and energy conservation [275], [276].

TES can be achieved using sensible heat storage materials, latent heat storage materials, physical sorption, or chemical reactions[257], [277], [278], [279]. For sensible heat storage materials, heat is stored by increasing the temperature of the storage material, and in the latent heat storage method thermal energy is stored in the material by changing its phase from one physical state to another [279], [280], [281]. For thermochemical heat storage methods heat is stored using a reversible chemical reaction. In adsorption-based TES (ATES) systems [5] an adsorbent is "charged" when it is subjected to heat and adsorbate molecules are desorbed from its surface. The heat is recovered during a "discharging" phase when adsorbate molecules adsorb onto the adsorbate surface. ATES is promising as an alternative to sensible and latent heat storage methods because higher energy storage densities (ESD) can be achieved and the storage period can be extended for an indefinite period of time as long as the charged adsorbent is kept isolated from adsorbate molecules [282], [283]. Furthermore, ATES systems can be regenerated using less energy and lower temperatures as compared to when using thermochemical heat storage methods. Due to their high ESD and ability to store thermal energy for long durations, adsorption-based TES systems have been investigated for storing solar thermal energy and waste heat.

Despite being the largest widely available energy source (1.8×10^{14} kW received by Earth)[284], the solar irradiance is underutilized as a source of thermal energy. One challenge with using solar thermal energy is the intermittency of the solar irradiance. In this regard solar-based TES is becoming increasingly important for enabling thermal energy demand profiles to be met with solar energy [285], [286], [287]. ATES systems have been investigated previously because their energy storage density (ESD) can be 8-10 times higher than the ESD of sensible heat-storage materials and because they are well-suited for daily or seasonal storage [288], [289]. In particular, using zeolites and water as the adsorbent-adsorbate pair have shown promising results for ATES applications [221], [290]. In zeolite-water solar ATES systems zeolites are charged by desorbing water from their surface using solar energy directly or indirectly [291], [292]. The ESD increases with increasing charging temperature up to about 200 – 250 °C for the zeolite-water pair [293], [294]. Parabolic trough solar collectors that concentrate sunlight can heat working fluids or TES materials at their focal line to temperatures in excess of 350 °C [295], [296], which is more than adequate for charging zeolite materials. However, in addition to being intermittent, the amount of solar radiation available per area is limited. The total daily solar irradiation ranges from about 300 to 700 kWh/m^2 per day for different locations across the globe [297], [298], which limits the amount of adsorbent that can be charged and challenges the economic viability of solar-driven ATES systems.

Industrial waste heat (IWH) is another attractive source for charging ATES systems [23]. Typically, waste heat is released into the environment, contributing significantly to global energy waste, however, heat exchangers and thermal fluids can be used to transfer waste heat to ATES systems [295], [299], [300]. The temperature of wasted heat from industrial processes ranges from about 30 °C for drying processes to over 1500 °C for furnaces used in metal casting [219] although most waste heat is at a temperature of less than 200 °C. The use of ATES for IWH recovery has been explored before, and has been identified as a

promising method for low-grade heat recovery [301]. However, the potential for combining waste heat and solar thermal energy to charge ATES systems has yet to be studied. In this Chapter the benefits of simultaneously charging zeolite 13X adsorbents with solar energy and low-grade waste heat are investigated. The results from this work show higher ESD values can be achieved by simultaneously charging zeolites with solar and waste heat as compared to when these heat sources are used alone, suggesting that combining solar and waste heat to charge ATES systems can be a good strategy [328], [332], [333], [336], [337].

6.3 Methods

The experiments are carried out using an adsorption bed with a volume of 90 x 90 x 50 mm^3, which is illustrated in Figure 6.1. A top surface area of 90 x 90 mm was used for the adsorption bed to match the area illuminated intensely and evenly by the lamps that provide the simulated solar radiation in the experimental set up. The adsorption bed has a 6 mm thick transparent Lexan polycarbonate sheet on its top side and a heating pad (Canadian Polar Pad, CP32, 5 W, 120 V) with an area of 5.08 cm x 7.62 cm resides at the bottom of the adsorption bed. A 0.48 mm thick aluminum sheet located beneath the polycarbonate sheet at a gap of 2 mm rests on top of the Zeolite 13X within the adsorbent bed. This thin aluminum sheet is coated with matte black paint to increase the amount of light it absorbs and converts to heat. The inlet and outlet of the adsorption bed are connected to PEX pipes with an internal diameter of 11.85 mm and an outer diameter of 15.85 mm. The inlet and outlet pipes are connected to Dahl 12.7 mm (521-13-13-BAG-HD) valves to control the airflow through the adsorption bed. A Winsinn 40mm 24V fan located at the outlet of the adsorption bed generates an airflow rate of 1.6 x 10^{-4} m^3/s measured at the inlet using a testo 405i hot wire anemometer. This flow rate is comparable to those used in experiments previously reported

in the literature, which typically range from about $8x10^{-6}$ m^3/s to $4x10^{-4}$ m^3/s [223], [233], [234], [238]. The adsorption bed is equipped with six K-Type thermocouples. Four thermocouples are located at the center of the adsorption bed at depths of 5, 15, 25 and 35 mm from the polycarbonate sheet. The thermocouples are aligned vertically to study the heat penetration in the adsorption bed due to the solar-simulated light coming from the top of the bed and from the heat pad at the bottom of the bed. One thermocouple is located at the inlet and another at the outlet to measure the inlet and outlet temperatures. The adsorption bed is filled with Zeolite 13X (CAS No: 63231-69-6) spherical beads supplied by Alfa Aesar with a diameter of 3 mm, a density of 688 kg/m^3, and a surface area of 585 m^2/g. Zeolite 13X and water were selected as the adsorbent-adsorbate pair due to their high ESD, high porosity, high surface area, non-toxicity, availability and because during the recharging phase water can be delivered to zeolite 13X by flowing air through the adsorbent bed; the water vapor in the air is adsorbed by the charged zeolites as air flows through the reactor. Furthermore, many studies have been reported in the literature showing zeolites perform well in ATES systems [261], [271] Further details regarding zeolite 13X are provided in Table 8.1 in the supplementary information.

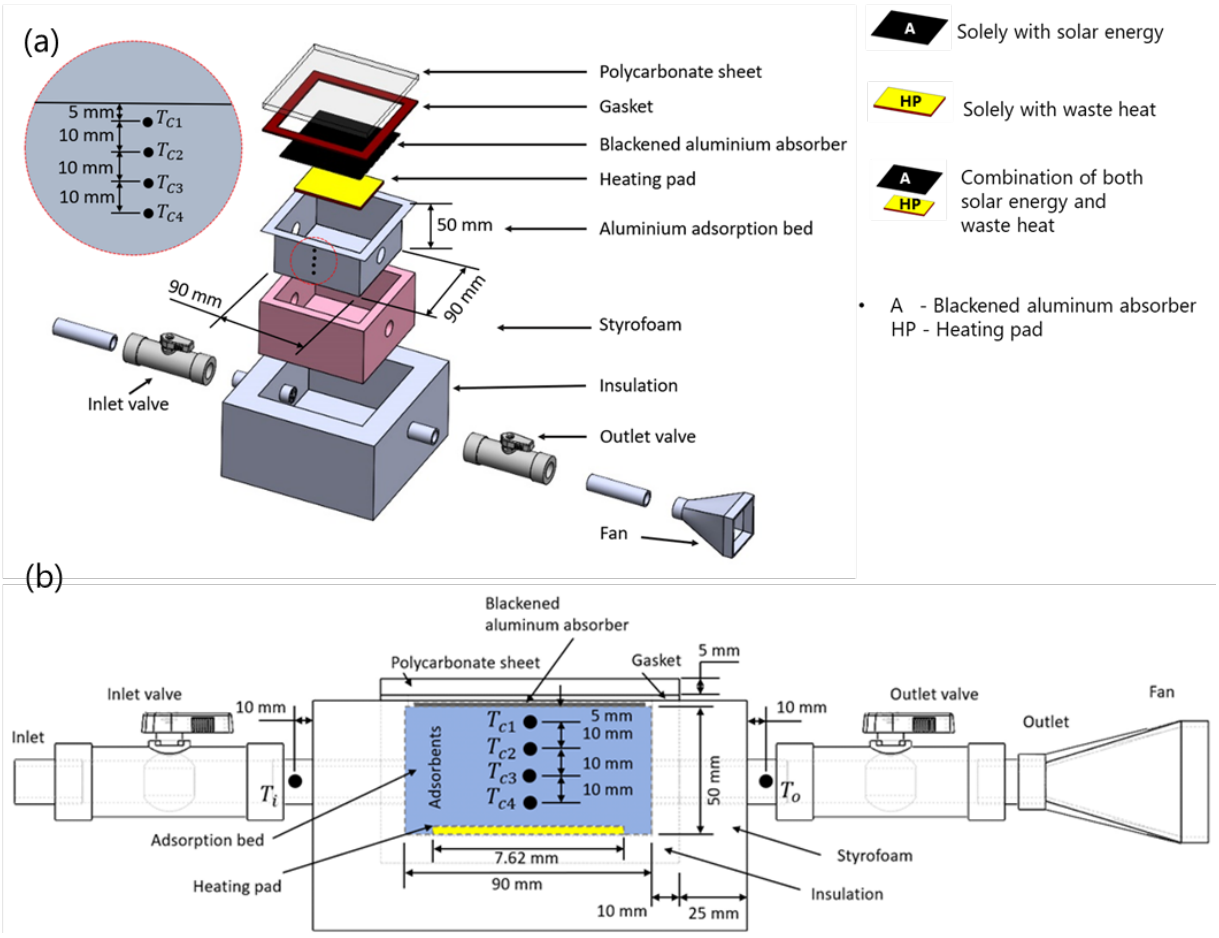

Figure 6.1 a) Schematic diagram of the adsorbent bed and test section. The insets at the bottom right illustrate the three experimental cases wherein 1) heat is provided solely from a solar absorber, 2) heat is provided by a heating pad, and 2) heat is provided from both the solar absorber and the heating pad. b) front view of the adsorbent bed and test section. The adsorbents reside in the blue-shaded area.

Each experiment consists of a charging phase, a storage phase, and a discharging phase. Three different cases are considered for the charging phase. For Case 1 the adsorbent bed is subjected to solar-simulated radiation from a 1000 W metal halide bulb (Sunmaster FULL NOVA) providing a light intensity of 53.6 mW/cm^2 measured using a ThorLabs, S401C Thermal Power Sensor. For Case 2, simulated waste heat is

generated using a heating pad located at the bottom of the adsorbent bed. For Case 3 the Zeolite 13X are charged by heating the adsorbent bed using the solar-simulated light and the heating pad simultaneously. For all cases the duration of the charging time is 3 h. The daily peak sun hours at locations that would benefit most from TES for building applications ranges from about 2 h to 5 h (for example, at locations with a latitude greater than ~ 40° N or less than ~ 40° S). For the experiments reported in this work the light intensity is about half a peak sun hour (1 peak sun hour = 100 mW/cm^2) over a duration of 3 h which is available daily at most locations. Moreover, for Case 3 the light intensity and power supplied to the heating pad were identical to that for Cases 1 and 2, respectively.

At the end of the charging phase the light and heating pad are turned off and the inlet and outlet valves are closed. During the storage phase the zeolite 13 X beads and adsorbent bed return to room temperature while the inlet and outlet valves are kept closed. The duration of the storage phase is 17 h for all experiments, which demonstrates that TES can be achieved over an extended period of time (overnight, for example) and this also provided enough time to ensure the adsorbents and the adsorbent bed cooled to the temperature of the surroundings before beginning the discharging phase. At the end of the storage phase the inlet and outlet valves are opened, and the fan is turned on to provide airflow through the reactor to begin the discharging phase. The water molecules present in the air entering the reactor are used as the adsorbate. The relative humidity of the air measured using a Govee hygrometer H5075 varied from 13-21% during the experiments, with the exception of one experiment; the relative humidity ranged from 22 to 33% during a repeated test for the case when only the heating pad was used to charge the adsorbents. Notably, this variation in the relative humidity did not have a significant effect on the results. The relative and absolute humidities measured during the charging and discharging phases for all experiments are reported in Table 8.2 in the supplementary information. The pressure drop during the experiment in the adsorption bed, measured with

a EHDIS CR410 digital monometer, was found to be 110 Pa when the airflow used during the experiments, 1.6 x 10^{-4} m^3/s, was used. This is in accordance with the values reported in the literature [272]. The discharging phase is allowed to proceed for over 25 hours, and the inlet and outlet temperatures are equal at the end of this phase.

The ESD, defined herein as the thermal energy transferred to the air flowing through the adsorption bed during the discharging phase, is calculated by

$$\mathrm{ESD} = \frac{1}{V_{ads}} \int \dot{m} \cdot Cp_{air} \cdot \Delta T \cdot dt \qquad (6.1)$$

Where V_{ads} is the adsorption bed volume, $\dot{m}$ is the mass flow rate of the air through the adsorption bed, Cp_{air} is the heat capacity of the air exiting the adsorption bed, and ΔT is the increase in temperature in going from the inlet to the outlet of the adsorption bed. The integral is carried out over the first 2.5 h of the discharging phase.

Energy storage efficiency (η) is calculated using:

$$\eta = \frac{\mathrm{ESD}}{\text{Energy Input}} \qquad (6.2)$$

6.4 Results and Discussion

The temperature in the adsorbent bed as a function of time for the three cases viz. Case 1 where the adsorbent bed is subjected to solar-simulated radiation, Case 2 where heat is generated from the heating pad at the bottom of the adsorbent bed, and Case 3 where Zeolite 13X are charged by heating the adsorbent bed using the solar-simulated light and the heating pad simultaneously, are shown in Figures 6.2a-c. As

shown in Figure 6.2a, for Case 1 the temperature in the adsorbent bed increases rapidly when the light is turned on at the beginning of the experiment. The temperature at the position of the uppermost thermocouple, T_{C1}, reaches a maximum of 64.3 °C, whereas the temperature at the thermocouple located closest to the bottom of the adsorption bed, T_{C4} reaches a maximum of 44.8 °C by the end of the 3 h charging phase. During the charging phase for Case 1 the temperature in the adsorption bed increases to a lesser extent for positions located progressively further from the top of the reactor. This is expected because heat is generated when light is absorbed by the blackened aluminum sheet at the top of the reactor. The inlet and outlet temperatures for Case 1 are shown in Figure 6.2d. During the charging phase the inlet temperature increases to about 35 °C and the outlet temperature increases to ~48 °C. The inlet temperature increases because the lamp heats the surrounding air before it enters the adsorption bed inlet. At the 3 h point of the experiment the charging phase ends when the light is switched off and the inlet and outlet valves are closed to begin the storage phase. As shown in Figures 6.2a and 6.2d, the temperature inside the adsorption bed and at the inlet and outlet decrease and then remain at room temperature over the duration of the storage phase. At the 20 h point of the experiment the discharging phase commences when the inlet and outlet valves are opened, and the fan is turned on. As shown in Figure 6.2a the temperature inside the adsorption bed is raised to about 24.2 °C during the discharging phase, and the temperature measured at different heights in the adsorption bed is fairly consistent. Furthermore, as shown in Figure 6.2d the air flowing through the inlet of the reactor remains at room temperature during the discharging phase, while the temperature of the air at the outlet is raised by 1.7 °C as compared to the inlet temperature. As the discharging phase proceeds the temperature at the outlet of the adsorption bed gradually decreases to the inlet temperature. Reproducibility of results is shown in Figure 8.15, Table 8.3. Temperature distribution at different positions inside the adsorbent bed is shown in Figure 8.16.

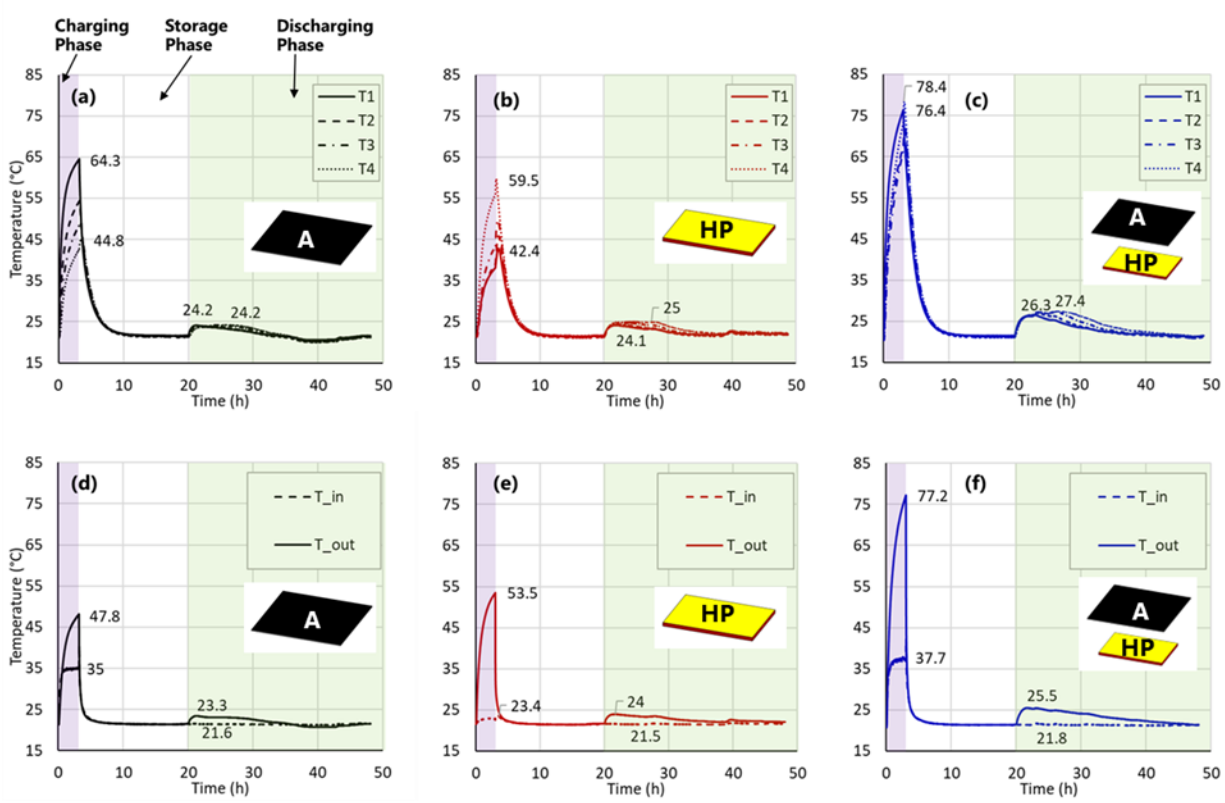

Figure 6.2 Temperature change during charging, thermal energy storage and discharging solely with solar energy (2.a), solely with waste heat (2.b), and with a combination of both cases (2.c). Inlet and outlet temperature during charging, thermal energy storage and discharging solely with solar energy (2.d), solely with waste heat (2.e), and with a combination of both cases (2f).

The temperature in the adsorption bed for Case 2 is shown as a function of time in Figure 6.2b. For Case 2, the temperature increases to a greater extent closer to the bottom of the adsorbent bed where the heating pad resides. At the end of the charging phase the maximum temperature at the thermocouple placed near the top of the adsorbent bed, T_{C1} reaches 42.4 °C. Comparatively, the maximum temperature at the thermocouple placed near the bottom of the adsorbent bed, T_{C4} reaches 59.5 °C. Figure 6.2e shows the

outlet temperature during the charging phase reaches 53.5 °C, whereas the inlet temperature remains at room temperature during the charging phase. Over the duration of the storage period the adsorption bed and inlet and outlet are at room temperature. During the discharging phase the temperature at the outlet is raised by 2.5 °C as compared to the temperature of the inlet. The outlet temperature decreases to that of the inlet by the end of the discharging phase.

The temperature in the adsorbent bed for Case 3, wherein the zeolite is heated from the top by incident light and from the bottom by the heating pad, is plotted as a function of time in Figure 6.2c. The highest temperature was measured at the bottom of the adsorbent bed, as T_{C4} reached 78.4 °C by the end of the charging phase. The maximum temperature measured by the thermocouple near the top, T_{C1}, reached 76.4 °C at the 3 h point when the charging phase ended. Notably, the temperature near the middle of the adsorption bed, measured by T_{C2} and T_{C3} , is lower than the temperature at the top and bottom of the adsorbent bed, which are heated by the light and heating pad, respectively. The inlet and outlet temperatures for Case 3 are shown in Figure 6.2f. The inlet and outlet temperatures increase to 37.7 °C and 77.2 °C, respectively, by the end of the charging phase. Similarly to Cases 1 and 2, the temperature in the adsorbent bed and at the inlet and outlet decreases to and then resides at room temperature over the 17 h duration of the storage period. At the 20 h point of the experiment the inlet and outlet valves are opened and air is flown through the adsorbent bed as the discharging phase commences. As shown in Figure 6.2c the temperature in the adsorbent bed rises during the discharging phase and points closer to the bottom of the adsorbent bed reside at higher temperatures for longer periods of time. As shown in Figure 6.2e the inlet remains at room temperature during the discharging phase, while the outlet temperature is raised by 3.7 °C as compared to the inlet temperature. It can be noted that the temperature increase between air flowing through the inlet and outlet of the adsorbent bed during the discharging phase is small for the experiments in this work as

compared to values reported in the literature, where airflow temperature increases of 20 °C or more between the inlet and outlet are not uncommon. Nevertheless, the conditions in the present experiment were set such that for Case 3 the increase in temperature of the Zeolite 13X at the top of the adsorbent bed due to heating from incident light was comparable to the increase in temperature at the bottom of the adsorbent bed due to the heating pad. This ensured that both heating sources made a noticeable contribution to increasing the ESD. In practice greater amounts of heat can be transferred to an adsorbent bed via light and waste heat to realize higher outlet air temperatures and ESD values during the discharging phase.

The energy storage efficiencies during Cases 1, 2 and 3 are 17.4 ± 1.6%, 7.5 ± 1% and 14.2 ± 0.4% respectively. The ESDs for Cases 1, 2 and 3 are plotted in Figure 6.3. For Case 1 the ESD is 5.6 ± 0.5 kWh/m^3 (equivalent to 8.1 ± 0.7 Wh/kg) and for Case 2 the ESD is 7.6 ± 1 kWh/m^3 (equivalent to 11.04 ± 1.4 Wh/kg). For Case 3, wherein the zeolite is charged from the top-side using incident light and from the bottom-side using the heating pad simultaneously the ESD is 18.9 ± 0.5 kWh/m^3 (equivalent to 27.4 ± 0.8 Wh/kg). The error on these values was determined by using 80 % confidence levels and the result from two experiments for each case. The temperature as a function of time at T1, T4, and the inlet and outlet of the adsorption bed are plotted as a function of time for all experiments in Figure 8.5 in the supplementary information.

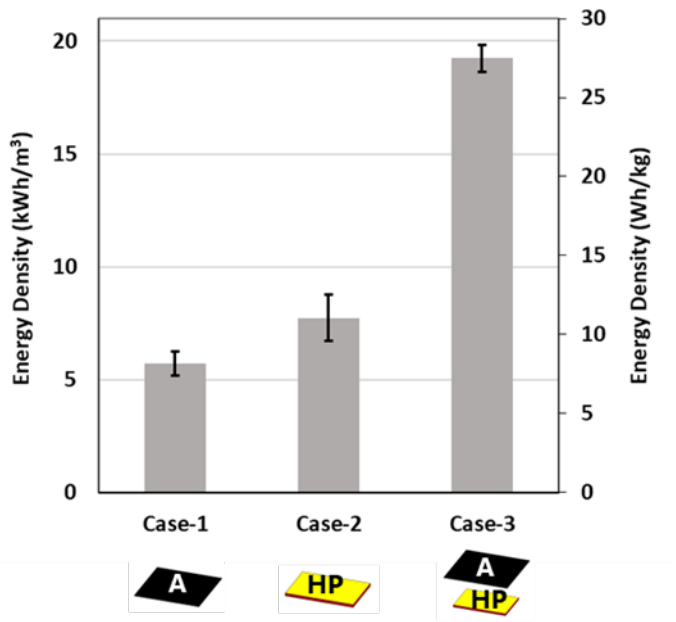

Figure 6.3 The volumetric and specific energy density of the thermal energy recovered from the zeolite 13X adsorbents for Case 1 (adsorbents are heated by incident light), Case 2 (adsorbents are heated by a heating pad at the bottom of the adsorbent bed), and Case 3 (adsorbents are heated by light and the heating pad simultaneously).

The results in Figure 6.3 show that combining solar and waste heat to charge Zeolite 13X for TES applications can be beneficial. Notably, the ESD for Case 3 is slightly greater than the sum of the ESD values attained for Cases 1 and 2.

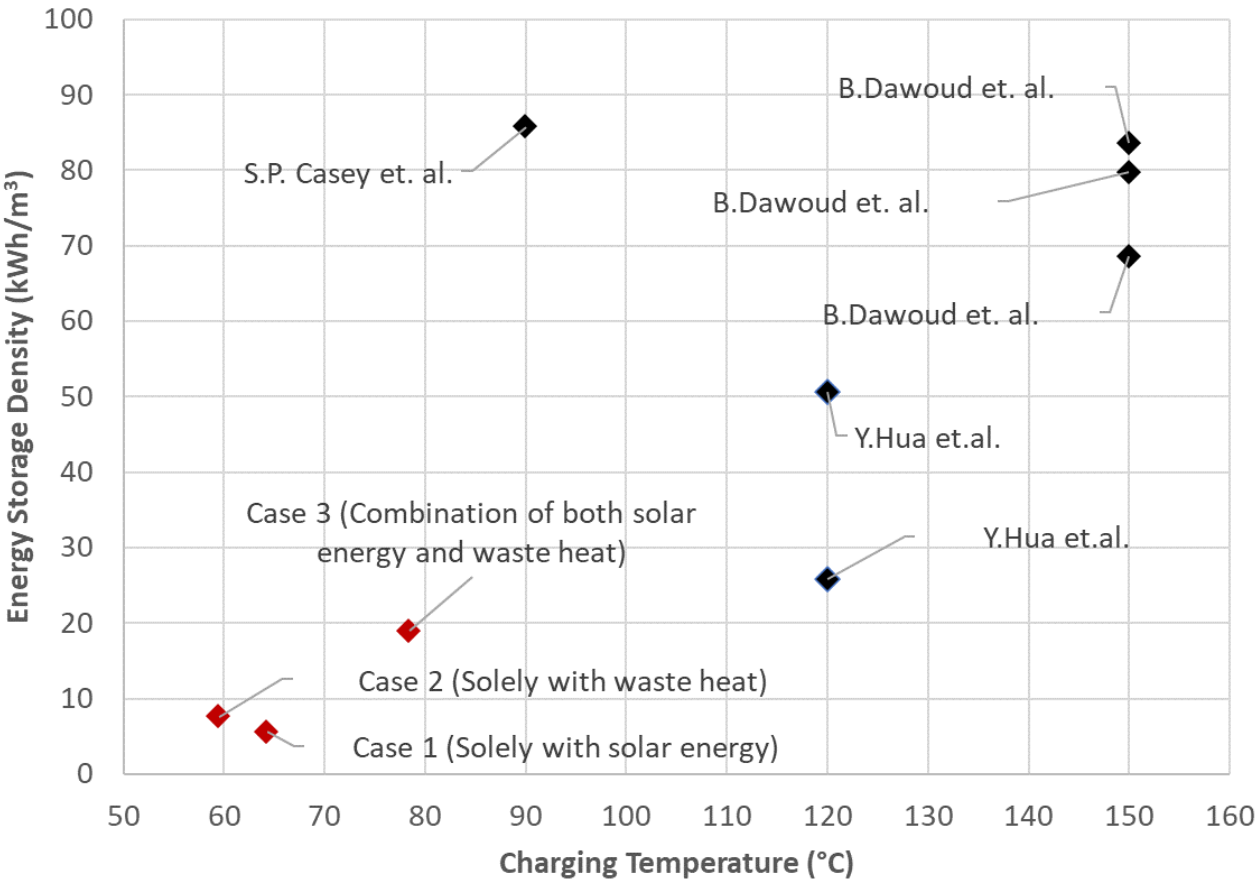

Figure 6.4 The volumetric energy density measured in this work (for Cases 1-3) compared to volumetric energy densities reported in literature when zeolite 13X was used as the adsorbent.

Using Zeolite 13X for thermochemical energy storage has been investigated under different charging and discharging conditions in a variety of reactor configurations in the literature. The results attained in this work are compared to examples of ESD values reported in the literature from different experiments in Figure 6.4. In viewing the results, it should be noted that the ESD depends on many factors including the charging and discharging conditions, the size of the reactor, the insulation and heat losses from the reactor, and the flow rate used during the discharging process. These conditions were not consistent for the different

results reported in Figure 6.4. The ESD of 85.7 kWh/m^3 was measured for a zeolite 13x charged at 90 °C in a rectangular shaped reactor (500 mm x 250 mm x 200 mm) with a sloping roof [293]. The energy densities of 68.5, 79.7 and 83.5 kWh/m^3 were reported for a system comprising of an adsorber/desorber unit having 13.2 kg of zeolite 13X adsorbent with flow rates of 0.5, 1 and 2 L/min, respectively [274]. The ESD values of 25.8 and 50.7 kWh/m^3 were measured when the flow rate was 24 L/min and the relative humidities were 50% and 90%, respectively, during the discharging phase. Furthermore, the zeolite 13x resided in a packed bed adsorbent column with a volume of 62.8 cm^3 and the regeneration temperature was 120 °C [240].

As can be noted in Figure 6.4, the ESD values measured in this work are lower than those reported in the literature. This is primarily due to the lower regeneration charging temperatures achieved in this work. Nevertheless, the conditions in the present experiment were set such that for Case 3 the increase in temperature of the zeolites at the top of the adsorbent bed due to heating from incident light was comparable to the increase in temperature at the bottom of the adsorbent bed due to the heating pad. This ensures the two heating sources made comparable contributions to increasing the ESD. Here it is important to note that if one of the sources provided a small amount of heat compared to the other then there may not be a benefit to using both sources simultaneously. For example, if the temperature of the heating pad were to be increased and the amount of incident light decreased then more heat may be lost from the top of the adsorbent bed then gained from the incident radiation; in this case higher ESD results could be achieved by replacing the window at the top of the reactor with a thermally insulating material. However, when the temperature of the adsorbents heated by the two sources are comparable more adsorbents can be heated as compared to a case where the sources are used individually. For example, the temperature of the zeolite 13X adsorbents near the middle of the reactor (at T2 and T3) was elevated to 45 – 55 °C when either

incident light or the heating pad were used as the sole heat sources. However, when both heat sources were used simultaneously the regeneration temperature at these points exceeded 65 °C. Thus, more adsorbents can be regenerated at higher temperatures using a single adsorbent bed when both heat sources are used simultaneously. It can also be noted that incident solar radiation can be combined with other heat sources to charge ATES systems. For example, IWH cold be transferred to solar-driven ATES system located outdoors (e.g. on a rooftop), or alternatively, heat pumps could provide heat to the ATES system on days when the time-of-use electricity prices are favorable [281]. It is important to note that here waste heat is used to upgrade the solar energy harvested to ensure a uniform charging of adsorbents inside the test section which is evident from the temperature distribution inside the test section during charging shown in Figure 6.2c.

6.5 Conclusion

Experiments were conducted to evaluate the benefits of heating adsorbent-based thermal energy storage systems with solar radiation and industrial waste heat simultaneously. Incident solar-simulated light was absorbed at the top of the adsorbent bed to provide heat to charge zeolite 13X beads. A heating pad at the bottom of the adsorbent bed was also used to charge the adsorbents. When solar-simulated light was used as the sole heating source the energy storage density is 5.61 kWh/m^3 (equivalent to 8.15 Wh/kg). When the heating pad is used as the sole heating source the energy storage density is 7.60 kWh/m^3 (equivalent to 11.05 Wh/kg). When the adsorbent bed was subjected to radiation from its top side and heated at its bottom side the energy storage density increased to 18.92 kWh/m^3 (equivalent to 27.49 Wh/kg). The energy storage density achieved when using both heating sources simultaneously is greater than the sum of the energy storage densities measured when the zeolite 13X beads were heated solely with the solar simulated light or

with the heating pad. The energy storage density is higher when both heating sources are used simultaneously because the zeolites are charged at higher temperatures. For example, the zeolite 13X beads near the middle of the adsorbent bed were heated to 45 – 55 °C when either incident light or the heating pad were used as the sole heat sources. However, when both heat sources were used simultaneously the regeneration temperature at these points exceeded 65 °C. Thes results from this work show that more adsorbents can be heated to higher temperatures in a single adsorbent bed by integrating solar heating with industrial waste heat thermal energy storage systems as compared to when these heat sources are used individually.

7 Conclusion and Future work

7.1 Conclusion

Adsorption-based Thermochemical Energy Storage (ATES) is emerging as a promising technology; however, it faces some challenges like adapting it for mobile applications, recharging adsorbents with solar energy, and utilizing diverse energy sources for charging.

This thesis explores and addresses some of these challenges and enhances the viability of adsorption-based TES. The successful charging of zeolite 13X outside the main reactor and subsequent external storage prior to discharging open exciting possibilities for mobile heat storage applications. Specifically, Zeolite 13X were charged by heating in an oven and subsequently stored externally from the discharging reactor. The results demonstrated that the energy storage density (ESD) of zeolite 13X, charged at 200 °C and stored external to the discharging unit, could reach up to 111.04±10 kWh/m^3 (161.4±10 Wh/kg). These findings were comparable to ESD values reported in the literature for systems where zeolite 13X were permanently housed within the adsorption/desorption bed throughout the thermal energy storage (TES) cycle. The encouraging outcomes of this study suggest the need for further research and development of TES systems that enable short-distance mobile heat storage, with future work focusing on optimizing the configuration of the zeolite 13X discharging reactor and exploring modular and portable containers for zeolite 13X transportation between heat sources.

This study also provides valuable insights about how solar collectors with integrated adsorbent beds can be designed to increase the temperature during the charging process. Three scenarios were examined: (1) the zeolite 13X adsorbents were subjected solar radiation that was transmitted through the window of the collector (2) the solar radiation was incident onto a blackened absorber plate, which transferred energy to

the zeolite 13X bed, and (3) a configuration similar to the second case, but wherein the blackened absorber plate was isolated, such that it was insulated from the walls of the adsorbent bed. The results indicated that the presence of an absorber significantly influenced the ESD during the charging process. When a full absorber was used, the ESD measured was 35.0 ± 7.7 kWh/m^3 (50.9 ± 7.7 Wh/kg). The isolated absorber scenario resulted in a higher ESD of 49.3 ± 7.7 kWh/m^3 (71.7 ± 7.7 Wh/kg) compared to the full absorber configuration. It is observed that when no absorber was present, the ESD was slightly lower at 44.6 ± 7.7 kWh/m^3 (64.8 ± 7.7 Wh/kg) compared to the isolated absorber scenario. These findings underscore the significant impact of the design of the solar collector on the adsorbent charging process and the ESD, with the full absorber configuration showing the lowest ESD, followed by the no absorber scenario, and finally the isolated absorber setup. This knowledge can guide the design and optimization of adsorption-based thermal energy storage systems, enhancing their efficiency and performance. It also serves as a foundation for exploring innovative configurations and materials to further optimize the energy storage density during thermal energy storage cycles.

Additionally, the integration of solar radiation and industrial waste heat for heating adsorbent-based thermal energy storage systems presents a promising avenue for utilizing industrial waste heat to achieve significant energy storage densities. The study focused on evaluating the benefits of simultaneously using solar radiation and industrial waste heat to heat an adsorbent-based thermal energy storage panel. Experiments were conducted in a lab-scale adsorption bed with a transparent polycarbonate window and a heating pad situated at the bottom. The results showed that when solar-simulated light was used as the sole heating source, the energy storage density achieved was 5.61±0.5 kWh/m^3 (equivalent to 8.15±0.7 Wh/kg). When the heating pad served as the sole heating source, the energy storage density increased to 7.60±1 kWh/m^3 (equivalent to 11.04±1.4 Wh/kg). However, the most significant improvement in energy storage density occurred when the adsorbent bed was exposed to radiation from the top side and simultaneously heated

from the bottom side, resulting in an energy storage density of 18.92±0.5 kWh/m^3 (equivalent to 27.49±0.8 Wh/kg). These findings indicate substantial potential benefits from integrating solar heating with industrial waste heat thermal energy storage systems. This integration could lead to significantly higher energy storage densities, making it a promising avenue for future research and practical implementation. The research thus motivates future investigations into advanced hybrid heating systems that leverage diverse energy sources, contributing to the development of more efficient and environmentally friendly thermal energy storage technologies.

7.2 Future work

7.2.1 Future Directions from this Work

7.2.1.1 Adsorption-Based Mobile Thermal Energy Storage (m-TES)

The first objective of this research aimed at exploring adsorption-based mobile thermal energy storage (m-TES). The key aspect involved investigating the thermal energy storage capability of zeolite 13X when charged externally to the heat recovery reactor. This was done by examining different charging temperatures and airflow rates. However, further investigation is needed to understand the effects of charging times, operating temperatures, and relative humidity levels on zeolite 13X's performance in m-TES systems. Experiments can be conducted wherein the charging time ranges from 2 hours to 12 hours or longer in some cases (e.g., waste heat recovery systems). The discharging phase can be conducted at different operating temperatures to simulate different operating conditions across the world which generally varies from -40°C to 45°C. Additionally, future work can focus on optimizing the configuration of the reactor used for zeolite 13X discharging and exploring the use of modular and portable segmented

containers for transporting zeolite 13X between heat sources of varying temperatures. A lab-scale adsorption panel of 30 cm x 30 cm x 5 cm can be considered for initial studies with 4-5 modular segments. Later, larger adsorption panels can be tested.

7.2.1.2 Solar-Driven Adsorption-Based Thermal Energy Storage Panel

The second aspect of the research focused on studying the thermal energy storage ability of zeolite 13X when charged within the adsorption panel and the subsequent recovery of stored heat. Initial experiments focused on maximizing the charging temperature inside the adsorption panel to charge zeolite 13X sufficiently. Therefore, different strategies were explored to maximize the charging using solar energy. Three charging strategies were tested. In Case 1, the incident light passes directly through the polycarbonate sheet to reach the upper surface of the zeolite 13X beads on the adsorption bed. In Case 2, a full aluminum absorber covers the upper edges of the aluminum adsorption bed, positioned between the polycarbonate sheet and the zeolite beads, featuring matte black paint to enhance heat absorption. In Case 3, an isolated absorber on the polycarbonate sheet rests atop the Zeolite 13X, with its top coated in matte black paint. Notably, in the third scenario, the aluminum absorber is deliberately kept from contacting the aluminum adsorption bed. The results showed that the isolated absorber offered the best charging performance. Future work could involve conducting experiments with adsorption panels fitted with isolated absorbers featuring fins of various shapes and sizes extended form the absorber down into the adsorption bed to enhance heat transfer. As discussed in Chapter 5, the low effective thermal conductivity of the Zeolite 13 X beads reduces the charging temperature within the adsorption bed, and attaching fins to the isolated absorber will increase the temperature at the middle of the adsorption bed by transferring heat to this area. Fins with rectangular, trapezoidal, and concave profiles can be considered. Furthermore, different solar energy intensities and

concentration strategies e.g. the use of solar concentrators, should be studied to achieve optimal charging of zeolite 13X adsorbents.

7.2.1.3 Integration of Solar Energy and Industrial Waste Heat to Charge Adsorption Panel

The third aspect of the research investigated the integration of solar energy and waste heat to charge the adsorbents within the adsorption panel. Promising results were obtained, and future work could involve experimenting with different solar energy intensities, varying grades and methods of delivery of waste heat to the adsorption bed, and the integration of fins in isolated absorbers.

Lastly, since all experiments were conducted using a small adsorption panel, it would be interesting to see the results of experiments conducted on a full-size adsorption panel. Therefore, future studies can focus on experimentation with different sizes of adsorption panels.

7.2.1.4 Modifying the experiment to reach higher temperatures and higher flow rates

It is expected that higher ESD values can be achieved by increasing the charging temperature for the experiments wherein light is used to heat the zeolite 13 X beads. For example, Figure 5.9 shows the maximum charging temperature at T_1 during the charging phase for the experiments conducted in Chapter 5 is 121 °C, and the corresponding energy density is about 50 kWh/m^3. However, results reported in the literature show that ESD values over 80 kWh/m3 are measured when the charging temperature is 150 °C. The regeneration temperature for experiments where zeolite 13X is charged using solar-simulated light can be increased by concentrating the incident light onto the adsorption bed. This can be done by incorporating light concentration methods such as using Fresnel lenses, parabolic reflectors, or mirrors to direct incident

light onto the adsorption bed. Furthermore, heat transfer fins could be attached to the bottom of the aluminum absorber to increase the temperature of the zeolite 13X beads and improve temperature uniformity throughout the adsorption bed. Furthermore, the amount of heat released during the first hour of the charging phase could be increased by increasing the airflow rate through the adsorption bed. Air flow rates could be increased by increasing the size of the inlets and outlets and by using larger fans to increase the amount of air pushed through the adsorption bed.

7.2.2 Future Work in the Field of Adsorption-Based Thermal Energy Storage

Adsorption-based solar thermal energy storage is an exciting field to harness solar energy in its thermal form and store it for later use when the sun or heat source is not available. The technology utilizes adsorption, a reversible thermochemical process to store heat for periods ranging from hours to days, months, and seasons. The potential of this technology has been proven experimentally through lab-scale experiments, however, for the development of commercial-scale systems further research is needed.

There are certain aspects of this technology that requires improvement, including improving the adsorption efficiency, increasing the energy storage density, optimizing the charging process, achieving higher operating temperatures, improving heat and mass transfer, developing hybrid systems, improving system integration, and reducing costs and attracting investments. These requirements are discussed below.

7.2.2.1 Analysis of adsorption process using dimensionless numbers

In future work the performance of the adsorption beds investigated in this work could be measured as a function of dimensionless numbers. Reporting in terms of dimensionless numbers is beneficial as it allows

the prediction of performance of adsorbant beds with different geometries operating under different conditions. Examples of using Reynold's number and Biot number are provided below:

The Reynolds number **(Re)** is important to understand the flow regime inside the adsorption bed. Reynolds number is described by the ratio of inertial forces to viscous forces, and is given by

$$\mathrm{Re} = \frac{\rho . V . L}{\mu}$$

Where, ρ is the density of fluid (kg/m^3), V is speed of moist air (m/s), L is length of characteristic length (m), and μ is dynamic viscosity of moist air. A Reynold's number less than 2000 means a laminar flow regime, between 2000 and 4000 means a mix of laminar and turbulent flow, and more than 4000 means turbulent flow regime.

Al Ezzi et al. conducted an experimental investigation to study the effect of flowrates on Zeolite 13X charging and discharging for indoor dehumidification [302]. A monolayer of Zeolite 13X beads is used having 4X8 mesh size and a pore diameter of 10 Å. Airflow rates with Re equal to 1773, 2586 and 3325 are considered. With 1773 Reynold's number the discharging time was observed to be 37 minutes which reduced with a Reynolds number of 2586 and 3325 by 27% and 43% respectively, and charging time was observed to be reduced from 66 minutes to 0.07% and 17% respectively. Discharging was done at a relative humidity of 99% and Charging at a temperature of 100 °C. Both charging and discharging of zeolite 13X.

The Biot number (**Bi**) is the ratio of convective heat transfer to the conductive heat transfer and is given by,

$$\mathrm{Bi} = \frac{\mathrm{h} . \mathrm{L}}{\mathrm{k}}$$

Where, h is convective heat transfer coefficient (W/m^2K), L is characteristic length (m), and k is the thermal conductivity (W/mK). Considering the diameter of the Zeolite 13 X beads is 3 mm, the thermal conductivity of the pure zeolite bead is 0.1 W/m·K [303], and h = 30 $W/m^2 \cdot K$ [304], the Biot number would be 0.15. This indicates the heat transfer resistance within the bead is larger than at its surface. During the charging phase heat transfer to the interior of the zeolite 13X Beads may be limited considering their low Biot number. In future work the bead shape and size could be altered to increase the Biot number, and thus increase charging temperatures.

7.2.2.2 Improvement in Efficiency

Despite offering a promising alternative to traditional systems for thermal energy storage, adsorption systems suffer from lower efficiencies. However, application-specific engineered highly porous adsorbents charged with highly efficient heat sources and added to efficiently insulated and highly optimized adsorption beds for improved heat and mass transfer can offer highly efficient adsorption systems. The overall performance of adsorption based thermal energy storage systems can be improved by selecting the suitable adsorbent-adsorbate working pairs, designing the suitable adsorption bed with respect to its size, collector area, volume and thermal conductivity, incorporation of fins of suitable height, thickness and area etc [305].

7.2.2.3 Increasing the Energy Storage Densities

Adsorbents with high storage densities are very important for this technology to compete with existing thermal energy storage technologies. With the development of lightweight high-performance adsorbents

offering higher per unit mass and volume of adsorbate adsorption and desorption, having lower charging temperatures and higher operating temperatures the energy densities of the adsorbents can be improved. As an example, one study highlights how using a compression-induced molding method for preparing high-performance modular adsorbents with high thermal conductivity and packing density by compacting loose particle adsorbents with tunable packing densities and thicknesses resulted in improved energy density of zeolite 13X adsorbent by 1.61 times compared to that of pristine particle adsorbent [306].

7.2.2.4 Optimizing the Charging Process

Currently most of the commercially available and popular adsorbents have either very low thermal energy storage densities or very high charging temperatures. One approach to dealing with the challenge is the development of adsorbents with high energy storage densities having lower charging temperatures and higher thermal conductivities. The other way and probably a more practical approach to dealing with this challenge is by integrating multiple heat sources together to charge these adsorbents efficiently. Theoretical models are developed to optimize the adsorbents for thermal energy storage using molecular simulations and Monte Carlo simulations [307].

7.2.2.5 Improving Heat and Mass Transfer

The adsorption systems can offer higher performances by improving heat and mass transfer. The use of highly porous high adsorbents of optimum size having a high heat transfer coefficient and lower thermal resistances placed in optimized adsorption systems operating under optimized adsorption-desorption cycles can significantly improve the heat and mass transfer in adsorption systems. Heat and mass transfer in the

adsorption bed can be enhanced using the fin type adsorbent heat exchanger, amalgamated adsorbent bed with a metal foam, consolidated adsorbent, adsorbent coating and adsorbent with multi cooling tubes [308].

7.2.2.6 Simplification of Adsorption Systems

Existing adsorption systems are generally very complex which made it hard for these to integrate into modern metropolitan city dwellings. Many current systems rely on the temperature swing or pressure swing for the charging and discharging of adsorbents which necessitates the use of heat exchangers, reactors, and thermal management systems resulting in overall bulky systems. Further, the use of sensory and control components makes the systems only bulkier. However, by simplification and standardisation of system designs, maintenance, and procedures these systems can fit into almost any setting. For example, there are existing adsorption-based thermal energy storage systems in which adsorption/desorption beds and condenser/evaporators are placed in the same unit [146].

7.2.2.7 Development of Hybrid Systems

The overall efficiency of adsorption systems is very low in comparison to their commercial counterparts which makes them uncompetitive. However, by integrating these systems with existing solar photovoltaics, geothermal, combined heating and power and waste heat recovery systems hybrid systems can be developed to meet the demands and achieve overall higher and improved performances. There are many examples of such hybrid systems e.g., solar-powered solid adsorption ice maker [146], solar driven adsorption desalination cooling system [130], and shallow geothermal and solar energy driven adsorption-compression air conditioning system [309].

7.2.2.8 System Integration

An unsaid and generally unappreciated roadblock in the commercialization and mass adoption of any new technology is the know-how on its integration into existing systems. However, with proper and careful planning for the identification of demand and supply gaps, modular designs, training, and auditing procedures can lead to the successful integration of adsorption systems into existing systems. The adsorption based thermal energy storage systems with modular adsorbers [310], [311]. and adsorbent coated adsorbers for thermal energy storage [312] are good expels for the design for system integration. The systems with modular adsorbers are of particular importance as these can reduce the maintenance costs by easy adsorber replacement and less metal consumption [311].

7.2.2.9 Reducing Costs and Attracting Investments

Lastly, it is the system cost that makes a technology attractive to investors and end users. Also, it is the availability of investments at early stages of development that makes a significant contribution to the faster development of technology to be market ready within the right timeframe. The costs of the adsorption systems can be reduced by optimal system design, standardization, and adopting low-cost materials and manufacturing. Further, for the investments government initiatives and funding can be explored however for a later stage a successful demonstration of the technology in the real-world setting is crucial to attracting institutional investors and venture capitalist funds. Studies have shown that the payback period of hybrid systems is found to be shorter than the conventional adsorption-based systems e.g. a hybrid system working with the shallow geothermal energy system and solar energy is found to have a payback period of 2.1 years

[309], where some conventional adsorption-based systems are found to have payback periods in the range of 5-11 years [313], [314].

7.2.2.10 Development of Sustainable Adsorbents

The environmentally friendly adsorbents with suitable thermochemical properties can be a greener alternative to conventional adsorbents. One such sustainable bio-adsorbent, flax/$CaCl_2$/LiCl hybrid is developed for the thermal energy storage for space heating is found to have an energy storage density at 74 kWh/m^3 for 50% inlet relative humidity after regeneration at 120°C [315].

8 Appendix

8.1 Supplementary Material for Chapter 4

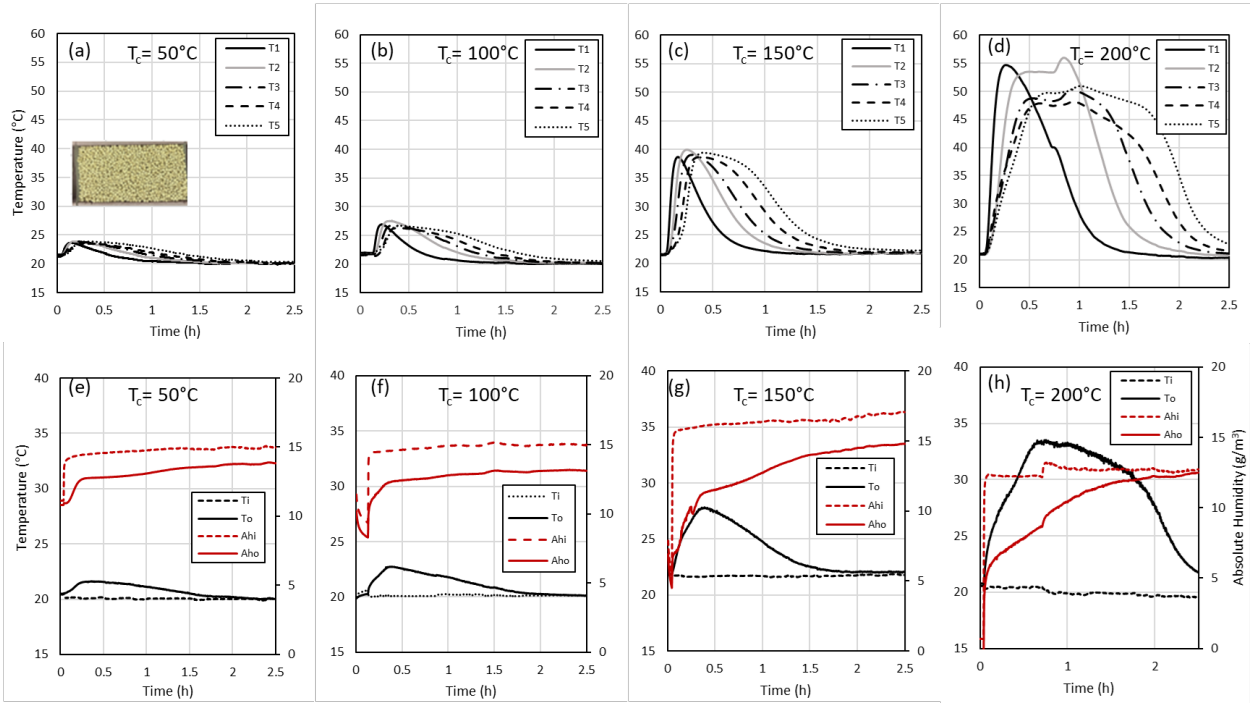

Figure 8.1 The temperature at thermocouple positions T_1 - T_5 as a function of time during the discharging phase when the Zeolite 13X were charged at (a) 50 ° C, (b) 100 ° C, (c) 150 °C, and (d) 200 °C. The inlet and outlet temperatures and absolute humidities plotted as a function of time during the discharging phase when the Zeolite 13X were charged at (e) 50 ° C, (f) 100 ° C, (g) 150 °C, and (h) 200 °C. The air flow velocity during the discharging phase was 0.35 m/s.

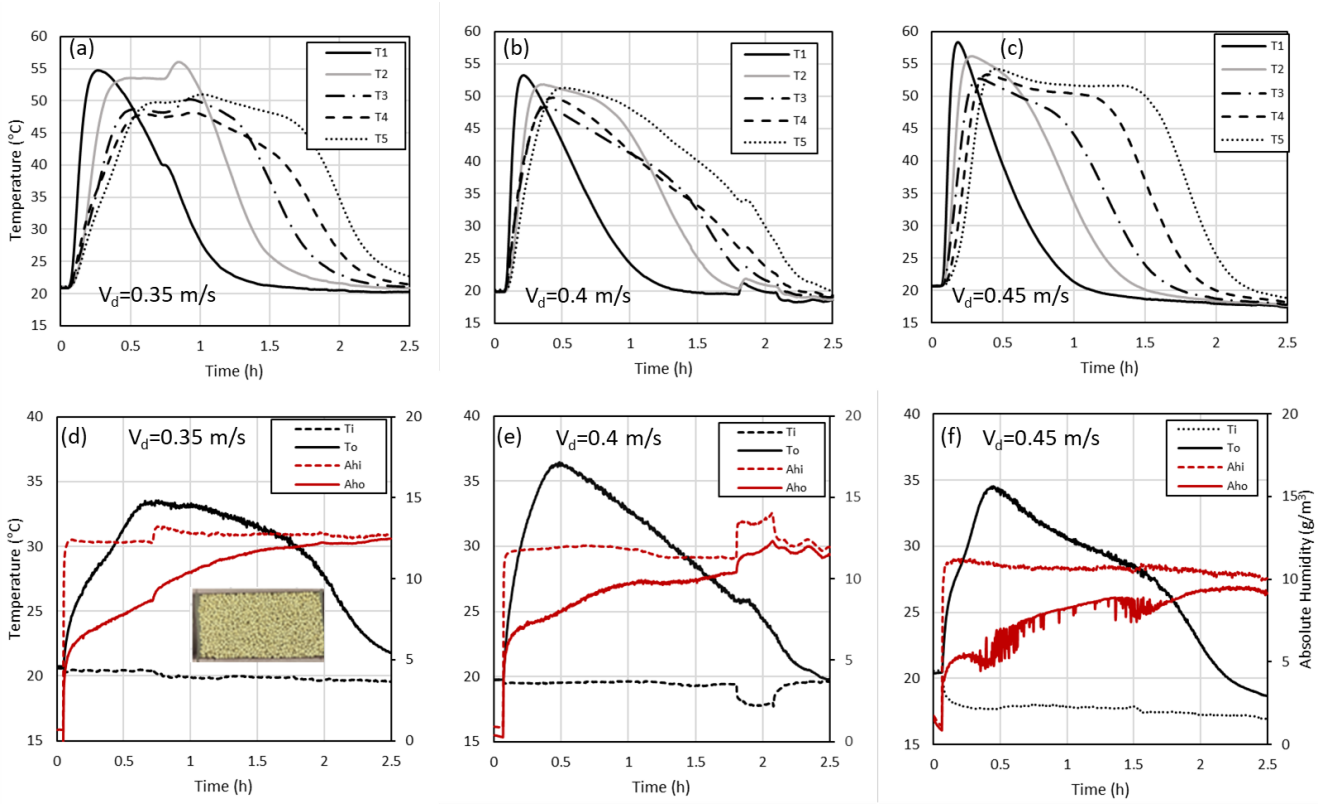

Figure 8.2 The temperature at thermocouple positions T_1 - T_5 as a function of time during the discharging phase when the Zeolite 13X were charged at 200 °C and the air flow velocity is (a) 0.35 m/s, (b) 0.4 m/s, and (c) 0.45 m/s. The inlet and outlet temperatures and absolute humidities plotted as a function of time during the discharging phase when the Zeolite 13X were charged at 200 °C and the air flow velocity during the discharging phase is (d) 0.35 m/s, (e) 0.4 m/s, and (f) 0.45 m/s.

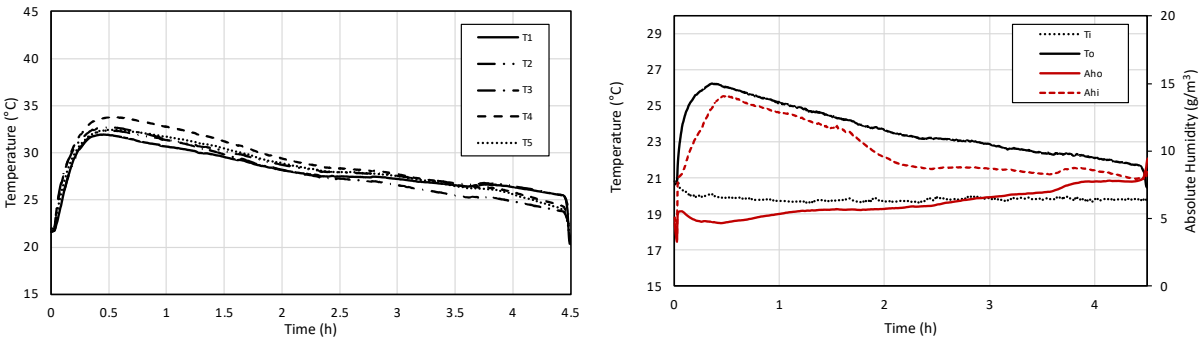

Figure 8.3 (a) Temperature profiles at thermocouple positions T_1 – T_5 as a function of time during the discharging phase when the Zeolite 13X were housed within tubes made from stainless steel mesh; (b) Corresponding inlet and outlet temperatures along with absolute humidities plotted as a function of time during the discharging phase.

8.1.1 Temperature Distribution inside the Adsorption Bed

The study of temperature as a function of position is instrumental for assessing thermal distribution at various locations within a specific timeframe. Figures 8.4 and 8.5 illustrate the temperature distribution at positions 0, 20, 40, 60, 80, 100, and 120 mm within the adsorbent bed over time intervals of 0, 0.5, 1, 1.5, 2, and 2.5 hours, and at the end of experiment. Figure 8.4a clearly shows a uniform temperature increase throughout the experiment. Initially, within the first thirty minutes, the temperature at the 20 mm mark in the adsorbent bed increases to 49.52 °C, peaks at 53.51 °C at the 40 mm mark, and then gradually declines at subsequent positions. In the following thirty minutes, the temperature at the 20 mm position decreases to 28.31 °C, reaches a high of 51.64 °C at the 40 mm position, and then decreases at positions beyond. The temperature decrease across the bed is gradual in the first and second thirty-minute periods and accelerates towards the end of experiment. After 1.5 hours, the temperature reaches a maximum of 48.17 °C at the 100 mm position and swiftly decreases thereafter. In the subsequent thirty minutes, the temperature peaks at 34.85 °C at the 100 mm mark before decreasing at the end of experiment. In Figure 8.4b, the temperature

distribution across the adsorbent bed is notably uniform, with initial temperatures peaking at 42.80 °C, 51.06 °C, 47.28 °C, 49.39 °C, and 51.34 °C at the 20 mm, 40 mm, 60 mm, 80 mm, and 100 mm positions respectively, within the first hour. This is followed by a steady decline until the end of experiment. Notably, at the 100 mm position, temperatures peak later in the experiment, reaching 40.08 °C after 1.5 hours and 29.88 °C after 2 hours. In Figure 8.4c, the temperature initially rises to 53.44 °C at the 40 mm position within the first half-hour, subsequently peaking at 54.01 °C at the 100 mm position. Over the next half-hour, the peak temperature at the 100 mm position is 51.67 °C, and in the subsequent half-hour, it reaches 50.13 °C before beginning a swift decline. The temperature peaks once more at 23.63 °C at the 100 mm position in the following half-hour. The observed variations in temperature peaks during the respective half-hour intervals can be linked to differences in flow velocity across the three cases: 0.35 m/s in Figure 8.4a, 0.40 m/s in Figure 8.4b, and 0.45 m/s in Figure 8.4c.

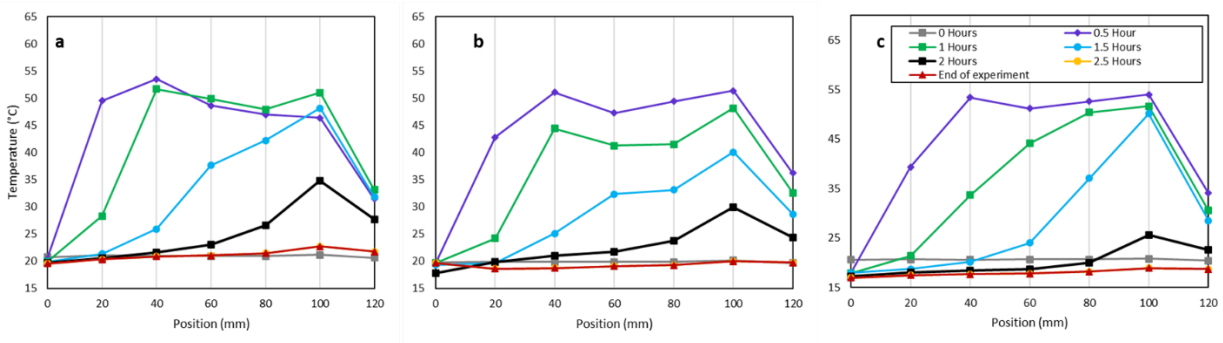

Figure 8.4 Temperature distribution at different positions at different times in the adsorbent bed during the discharging phase when adsorbents are charged at the flow rates of a) 0.35, b) 0.4, and c) 0.45 m/s respectively

Figure 8.5 shows the temperature distribution within the adsorbent bed when the adsorbents are charged at the charging temperatures of 50 °C, 100 °C, 150 °C, and 200 °C. It is evident that with the increase in charging temperature the peak temperature during the discharging phase increases, ranging from 23.73 °C

for adsorbents charged at 50 °C to 53.51 °C for those charged at 200 °C. In the early stages of the experiment, temperatures at the 20 mm position rise sharply for all four charging temperatures, reaching a peak before decreasing significantly. For the adsorbents charged at 50 °C (Figure 8.5a), the peak temperature of 23.73°C is observed at the 100 mm position, with no significant temperature increases in the later stages of the experiment. In the scenario where the charging temperature is 100 °C (Figure 8.5b), a peak temperature of 26.37 °C is reached within the first 30 minutes at the 40 mm position, followed by a decrease. The temperature peaks again at 25.28 °C at the 100 mm position in the subsequent half-hour, with minimal increases thereafter. When the charging temperature is set to 150 °C (Figure 8.5c), the temperature peaks at 29.19 °C at the 100 mm position, with a subsequent peak of 33.42 °C at the same position in the next half-hour, before decreasing again. No significant temperature increases are noted in the later stages. At a charging temperature of 200 °C (Figure 8.5d), the temperature quickly reaches a high of 53.51 °C in the first hour at the 40 mm position, followed by a series of peaks: 50.976 °C, 48.17 °C, and finally 34.85 °C at the 100 mm position in subsequent half-hour intervals.

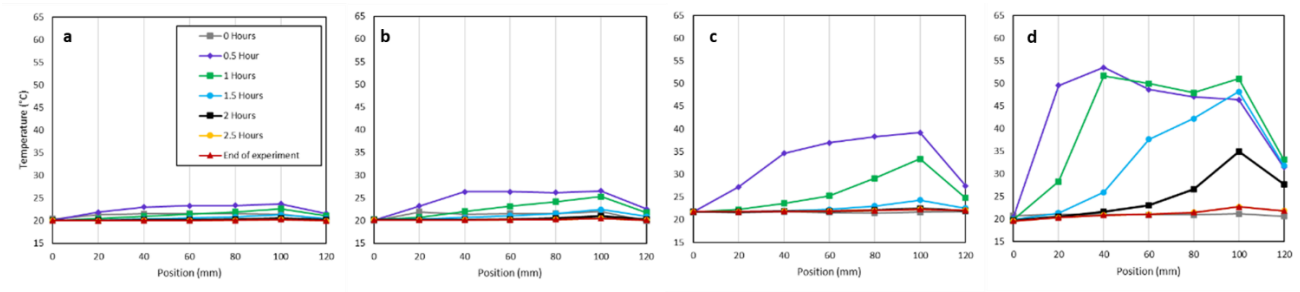

Figure 8.5 Temperature distribution at different positions at different times in the adsorbent bed during the discharging phase when adsorbents are charged at 50, 100, 150 and 200 °C respectively.

The temperature distribution in the Figure 8.6 is very uniform at all positions in the adsorbent bed. In the initial 30 minutes, there is a rapid increase in temperature, peaking at 33.77 °C at the 60 mm position, followed by a decrease. This pattern persists during the next 30-minute interval. However, after 4.5 hours from the start of experiment, no significant temperature gain is observed.

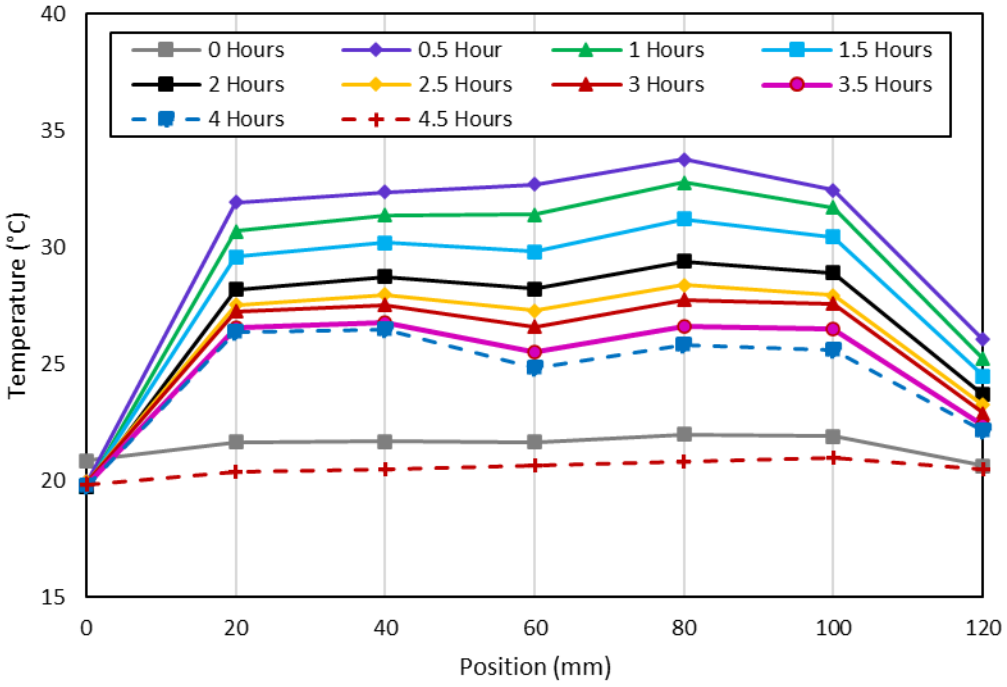

Figure 8.6 Temperature distribution at different positions at different times in the adsorbent bed during the discharging phase when adsorbent pipes.

8.1.2 Breakeven Distance

Although the adsorption-based thermal energy storage process itself is distance-independent, other factors such as the energy consumed during transportation, transportation costs, and associated emissions may be dominant considerations. Therefore, this study focuses exclusively on thermal energy storage for short distances.

For this analysis, both gasoline and electric versions of the Ford F150 pickup 4WD vehicle are considered, with the gasoline vehicle having a fuel efficiency of 20 miles per gallon (MPG) and the electric vehicle having an efficiency of 0.15 kilowatt-hours per kilometer (kWh/km). Additionally, the vehicle fuel efficiency loss due to a 1 kilogram weight increase over a distance is also considered, which is estimated to be 1.18 MPG, as well as the extra emissions resulting from this weight increase, which are assumed to be 0.45 grams of carbon dioxide per mile [316].

Based on the highest ESD values obtained in Chapter 4, the energy stored in 100 kg zeolite 13X is 71 Wh/kg. It takes 25.56 MJ to transport 100 kg of zeolite 13X 48 km using an electric powered Ford F150. Thus, for mobile heat storage to be beneficial the transport distance must be considerably less than 132 km (especially considering the energy stored is in the form of thermal energy while the energy used for transport is provided as electric power). If the energy consumed to transport the zeolite 13 X were to be limited to 20% of the thermal energy stored in the zeolite 13X then the maximum distance the zeolite could be transported would be 26 km. What is meant by short distance will depend on a number of factors including the type of adsorbent and method of transport. For the present case, considering the electric powered Ford F150, “short distance” is less than about 17 km. For the case of the gas-powered Ford F150 the amount of energy consumed per distance travelled is much higher. With the limitation that the energy used for

transport is less than 20% of the energy stored, the maximum transportation distance would be just 3.4 km, suggesting that mobile heat transfer is viable only within an industrial complex.

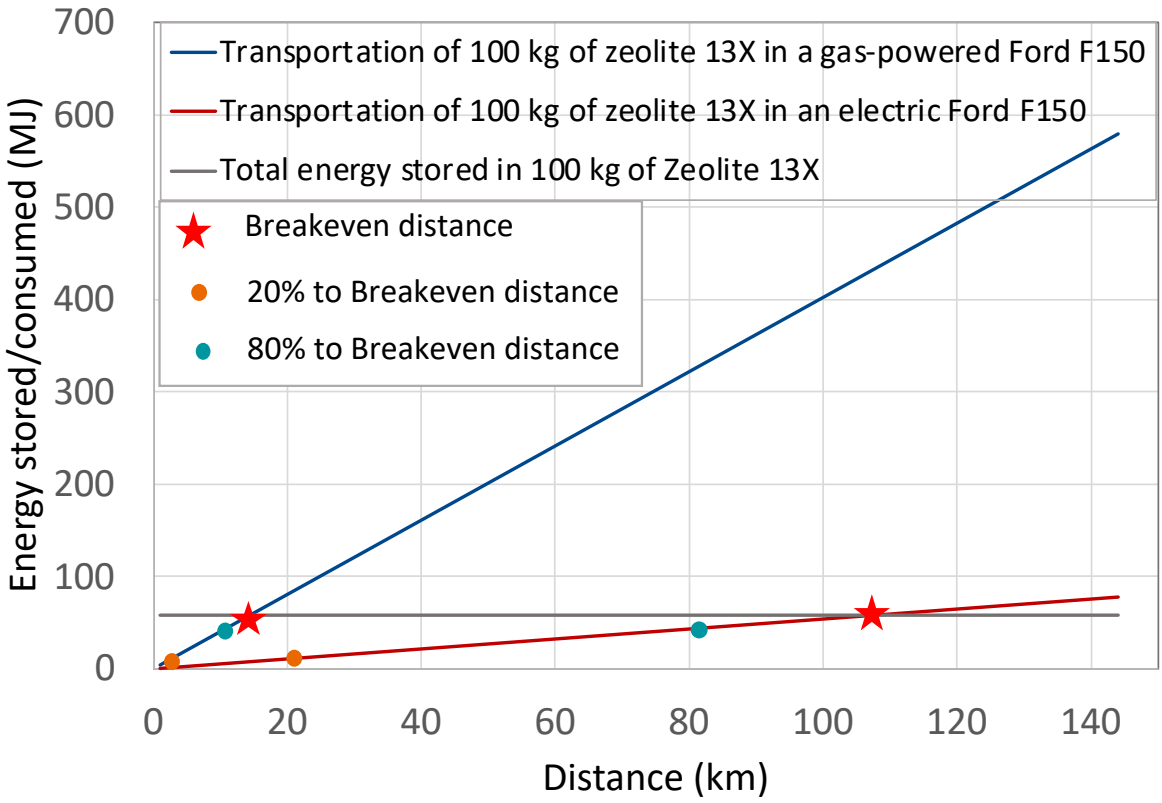

Figure 8.7 Optimal distance to use adsorption-based thermal energy modules for mobile thermal energy storage.

8.2 Supplementary Material for Chapter 5

Table 8.1 The experimental and simulated temperatures 5 mm from the top surface of the zeolite 13X beads

	Case 1	Case 2	Case 3
Experimental results	391 K	357 K	395 K
Simulated results	364 K	356 K	417 K

There is some discrepancy between the experimental and simulated results. For example, the temperature at T1 for the experimental results is 391 K, whereas this temperature is 364 K for the simulated results. These differences arise due to the fact that the simulation is carried out in 2 dimensions and assumptions were made about the permeability of the packed zeolite beads. Nevertheless, the trend for the experimental and simulated results are similar. The highest temperature at T1 occurs for Case 3 (the case of the isolated aluminum absorber) and the lowest temperature at T1 occurs for Case 2 (the full aluminum absorber).

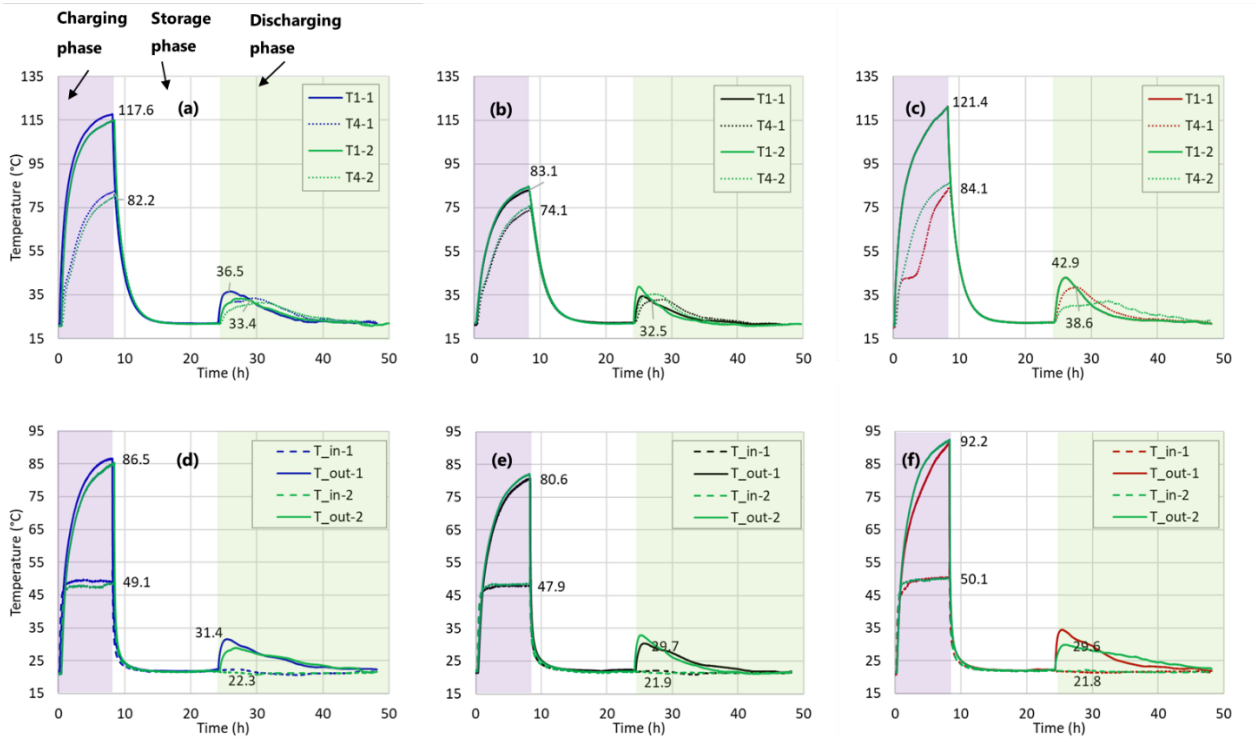

Figure 8.8 Temperature as a function of time at T1 and T4 for two experiments wherein the zeolite 13X beads were charged for 8 hours with (a) no absorber, (b) a full absorber, and (c) an isolated absorber. The temperature as a function of time at the inlet and outlet for two experiments wherein the zeolite 13X beads were charged for 8 hours with (d) no absorber, (e) a full absorber, and (f) an isolated absorber.

Table 8.2 Energy storage densities during experiments

		Charging phase		Discharging phase		Energy storage density (g/m^3)	Energy storage density (Wh/kg)
	Charging time (h)	Temperature at the inlet (°C)	Max charging temperature achieved (°C)	Temperature at the inlet (°C)	Max temperature outlet (°C)		
Case-1: No absorber-1	8	21.7	117.6	21.7	31.4	42.62	61.94
Case-1: No absorber-2	8	21	114.7	21.8	28.7	44.56	64.77

Case-2: Full absorber-1	8	21.5	83.1	21.9	29.7	35.03	50.91
Case-2: Full absorber-2	8	21.9	82.7	21.7	32	31.55	45.86
Case-3: Isolated absorber-1	8	20.7	121.4	22	34	48.35	70.27
Case-3: Isolated absorber-2	8	21.3	121.4	22.1	29.6	49.34	71.72
Case-3: Isolated absorber	2	21.7	98.7	22.5	30.4	9.11	13.24
Case-3: Isolated absorber	4	21.6	114.5	22.3	32.3	21.25	30.89
Case-3: Isolated absorber	6	21.7	118.9	21.7	30.4	38.39	55.79

8.2.1 Case study for rooftop solar powered adsorption panels

Adsorption-based TES systems can be integrated in building ventilation systems to provide heat for buildings [317], [318]. For solar powered systems, the charging phase (desorption) occurs when air entering the adsorbent bed, or the adsorbent bed itself, is heated using sunlight. During the discharging phase moist air passing through the adsorption bed is heated as adsorption occurs. Hot air leaving the adsorption bed can be used to transfer heat to fresh air using a heat exchanger within the buildings ventilation system.

The purpose of this case study is to investigate the feasibility of using the solar powered adsorbent-based TES systems investigated in this thesis to store heat for a typical residential home located in Toronto, Canada, as described in Section 3.4. The calculations in this case study are based on the experimental results reported in Chapter 5. Calculations are performed to determine the volume of zeolite 13X

adsorbents, the amount of light required to charge the zeolite 13 X adsorbents, as well as the area of the adsorbent bed. The required amount of solar concentration and limitations are also discussed below.

Amount of light required to charge the zeolite 13X adsorbents

The highest ESD value of 49.3 kWh/m^3 was achieved for the isolated absorber.

The Light intensity during the experiments is 128.8 mW/cm^2 = 1288 W/m^2

The duration of the charging phase in the experiments is 8 h

The amount of light needed to charge the zeolites is 1288 W/m^2 x 8 h = 10304 Wh/m^2

Required volume of Zeolite 13 X

The average daily energy requirement for spatial heating is 0.23 GJ = 63.889 kWh

The highest energy storage density attained is 49.3 kWh/m^3

The volume of zeolite 13 X needed is 63.889 kWh/(49.3 kWh/m^3) = 1.296 m^3

Required area of the adsorbent bed

The height of the adsorbent bed used in the experiments is 0.05 m.

The area of adsorbent beds required is 1.296 m^3/0.05 m = 25.9 m^2

Required amount of solar concentration

The average daily irradiance in Toronto is 4.3 kWh/m^2

The amount of light needed to charge the zeolites is 1288 W/m^2 x 8 h = 10304 Wh/m^2

The concentration factor needed for the averaged values is (10304 Wh/m^2)/(4.3 kWh/m^2) = 2.4

Flat solar reflectors can be used to concentrate light onto the adsorption bed [319].

Maximum number of solar concentrations and limitations

The rooftop area for the case study is 200 m^2.

Using the experimental conditions, the required area of the adsorbent beds is 25.9 m^2

Limitations throughout the year

- The maximum concentration that could be attained when placing the adsorbent beds on the rooftop is (200 m^2/25.9 m^2) - 1 = 6.72
- The maximum concentration is 2.8 higher than the concentration needed for average conditions (Based on the calculations above, the area of the adsorbent beds is 25.9 m^2 and the concentration factor is 2.4. In this case the area of the adsorbent beds and the collectors would be 25.9 m^2 + 62.2 m^2 = 88.1 m^2. If the concentration factor was 6.72 then the area of the adsorbent beds and the collectors would be 25.9 m^2 + 174.05 m^2 = 200 m^2, which is the area of the rooftop. Notably, this analysis assumes all area on the rooftop could be occupied by PV panels and concentrators, however in practice this would not be possible, and the maximum concentration factor would need to be lowered according to the amount of rooftop space available).
- If sunlight is concentrated at a factor of 6.72 the solar irradiance required before concentration is (10304 Wh/m^2/6.72) = 1533.33 Wh/m^2 = 1.53 kWh/m^2.
- The average daily solar irradiance in Toronto is the lowest during the month of December (1.82 kWh/m^2·d) and is the second lowest during the month of January (2.33 kWh/m^2·d) [320]

- The amount of solar irradiance during the winter is enough to provide for the average heating requirement. However, noting that the heating requirement is significantly larger during the winter, it may only be possible to satisfy a portion of the heating load.

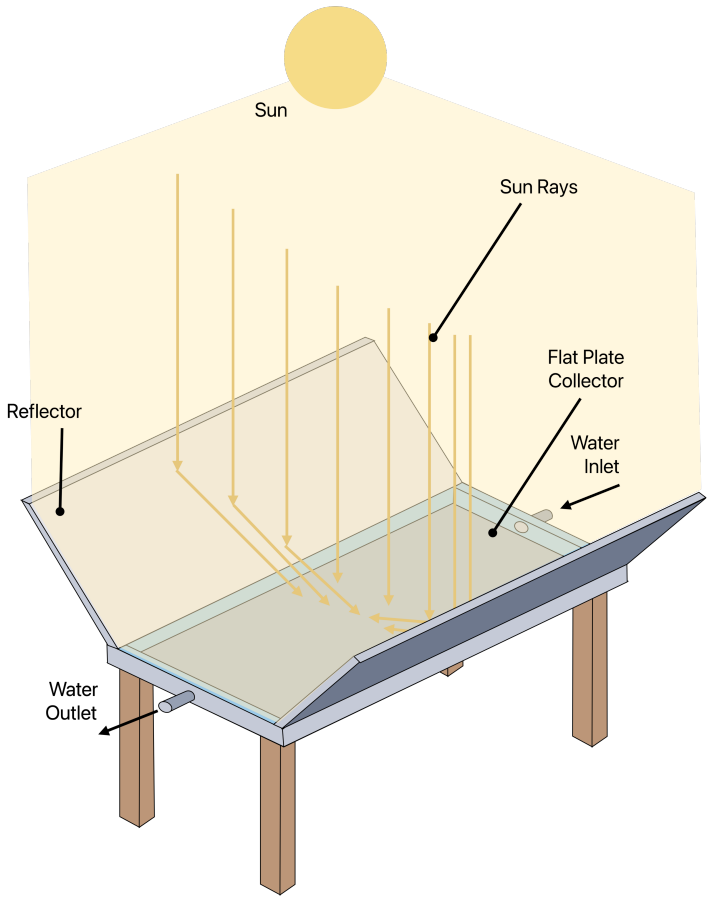

Figure 8.9 Schematic view of flat plate collector with reflectors

8.3 Supplementary Material for Chapter 6

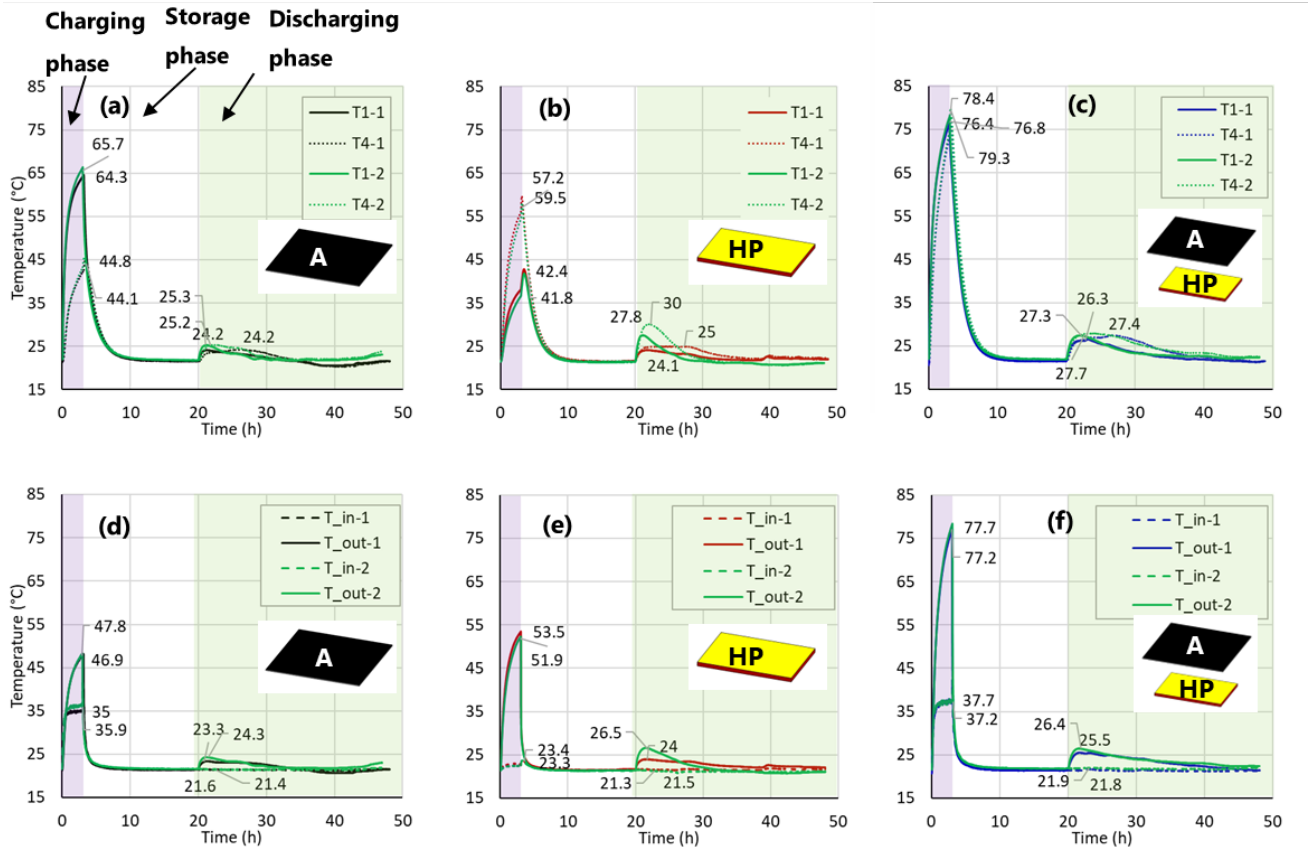

Figure 8.10 Temperature as a function of time at T1 and T4 for two experiments wherein the zeolite 13X beads were charged with (a) solar-simulated radiation incident onto an absorber, (b) a heating pad at the bottom of the adsorption bed, and (c) solar-simulated radiation incident onto an absorber and a heating pad at the bottom of the adsorption bed. The temperature as a function of time at the inlet and outlet for two experiments wherein the zeolite 13X beads were charged with (d) solar-simulated radiation incident onto an absorber, (e) a heating pad at the bottom of the adsorption bed, and (f) solar-simulated radiation incident onto an absorber and a heating pad at the bottom of the adsorption bed.

Table 8.3 Energy storage densities during experiments

	Charging phase			Discharging phase			Energy storage density (g/m^3)	Energy storage density (Wh/kg)
	Relative humidity (%)	**Initial temperature (°C)**	**Absolute humidity (g/m^3)**	**Relative humidity (%)**	**Initial temperature (°C)**	**Absolute humidity (g/m^3)**		
Light-1	16	21.4	1.1	19	21.6	1.4	5.9	8.6
Light-2	20	22.0	1.4	21	21.7	1.6	5.3	7.7
Dark-1	13	21.6	0.9	14	21.7	1.0	8.2	11.9
Dark-2	22	21.5	1.5	33	21.8	2.7	7.0	10.2
Light+Dark-1	19	22.1	1.4	21	22.1	1.7	18.6	27.0
Light+Dark-2	13	20.8	0.8	16	21.5	1.1	19.2	28.0

9 References

[1] P. M. Forster et al., “Indicators of Global Climate Change 2022: Annual update of large-scale indicators of the state of the climate system and human influence,” Earth Syst Sci Data, vol. 15, no. 6, pp. 2295–2327, Jun. 2023, doi: 10.5194/ESSD-15-2295-2023.

[2] W. F. Lamb et al., “A review of trends and drivers of greenhouse gas emissions by sector from 1990 to 2018,” Environmental Research Letters, vol. 16, no. 7, p. 073005, Jun. 2021, doi: 10.1088/1748-9326/ABEE4E.

[3] “Air quality and health.” Accessed: Jul. 23, 2023. [Online]. Available: https://www.who.int/teams/environment-climate-change-and-health/air-quality-and-health/health-impacts/types-of-pollutants

[4] K. Vohra, A. Vodonos, J. Schwartz, E. A. Marais, M. P. Sulprizio, and L. J. Mickley, “Global mortality from outdoor fine particle pollution generated by fossil fuel combustion: Results from GEOS-Chem,” Environ Res, vol. 195, Apr. 2021, doi: 10.1016/J.ENVRES.2021.110754.

[5] C. A. McLinden et al., “Inconsistencies in sulfur dioxide emissions from the Canadian oil sands and potential implications,” Environmental Research Letters, vol. 16, no. 1, p. 014012, Dec. 2020, doi: 10.1088/1748-9326/ABCBBB.

[6] P. Pablo-Romero et al., “A Global Assessment: Can Renewable Energy Replace Fossil Fuels by 2050?,” Sustainability 2022, Vol. 14, Page 4792, vol. 14, no. 8, p. 4792, Apr. 2022, doi: 10.3390/SU14084792.

[7] Z. Liu, Z. Deng, S. Davis, and P. Ciais, “Near-real-time monitoring of global CO 2 emissions reveals the effects of the COVID-19 pandemic,” Nat Rev Earth Environ, vol. 15, pp. 412–414, 2023, doi: 10.1038/s43017-023-00406-zï.

[8] Z. Liu, Z. Deng, S. Davis, and P. Ciais, “Monitoring global carbon emissions in 2022,” Nat Rev Earth Environ, vol. 4, no. 4, pp. 205–206, Apr. 2023, doi: 10.1038/S43017-023-00406-Z.

[9] “Emission Reductions From Pandemic Had Unexpected Effects on Atmosphere.” Accessed: Jul. 23, 2023. [Online]. Available: https://www.jpl.nasa.gov/news/emission-reductions-from-pandemic-had-unexpected-effects-on-atmosphere

[10] W. F. Lamb et al., “A review of trends and drivers of greenhouse gas emissions by sector from 1990 to 2018,” Environmental Research Letters, vol. 16, no. 7, p. 073005, Jun. 2021, doi: 10.1088/1748-9326/ABEE4E.

[11] “CO2 emissions - Our World in Data.” Accessed: Jul. 19, 2023. [Online]. Available: https://ourworldindata.org/co2-emissions?utm_source=tri-city%20news&utm_campaign=tricity%20news%3A%20outbound&utm_medium=referral

[12] I. Renewable Energy Agency, “Renewable energy and Jobs: Annual review 2022,” 2022, Accessed: Jul. 23, 2023. [Online]. Available: www.irena.org

[13] IRENA, “Global Renewables Outlook Edition: 2020,” p. 292, 2020, Accessed: Jul. 23, 2023. [Online]. Available: https://irena.org/publications/2020/Apr/Global-Renewables-Outlook-2020

[14] S. Iyer, A. Nayyar, M. Naved, and F. Al-Turjman, “Renewable Energy and AI for Sustainable Development,” CRC Press, July 2023, 1st edition, doi: 10.1201/9781003369554.

[15] “Investment Flows.” Accessed: Jul. 26, 2023. [Online]. Available: https://www.ren21.net/gsr-2021/chapters/chapter_05/chapter_05/

[16] “Overview and key findings – World Energy Investment 2023 – Analysis - IEA.” Accessed: Jul. 26, 2023. [Online]. Available: https://www.iea.org/reports/world-energy-investment-2023/overview-and-key-findings

[17] “Executive summary – Renewables 2021 – Analysis - IEA.” Accessed: Jul. 26, 2023. [Online]. Available: https://www.iea.org/reports/renewables-2021/executive-summary

[18] U. Epa and C. Protection Partnerships Division, “State and Local Climate and Energy Program Rules of Thumb”, Accessed: Jul. 26, 2023. [Online]. Available: http://www.epa.gov/cleanenergy/documents/epa_lbe.pdf

[19] IRENA International Renewable Energy Agency and I. Renewable Energy Agency, “Global Energy Transformation: A Roadmap to 2050 (2019 Edition),” Global Energy Transformation. A Roadmap to 2050, p. 52, 2019.

[20] “LED Lighting | Department of Energy.” Accessed: Jul. 26, 2023. [Online]. Available: https://www.energy.gov/energysaver/led-lighting

[21] Canada, “A Healthy Environment and a Healthy Economy”, Accessed: Jul. 27, 2023, [Online]. Available: https://www.canada.ca/en/services/environment/weather/climatechange/climate-plan/climate-plan-overview/healthy-environment-healthy-economy.html

[22] “Carbon Prices now Apply to Over a Fifth of Global Greenhouse Gases.” Accessed: Jul. 26, 2023. [Online]. Available: https://www.worldbank.org/en/news/press-release/2021/05/25/carbon-prices-now-apply-to-over-a-fifth-of-global-greenhouse-gases

[23] “State and Trends of Carbon Pricing 2023.” Accessed: Jul. 26, 2023. [Online]. Available: https://www.worldbank.org/en/news/press-release/2023/05/23/record-high-revenues-from-global-carbon-pricing-near-100-billion

[24] “Executive summary – Global EV Outlook 2022 – Analysis - IEA.” Accessed: Jul. 26, 2023. [Online]. Available: https://www.iea.org/reports/global-ev-outlook-2022/executive-summary

[25] “Deforestation has slowed down but still remains a concern, new UN report reveals | UN News.” Accessed: Jul. 26, 2023. [Online]. Available: https://news.un.org/en/story/2020/07/1068761

[26] “Bonn Challenge approaches target to restore 150 million hectares of degraded land | IUCN.” Accessed: Jul. 26, 2023. [Online]. Available: https://www.iucn.org/news/secretariat/201609/bonn-challenge-approaches-target-restore-150-million-hectares-degraded-land

[27] “Global solar capacity additions hit 268 GW in 2022, says BNEF – pv magazine International.” Accessed: Jul. 26, 2023. [Online]. Available: https://www.pv-magazine.com/2022/12/23/global-solar-capacity-additions-hit-268-gw-in-2022-says-bnef/

[28] N. Ahmed, M. Abdel-Hamid, M. M. Abd El-Razik, and K. M. El-Dash, “Impact of sustainable design in the construction sector on climate change,” Ain Shams Engineering Journal, vol. 12, no. 2, pp. 1375–1383, Jun. 2021, doi: 10.1016/J.ASEJ.2020.11.002.

[29] “What is LEED Certification & Steps for Getting a Certification | RTS.” Accessed: Jul. 26, 2023. [Online]. Available: https://www.rts.com/resources/guides/what-is-leed-certification/

[30] “Canada ranks 3rd in the world for LEED certified buildings in 2022 - Canada Green Building Council (CAGBC).” Accessed: Jul. 26, 2023. [Online]. Available: https://www.cagbc.org/news-resources/cagbc-news/canada-ranks-3rd-in-the-world-for-leed-certified-buildings-in-2022/

[31] “World Energy Investment 2023 – Analysis - IEA.” Accessed: Jul. 26, 2023. [Online]. Available: https://www.iea.org/reports/world-energy-investment-2023

[32] “More Than 40 Countries Pledge to Phase Out Coal Power Generation | Earth.Org.” Accessed: Jul. 26, 2023. [Online]. Available: https://earth.org/more-than-40-countries-pledge-to-phase-out-coal-power-generation/

[33] “End to coal power brought forward to October 2024 - GOV.UK.” Accessed: Jul. 26, 2023. [Online]. Available: https://www.gov.uk/government/news/end-to-coal-power-brought-forward-to-october-2024

[34] “The Paris Agreement | UNFCCC.” Accessed: Jul. 26, 2023. [Online]. Available: https://unfccc.int/process-and-meetings/the-paris-agreement

[35] U. Nations, “Net Zero Coalition | United Nations”, Accessed: Jul. 26, 2023. [Online]. Available: https://www.un.org/en/climatechange/net-zero-coalition

[36] U. Nations, “The Paris Agreement | United Nations”, Accessed: Jul. 26, 2023. [Online]. Available: https://www.un.org/en/climatechange/paris-agreement

[37] “A year of exponential growth - Science Based Targets.” Accessed: Jul. 26, 2023. [Online]. Available: https://sciencebasedtargets.org/reports/sbti-progress-report-2021/a-year-of-exponential-growth

[38] “Special Eurobarometer 513 Climate Change Report Summary Project title Special Eurobarometer 513 Climate, Report”, European Commission, March-April 2021, doi: 10.2834/437.

[39] IRENA, “World energy transitions outlook:1.5°C Pathway,” Irena, pp. 1–312, 2021, Accessed: Jul. 26, 2023. [Online]. Available: https://www.irena.org/

[40] “How Canada can decarbonize by 2050 | Deloitte Canada.” Accessed: Jul. 27, 2023. [Online]. Available: https://www2.deloitte.com/ca/en/pages/strategy/articles/how-canada-can-decarbonize-by-2050.html

[41] “Canada installed almost 1 GW of wind and solar energy in 2021, driven by strong growth in Alberta. - Canadian Renewable Energy Association.” Accessed: Jul. 27, 2023. [Online]. Available: https://renewablesassociation.ca/press-release-canada-installed-almost-1-gw-of-wind-and-solar-energy-in-2021/

[42] “Solar Power Statistics in Canada 2021 - SolarFeeds Magazine.” Accessed: Jul. 27, 2023. [Online]. Available: https://www.solarfeeds.com/mag/solar-power-statistics-in-canada-2021/

[43] IRENA, “Innovation Outlook: Thermal Energy Storage,” International Renewable Energy Agency, Abu Dhabi, p. 144, 2020, Accessed: Jul. 26, 2023. [Online]. Available: https://www.irena.org/publications/2020/Nov/Innovation-outlook-Thermal-energy-storage

[44] “Global thermal energy storage market size 2022-2030 | Statista.” Accessed: Jul. 26, 2023. [Online]. Available: https://www.statista.com/statistics/1304464/global-thermal-energy-storage-market-value/

[45] “Thermal Energy Storage Market - Global Size, Share | 2030.” Accessed: Jul. 26, 2023. [Online]. Available: https://www.openpr.com/news/3146329/thermal-energy-storage-market-global-size-share-2030

[46] B. D. Lefebvre, “Thermal Energy Storage Using Adsorption Processes for Solar and Waste Heat Applications: Material Synthesis , Testing and Modeling,” University of Ottawa, Canada, December 2016, Available: http://dx.doi.org/10.20381/ruor-889

[47] D. Lefebvre and F. H. Tezel, “A review of energy storage technologies with a focus on adsorption thermal energy storage processes for heating applications,” Renewable and Sustainable Energy Reviews, vol. 67, pp. 116–125, 2017, doi: 10.1016/j.rser.2016.08.019.

[48] J. Lizana, R. Chacartegui, A. Barrios-Padura, and J. M. Valverde, “Advances in thermal energy storage materials and their applications towards zero energy buildings: A critical review”, Applied Energy, Volume 203, 1 October 2017, Pages 219-239 Available: https://doi.org/10.1016/j.apenergy.2017.06.008

[49] D. Dicaire and F. H. Tezel, “Use of adsorbents for thermal energy storage of solar or excess heat: improvement of energy density,” Int J Energy Res, vol. 37, no. 9, pp. 1059–1068, Jul. 2013, doi: 10.1002/ER.2913.

[50] R. Wang, “Adsorption refrigeration-green cooling driven by low grade thermal energy,” Chinese Science Bulletin, vol. 50, no. 3, p. 193, 2005, doi: 10.1360/982004-62.

[51] K. S. W. Sing et al., “Reporting Physisorption Data for Gas/Solid Systems with Special Reference to the Determination of Surface Area and Porosity,” Pure and Applied Chemistry, vol. 57, no. 4, pp. 603–619, Jan. 1985, Available: https://doi.org/10.1351/pac198557040603

[52] A. Sharafian and M. Bahrami, “Assessment of adsorber bed designs in waste-heat driven adsorption cooling systems for vehicle air conditioning and refrigeration,” Renewable and Sustainable Energy Reviews, vol. 30, pp. 440–451, 2014, doi: 10.1016/j.rser.2013.10.031.

[53] J. White, “CFD Simulation of Silica Gel and Water Adsorbent Beds Used in Adsorption Cooling System,” The University of Birmingham, 2012. doi: 10.13140/RG.2.1.1954.2240.

[54] Z. Li, S. Michiyuki, and F. Takeshi, “International Journal of Heat and Mass Transfer Experimental study on heat and mass transfer characteristics for a desiccant-coated fin-tube heat exchanger,” Int J Heat Mass Transf, vol. 89, pp. 641–651, 2015, doi: 10.1016/j.ijheatmasstransfer.2015.05.095.

[55] A. H. H. N. Khalifa, A. H. Jabbar, and Muhsin Jamal A., “Effect of Exhaust Gas Temperature on the Performance of Automobile Effect of Exhaust Gas Temperature on the Performance of Automobile Adsorption Air-Conditioner,” American Journal of Engineering and Applied Sciences, no. November, 2015, doi: 10.3844/ajeassp.2015.575.581.

[56] A. Rezk, S. Mahmoud, and A. Elsayed, “Effects of contact resistance and metal additives in finned-tube adsorbent beds on the performance of silica gel/water adsorption chiller,” Appl Therm Eng, vol. 53, pp. 278–284, 2013, doi: 10.1016/j.applthermaleng.2012.04.008.

[57] Y. Liu, R. Wang, and Z. Xia, “Continuous adsorption water chiller with novel design,” Huagong Xuebao/Journal of Chemical Industry and Engineering (China), vol. 56, no. 4, pp. 608–613, 2005, doi: 10.1016/j.ijrefrig.2004.09.004.

[58] Y. Liu, R. Wang, and Z. Xia, “Experimental study on a continuous adsorption water chiller with novel design,” Huagong Xuebao/Journal of Chemical Industry and Engineering (China), vol. 56, no. 4, pp. 608–613, 2005, doi: 10.1016/j.ijrefrig.2004.09.004.

[59] Z. Lu, R. Wang, and Z. Xia, “Experimental analysis of an adsorption air conditioning with micro-porous silica gel-water,” Appl Therm Eng, vol. 50, pp. 1015–1020, 2013, doi: 10.1016/j.applthermaleng.2012.07.041.

[60] R. Z. Wang, “Performance improvement of adsorption cooling by heat and mass recovery operation,” International Journal of Refrigeration, vol. 24, no. 7, pp. 602–611, 2001, doi: 10.1016/S0140-7007(01)00004-4.

[61] R. Z. Wang, J. Y. Wu, Y. X. Xu, and W. Wang, “Performance researches and improvements on heat regenerative adsorption refrigerator and heat pump,” Energy Conversion and Management, vol. 42, no. 2, pp. 233–249, 2001, doi: 10.1016/S0196-8904(99)00189-2.

[62] Y. B. Gui, R. Z. Wang, W. Wang, J. Y. Wu, and Y. X. Xu, “Performance modeling and testing on a heat-regenerative adsorptive reversible heat pump,” Appl Therm Eng, vol. 22, no. 3, pp. 309–320, 2002, doi: 10.1016/S1359-4311(01)00082-5.

[63] X. Ji, M. Li, J. Fan, P. Zhang, B. Luo, and L. Wang, “Structure optimization and performance experiments of a solar-powered finned-tube adsorption refrigeration system,” vol. 113, pp. 1293–1300, 2014, doi: 10.1016/j.apenergy.2013.08.088.

[64] M. S. Fernandes, A. R. Gaspar, V. A. F. Costa, J. J. Costa, and G. J. V. N. Brites, “Optimization of a thermal energy storage system provided with an adsorption module – A GenOpt application in a TRNSYS / MATLAB model,” Energy Convers Manag, vol. 162, no. September 2017, pp. 90–97, 2018, doi: 10.1016/j.enconman.2018.02.027.

[65] R. Z. Wang and R. G. Oliveira, “Adsorption refrigeration-An efficient way to make good use of waste heat and solar energy,” Prog Energy Combust Sci, vol. 32, no. 4, pp. 424–458, 2006, doi: 10.1016/j.pecs.2006.01.002.

[66] T. X. Li, R. Z. Wang, R. G. Oliveira, J. K. Kiplagat, and L. W. Wang, “A combined double-way chemisorption refrigeration cycle based on adsorption and resorption processes,” International Journal of Refrigeration, vol. 32, pp. 47–57, 2009, doi: 10.1016/j.ijrefrig.2008.07.007.

[67] T. X. Li, R. Z. Wang, L. W. Wang, and J. K. Kiplagat, “Study on the heat transfer and sorption characteristics of a consolidated composite sorbent for solar-powered thermochemical cooling systems,” Solar Energy, vol. 83, pp. 1742–1755, 2009, doi: 10.1016/j.solener.2009.06.013.

[68] J. Jänchen et al., “Performance of an open thermal adsorption storage system with Linde type A zeolites: Beads versus honeycombs,” Microporous and Mesoporous Materials, vol. 207, pp. 179–184, 2015, doi: 10.1016/j.micromeso.2015.01.018.

[69] A. Shara and M. Bahrami, “Assessment of adsorber bed designs in waste-heat driven adsorption cooling systems for vehicle air conditioning and refrigeration,” Renewable and Sustainable Energy Reviews, vol. 30, pp. 440–451, 2014, doi: 10.1016/j.rser.2013.10.031.

[70] A. Sharafian, C. Mccague, and M. Bahrami, “Impact of fin spacing on temperature distribution in adsorption cooling system for vehicle A / C applications,” International Journal of Refrigeration, vol. 51, pp. 135–143, 2014, doi: 10.1016/j.ijrefrig.2014.12.003.

[71] F. Bagheri, M. A. Fayazbakhsh, P. C. Thimmaiah, and M. Bahrami, “Theoretical and experimental investigation into anti-idling A / C system for trucks,” Energy Convers Manag, vol. 98, pp. 173–183, 2015, doi: 10.1016/j.enconman.2015.03.114.

[72] A. Sharafianardakani, “Waste heat-driven adsorption cooling systems for vehicle air conditioning applications,” Simon Fraser University, 2015.

[73] A. Shara and M. Bahrami, “Critical analysis of thermodynamic cycle modeling of adsorption cooling systems for light-duty vehicle air conditioning applications,” Renewable and Sustainable Energy Reviews, vol. 48, pp. 857–869, 2015, doi: 10.1016/j.rser.2015.04.055.

[74] A. Shara, S. Mahdi, N. Mehr, P. C. Thimmaiah, W. Huttema, and M. Bahrami, “Effects of adsorbent mass and number of adsorber beds on the performance of a waste heat-driven adsorption cooling system for vehicle air conditioning applications,” Energy, vol. 112, pp. 481–493, 2016, doi: 10.1016/j.energy.2016.06.099.

[75] J. Jones, “Development of Efficient Air Conditioning and Refrigeration System for Service Vehicles,” International Journal of Science and Research (IJSR), ISSN (Online): 2319-7064, 2016.

[76] A. Sharafian, P. C. Dan, W. Huttema, and M. Bahrami, “Performance analysis of a novel expansion valve and control valves designed for a waste heat-driven two-adsorber bed adsorption cooling system,” Appl Therm Eng, vol. 100, pp. 1119–1129, 2016, doi: 10.1016/j.applthermaleng.2016.02.118.

[77] M. A. Fayazbakhsh, “Investigation of Optimum Refrigerant Charge and Fans ’ Speed for a Vehicle Air Conditioning System,” Journal of Thermal Science and Engineering Applications, Vol. 9 / 011014-1, no. March 2017, pp. 1–9, 2018, doi: 10.1115/1.4034852.

[78] A. Baniassadi, M. Momen, M. Amidpour, and O. Pourali, “Modeling and design of solar heat integration in process industries with heat storage,” J Clean Prod, vol. 170, pp. 522–534, Jan. 2018, doi: 10.1016/j.jclepro.2017.09.183.

[79] B. Xue, X. Meng, X. Wei, K. Nakaso, and J. Fukai, “Dynamic study of steam generation from low-grade waste heat in a zeolite-water adsorption heat pump,” Appl Therm Eng, vol. 88, pp. 451–458, 2014, doi: 10.1016/j.applthermaleng.2014.11.050.

[80] L. Z. Zhang and L. Wang, “Effects of coupled heat and mass transfers in adsorbent on the performance of a waste heat adsorption cooling unit,” Appl Therm Eng, vol. 19, no. 2, pp. 195–215, 1999, doi: 10.1016/S1359-4311(98)00023-4.

[81] R. Z. Wang and R. G. Oliveira, “Adsorption refrigeration-An efficient way to make good use of waste heat and solar energy,” Prog Energy Combust Sci, vol. 32, no. 4, pp. 424–458, 2006, doi: 10.1016/j.pecs.2006.01.002.

[82] Z. Lu and R. Wang, “Experimental performance study of sorption refrigerators driven by waste gases from fishing vessels diesel engine,” Appl Energy, vol. 174, pp. 224–231, 2016, doi: 10.1016/j.apenergy.2016.04.102.

[83] A. Bin Ismail, A. Li, K. Thu, K. C. Ng, and W. Chun, “Pressurized adsorption cooling cycles driven by solar/waste heat,” Appl Therm Eng, vol. 67, no. 1–2, pp. 106–113, 2014, doi: 10.1016/j.applthermaleng.2014.02.063.

[84] D. C. Wang and J. Y. Wu, “Influence of intermittent heat source on adsorption ice maker using waste heat,” Energy Convers Manag, vol. 46, no. 6, pp. 985–998, 2005, doi: 10.1016/j.enconman.2004.06.002.

[85] L. Q. Zhu et al., “Experimental investigation on composite adsorbent – Water pair for a solar-powered adsorption cooling system,” Appl Therm Eng, vol. 131, pp. 649–659, 2018, doi: 10.1016/j.applthermaleng.2017.12.053.

[86] C. Y. Tso, S. C. Fu, and C. Y. H. Chao, “Modeling a solar-powered double bed novel composite adsorbent (silica activated carbon/CaCl2)-water adsorption chiller,” Build Simul, vol. 7, no. 2, pp. 185–196, 2014, doi: 10.1016/j.ijhm.2017.10.010.

[87] L. Q. Zhu, C. Y. Tso, W. He, C. L. Wu, and C. Y. H. Chao, “A field investigation of a solar-powered adsorption cooling system under Guangzhou’s climate with various numbers of heat exchangers in the adsorbers,” Sci Technol Built Environ, vol. 23, no. 8, pp. 1282–1292, 2017, doi: 10.1080/23744731.2017.1296322.

[88] B. D. Lefebvre, “Thermal Energy Storage Using Adsorption Processes for Solar and Waste Heat Applications: Material Synthesis , Testing and Modeling,” University of Ottawa, Ottawa, Canada, December 2016.

[89] D. Dicaire and F. H. Tezel, “Use of adsorbents for thermal energy storage of solar or excess heat: Improvement of energy density,” Int J Energy Res, 37:1059–1068, 2013, doi: 10.1002/er.2913.

[90] C. Fella, P. Silva, and C. A. I. Roldan, “Performance analysis of a Solar-Powered Air-Conditioning System Using Absorption Refrigeration Cycle and High Efficiency Cooling Technologies,” ISES Solar World Conference 2017 and the IEA SHC Solar Heating and Cooling Conference for Buildings and Industry 2017, Politecnico Di Milano, 2017. doi: 10.18086/swc.2017.28.06.

[91] L. Wang, A. P. Roskilly, and R. Wang, “Solar powered cascading cogeneration cycle with ORC and adsorption technology for electricity and refrigeration,” Heat Transfer Engineering, vol. 35, no. 11–12, pp. 1028–1034, 2014, doi: 10.1080/01457632.2013.863067.

[92] V. Palomba, S. Vasta, A. Freni, Q. Pan, R. Wang, and X. Zhai, “Increasing the share of renewables through adsorption solar cooling: A validated case study,” Renew Energy, vol. 110, pp. 126–140, 2017, doi: 10.1016/j.renene.2016.12.016.

[93] T. X. Li, R. Z. Wang, and T. Yan, “Solid-gas thermochemical sorption thermal battery for solar cooling and heating energy storage and heat transformer,” Energy, vol. 84, pp. 745–758, 2015, doi: 10.1016/j.energy.2015.03.040.

[94] I. Sarbu and C. Sebarchievici, “Solar Heating and Cooling Systems: Fundamentals, Experiments and Applications.”, Elsevier, 2017, ISBN 978-0-12-811662-3.

[95] T. X. Li, R. Z. Wang, L. W. Wang, and J. K. Kiplagat, “Study on the heat transfer and sorption characteristics of a consolidated composite sorbent for solar-powered thermochemical cooling systems,” Solar Energy, vol. 83, pp. 1742–1755, 2009, doi: 10.1016/j.solener.2009.06.013.

[96] C. H. Cox and P. Raghuraman, “Design considerations for flat-plate-photovoltaic/thermal collectors,” Solar Energy, vol. 35, no. 3, pp. 227–241, 1985, doi: 10.1016/0038-092X(85)90102-1.

[97] C. Lamnatou and D. Chemisana, “Solar thermal systems for sustainable buildings and climate change mitigation: Recycling, storage and avoided environmental impacts based on different electricity mixes,” Solar Energy, vol. 231, pp. 209–227, Jan. 2022, doi: 10.1016/J.SOLENER.2021.11.022.

[98] M. S. Fernandes, G. J. V. N. Brites, J. J. Costa, A. R. Gaspar, and V. A. F. Costa, “Modeling and parametric analysis of an adsorber unit for thermal energy storage,” Energy, vol. 102, pp. 83–94, May 2016, doi: 10.1016/J.ENERGY.2016.02.014.

[99] H. Bahrehmand, M. Ahmadi, and M. Bahrami, “Analytical modeling of oscillatory heat transfer in coated sorption beds,” Int J Heat Mass Transf, vol. 121, pp. 1–9, 2018, doi: 10.1016/j.ijheatmasstransfer.2017.12.147.

[100] K. Fayazmanesh, C. Mccague, and M. Bahrami, “Consolidated adsorbent containing graphite flakes for heat-driven water sorption cooling systems,” Appl Therm Eng, vol. 123, pp. 753–760, 2017, doi: 10.1016/j.applthermaleng.2017.05.114.

[101] C. Y. Tso and C. Y. H. Chao, “Activated carbon, silica-gel and calcium chloride composite adsorbents for energy efficient solar adsorption cooling and dehumidification systems,” International Journal of Refrigeration, vol. 35, no. 6, pp. 1626–1638, 2012, doi: 10.1016/j.ijrefrig.2012.05.007.

[102] D. Lefebvre and F. H. Tezel, “A review of energy storage technologies with a focus on adsorption thermal energy storage processes for heating applications,” Renewable and Sustainable Energy Reviews, vol. 67, pp. 116–125, 2017, doi: 10.1016/j.rser.2016.08.019.

[103] H. Jouhara and A. G. Olabi, “Editorial: Industrial waste heat recovery,” Energy, vol. 160, pp. 1–2, Oct. 2018, doi: 10.1016/J.ENERGY.2018.07.013.

[104] S. Quoilin, S. Declaye, B. F. Tchanche, and V. Lemort, “Thermo-economic optimization of waste heat recovery Organic Rankine Cycles,” Appl Therm Eng, vol. 31, no. 14–15, pp. 2885–2893, Oct. 2011, doi: 10.1016/J.APPLTHERMALENG.2011.05.014.

[105] Z. Su et al., “Opportunities and strategies for multigrade waste heat utilization in various industries: A recent review,” Energy Convers Manag, vol. 229, p. 113769, Feb. 2021, doi: 10.1016/J.ENCONMAN.2020.113769.

[106] A. Krönauer, E. Lävemann, S. Brückner, and A. Hauer, “Mobile sorption heat storage in industrial waste heat recovery,” Energy Procedia, Elsevier Ltd, 2015, pp. 272–280. doi: 10.1016/j.egypro.2015.07.688.

[107] F. Huang, J. Zheng, J. M. Baleynaud, and J. Lu, “Heat recovery potentials and technologies in industrial zones,” Journal of the Energy Institute, vol. 90, no. 6, pp. 951–961, Dec. 2017, doi: 10.1016/J.JOEI.2016.07.012.

[108] G. Najeh, G. Slimane, M. Souad, B. Riad, and E. Ganaoui, “Performance of silica gel-water solar adsorption cooling system,” Case Studies in Thermal Engineering, vol. 8, no. July, pp. 337–345, 2016, doi: 10.1016/j.csite.2016.07.002.

[109] A. El Fadar, A. Mimet, and M. Pe, “Study of an adsorption refrigeration system powered by parabolic trough collector and coupled with a heat pipe,” Renewable Energy, vol. 34, pp. 2271–2279, 2009, doi: 10.1016/j.renene.2009.03.009.

[110] Z. X. Yuan, Y. X. Li, and C. X. Du, “Experimental System of Solar Adsorption Refrigeration with Concentrated Collector,” Journal of Visualized Experiments, October, pp. 1–8, 2017, doi: 10.3791/55925.

[111] A. Mahesh, “Solar collectors and adsorption materials aspects of cooling system,” Renewable and Sustainable Energy Reviews, vol. 73, pp. 1300–1312, 2017, doi: 10.1016/j.rser.2017.01.144.

[112] R. A. Almasri, N. H. Abu-Hamdeh, K. K. Esmaeil, and S. Suyambazhahan, “Thermal solar sorption cooling systems, a review of principle, technology, and applications,” Alexandria Engineering Journal, vol. 61, no. 1, pp. 367–402, Jan. 2022, doi: 10.1016/j.aej.2021.06.005.

[113] “3.1 Overview of Flat Plate Collectors | EME 811: Solar Thermal Energy for Utilities and Industry.” Accessed: Aug. 28, 2022. [Online]. Available: https://www.e-education.psu.edu/eme811/node/685

[114] S. Kalogirou, “Solar energy engineering. [electronic resource] : processes and systems.,” 2009, Accessed: Aug. 28, 2022. [Online]. Available: http://libproxy.udayton.edu/login?url=http://search.ebscohost.com/login.aspx?direct=true&db=cat02016a&AN=day.b3725065&site=eds-live

[115] “A Solar Powered Adsorption Freezer: A Case Study for Egypt’s Climate.” International Journal of Energy Harvesting, 3(1):21-29, 2013, p-ISSN: 2163-1891, e-ISSN: 2163-1905, [Online]. Available: http://article.sapub.org/10.5923.j.ijee.20130301.04.html

[116] M. Li, R. Z. Wang, Y. X. Xu, J. Y. Wu, and A. O. Dieng, “Experimental study on dynamic performance analysis of a flat-plate solar solid-adsorption refrigeration for ice maker,” Renew Energy, vol. 27, no. 2, pp. 211–221, Oct. 2002, doi: 10.1016/S0960-1481(01)00188-4.

[117] M. Li and R. Z. Wang, “A study of the effects of collector and environment parameters on the performance of a solar powered solid adsorption refrigerator,” Renew Energy, vol. 27, no. 3, pp. 369–382, Nov. 2002, doi: 10.1016/S0960-1481(02)00009-5.

[118] M. Souissi, Z. Guidara, and A. Maalej, “Experimental study on a new solar refrigerator with intermittent adsorption cycle,” Energy for Sustainable Development, vol. 49, pp. 89–99, Apr. 2019, doi: 10.1016/j.esd.2019.01.006.

[119] L. Q. Zhu et al., “Experimental investigation on composite adsorbent – Water pair for a solar-powered adsorption cooling system,” Appl Therm Eng, vol. 131, pp. 649–659, Feb. 2018, doi: 10.1016/j.applthermaleng.2017.12.053.

[120] F. Lemmini and A. Errougani, “Building and experimentation of a solar powered adsorption refrigerator,” Renew Energy, vol. 30, no. 13, pp. 1989–2003, Oct. 2005, doi: 10.1016/J.RENENE.2005.03.003.

[121] F. Lemmini and A. Errougani, “Experimentation of a solar adsorption refrigerator in Morocco,” Renew Energy, vol. 32, pp. 2629–2641, Dec. 2007, doi: 10.1016/J.RENENE.2007.01.004.

[122] M. Li, H. B. Huang, R. Z. Wang, L. L. Wang, W. M. Yang, and W. D. Cai, “Study on intermittent refrigeration phenomenon for solar solid adsorption refrigeration,” Appl Therm Eng, vol. 25, no. 11–12, pp. 1614–1622, Aug. 2005, doi: 10.1016/J.APPLTHERMALENG.2004.11.010.

[123] R. Z. Wang, M. Li, Y. X. Xu, and J. Y. Wu, “An energy efficient hybrid system of solar powered water heater and adsorption ice maker,” Solar Energy, vol. 68, no. 2, pp. 189–195, 2000, doi: 10.1016/S0038-092X(99)00062-6.

[124] E. S. Ali, K. Harby, A. A. Askalany, M. R. Diab, and A. S. Alsaman, “Weather effect on a solar powered hybrid adsorption desalination-cooling system: A case study of Egypt’s climate,” Appl Therm Eng, vol. 124, pp. 663–672, 2017, doi: 10.1016/j.applthermaleng.2017.06.048.

[125] M. Attalla, S. Sadek, M. Salem Ahmed, I. M. Shafie, and M. Hassan, “Experimental study of solar powered ice maker using adsorption pair of activated carbon and methanol,” Appl Therm Eng, vol. 141, pp. 877–886, Aug. 2018, doi: 10.1016/j.applthermaleng.2018.06.038.

[126] T. Robbins and S. Garimella, “An autonomous solar driven adsorption cooling system,” Solar Energy, vol. 211, pp. 1318–1324, Nov. 2020, doi: 10.1016/j.solener.2020.10.068.

[127] E. E. Anyanwu and C. I. Ezekwe, “Design, construction and test run of a solid adsorption solar refrigerator using activated carbon/methanol, as adsorbent/adsorbate pair,” Energy Convers Manag, vol. 44, no. 18, pp. 2879–2892, Nov. 2003, doi: 10.1016/S0196-8904(03)00072-4.

[128] N. V. Ogueke and E. E. Anyanwu, “Design improvements for a collector/generator/adsorber of a solid adsorption solar refrigerator,” Renew Energy, vol. 33, no. 11, pp. 2428–2440, Nov. 2008, doi: 10.1016/J.RENENE.2008.02.007.

[129] W. S. Chang, C. C. Wang, and C. C. Shieh, “Design and performance of a solar-powered heating and cooling system using silica gel/water adsorption chiller,” Appl Therm Eng, vol. 29, no. 10, pp. 2100–2105, Jul. 2009, doi: 10.1016/J.APPLTHERMALENG.2008.10.021.

[130] A. S. Alsaman, A. A. Askalany, K. Harby, and M. S. Ahmed, “Performance evaluation of a solar-driven adsorption desalination-cooling system,” Energy, vol. 128, pp. 196–207, 2017, doi: 10.1016/j.energy.2017.04.010.

[131] H. Z. Hassan, A. Mohamad, and R. Bennacer, “Simulation of an adsorption solar cooling system,” Energy, vol. 36, no. 1, pp. 530–537, Jan. 2011, doi: 10.1016/J.ENERGY.2010.10.011.

[132] M. Louajari, A. Mimet, and A. Ouammi, “Study of the effect of finned tube adsorber on the performance of solar driven adsorption cooling machine using activated carbon–ammonia pair,” Appl Energy, vol. 88, no. 3, pp. 690–698, Mar. 2011, doi: 10.1016/J.APENERGY.2010.08.032.

[133] A. El Fadar, A. Mimet, A. Azzabakh, M. Pérez-García, and J. Castaing, “Study of a new solar adsorption refrigerator powered by a parabolic trough collector,” Appl Therm Eng, vol. 29, no. 5–6, pp. 1267–1270, Apr. 2009, doi: 10.1016/J.APPLTHERMALENG.2008.06.012.

[134] S. Edin Hamrahi, K. Goudarzi, and M. Yaghoubi, “Experimental study of the performance of a continues solar adsorption chiller using Nano-activated carbon/methanol as working pair,” Solar Energy, vol. 173, pp. 920–927, Oct. 2018, doi: 10.1016/j.solener.2018.08.030.

[135] M. I. González and L. R. Rodríguez, “Solar powered adsorption refrigerator with CPC collection system: Collector design and experimental test,” Energy Convers Manag, vol. 48, no. 9, pp. 2587–2594, Sep. 2007, doi: 10.1016/J.ENCONMAN.2007.03.016.

[136] O. S. C. Headley, A. F. Kothdiwala, and I. A. McDoom, “Charcoal-methanol adsorption refrigerator powered by a compound parabolic concentrating solar collector,” Solar Energy, vol. 53, no. 2, pp. 191–197, Aug. 1994, doi: 10.1016/0038-092X(94)90481-2.

[137] C. Hildbrand, P. Dind, M. Pons, and F. Buchter, “A new solar powered adsorption refrigerator with high performance,” Solar Energy, vol. 77, no. 3, pp. 311–318, Sep. 2004, doi: 10.1016/J.SOLENER.2004.05.007.

[138] M. Y. H. Othman, B. Yatim, K. Sopian, and M. N. Abu Bakar, “Performance analysis of a double-pass photovoltaic/thermal (PV/T) solar collector with CPC and fins,” Renew Energy, vol. 30, no. 13, pp. 2005–2017, Oct. 2005, doi: 10.1016/j.renene.2004.10.007.

[139] C. Zhao, Y. Wang, M. Li, and W. Du, “Heat transfer performance investigation on a finned tube adsorbent bed with a compound parabolic concentrator (CPC) for solar adsorption refrigeration,” Appl Therm Eng, vol. 152, pp. 391–401, Apr. 2019, doi: 10.1016/j.applthermaleng.2019.02.063.

[140] C. Li et al., “An Experimental Investigation of an Adsorption Ice-Maker Driven by Parabolic Trough Collector,” Heat Transf Res, vol. 46, no. 4, pp. 347–368, 2015, doi: 10.1615/HEATTRANSRES.2014007104.

[141] M. Umair, A. Akisawa, and Y. Ueda, “Performance Evaluation of a Solar Adsorption Refrigeration System with a Wing Type Compound Parabolic Concentrator,” Energies 2014, Vol. 7, Pages 1448-1466, vol. 7, no. 3, pp. 1448–1466, Mar. 2014, doi: 10.3390/EN7031448.

[142] A. Kumar, A. Chaudhary, and A. Yadav, “The Regeneration of Various Solid Desiccants by Using a Parabolic Dish Collector and Adsorption Rate: An Experimental Investigation,” International Journal of Green Energy , pp 936-953, 2014, doi: 10.1080/15435075.2013.833514.

[143] M. G. Gado, S. Ookawara, S. Nada, and H. Hassan, “Renewable energy-based cascade adsorption-compression refrigeration system: Energy, exergy, exergoeconomic and enviroeconomic perspectives,” Energy, vol. 253, Aug. 2022, doi: 10.1016/j.energy.2022.124127.

[144] A. Kotb, M. B. Elsheniti, and O. A. Elsamni, “Optimum number and arrangement of evacuated-tube solar collectors under various operating conditions,” Energy Convers Manag, vol. 199, Nov. 2019, doi: 10.1016/j.enconman.2019.112032.

[145] A. Buonomano, F. Calise, and A. Palombo, “Solar heating and cooling systems by absorption and adsorption chillers driven by stationary and concentrating photovoltaic/thermal solar collectors: Modelling and simulation,” Renewable and Sustainable Energy Reviews, vol. 82, pp. 1874–1908, Feb. 2018, doi: 10.1016/J.RSER.2017.10.059.

[146] M. Pons and J. J. Guilleminot, “Design of an experimental solar-powered, solid-adsorption ice maker,” Journal of Solar Energy Engineering, Transactions of the ASME, vol. 108, no. 4, pp. 332–337, 1986, doi: 10.1115/1.3268115.

[147] M. Souissi, Z. Guidara, and A. Maalej, “Numerical simulation and experimental investigation on a solar refrigerator with intermittent adsorption cycle,” Solar Energy, vol. 180, pp. 277–292, Mar. 2019, doi: 10.1016/j.solener.2019.01.040.

[148] T. C. Roumpedakis et al., “Performance Results of a Solar Adsorption Cooling and Heating Unit,” Energies 2020, Vol. 13, Page 1630, vol. 13, no. 7, p. 1630, Apr. 2020, doi: 10.3390/EN13071630.

[149] P. Amyot, D. Lefebvre, A. Godin, and F. H. Tezel, “Adsorbent Screening for Thermal Energy Storage Application,” in 66th Canadian Chemical Engineering Conference, Quebec City, Quebec, 2016.

[150] D. Lefebvre and F. H. Tezel, “A review of energy storage technologies with a focus on adsorption thermal energy storage processes for heating applications,” Renewable and Sustainable Energy Reviews, vol. 67, pp. 116–125, 2017, doi: 10.1016/j.rser.2016.08.019.

[151] J. Jänchen and H. Stach, “Adsorption properties of porous materials for solar thermal energy storage and heat pump applications,” Energy Procedia, vol. 30, pp. 289–293, 2012, doi: 10.1016/j.egypro.2012.11.034.

[152] K. C. Chan, C. Y. H. Chao, G. N. Sze-To, and K. S. Hui, “Development of New Zeolite 13X/CACL2 composite adsorbent for air-conditioning application,” ASME 2011 5th International Conference on Energy Sustainability, ES 2011, Parts A, B, and C, 2011, doi: 10.1115/ES2011-54052.

[153] U. Wittstadt, G. Füldner, O. Andersen, R. Herrmann, and F. Schmidt, “A new adsorbent composite material based on metal fiber technology and its application in adsorption heat exchangers,” Energies (Basel), vol. 8, no. 8, pp. 8431–8446, 2015, doi: 10.3390/en8088431.

[154] K. Fayazmanesh, C. McCague, and M. Bahrami, “Consolidated adsorbent containing graphite flakes for heat-driven water sorption cooling systems,” Appl Therm Eng, vol. 123, pp. 753–760, 2017, doi: 10.1016/j.applthermaleng.2017.05.114.

[155] K. C. Chan, C. Y. H. Chao, and M. Bahrami, “Heat and Mass Transfer Characteristics of a Zeolite 13X/CACL2 Composite Adsorbent in Adsorption Cooling Systems,” in Proceedings of the ASME 2012 6th International Conference on Energy Sustainability & 10th Fuel Cell Science, Engineering and Technology Conference (ESFuelCell2012), 2012, pp. 1–10.

[156] K. C. Chan, C. Y. H. Chao, G. N. Sze-To, and K. S. Hui, “Performance predictions for a new zeolite 13X/CaCl2composite adsorbent for adsorption cooling systems,” Int J Heat Mass Transf, vol. 55, no. 11–12, pp. 3214–3224, 2012, doi: 10.1016/j.ijheatmasstransfer.2012.02.054.

[157] C. Mccague, K. Fayazmanesh, and C. Berlanga, “Evaluation of $CaCl_2$– Silica Gel Sorbent for Water Sorption Cooling Systems,” IX Minsk International Seminar “Heat Pipes, Heat Pumps, Refrigerators, Power Sources”, Minsk, Belarus, 07-10 September 2015.

[158] K. C. Chan, C. Y. H. Chao, and C. L. Wu, “Measurement of properties and performance prediction of the new MWCNT-embedded zeolite 13X/$CaCl_2$ composite adsorbents,” Int J Heat Mass Transf, vol. 89, pp. 308–319, 2015, doi: 10.1016/j.ijheatmasstransfer.2015.05.063.

[159] C. Y. Tso, K. C. Chan, C. Y. H. Chao, and C. L. Wu, “Experimental performance analysis on an adsorption cooling system using zeolite 13X/CaCl2adsorbent with various operation sequences,” Int J Heat Mass Transf, vol. 85, pp. 343–355, 2015, doi: 10.1016/j.ijheatmasstransfer.2015.02.005.

[160] K. C. Chan, C. Y. H. Chao, and M. Bahrami, “Heat and Mass Transfer Characteristics of a Zeolite 13X/CaCl2 Composite Adsorbent in Adsorption a Cooling Systems,” ASME 2012 6th International

Conference on Energy Sustainability, Parts A and B, January 2015, p. 49, 2012, doi: 10.1115/ES2012-91246.

[161] L. W. Wang, R. Z. Wang, and R. G. Oliveira, “A review on adsorption working pairs for refrigeration,” Renewable and Sustainable Energy Reviews, vol. 13, pp. 518–534, 2009, doi: 10.1016/j.rser.2007.12.002.

[162] A. Erto, R. Andreozzi, A. Lancia, and D. Musmarra, “Factors affecting the adsorption of trichloroethylene onto activated carbons,” Appl Surf Sci, vol. 256, no. 17, pp. 5237–5242, 2010, doi: 10.1016/j.apsusc.2009.12.110.

[163] D. Lefebvre, P. Amyot, B. Ugur, and F. H. Tezel, “Adsorption Prediction and Modeling of Thermal Energy Storage Systems: A Parametric Study,” Ind Eng Chem Res, vol. 55, pp. 4760–4772, 2016.

[164] D. Dicaire and F. H. Tezel, “Use of adsorbents for thermal energy storage of solar or excess heat: Improvement of energy density,” Int J Energy Res, 2013, doi: 10.1002/er.2913.

[165] R. H. Mohammed, O. Mesalhy, M. L. Elsayed, S. Hou, M. Su, and L. C. Chow, “Physical properties and adsorption kinetics of silica-gel/water for adsorption chillers,” Appl Therm Eng, vol. 137, no. October 2017, pp. 368–376, 2018, doi: 10.1016/j.applthermaleng.2018.03.088.

[166] C. Y. Tso and C. Y. H. Chao, “Activated carbon, silica-gel and calcium chloride composite adsorbents for energy efficient solar adsorption cooling and dehumidification systems,” International Journal of Refrigeration, vol. 35, no. 6, pp. 1626–1638, 2012, doi: 10.1016/j.ijrefrig.2012.05.007.

[167] J. Ammann, P. Ruch, B. Michel, and A. R. Studart, “International Journal of Heat and Mass Transfer Quantification of heat and mass transport limitations in adsorption heat exchangers : Application to

the silica gel / water working pair," Int J Heat Mass Transf, vol. 123, pp. 331–341, 2018, doi: 10.1016/j.ijheatmasstransfer.2018.02.076.

[168] J. Ammann, B. Michel, and P. W. Ruch, "International Journal of Heat and Mass Transfer Characterization of transport limitations in SAPO-34 adsorbent coatings for adsorption heat pumps," Int J Heat Mass Transf, vol. 129, pp. 18–27, 2019, doi: 10.1016/j.ijheatmasstransfer.2018.09.053.

[169] G. Li, S. Qian, H. Lee, Y. Hwang, and R. Radermacher, "Experimental investigation of energy and exergy performance of short term adsorption heat storage for residential application," Energy, vol. 65, pp. 675–691, 2014, doi: 10.1016/j.energy.2013.12.017.

[170] D. C. Wang, Z. Z. Xia, and J. Y. Wu, "Design and performance prediction of a novel zeolite-water adsorption air conditioner," Energy Convers Manag, vol. 47, no. 5, pp. 590–610, 2006, doi: 10.1016/j.enconman.2005.05.011.

[171] Y. Wang, M. Li, W. Du, X. Ji, and L. Xu, "Experimental investigation of a solar-powered adsorption refrigeration system with the enhancing desorption," Energy Conversion and Management, vol. 155, no. October 2017, pp. 253–261, 2018, doi: 10.1016/j.enconman.2017.10.065.

[172] Z. Z. Xia, R. Z. Wang, D. C. Wang, Y. L. Liu, J. Y. Wu, and C. J. Chen, "Development and comparison of two-bed silica gel-water adsorption chillers driven by low-grade heat source," International Journal of Thermal Sciences, vol. 48, no. 5, pp. 1017–1025, 2009, doi: 10.1016/j.ijthermalsci.2008.07.004.

[173] K. Oertel and M. Fischer, “Adsorption cooling system for cold storage using methanol /silicagel,” Applied Thermal Engineering, vol. 18, pp 773-786, 1998. https://doi.org/10.1016/S1359-4311(97)00107-5

[174] L. W. Wang, H. S. Bao, and R. Z. Wang, “A comparison of the performances of adsorption and resorption refrigeration systems powered by the low grade heat,” Renew Energy, vol. 34, pp. 2273–2379, 2009, doi: 10.1016/j.renene.2009.02.011.

[175] W. S. Chang, C. C. Wang, and C. C. Shieh, “Experimental study of a solid adsorption cooling system using flat-tube heat exchangers as adsorption bed,” Appl Therm Eng, vol. 27, no. 13, pp. 2195–2199, 2007, doi: 10.1016/j.applthermaleng.2005.07.022.

[176] Y. Liu, R. Wang, and Z. Xia, “Continuous adsorption water chiller with novel design,” Huagong Xuebao/Journal of Chemical Industry and Engineering (China), 2005, doi: 10.1016/j.ijrefrig.2004.09.004.

[177] R. H. Mohammed, O. Mesalhy, M. L. Elsayed, M. Su, and L. C. Chow, “Revisiting the adsorption equilibrium equations of silica-gel/water for adsorption cooling applications,” International Journal of Refrigeration, vol. 86, pp. 40–47, 2018, doi: 10.1016/j.ijrefrig.2017.10.038.

[178] D. Lefebvre, P. Amyot, B. Ugur, and F. H. Tezel, “Adsorption Prediction and Modeling of Thermal Energy Storage Systems: A Parametric Study,” Ind Eng Chem Res, vol. 55, no. 16, pp. 4760–4772, 2016, doi: 10.1021/acs.iecr.5b04767.

[179] B. Dawoud et al., “On the effective thermal conductivity of wetted zeolite under the working conditions of an adsorption chiller” Applied Thermal Engineering, Vol. 31, Issues 14-15, pp 2241-2246, 2011, doi: 10.1016/j.applthermaleng.2011.03.016.

[180] A. Sharafian, K. Fayazmanesh, C. McCague, and M. Bahrami, “Thermal conductivity and contact resistance of mesoporous silica gel adsorbents bound with polyvinylpyrrolidone in contact with a metallic substrate for adsorption cooling system applications,” Int J Heat Mass Transf, vol. 79, pp. 64–71, 2014, doi: 10.1016/j.ijheatmasstransfer.2014.07.086.

[181] M. Rouhani, W. Huttema, and M. Bahrami, “Effective thermal conductivity of packed bed adsorbers : Part 1 – Experimental study,” Int J Heat Mass Transf, vol. 123, pp. 1204–1211, 2018, doi: 10.1016/j.ijheatmasstransfer.2018.01.142.

[182] Khaliji Oskouei M. and Z. Tamainot-Telto, “Effect of packing density on thermal properties of granular activated carbon packed bed by using of inverse heat conduction method,” in HEFAT2014 10th International Conference on Heat Transfer, Fluid Mechanics and Thermodynamics, 2014, pp. 14–16.

[183] A. Sharafian, K. Fayazmanesh, C. Mccague, and M. Bahrami, “Thermal conductivity and contact resistance of mesoporous silica gel adsorbents bound with polyvinylpyrrolidone in contact with a metallic substrate for adsorption cooling system applications Amir,” Int J Heat Mass Transf, vol. 79, pp. 64–71, 2014, doi: 10.1016/j.ijheatmasstransfer.2014.07.086.

[184] L. F. Cabeza, A. Solé, and C. Barreneche, “Review on sorption materials and technologies for heat pumps and thermal energy storage,” Renew Energy, vol. 110, pp. 3–39, Sep. 2017, doi: 10.1016/j.renene.2016.09.059.

[185] D. Lefebvre, P. Amyot, B. Ugur, and F. H. Tezel, “Adsorption Prediction and Modeling of Thermal Energy Storage Systems: A Parametric Study,” Ind Eng Chem Res, vol. 55, no. 16, pp. 4760–4772, 2016, doi: 10.1021/acs.iecr.5b04767.

[186] S. V. Id et al., “Adsorption Heat Storage : State-of-the-Art and Future Perspectives,” Nanomaterials, vol. 8, no. 522, pp. 1–13, 2018, doi: 10.3390/nano8070522.

[187] S. Kreussler and D. Bolz, “Experiments on Solar Adsorption Refrigeration Solar Regeneration”. Environmental Science, Engineering, Materials Science, 2000, Accessed: Aug. 25, 2022. https://www.semanticscholar.org/paper/EXPERIMENTS-ON-SOLAR-ADSORPTION-REFRIGERATION-USING-Kreussler-Bolz/a63d14269ed02ce81121ad875941f4babc58a977#citing-papers

[188] “Statistics Canada (2007) Households and the Environment Use, Cat no. 11-526-S.” Accessed: Aug. 23, 2022. [Online]. Available: https://www.statcan.gc.ca/pub/11-526-s/11-526-s2010001-eng.pdf

[189] “Energy statistics - quantities (nrg_quant).” Accessed: Aug. 23, 2022. [Online]. Available: https://ec.europa.eu/eurostat/cache/metadata/en/nrg_quant_esms.htm

[190] K. Narwal, R. Kempers, and P. G. O’brien, “Adsorbent-Adsorbate Pairs for Solar Thermal Energy Storage in Residential Heating Applications: A Comparative Study,” Proceedings of The Canadian Society for Mechanical Engineering International Congress 2018, CSME International Congress 2018, May 27-30, 2018, Toronto, On, Canada

[191] R. Tamme, T. Bauer, and E. Hahne, “Heat Storage Media,” Ullmann’s Encyclopedia of Industrial Chemistry, Oct. 2009, doi: 10.1002/14356007.A12_B30.PUB2.

[192] C. K. Chau, T. M. Leung, and W. Y. Ng, “A review on Life Cycle Assessment, Life Cycle Energy Assessment and Life Cycle Carbon Emissions Assessment on buildings,” Appl Energy, vol. 143, no. 1, pp. 395–413, Apr. 2015, doi: 10.1016/J.APENERGY.2015.01.023.

[193] B. Nienborg, T. Helling, D. Fröhlich, R. Horn, G. Munz, and P. Schossig, “Closed Adsorption Heat Storage—A Life Cycle Assessment on Material and Component Levels,” Energies 2018, Vol. 11, Page 3421, vol. 11, no. 12, p. 3421, Dec. 2018, doi: 10.3390/EN11123421.

[194] B. Nienborg et al., “Life Cycle Assessment of thermal energy storage materials and components,” Energy Procedia, vol. 155, pp. 111–120, Nov. 2018, doi: 10.1016/J.EGYPRO.2018.11.063.

[195] C. Denzinger et al., “Toward sustainable refrigeration systems: Life cycle assessment of a bench-scale solar-thermal adsorption refrigerator,” International Journal of Refrigeration, vol. 121, pp. 105–113, Jan. 2021, doi: 10.1016/J.IJREFRIG.2020.09.022.

[196] R. Horn et al., “Life Cycle Assessment of Innovative Materials for Thermal Energy Storage in Buildings,” Procedia CIRP, vol. 69, pp. 206–211, Jan. 2018, doi: 10.1016/J.PROCIR.2017.11.095.

[197] C. Colella and A. F. Gualtieri, “Cronstedt’s zeolite,” Microporous and Mesoporous Materials, vol. 105, no. 3, pp. 213–221, Oct. 2007, doi: 10.1016/J.MICROMESO.2007.04.056.

[198] R. Millini and G. Bellussi Eni SpA, “Zeolite Science and Perspectives,” Zeolite in Catalysis: Properties and Applications, Royal Society of Chemistry, Edited by: Jiri Cejka, Russell E morris, and Petr Nachtigall, pp. 1–36, Jun. 2017, doi: 10.1039/9781788010610-00001.

[199] R. Roque-Malherbe, “Applications of Natural Zeolites in Pollution Abatement and Industry,” Handbook of Surfaces and Interfaces of Materials, pp. 495–522, Jan. 2001, doi: 10.1016/B978-012513910-6/50069-4.

[200] K. Margeta and A. Farkaš, “Introductory Chapter: Zeolites - From Discovery to New Applications on the Global Market,” Zeolites - New Challenges, Intech Open, Jul. 2020, doi: 10.5772/INTECHOPEN.92907.

[201] Á. Berenguer Murcia, “Ordered Porous Nanomaterials: The Merit of Small,” ISRN Nanotechnology, vol. 2013, pp. 1–29, Feb. 2013, doi: 10.1155/2013/257047.

[202] Ch. Baerlocher, W. M. (Walter M.) Meier, D. H. (David H.) Olson, and W. M. (Walter M.). Meier, “Atlas of zeolite framework types.,” Elsevier, p. 302, 2001. ISBN: 978-0-444-50701-3 https://doi.org/10.1016/B978-0-444-50701-3.X5000-9

[203] “Zeolites : Minerals, Properties, Occurrence, Uses Geology Science.” Accessed: Nov. 16, 2023. [Online]. Available: https://geologyscience.com/minerals/zeolite/

[204] “Database of Zeolite Structures.” Accessed: Nov. 16, 2023. [Online]. Available: http://www.iza-structure.org/databases/

[205] F. B. Cortés, F. Chejne, F. Carrasco-Marín, C. Moreno-Castilla, and A. F. Pérez-Cadenas, “Water adsorption on zeolite 13X: Comparison of the two methods based on mass spectrometry and thermogravimetry,” Adsorption, vol. 16, no. 3, pp. 141–146, Aug. 2010, doi: 10.1007/S10450-010-9206-5/METRICS.

[206] V. Garshasbi, M. Jahangiri, and M. Anbia, “Equilibrium CO_2 adsorption on zeolite 13X prepared from natural clays,” Appl Surf Sci, vol. 393, pp. 225–233, Jan. 2017, doi: 10.1016/J.APSUSC.2016.09.161.

[207] Ş. Ç. Sayilgan, M. Mobedi, and S. Ülkü, “Effect of regeneration temperature on adsorption equilibria and mass diffusivity of zeolite 13x-water pair,” Microporous and Mesoporous Materials, vol. 224, pp. 9–16, Apr. 2016, doi: 10.1016/J.MICROMESO.2015.10.041.

[208] “Molecular sieves, 13X, 3-5mm (0.12-0.20in) beads, Thermo Scientific Chemicals.” Accessed: Nov. 26, 2023. [Online]. Available: https://www.thermofisher.com/order/catalog/product/L06085.30

[209] E. Pérez-Botella, S. Valencia, and F. Rey, “Zeolites in Adsorption Processes: State of the Art and Future Prospects,” Chem Rev, vol. 122, no. 24, pp. 17647–17695, Dec. 2022, doi: 10.1021/ACS.CHEMREV.2C00140/ASSET/IMAGES/MEDIUM/CR2C00140_M037.GIF.

[210] Y. Guo, H. Zhang, and Y. Liu, “Desorption characteristics and kinetic parameters determination of molecular sieve by thermogravimetric analysis/differential thermogravimetric analysis technique,” Adsorption Science and Technology, vol. 36, no. 7–8, pp. 1389–1404, Oct. 2018, doi: 10.1177/0263617418772665/ASSET/IMAGES/LARGE/10.1177_0263617418772665-FIG10.JPEG.

[211] T. Wajima and Y. Ikegami, “Synthesis of crystalline zeolite-13X from waste porcelain using alkali fusion,” Ceram Int, vol. 35, no. 7, pp. 2983–2986, Sep. 2009, doi: 10.1016/J.CERAMINT.2009.03.014.

[212] C. Forman, I. K. Muritala, R. Pardemann, and B. Meyer, “Estimating the global waste heat potential,” Renewable and Sustainable Energy Reviews, vol. 57, pp. 1568–1579, May 2016, doi: 10.1016/J.RSER.2015.12.192.

[213] E. Woolley, Y. Luo, and A. Simeone, “Industrial waste heat recovery: A systematic approach,” Sustainable Energy Technologies and Assessments, vol. 29, pp. 50–59, Oct. 2018, doi: 10.1016/J.SETA.2018.07.001.

[214] O. Farhat, J. Faraj, F. Hachem, C. Castelain, and M. Khaled, “A recent review on waste heat recovery methodologies and applications: Comprehensive review, critical analysis and potential recommendations,” Clean Eng Technol, vol. 6, p. 100387, Feb. 2022, doi: 10.1016/J.CLET.2021.100387.

[215] H. Jouhara, N. Khordehgah, S. Almahmoud, B. Delpech, A. Chauhan, and S. A. Tassou, “Waste heat recovery technologies and applications,” Thermal Science and Engineering Progress, vol. 6, pp. 268–289, Jun. 2018, doi: 10.1016/J.TSEP.2018.04.017.

[216] S. Broberg, S. Backlund, M. Karlsson, and P. Thollander, “Industrial excess heat deliveries to Swedish district heating networks: Drop it like it’s hot,” Energy Policy, vol. 51, pp. 332–339, Dec. 2012, doi: 10.1016/J.ENPOL.2012.08.031.

[217] M. T. Johansson and M. Söderström, “Electricity generation from low-temperature industrial excess heat-an opportunity for the steel industry,” Energy Effic, vol. 7, no. 2, pp. 203–215, Jun. 2014, doi: 10.1007/S12053-013-9218-6/TABLES/3.

[218] L. Miró, J. Gasia, and L. F. Cabeza, “Thermal energy storage (TES) for industrial waste heat (IWH) recovery: A review,” Appl Energy, vol. 179, pp. 284–301, Oct. 2016, doi: 10.1016/J.APENERGY.2016.06.147.

[219] S. Brückner, S. Liu, L. Miró, M. Radspieler, L. F. Cabeza, and E. Lävemann, “Industrial waste heat recovery technologies: An economic analysis of heat transformation technologies,” Appl Energy, vol. 151, pp. 157–167, Aug. 2015, doi: 10.1016/J.APENERGY.2015.01.147.

[220] H. Jarimi, D. Aydin, Z. Yanan, G. Ozankaya, X. Chen, and S. Riffat, “Review on the recent progress of thermochemical materials and processes for solar thermal energy storage and industrial waste

heat recovery," International Journal of Low-Carbon Technologies, vol. 14, no. 1, pp. 44–69, Mar. 2019, doi: 10.1093/IJLCT/CTY052.

[221] D. Jung, N. Khelifa, E. Lävemann, and R. Sizmann, "Energy Storage in Zeolites and Application to Heating and Air Conditioning," Stud Surf Sci Catal, vol. 24, no. C, pp. 555–562, Jan. 1985, doi: 10.1016/S0167-2991(08)65325-2.

[222] S. Rönsch, B. Auer, M. Kinateder, and K. Gleichmann, "Zeolite Heat Storage: Key Parameters from Experimental Results with Binder-Free NaY," Chem Eng Technol, vol. 43, no. 12, pp. 2530–2537, Dec. 2020, doi: 10.1002/CEAT.202000342.

[223] S. Hongois, F. Kuznik, P. Stevens, and J. J. Roux, "Development and characterisation of a new MgSO4−zeolite composite for long-term thermal energy storage," Solar Energy Materials and Solar Cells, vol. 95, no. 7, pp. 1831–1837, Jul. 2011, doi: 10.1016/J.SOLMAT.2011.01.050.

[224] K. Johannes, F. Kuznik, J. L. Hubert, F. Durier, and C. Obrecht, "Design and characterisation of a high powered energy dense zeolite thermal energy storage system for buildings," Appl Energy, vol. 159, pp. 80–86, Dec. 2015, doi: 10.1016/J.APENERGY.2015.08.109.

[225] P. Tatsidjodoung, N. Le Pierrès, J. Heintz, D. Lagre, L. Luo, and F. Durier, "Experimental and numerical investigations of a zeolite 13X/water reactor for solar heat storage in buildings," Energy Convers Manag, vol. 108, pp. 488–500, Jan. 2016, doi: 10.1016/J.ENCONMAN.2015.11.011.

[226] B. Mette, H. Kerskes, H. Drück, and H. Müller-Steinhagen, "New highly efficient regeneration process for thermochemical energy storage," Appl Energy, vol. 109, pp. 352–359, Sep. 2013, doi: 10.1016/J.APENERGY.2013.01.087.

[227] K. Lim, J. Kim, and J. Lee, “Comparative study on adsorbent characteristics for adsorption thermal energy storage system,” Int J Energy Res, vol. 43, no. 9, pp. 4281–4294, Jul. 2019, doi: 10.1002/ER.4553.

[228] A. Komorowska and M. Kuta, “Mobilized Thermal Energy Storage for Waste Heat Recovery and Utilization-Discussion on Crucial Technology Aspects,” Energies 2022, Vol. 15, Page 8713, vol. 15, no. 22, p. 8713, Nov. 2022, doi: 10.3390/EN15228713.

[229] M. Shehadeh, E. Kwok, J. Owen, and M. Bahrami, “Integrating Mobile Thermal Energy Storage (M-TES) in the City of Surrey’s District Energy Network: A Techno-Economic Analysis,” Applied Sciences 2021, Vol. 11, Page 1279, vol. 11, no. 3, p. 1279, Jan. 2021, doi: 10.3390/APP11031279.

[230] S. Fujii, T. Nakagaki, Y. Kanematsu, and Y. Kikuchi, “Prospective life cycle assessment for designing mobile thermal energy storage system utilizing zeolite,” J Clean Prod, vol. 365, p. 132592, Sep. 2022, doi: 10.1016/J.JCLEPRO.2022.132592.

[231] A. Krönauer, E. Lävemann, S. Brückner, and A. Hauer, “Mobile Sorption Heat Storage in Industrial Waste Heat Recovery,” Energy Procedia, vol. 73, pp. 272–280, Jun. 2015, doi: 10.1016/J.EGYPRO.2015.07.688.

[232] Z. Zhang, H. H. Mortensen, J. V. Jensen, and M. A. E. Andersen, “Fuel cell and battery powered forklifts,” 2013 9th IEEE Vehicle Power and Propulsion Conference, IEEE VPPC 2013, pp. 164–168, 2013, doi: 10.1109/VPPC.2013.6671683.

[233] B. Dawoud, E. H. Amer, and D. M. Gross, “Experimental investigation of an adsorptive thermal energy storage,” Int J Energy Res, vol. 31, no. 2, pp. 135–147, Feb. 2007, doi: 10.1002/ER.1235.

[234] D. Dicaire and F. H. Tezel, “Use of adsorbents for thermal energy storage of solar or excess heat: improvement of energy density,” Int J Energy Res, vol. 37, no. 9, pp. 1059–1068, Jul. 2013, doi: 10.1002/ER.2913.

[235] D. P. Gatley “Understanding Psychrometrics,” American Society of Heating, ISBN: 1931862834, 9781931862837, 2013.

[236] D. Dicaire and F. H. Tezel, “Use of adsorbents for thermal energy storage of solar or excess heat: improvement of energy density,” Int J Energy Res, vol. 37, no. 9, pp. 1059–1068, Jul. 2013, doi: 10.1002/ER.2913.

[237] D. Lefebvre, P. Amyot, B. Ugur, and F. H. Tezel, “Adsorption Prediction and Modeling of Thermal Energy Storage Systems: A Parametric Study,” Ind Eng Chem Res, vol. 55, no. 16, pp. 4760–4772, Apr. 2016, doi: 10.1021/acs.iecr.5b04767.

[238] D. Dicaire and F. H. Tezel, “Regeneration and efficiency characterization of hybrid adsorbent for thermal energy storage of excess and solar heat,” Renew Energy, vol. 36, no. 3, pp. 986–992, Mar. 2011, doi: 10.1016/J.RENENE.2010.08.031.

[239] J. Jänchen, D. Ackermann, H. Stach, and W. Brösicke, “Studies of the water adsorption on Zeolites and modified mesoporous materials for seasonal storage of solar heat,” Solar Energy, vol. 76, no. 1–3, pp. 339–344, Jan. 2004, doi: 10.1016/J.SOLENER.2003.07.036.

[240] Y. Hua, B. Ugur, and F. Handan Tezel, “Adsorbent screening for thermal energy storage application,” Solar Energy Materials and Solar Cells, vol. 196, pp. 119–123, Jul. 2019, doi: 10.1016/J.SOLMAT.2019.01.052.

[241] M. Gaeini, R. van Alebeek, L. Scapino, H. A. Zondag, and C. C. M. Rindt, “Hot tap water production by a 4 kW sorption segmented reactor in household scale for seasonal heat storage,” J Energy Storage, vol. 17, pp. 118–128, Jun. 2018, doi: 10.1016/J.EST.2018.02.014.

[242] J. Lizana, R. Chacartegui, A. Barrios-Padura, and C. Ortiz, “Advanced low-carbon energy measures based on thermal energy storage in buildings: A review,” Renewable and Sustainable Energy Reviews, vol. 82, no. October 2017, pp. 3705–3749, 2018, doi: 10.1016/j.rser.2017.10.093.

[243] B. Dawoud, E. H. Amer, and D. M. Gross, “Experimental investigation of an adsorptive thermal energy storage,” Int J Energy Res, vol. 31, no. 2, pp. 135–147, Feb. 2007, doi: 10.1002/ER.1235.

[244] S. Hongois, F. Kuznik, P. Stevens, and J. J. Roux, “Development and characterisation of a new MgSO4−zeolite composite for long-term thermal energy storage,” Solar Energy Materials and Solar Cells, vol. 95, no. 7, pp. 1831–1837, Jul. 2011, doi: 10.1016/J.SOLMAT.2011.01.050.

[245] D. Dicaire and F. H. Tezel, “Regeneration and efficiency characterization of hybrid adsorbent for thermal energy storage of excess and solar heat,” Renew Energy, vol. 36, no. 3, pp. 986–992, Mar. 2011, doi: 10.1016/J.RENENE.2010.08.031.

[246] J. Jänchen and H. Stach, “Shaping adsorption properties of nano-porous molecular sieves for solar thermal energy storage and heat pump applications,” Solar Energy, vol. 104, pp. 16–18, Jun. 2014, doi: 10.1016/J.SOLENER.2013.07.018.

[247] C. Finck et al., “Experimental Results of a 3 kWh Thermochemical Heat Storage Module for Space Heating Application,” Energy Procedia, vol. 48, pp. 320–326, Jan. 2014, doi: 10.1016/J.EGYPRO.2014.02.037.

[248] B. Zettl, G. Englmair, and G. Steinmaurer, “Development of a revolving drum reactor for open-sorption heat storage processes,” Appl Therm Eng, vol. 70, no. 1, pp. 42–49, Sep. 2014, doi: 10.1016/J.APPLTHERMALENG.2014.04.069.

[249] R. Köll et al., “An experimental investigation of a realistic-scale seasonal solar adsorption storage system for buildings,” Solar Energy, vol. 155, pp. 388–397, Oct. 2017, doi: 10.1016/J.SOLENER.2017.06.043.

[250] R. Zhu, B. Han, M. Lin, and Y. Yu, “Experimental investigation on an adsorption system for producing chilled water,” International Journal of Refrigeration, vol. 15, no. 1, pp. 31–34, Jan. 1992, doi: 10.1016/0140-7007(92)90064-2.

[251] C. Arzbaecher, E. Fouche, and K. Parmenter, “Industrial Waste-Heat Recovery: Benefits and Recent Advancements in Technology and Applications,” American Council for an Energy-Efficient Economy (ACEEE), 2007.

[252] B. Mette, H. Kerskes, and H. Drück, “Experimental and Numerical Investigations of Different Reactor Concepts for Thermochemical Energy Storage,” Energy Procedia, vol. 57, pp. 2380–2389, Jan. 2014, doi: 10.1016/J.EGYPRO.2014.10.246.

[253] R. Weber, S. Asenbeck, H. Kerskes, and H. Drück, “SolSpaces – Testing and Performance Analysis of a Segmented Sorption Store for Solar Thermal Space Heating,” Energy Procedia, vol. 91, pp. 250–258, Jun. 2016, doi: 10.1016/J.EGYPRO.2016.06.214.

[254] A. Lass-Seyoum, M. Blicker, D. Borozdenko, T. Friedrich, and T. Langhof, “Transfer of laboratory results on closed sorption thermo- chemical energy storage to a large-scale technical system,” Energy Procedia, vol. 30, pp. 310–320, Jan. 2012, doi: 10.1016/J.EGYPRO.2012.11.037.

[255] “Shining brightly | MIT News | Massachusetts Institute of Technology.” Accessed: Jul. 30, 2023. [Online]. Available: https://news.mit.edu/2011/energy-scale-part3-1026

[256] C. J. Rhodes, “Solar Energy: Principles and Possibilities,” Science Progress (2010), 93(1), 37–112, Mar. 2010, doi: 10.3184/003685010X12626410325807.

[257] Y. Zhang and R. Wang, “Sorption thermal energy storage: Concept, process, applications and perspectives,” Energy Storage Mater, vol. 27, pp. 352–369, May 2020, doi: 10.1016/J.ENSM.2020.02.024.

[258] Z. Zeng et al., “Predictive thermal performance analysis of T-wall based adsorption thermal battery for solar building heating,” Energy, vol. 294, p. 130820, May 2024, doi: 10.1016/J.ENERGY.2024.130820.

[259] Y. Tian and C. Y. Zhao, “A review of solar collectors and thermal energy storage in solar thermal applications,” Appl Energy, vol. 104, pp. 538–553, Apr. 2013, doi: 10.1016/J.APENERGY.2012.11.051.

[260] S. Gorjian, H. Ebadi, F. Calise, A. Shukla, and C. Ingrao, “A review on recent advancements in performance enhancement techniques for low-temperature solar collectors,” Energy Convers Manag, vol. 222, p. 113246, Oct. 2020, doi: 10.1016/J.ENCONMAN.2020.113246.

[261] D. Lefebvre and F. H. Tezel, “A review of energy storage technologies with a focus on adsorption thermal energy storage processes for heating applications,” Renewable and Sustainable Energy Reviews, vol. 67, pp. 116–125, Jan. 2017, doi: 10.1016/J.RSER.2016.08.019.

[262] A. Mahesh, “Solar collectors and adsorption materials aspects of cooling system,” Renewable and Sustainable Energy Reviews, vol. 73, pp. 1300–1312, Jun. 2017, doi: 10.1016/J.RSER.2017.01.144.

[263] Y. M. Liu, Z. X. Yuan, X. Wen, and C. X. Du, “Evaluation on performance of solar adsorption cooling of silica gel and SAPO-34 zeolite,” Appl Therm Eng, vol. 182, p. 116019, Jan. 2021, doi: 10.1016/J.APPLTHERMALENG.2020.116019.

[264] H. Ambarita and H. Kawai, “Experimental study on solar-powered adsorption refrigeration cycle with activated alumina and activated carbon as adsorbent,” Case Studies in Thermal Engineering, vol. 7, pp. 36–46, Mar. 2016, doi: 10.1016/J.CSITE.2016.01.006.

[265] Z. Zeng, X. Yang, B. Zhao, Z. Chen, K. J. E. Chua, and R. Wang, “A scalable solar-based adsorption thermal battery for day and night heating in a low-carbon scenario,” Energy Environ Sci, vol. 17, no. 2, pp. 800–812, Jan. 2024, doi: 10.1039/D3EE03519K.

[266] M. Li and R. Z. Wang, “Heat and mass transfer in a flat plate solar solid adsorption refrigeration ice maker,” Renew Energy, vol. 28, no. 4, pp. 613–622, Apr. 2003, doi: 10.1016/S0960-1481(02)00094-0.

[267] T. B. Sitorus, F. Napitupulu, H. Ambarita, and T. Manik, “Performance Analyses of Solar Adsorption Refrigeration System Using Indonesian Activated Carbon and Methanol as Working Pair,” 6th International Conference on Trends in Agricultural Engineering, 7 - 9 September 2016, Prague, Czech Republic

[268] A. Elkholy, M. Rouby, and R. Kempers, “Characterization of the anisotropic thermal conductivity of additively manufactured components by fused filament fabrication,” Progress in Additive Manufacturing, vol. 4, no. 4, pp. 497–515, Dec. 2019, doi: 10.1007/S40964-019-00098-2/FIGURES/21.

[269] A. Elkholy and R. Kempers, “An accurate steady-state approach for characterizing the thermal conductivity of Additively manufactured polymer composites,” Case Studies in Thermal Engineering, vol. 31, p. 101829, Mar. 2022, doi: 10.1016/J.CSITE.2022.101829.

[270] “Ullmann’s Encyclopedia of Industrial Chemistry,” Ullmann’s Encyclopedia of Industrial Chemistry, Mar. 2003, doi: 10.1002/14356007.

[271] C. Feng et al., “Key technology and application analysis of zeolite adsorption for energy storage and heat-mass transfer process: A review,” Renewable and Sustainable Energy Reviews, vol. 144, p. 110954, Jul. 2021, doi: 10.1016/J.RSER.2021.110954.

[272] B. Baghapour, M. Rouhani, A. Shara, S. B. Kalhori, and M. Bahrami, “A pressure drop study for packed bed adsorption thermal energy storage,” Appl Therm Eng, vol. 138, pp. 731–739, 2018, doi: 10.1016/j.applthermaleng.2018.03.098.

[273] S. P. Casey, D. Aydin, J. Elvins, and S. Riffat, “Salt impregnated desiccant matrices for ‘open’ thermochemical energy conversion and storage – Improving energy density utilisation through hygrodynamic & thermodynamic reactor design,” Energy Convers Manag, vol. 142, pp. 426–440, Jun. 2017, doi: 10.1016/J.ENCONMAN.2017.03.066.

[274] B. Dawoud, E. H. Amer, and D. M. Gross, “Experimental investigation of an adsorptive thermal energy storage,” Int J Energy Res, vol. 31, no. 2, pp. 135–147, Feb. 2007, doi: 10.1002/ER.1235.

[275] I. Dincer, “Thermal energy storage systems as a key technology in energy conservation,” Int J Energy Res, vol. 26, no. 7, pp. 567–588, 2002, doi: 10.1002/er.805.

[276] M. Sun et al., “Roles of thermal energy storage technology for carbon neutrality,” Carbon Neutrality 2023 2:1, vol. 2, no. 1, pp. 1–54, Jun. 2023, doi: 10.1007/S43979-023-00052-W.

[277] G. Alva, Y. Lin, and G. Fang, “An overview of thermal energy storage systems,” Energy, vol. 144, pp. 341–378, 2018, doi: 10.1016/j.energy.2017.12.037.

[278] I. Gur, K. Sawyer, and R. Prasher, “Searching for a better thermal battery,” Science (1979), vol. 335, no. 6075, pp. 1454–1455, Mar. 2012, doi: 10.1126/SCIENCE.1218761/ASSET/92ED7784-0CCE-45E6-9C90-B06C657F39B1/ASSETS/GRAPHIC/335_1454_F1.GIF.

[279] Z. Li et al., “Applications and technological challenges for heat recovery, storage and utilisation with latent thermal energy storage,” Appl Energy, vol. 283, p. 116277, Feb. 2021, doi: 10.1016/J.APENERGY.2020.116277.

[280] X. Yu et al., “Synergistic improvement of melting rate and heat storage capacity by a rotation-based method for shell-and-tube latent thermal energy storage,” Appl Therm Eng, vol. 219, p. 119480, Jan. 2023, doi: 10.1016/J.APPLTHERMALENG.2022.119480.

[281] Z. Li et al., “Role of different energy storage methods in decarbonizing urban distributed energy systems: A case study of thermal and electricity storage,” J Energy Storage, vol. 73, p. 108931, Dec. 2023, doi: 10.1016/J.EST.2023.108931.

[282] D. Lefebvre and F. H. Tezel, “A review of energy storage technologies with a focus on adsorption thermal energy storage processes for heating applications,” Renewable and Sustainable Energy Reviews, vol. 67, pp. 116–125, Jan. 2017, doi: 10.1016/J.RSER.2016.08.019.

[283] A. Frazzica and A. Freni, “Adsorbent working pairs for solar thermal energy storage in buildings,” Renew Energy, vol. 110, pp. 87–94, Sep. 2017, doi: 10.1016/J.RENENE.2016.09.047.

[284] N. L. Panwar, S. C. Kaushik, and S. Kothari, “Role of renewable energy sources in environmental protection: A review,” Renewable and Sustainable Energy Reviews, vol. 15, no. 3, pp. 1513–1524, Apr. 2011, doi: 10.1016/J.RSER.2010.11.037.

[285] C. Suresh and R. P. Saini, “Review on solar thermal energy storage technologies and their geometrical configurations,” Int J Energy Res, vol. 44, no. 6, pp. 4163–4195, May 2020, doi: 10.1002/ER.5143.

[286] G. Alva, L. Liu, X. Huang, and G. Fang, “Thermal energy storage materials and systems for solar energy applications,” Renewable and Sustainable Energy Reviews, vol. 68, pp. 693–706, Feb. 2017, doi: 10.1016/J.RSER.2016.10.021.

[287] A. Gautam and R. P. Saini, “A review on technical, applications and economic aspect of packed bed solar thermal energy storage system,” J Energy Storage, vol. 27, p. 101046, Feb. 2020, doi: 10.1016/J.EST.2019.101046.

[288] D. Aydin, S. P. Casey, and S. Riffat, “The latest advancements on thermochemical heat storage systems,” Renewable and Sustainable Energy Reviews, vol. 41, pp. 356–367, Jan. 2015, doi: 10.1016/J.RSER.2014.08.054.

[289] A. H. Abedin and M. A. Rosen, “Closed and open thermochemical energy storage: Energy- and exergy-based comparisons,” Energy, vol. 41, no. 1, pp. 83–92, May 2012, doi: 10.1016/J.ENERGY.2011.06.034.

[290] S. Rönsch, B. Auer, M. Kinateder, and K. Gleichmann, “Zeolite Heat Storage: Key Parameters from Experimental Results with Binder-Free NaY,” Chem Eng Technol, vol. 43, no. 12, pp. 2530–2537, Dec. 2020, doi: 10.1002/CEAT.202000342.

[291] N. Yu, R. Z. Wang, and L. W. Wang, “Sorption thermal storage for solar energy,” Prog Energy Combust Sci, vol. 39, no. 5, pp. 489–514, Oct. 2013, doi: 10.1016/J.PECS.2013.05.004.

[292] O. Bilgin, “Natural Zeolite Minerals as Storage of Solar Energy,” International Journal of Engineering Research & Technology (IJERT), vol. 3, no. 2, pp. 741–744, 2014, ISSN: 2278-0181

[293] J. Jänchen and H. Stach, “Shaping adsorption properties of nano-porous molecular sieves for solar thermal energy storage and heat pump applications,” Solar Energy, vol. 104, pp. 16–18, Jun. 2014, doi: 10.1016/J.SOLENER.2013.07.018.

[294] D. Dicaire and F. H. Tezel, “Use of adsorbents for thermal energy storage of solar or excess heat: improvement of energy density,” Int J Energy Res, vol. 37, no. 9, pp. 1059–1068, Jul. 2013, doi: 10.1002/ER.2913.

[295] S. A. Kalogirou, “Solar Energy Engineering: Processes and Systems: Second Edition,” Solar Energy Engineering: Processes and Systems: Second Edition, pp. 1–819, 2014, doi: 10.1016/C2011-0-07038-2.

[296] Y. Tian and C. Y. Zhao, “A review of solar collectors and thermal energy storage in solar thermal applications,” Appl Energy, vol. 104, pp. 538–553, Apr. 2013, doi: 10.1016/J.APENERGY.2012.11.051.

[297] D. P. Schneider, C. Deser, J. Fasullo, and K. E. Trenberth, “Climate data guide spurs discovery and understanding,” Eos (Washington DC), EOS, Transactions, American Geophysical Union, vol. 94, no. 13, pp. 121–122, Mar. 2013, doi: 10.1002/2013EO130001.

[298] S. T. Mohammad, H. H. Al-Kayiem, M. A. Aurybi, and A. K. Khlief, “Measurement of global and direct normal solar energy radiation in Seri Iskandar and comparison with other cities of Malaysia,”

Case Studies in Thermal Engineering, vol. 18, p. 100591, Apr. 2020, doi: 10.1016/J.CSITE.2020.100591.

[299] Z. Su et al., “Opportunities and strategies for multigrade waste heat utilization in various industries: A recent review,” Energy Convers Manag, vol. 229, p. 113769, Feb. 2021, doi: 10.1016/J.ENCONMAN.2020.113769.

[300] M. Papapetrou, G. Kosmadakis, A. Cipollina, U. La Commare, and G. Micale, “Industrial waste heat: Estimation of the technically available resource in the EU per industrial sector, temperature level and country,” Appl Therm Eng, vol. 138, pp. 207–216, Jun. 2018, doi: 10.1016/J.APPLTHERMALENG.2018.04.043.

[301] E. Scuiller, S. Bennici, P. Dutournié, and F. Principaud, “Towards industrial-scale adsorptive heat storage systems: From state-of-the-art selected examples to preliminary conception guidelines,” J Energy Storage, vol. 53, p. 105103, Sep. 2022, doi: 10.1016/J.EST.2022.105103.

[302] A. Al Ezzi et al., “Experimental investigation of dehumidification and regeneration of zeolite coated energy exchanger,” International Journal of Thermofluids, vol. 15, p. 100164, Aug. 2022, doi: 10.1016/J.IJFT.2022.100164.

[303] S. Narayanan, X. Li, S. Yang, I. McKay, H. Kim, and E. N. Wang, “Design and optimization of high performance adsorption-based thermal battery,” Proceedings of the ASME 2013 Heat Transfer Summer Conference, HT 2013, vol. 1, 2013, doi: 10.1115/HT2013-17472.

[304] L. M. Sun and F. Meunier, “A detailed model for nonisothermal sorption in porous adsorbents,” Chem Eng Sci, vol. 42, no. 7, pp. 1585–1593, Jan. 1987, doi: 10.1016/0009-2509(87)80163-X.

[305] Y. Matsumoto et al., “Methods of Improving the Performance of Adsorption Thermophysical battery based on the Operating Conditions and Structure: A Review,” IOP Conf Ser Mater Sci Eng, vol. 928, no. 2, p. 022040, Nov. 2020, doi: 10.1088/1757-899X/928/2/022040.

[306] J. Chao et al., “Enhanced thermal conductivity and adsorption rate of zeolite 13X adsorbent by compression-induced molding method for sorption thermal battery,” Energy, vol. 240, p. 122797, Feb. 2022, doi: 10.1016/J.ENERGY.2021.122797.

[307] F. Schmidt, “Dissertation: Optimizing Adsorbents for Heat Storage Applications: Estimation of thermodynamic limits and Monte Carlo,” Accessed: 2004, [Online]. Available: http://www.freidok.uni-freiburg.de/volltexte/1506/pdf/Diss_final_online_UB_20041011.pdf

[308] H. Schreiber, F. Lanzerath, and A. Bardow, “Predicting performance of adsorption thermal energy storage: From experiments to validated dynamic models,” Appl Therm Eng, vol. 141, pp. 548–557, Aug. 2018, doi: 10.1016/J.APPLTHERMALENG.2018.05.094.

[309] C. H. Chen, J. H. Lu, J. C. Perng, and J. J. Chen, “Shallow Geothermal and Solar Energy-Driven Adsorption-Compression Hybrid Air Conditioning System,” 2023 7th International Conference on Green Energy and Applications, ICGEA 2023, pp. 209–212, 2023, doi: 10.1109/ICGEA57077.2023.10125690.

[310] R. H. Mohammed, O. Mesalhy, M. L. Elsayed, and L. C. Chow, “Performance evaluation of a new modular packed bed for adsorption cooling systems,” Appl Therm Eng, 2018, doi: 10.1016/j.applthermaleng.2018.02.103.

[311] Q. W. Pan, R. Z. Wang, L. W. Wang, and D. Liu, “Design and experimental study of a silica gel-water adsorption chiller with modular adsorbers,” International Journal of Refrigeration, vol. 67, pp. 336–344, 2016, doi: 10.1016/j.ijrefrig.2016.03.001.

[312] S. Vasta, G. Giacoppo, O. Barbera, L. Calabrese, L. Bonaccorsi, and A. Freni, “Innovative zeolite coatings on graphite plates for advanced adsorbers,” Appl Therm Eng, vol. 72, no. 2, pp. 153–159, Nov. 2014, doi: 10.1016/J.APPLTHERMALENG.2014.04.079.

[313] B. Choudhury, B. B. Saha, P. K. Chatterjee, and J. P. Sarkar, “An overview of developments in adsorption refrigeration systems towards a sustainable way of cooling,” Appl Energy, vol. 104, pp. 554–567, Apr. 2013, doi: 10.1016/J.APENERGY.2012.11.042.

[314] A. Buonomano, F. Calise, A. Palombo, and M. Vicidomini, “Adsorption chiller operation by recovering low-temperature heat from building integrated photovoltaic thermal collectors: Modelling and simulation,” Energy Convers Manag, vol. 149, pp. 1019–1036, Oct. 2017, doi: 10.1016/J.ENCONMAN.2017.05.005.

[315] S. Shervani, I. Riad, C. Strong, and F. H. Tezel, “A sustainable bio-adsorbent for thermal energy storage for space heating applications,” Can J Chem Eng, vol. 101, no. 3, pp. 1162–1170, Mar. 2023, doi: 10.1002/CJCE.24648.

[316] “Learn the facts: Weight affects fuel consumption?”, Natural Resources Canada, Canada, Accessed: Jul. 2023 Available: https://natural-resources.canada.ca/sites/www.nrcan.gc.ca/files/oee/pdf/transportation/fuel-efficient-technologies/autosmart_factsheet_16_e.pdf

[317] K. Johannes, F. Kuznik, J. L. Hubert, F. Durier, and C. Obrecht, “Design and characterisation of a high powered energy dense zeolite thermal energy storage system for buildings,” Appl Energy, vol. 159, pp. 80–86, Dec. 2015, doi: 10.1016/J.APENERGY.2015.08.109.

[318] J.-C. Hadorn and G. Berney -Base, “IEA Solar Heating and Cooling Programme TASK 32: Advanced Storage Concepts for Solar and Low Energy Buildings Operating agent of IEA SHC Task 32 on behalf the Swiss Federal Office of Energy”. Ecostock conference 2006 – Proposed paper, Accessed: September 2023, Available: http://www.archive.iea-shc.org/data/sites/1/publications/task32-ecostock2006_paper.pdf

[319] H. Bhowmik and R. Amin, “Efficiency improvement of flat plate solar collector using reflector,” Energy Reports, vol. 3, pp. 119–123, Nov. 2017, doi: 10.1016/J.EGYR.2017.08.002.

[320] “Solar Panels Power Calculator for Toronto, Ontario Canada.” Accessed: Jul. 15, 2024. [Online]. Available: https://solarcalculator.ca/report/Ontario/Toronto/